Étude de l'implémentation de supraconducteurs à haute température critique dans les aimants d'accélérateur

Jérôme Fleiter

To cite this version:

Jérôme Fleiter. Étude de l'implémentation de supraconducteurs à haute température critique dans les aimants d'accélérateur. Sciences de l'ingénieur [physics]. Université de Grenoble, 2013. Français. NNT : . tel-00911430

HAL Id: tel-00911430
https://theses.hal.science/tel-00911430

Submitted on 29 Nov 2013

UNIVERSITÉ DE GRENOBLE

THÈSE

Pour obtenir le grade de

DOCTEUR DE L'UNIVERSITÉ DE GRENOBLE

Spécialité : **Génie Électrique**

Arrêté ministériel : 7 août 2006

Présentée par

Jérôme Fleiter

Thèse dirigée par **Pascal Tixador**
et codirigée par **Amalia Ballarino**

préparée au sein **l'Institut Néel et du CERN**
et de **l'École Doctorale EEATS**

Étude de l'implémentation de supraconducteurs à haute température critique dans les aimants d'accélérateur

Thèse soutenue publiquement le **16 mai 2013**,
devant le jury composé de :

Yifeng Yang
Professeur (Université de Southampton), Rapporteur
Daniel Ciazynski,
Docteur (CEA Cadarache), Rapporteur
Arnaud Devred
Docteur (ITER), Examinateur
Lucio Rossi
Professeur (Université de Milan), Examinateur

Contents

Chapter 1

Résumé de thèse

1.1 Introduction générale

Les collisionneurs de particules sont des outils indispensables pour l'étude et la compréhension des lois fondamentales de la physique. Le plus grand accélérateur de particules jamais construit, le Large Hadron Collider (LHC), installé au CERN, est un accélérateur circulaire de type synchrotron à faisceaux contrarotatifs. Le LHC dispose de quatre points de collisions où les produits issus des interactions entre particules sont analysés par des détecteurs. Dans un synchrotron, les particules chargées sont accélérées à l'aide de champs électriques (cavités et quadripôles radio fréquence) et sont manipulées avec des inductions magnétiques (électroaimants). Dans des conditions relativistes, l'énergie des particules E_{beam} (en TeV) est proportionnelle au produit de l'induction magnétique des dipôles B_d (en T) et du rayon de courbure du faisceau R_b (en km) :

$$E_{beam} = 0,3\ R_b\ B_d \tag{1.1}$$

L'énergie maximale des particules dans un accélérateur circulaire de dimensions données est donc limitée par l'induction des dipôles. Dans le LHC, qui emploie 1232 dipôles supraconducteurs en Nb-Ti générant une induction maximale de 8,3 T, les particules évoluent sur une trajectoire circulaire de 4,3 km de rayon et ont donc une énergie de collision de 14 TeV dans le centre de masse. L'opération du LHC depuis 2009 a permis au CERN d'annoncer en 2012 la découverte d'une particule s'apparentant au boson de Higgs, la particule liée au mécanisme donnant une masse aux particules élémentaires.

La communauté scientifique est en demande de collisions entre particules à plus hautes énergies que celles produites par le LHC. Des aimants dipôlaires générant des inductions magnétiques plus élevées sont donc nécessaires. Le supraconducteur Nb_3Sn est une option pour les dipôles générant jusqu'à environ 14 T. Une possible augmentation de l'énergie de collision du LHC de 14 TeV à 33 TeV est actuellement en discussion. Ce niveau d'énergie nécessitera l'utilisation de supraconducteurs à haute température (HTS) ayant des inductions irréversibles bien supérieures à celles du Nb_3Sn et du Nb-Ti. Trois types de conducteurs HTS sont industriellement disponibles : YBCO, Bi-2212 et Bi-2223. A basse température les conducteurs YBCO présentent une induction irréversible et une densité de courant critique supérieure à celles des conducteurs Bi-2212 et Bi-2223. En outre, contrairement aux conducteurs Bi-2212, les conducteurs YBCO ne nécessitent pas de délicat traitement thermique post câblage, ce qui simplifie leur utilisation et leur mise en oeuvre. Au nominal, les aimants supraconducteurs d'accélérateur fonctionnent à des courants de l'ordre de 10-20 kA. Ce niveau de courant bien supérieur aux capacités individuelles de transport des conducteurs HTS requerra l'utilisation de câbles supraconducteurs multibrins.

A partir de là, je reformulerais mes travaux de recherche. Tout d'abord (chapitre 2), je présente les différentes contraintes portant sur les aimants HTS d'accélérateurs ainsi que les inductions magnétiques ultimes qu'ils pourront produire. Puis je caractérise les performances des conducteurs HTS dans les conditions environnementales des aimants d'accélérateur (chapitre 3). J'apporte par la suite une description mathématique de ces performances (chapitre 4) permettant de calculer les marges opérationnelles des dipôles en matériaux HTS. Enfin, je caractérise les performances des câbles HTS à fort courant (chapitre 5) que je compare à celles attendues (chapitre 6).

1.2 Chapitre 2 : Les aimants d'accélérateurs de particules : état de l'art et perspectives pour les matériaux HTS

Les contraintes se rapportant aux aimants d'accélérateurs sont décrites dans ce chapitre et leur conception de base détaillée. Une nouvelle formulation semi-analytique permettant d'estimer les performances ultimes des dipôles d'accélérateurs en matériaux HTS est introduite. Les aimants d'accélérateur requièrent l'utilisation de câble supraconducteur à fort courant. Les différentes topologies de câbles HTS à fort courant sont présentées dans une courte revue et les plus prometteuses pour une application dans les aimants d'accélérateur sont sélectionnées.

1.2.1 Contraintes reposant sur le design des aimants d'accélérateur

De nombreuses contraintes reposent sur le design des aimants d'accélérateurs. Les plus importantes sont listées ci-dessous.

Ouverture

Dans les collisionneurs, les faisceaux de particules circulant dans les ouvertures des aimants ont une certaine extension spatiale, ce qui impose une ouverture minimale de l'ordre de 30-40 mm. Un tube faisceau ainsi qu'un tube d'écrantage doivent également être insérés dans l'ouverture des aimants. Dans le cas du LHC l'ouverture des aimants est de 56 mm dans les arcs et de 70 mm dans les zones d'interactions ou les dimensions transverses du faisceau sont plus importantes.

Utilisation de câbles forts courants

Les aimants supraconducteurs d'accélérateur stockent de haute énergie magnétique. Ils utilisent des câbles à fort ampérage afin de minimiser leur temps de décharge en cas de défaillance (perte de l'état supraconducteur). Cette minimisation permet de contenir la température atteinte lors de la décharge résistive et ainsi de préserver l'intégrité de l'aimant. **L'utilisation de câbles supraconducteurs multibrins fort courant présente de nombreux autres avantages :**

- **le nombre de tour dans le bobinage est réduit** permettant de limiter les longueurs unitaires de fil à produire. Le bobinage en est facilité.
- **une plus grande fiabilité** : en cas de défaut localisé ou d'un démarrage de transition d'un brin, le courant qu'il transporte peut être redistribué sur les autres.
- **la réduction du niveau d'isolation électrique à la masse.** Compte tenu de la réduction d'inductance, le niveau d'isolation électrique à la masse est automatiquement réduit. Cette réduction s'applique pour le bobinage mais aussi pour toute l'instrumentation.

L'utilisation de câbles multibrins fort courant présente également des désavantages :

- **la flexibilité sur la minimisation des multipoles est réduite.** Le câble fort courant impose moins de flexibilité sur le positionnement des conducteurs autour de l'ouverture. Ce qui complexifie l'optimisation magnétique.
- **une distorsion dynamique de l'induction magnétique.** Des courants de couplages entre les brins d'un câble d'aimant d'accélérateur détériorent la qualité de l'induction. Le niveau de courant de couplage doit être maitrisé afin de réduire les distorsions de l'induction tout en assurant un échange possible entre conducteurs pour ne pas réduire la stabilité électrique.

1.2.2 Design d'un aimant de type dipôle

Dans une première étape du design des aimants d'accélérateur, ceux-ci sont considérés comme étant infiniment long. Cette approximation est justifiée par le fait que leurs dimensions transverses sont habituellement plusieurs ordres de grandeurs plus petites devant leur longueur. Une première étude 2D de la section droite de ces aimants permet de statuer sur leur faisabilité. Les bases du design 2 D des aimants dipolaires d'accélérateur sont introduites dans cette section. Un paramétrage analytique est alors introduit afin de prédire les performances de tels aimants bobinés à partir de conducteur HTS.

Configuration magnétique idéale et réelle des dipôles

Dans les collisionneurs circulaires, les particules circulent de nombreuses fois dans l'ouverture des dipôles, ils doivent donc générer une qualité d'induction magnétique élevée, afin de limiter les instabilités du faisceau. Deux configurations magnétiques permettent de générer une induction purement dipolaire : l'intersection d'ellipse portant des densités volumique de courant de signe opposé et une répartition en $cos\phi$ de la densité de courant portée par un tube circulaire. Ces deux répartitions idéales de courant sont difficiles à mettre en oeuvre et sont souvent approximées par une configuration en secteur angulaire dans laquelle les conducteurs sont répartis en « éventail » autour de l'ouverture circulaire avec une densité de courant constante (figure 1.1). Cette configuration est celle utilisée pour les aimants d'accélérateurs actuels en Nb-Ti (HERA, Tevatron, LHC...) avec une induction record de 8,3 T pour le LHC.

La répartition idéale de courant peut aussi être approchée par un arrangement en blocs rectangulaires de densité de courant homogène, comme indiqué dans la figure 1.1. Cette configuration en blocs a été retenue par plusieurs groupes pour des aimants à hautes inductions en Nb$_3$Sn afin de limiter les contraintes mécaniques sur le bobinage. Une induction dipolaire record de 16 T a été générée par l'aimant HD1.

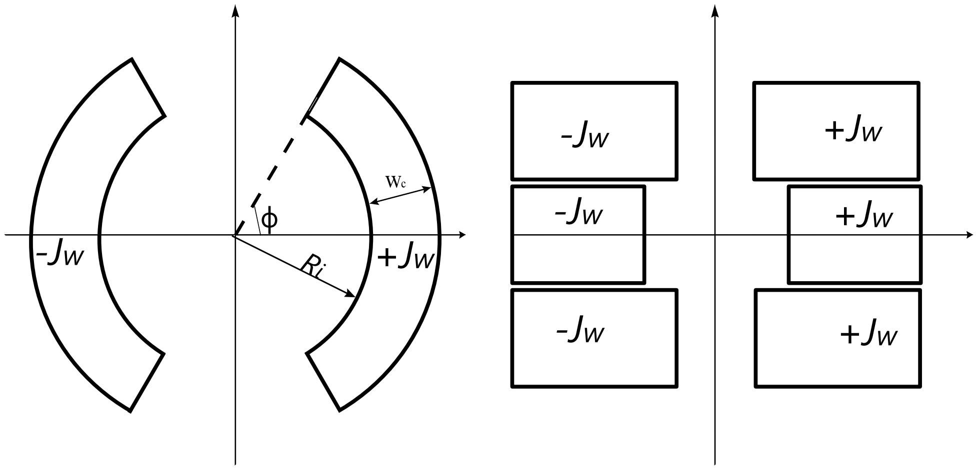

Figure 1.1: La répartition de la densité de courant en secteurs angulaires (gauche) et en blocs (droite) des dipôles d'accélérateurs.

Contraintes mécaniques dans le bobinage des dipôles

Dans le bobinage d'un aimant d'accélérateur, les forces de Laplace induisent de fortes contraintes mécaniques transverses sur les supraconducteurs. Les matériaux supraconducteurs sont sensibles à la contrainte : les conducteurs BSCCO présentent une réduction de leurs performances pour des contraintes transverses excédant 100-120 MPa. Les conducteurs YBCO sont quant à eux plus résilient avec des seuils supérieurs à 300 MPa. Les forces magnétiques dépendent de la géométrie de la bobine, qui doit donc être soigneusement conçue afin de ne pas dépasser les limites mécaniques du supraconducteur.

Culasse magnétique

Une culasse en matériau magnétique (fer) encerclant le bobinage d'un électroaimant a pour fonction première de limiter l'induction de fuite, mais également d'augmenter celle dans l'ouverture de l'aimant. La quantité de supraconducteur nécessaire pour générer une induction souhaitée est ainsi réduite.

1.2.3 Performances d'un aimant HTS

Les deux caractéristiques principales des supraconducteurs pour les aimants d'accélérateurs, sont : la densité de courant critique (J_{ce}) et l'induction irréversible (B_{irr}). La densité de courant critique est le rapport du courant critique (I_c) du conducteur à sa section transverse. Le courant critique (I_c) étant défini comme le courant au-dessus duquel le conducteur est dissipatif (seuil de 1 μV/cm, voir chapitre 3). Au-dessus de l'induction irréversible (B_{irr}), le I_c devient nul. Ces deux paramètres dépendent de la température (voir le chapitre 4). L'induction ultime que produit un aimant supraconducteur est atteinte dès qu'en un point de son bobinage la densité de courant atteint ou dépasse J_{ce}. Les performances des aimants d'accélérateurs sont donc intrinsèquement limitées par celles du supraconducteur. Dans cette section, les performances des aimants HTS de type solénoïde et dipôle sont tout d'abord passées en revue. Il s'ensuit une estimation des performances ultimes des dipôles d'accélérateur bobinés à partir de conducteurs HTS.

Revue des performances des aimants HTS

Après la découverte des matériaux HTS en 1986, leur potentiel pour générer des hautes inductions magnétiques fut reconnus et plusieurs démonstrateurs, furent construit et opérés. Les inductions les plus signifiantes furent obtenues par des aimants du type solénoïde avec un record de 35,4 T dont 4,2 T provenant d'une bobine en YBCO avec une densité de courant dans le conducteur de 308 A/mm^2. Le record d'induction pour un solénoïde en BSCCO est de 25 T dont 5 T provenant d'une bobine en Bi-2212 avec une densité de courant de seulement 80 A/mm^2.

Dans le même temps seulement quelques dipôles en HTS furent construits. Une induction dipolaire record de 2,6 T (à 18 K) fut obtenue en 2012 par un aimant YBCO produit par la firme Danfysik (figure 1.2).

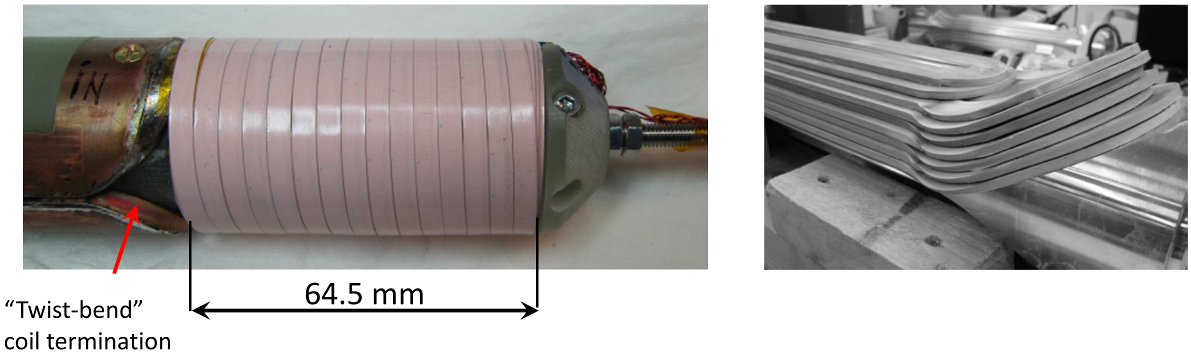

Figure 1.2: Le solénoïde YBCO générant 4,2 T dans une induction de fond de 31,2 T (gauche) et le dipôle YBCO générant 2,6 T (droite).

Les performances maximales des dipôles HTS

L'induction maximale créée par un dipôle d'accélérateur de type secteur angulaire en matériau HTS tel que représenté sur la figure 1.1 est donné par l'expression :

$$B_{0,ss} = \frac{1}{\lambda}\left(\frac{\gamma_0 w_c \lambda K r_0}{1+\gamma_0 w_c \lambda K d}\right)^{\frac{1}{s+1}} \tag{1.2}$$

Ou w_c est l'épaisseur du bobinage. La surface critique du supraconducteur est décrite par s, r_0 et d. Les facteurs de forme de l'aimant sont γ_0, K et λ. Dans la figure 1.3, l'expression (1.2) est compilée pour des aimants ayant une ouverture de 30 mm. L'épaisseur du bobinage nécessaire pour générer une induction de 20 T est de 110 mm dans le cas du Bi-2212 et 90 mm pour l'YBCO (considéré sous induction perpendiculaire). Dans la même figure, l'induction générée par des dipôles en Nb-Ti et Nb_3Sn est reportée : elle sature respectivement à 11 T et 19 T. Une telle saturation n'apparaît pas dans les dipôles en YBCO ou Bi-2212 qui ont des inductions irréversibles bien plus élevées.

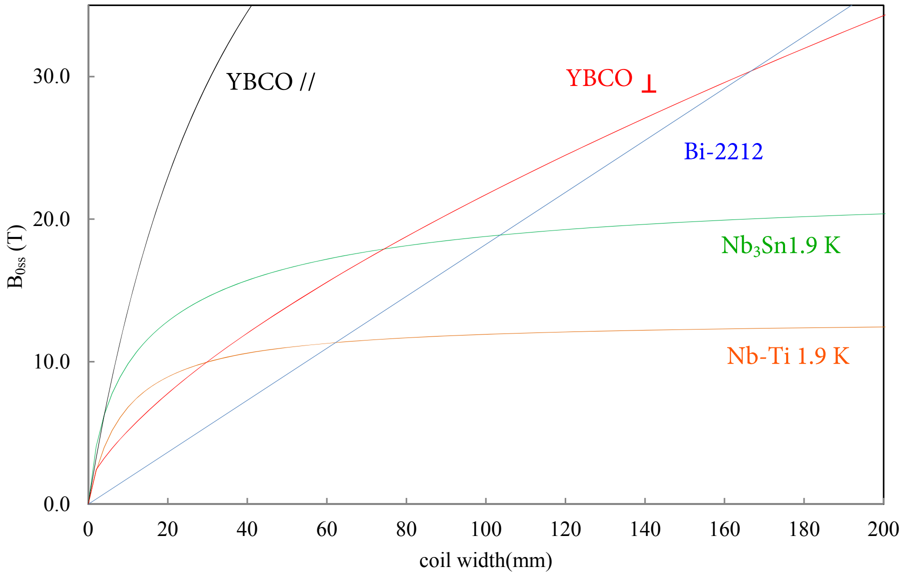

Figure 1.3: Le $B_{0,ss}$ des dipôles HTS de 30 mm d'ouverture en fonction de l'épaisseur du bobinage.

1.2.4 Revue des différents concepts de câbles supraconducteurs

Pour les aimants d'accélérateur, il est préférable d'avoir des supraconducteurs sous forme de fils. Les conducteurs disponibles sous forme de fils (Nb-Ti, Nb_3Sn et Bi-2212) sont applicables dans les câbles transposés de type Rutherford. Les conducteurs YBCO et Bi-2223 ne présentent de bonnes performances que sous la forme de rubans, qui sont applicables dans les câbles transposés de type Roebel. Des topologies alternatives de câbles non transposées sont également disponibles pour des conducteurs sous forme de rubans : les câbles autour d'un conduit et les câbles à empilement. Les différents concepts de câbles sont détaillés dans cette section et les plus adéquats pour les aimants d'accélérateur sont sélectionnés.

Câbles de type Rutherford

Le câble Rutherford est constitué de quelques dizaines de brins, torsadés entre eux, et assemblés de manière à former un conducteur plat à deux couches. Cette topologie de câble transposée ; couramment utilisée pour les conducteurs Nb-Ti ou Nb_3Sn ; a été appliquée plus récemment aux conducteurs Bi-2212. Le traitement thermique délicat des conducteurs Bi-2212 (+/-1 K sous une atmosphère d'oxygène à 880 °C) complexifie grandement leur mise en oeuvre dans les aimants de grandes dimensions. Plusieurs câbles Rutherford Bi-2212 ont été fabriqués et testés au cours de ces 20 dernières années avec des performances allant de seulement 20 % à plus de 90 % de celles attendues. Les performances des conducteurs Bi-2212 ont été rapportées pour être liées à l'uniformité de température mais aussi à la longueur des conducteurs. Récemment, un procédé de traitement thermique sous pression a augmenté de façon drastique les performances des conducteurs Bi-2212.

Câbles de type Roebel

Le concept du câble continuellement transposé ou câble Roebel a été introduit par Ludwig Roebel en 1911 afin de réduire les pertes AC dans les conducteurs résistifs d'alternateurs. Le câble Roebel, consiste en l'arrangement de conducteur de section rectangulaire en deux empilements (figure 1.4). Les conducteurs passent d'une pile à l'autre au sommet ou la base de cette dernière. La forme en ruban et la sensibilité à la déformation des supraconducteurs YBCO restreint leur application directe dans les câbles Roebel. La possibilité de préformer les conducteurs YBCO par découpage a été démontrée en 2006. Depuis cette date, le potentiel de ce câble a uniquement été démontré à 77 K, où le courant critique reste faible comparé à ce qu'il pourrait être à 4 K.

Figure 1.4: Vue de dessus (gauche) et schématique (droite) du câble Roebel.

Câbles autour d'une âme

Les rubans YBCO sont résiliant à la déformation axiale ; ils peuvent être enroulés en hélice autour d'une âme de diamètre restreint (5 mm) sans réduction de leur I_c. Un câble autour d'une âme de 5 mm, constitué de 52 brins YBCO a atteint un courant critique de 5,1 kA à 4,2 K sous une induction de 19 T avec une densité de courant de 117 A/mm^2. Ce type de câble présente une dilution du conducteur trop importante dans le câble pour obtenir les fortes densités de courants critiques requises par les aimants d'accélérateurs (200-400 A/mm^2).

Câbles à empilement

La façon la plus simple d'assembler des rubans supraconducteurs dans un câble multibrin est de les empiler les uns sur les autre. Cette solution, largement utilisée pour les solénoïdes HTS, ne présente pas de transposition des conducteurs. Cela peut influer sur la répartition du courant entre les brins et créer des distorsions indésirables de l'induction magnétique.

1.2.5 Conclusion

Les différentes contraintes reposant sur le design des aimants d'accélérateur sont décrites dans ce chapitre. Une nouvelle formulation semi-analytique permettant d'estimer les performances ultimes de dipôles d'accélérateur en matériaux HTS est introduite. Cette formulation basée sur la conception électromagnétique 2D des dipôles en secteur angulaire et les performances des conducteurs HTS, est utilisée pour déterminer l'épaisseur du bobinage d'un aimant HTS générant une induction de 20 T. Cette épaisseur est de 110 mm pour les conducteurs Bi-2212, et de 90 mm pour les conducteurs YBCO. Les aimants d'accélérateur requièrent des câbles transposés à forts courants. Une revue des différents concepts de câbles HTS est proposée. De ces différentes topologies de câbles, les câbles Rutherford Bi-2212 et Roebel YBCO sont identifiés comme prometteurs pour les aimants d'accélérateur à très haute induction (>20 T).

1.3 Chapitre 3 : Performances des conducteurs HTS

Les objectifs de cette thèse nécessitent d'importants travaux expérimentaux afin d'analyser le niveau de performance de la génération actuelle des conducteurs HTS sous les différentes conditions environnementales rencontrées dans les bobinages des aimants supraconducteurs. Le courant critique (I_c), qui reflète la capacité de transport de courant des supraconducteurs est affecté par l'intensité et la direction de l'induction magnétique, la température et la déformation mécanique. Dans les bobinages d'aimants, les supraconducteurs sont soumis à une combinaison de ces paramètres. L'induction magnétique maximale générée par un aimant supraconducteur est limitée par les propriétés intrinsèques du supraconducteur à partir duquel il est bobiné. Il est donc nécessaire d'avoir une bonne connaissance de la surface critique de ces derniers. Dans le cadre de ce travail, le courant critique de différents conducteurs YBCO et Bi-2223 a été mesuré à 4,2 K sous des inductions perpendiculaire et parallèle allant jusqu'à 12 T. Les aimants d'accélérateurs en matériaux HTS nécessiteront des quantités de conducteurs dépassant les longueurs unitaires produites. Des jonctions électriques de faible résistance entre conducteurs HTS seront nécessaires. La résistance de ces jonctions a été étudiée à 77 K dans ce travail : la procédure expérimentale et les mesures sont reportées dans ce chapitre. Au cours du bobinage des aimants supraconducteurs, les rubans HTS peuvent être soumis à de la torsion ou du cintrage. Afin de déterminer les déformations maximales admissibles, la rétention du I_c des rubans HTS sous différents niveaux de torsion a été mesuré à 77 K.

1.3.1 Les différents conducteurs étudiés

Pour des applications dans les aimants d'accélérateurs, les conducteurs HTS doivent à la fois présenter de bonnes propriétés électromécaniques et être disponibles dans de grandes longueurs. Au regard de ces deux critères, 5 conducteurs HTS ont été sélectionnés pour une étude plus approfondie. Il s'agit des conducteurs YBCO des firmes SuperPower et AMSC, des conducteurs Bi-2223 des firmes Sumitomo et BHTS ainsi que du conducteur Bi-2212 de la firme OST.

Conducteurs BSCCO

Les températures critiques des deux composés usuels du BSCCO sont de 86 K (Bi-2212) et 110 K (Bi-2223). Les conducteurs à base de BSCCO sont composés d'une céramique supraconductrice placée dans une matrice d'argent. Ils sont fabriqués par le procédé PIT (Powder in Tube) : une poudre (le précurseur) est introduite dans des cylindres en argent, qui subissent par la suite une série de procédés mécaniques (extrusion, laminage, recuit) jusqu'à l'obtention d'un ruban (Bi-2223) où d'un fil (Bi-2212). Une fois le conducteur mis en forme, un traitement thermique est nécessaire pour faire réagir le précurseur de la phase supraconductrice. Ce traitement peut être effectué avant le bobinage (Bi-2223) ou bien après le bobinage (Bi-2212). Dans cette thèse, deux rubans Bi-2223 ont été étudiés. Le premier, produit par la firme Sumitomo (SEI), a une largeur de 4,5 mm et une épaisseur de 0,36 mm. Le second, produit par Bruker (BHTS) a une largeur de 3,95 mm pour une épaisseur de 0,21 mm. Ces deux conducteurs ont un I_c en induction propre de l'ordre de respectivement 900 A et 450 A à 4 K. Un fil Bi-2212 de 0,8 mm de diamètre produit par Oxford Instruments (OST) a aussi été étudié de façon bibliographique dans cette thèse.

Conducteurs YBCO

L'YBCO est un supraconducteur ayant une température critique de 92 K. Contrairement aux conducteurs BSCCO utilisant des méthodes de productions métallurgiques (extrusion, laminage, recuit), les

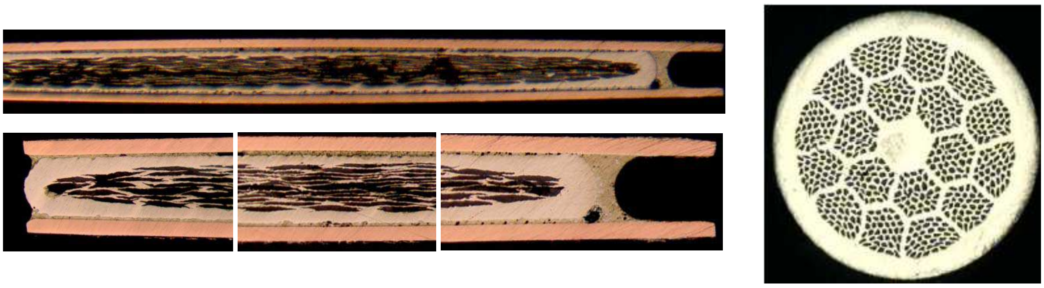

Figure 1.5: Vue en coupe du conducteur Bi-2223 SEI (gauche) et du fil Bi-2212 OST (droite).

conducteurs YBCO sont fabriqués par la technologie du dépôt de couches minces. La couche supraconductrice (0,1-2 μm) est déposée sur un support mécanique (Hastelloy ou NiW) au travers de différentes couches tampons qui permettent le bon alignement des grains d'YBCO. Cet alignement est primordial pour l'obtention de fort courant critique. Une fine couche stabilisatrice d'argent est ensuite déposée sur la couche supraconductrice pour la protéger de l'environnement et faciliter l'injection de courant. Cette âme est ensuite stabilisée par électro-dépôt de cuivre ou bien par brasure de laminés d'alliage de cuivre. Deux conducteurs YBCO commercialement disponibles ont été étudiés dans cette thèse. Le premier, produit par la firme AmericanSuperconductor (AMSC), a une largeur de 4,4 mm et une épaisseur de 0,44 mm. Le second, produit par SuperPower (SP) a une largeur de 4 mm (pouvant être de 12 mm) pour une épaisseur de 0,1 mm. Ces deux conducteurs ont un I_c en champ propre de l'ordre de 100 A à 77 K et 1300 A à 4 K.

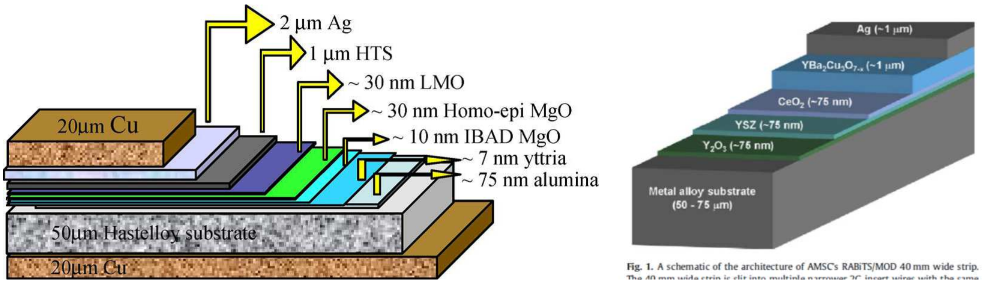

Figure 1.6: Vue schématique de la section des conducteurs YBCO des firmes SuperPower (gauche) et American Superconductor (droite).

1.3.2 Techniques expérimentales

Dans les aimants, les supraconducteurs sont soumis à diverses conditions environnementales qui affectent leur capacité de transport de courant. La connaissance de la surface critique des supraconducteurs passe par des mesures de caractérisation, dans lesquelles les conditions environnementales rencontrées dans les bobinages d'aimants sont reproduites dans des stations d'essais. Les différentes techniques expérimentales afférentes à ces mesures sont détaillées dans cette section. Le courant critique d'un supraconducteur peut être mesuré selon deux protocoles expérimentaux distincts : la magnétisation et le transport de courant. Ce dernier protocole, plus représentatif de ce qui se passe dans un aimant supraconducteur, a été utilisé dans cette thèse pour la caractérisation des divers conducteurs et câbles HTS. Ce protocole consiste à faire circuler un courant croissant dans un supraconducteur jusqu'à obtenir un état dissipatif. Le courant critique est défini pour un champ électrique équivalent à 1μV/cm le long de l'échantillon. Dans cette thèse, le courant critique a été mesuré à température, orientation et intensité de champ constant tandis que le courant dans l'échantillon était augmenté à taux constant. Les rubans HTS présentent une forte anisotropie du I_c à 4,2 K : le plus faible étant sous induction perpendiculaire, le plus élevé sous induction parallèle. Les rubans HTS ont été mesurés sous ces deux orientations.

Mesures du I_c sous induction magnétique à 4,2 K

Les stations d'essais et les portes échantillons

Les mesures de courant critique des rubans HTS ont été effectuées dans les stations d'essais du bâtiment 163 du CERN. Les échantillons, insérés dans l'ouverture de solénoïdes produisant jusqu'à 12 T ont été caractérisés sous induction parallèle et perpendiculaire à une température de 4,2 K. Des convertisseurs de puissance alimentaient les échantillons en courant tandis que la différence de potentiel électrique le long du conducteur était mesurée par l'intermédiaire d'un nano voltmètre de type Keithley 1890. Les échantillons HTS étaient protégés des surtensions par un système s'activant au delà d'un seuil de 1 mV et d'un temps de 100 ms. Sur les nombreuses mesures réalisées, aucun échantillon n'a été endommagé.

Mesures

A une température de 4,2 K et sous induction magnétique constante, le courant circulant dans les échantillons a été progressivement augmenté avec des rampes de 12-20 A/s jusqu'à l'activation de la protection. Les caractérisations ont été répétées et effectuées en induction croissante et décroissante afin de relever une éventuelle hystérésis du I_c. Les conducteurs YBCO ne présentent pas d'hystérésis, contrairement aux conducteurs BSCCO. Les mesures du courant critique du conducteur YBCO SP sous inductions parallèle et perpendiculaire sont rapportées dans la figure 1.7. Le I_c est fortement/faiblement réduit sous inductions perpendiculaire/parallèle. Des densités de courant critique de 300-2300 A/mm^2 ont été obtenues sous des inductions de 17 T. Les densités de courants dans les rubans YBCO AMSC sont bien plus faibles. Les conducteurs Bi-2212 d'OST ont un J_c isotrope qui est de l'ordre de 200 A/mm^2 sous 15 T. Récemment cette valeur a été largement augmentée par des traitements thermiques sous pression. Les deux conducteurs YBCO SP et Bi-2212 OST sont des candidats prometteurs pour les aimants d'accélérateurs à haute induction magnétique.

1.3.3 Mesures de la résistance de connexion entre conducteurs HTS

La quantité de supraconducteurs requise pour la construction d'un aimant d'accélérateur, dépasse de loin les longueurs unitaires de conducteur HTS actuellement produites. Des connexions électriques entre supraconducteurs sont donc nécessaires. Une jonction se doit d'avoir une faible résistance électrique mais également une bonne tenue mécanique. La résistance d'une jonction se compose d'une part de la résistance d'interface (soudure) mais également de la résistance interne du conducteur. Cette dernière se compose des nombreuses résistances d'interfaces qui sont difficilement prédictibles : une caractérisation est donc inévitable. Une série de mesure à 77 K et en indiction propre a été effectuée sur des jonctions entre les rubans YBCO SP/AMSC ainsi que les rubans Bi-2223 SEI/Bruker.

Résistance de contact à 77 K et en champ propre

La section droite des conducteurs YBCO n'est pas symétrique : en effet, le film HTS n'est déposé que d'un seul côté du substrat (Hastelloy ou NiW). Il existe donc trois types de jonctions entre conducteurs YBCO : le face à face, le face à dos et le dos à dos qui correspondent respectivement à 0, 1 et 2 substrats interposés entre les films HTS. Les conducteurs Bi-2223 ont une section droite symétrique, il existe donc un seul type de jonction possible. La résistance de jonction dépend bien évidement de la longueur d'interface. Il convient donc de normaliser la résistance de contact avec la surface de contact. Avec ce paramètre, des jonctions de différentes longueurs peuvent être comparées. Pour les rubans YBCO SP/AMSC dans la configuration face à face, la résistivité de contact mesurée (77 K, induction propre) est de 33/159 nΩ.cm^2. Ces valeurs sont un ordre de grandeur inférieur à la résistivité de contact dans les autres configurations (dos à dos et face à dos). Ce résultat s'explique par la forte résistivité des substrats (NiW et Hastelloy) et des couches tampons. Pour les rubans Bi-2223, la résistivité de contact est bien moindre : 37 nΩ.cm^2 pour les conducteurs SEI et 14 nΩ.cm^2 pour les conducteur BHTS.

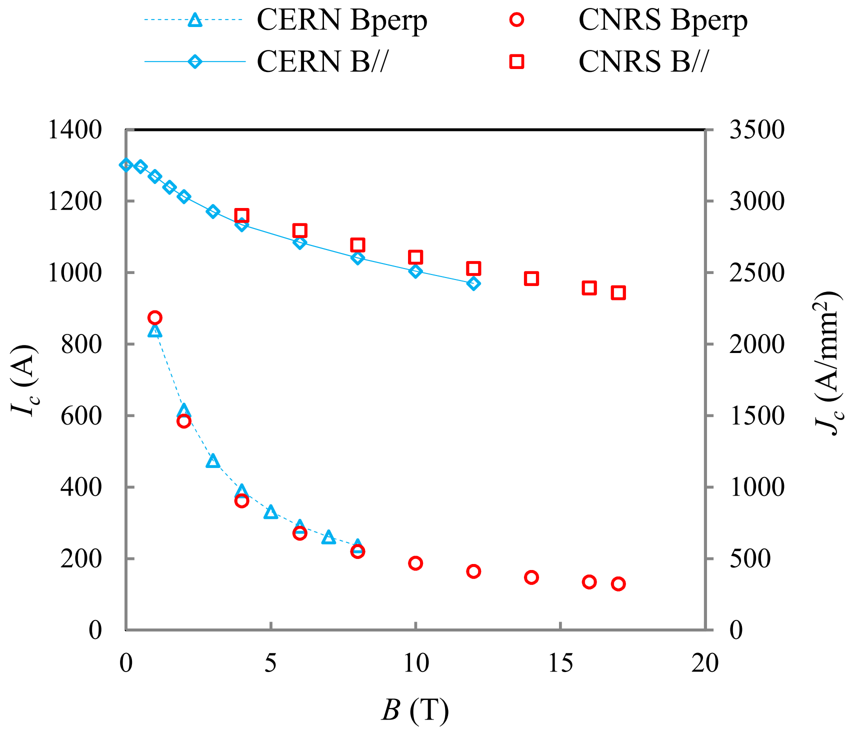

Figure 1.7: Le I_c et J_{ce} à 4,2 K du conducteur YBCO SP sous inductions parallèle et perpendiculaire.

1.3.4 Réduction du I_c des rubans HTS soumis à de la torsion

Les rubans YBCO et Bi-2223 ont des sections droites à forts rapports d'aspect, typiquement 10 à 200. Lors du câblage ou du bobinage des aimants, ces conducteurs peuvent être soumis à de la torsion. Un dispositif expérimental a été développé afin de déterminer la torsion maximale admissible de ces conducteurs. La réduction du courant critique de ces conducteurs en fonction du pas de torsion a été mesurée à 77 K. Deux terminaux en cuivre, distant de 280 mm, imposant les conditions aux limites pour la torsion servaient également d'amenées de courant pour le conducteur HTS. Le courant critique des conducteurs a été mesuré pour des pas de torsion progressivement réduits. Partant d'un pas de torsion infini, la réduction du I_c des rubans YBCO SP/AMSC est insignifiante jusqu'à 120 mm ou elle devient plus soutenue, pour devenir franche en dessous de 60 mm (figure 1.8). Une rétention de 95% du I_c est obtenue pour des pas de torsion de 80-90 mm. Les rubans Bi-2223 présentent une rétention de l'ordre de 80% à ces pas de torsion.

1.3.5 Conclusion

Dans ce chapitre, les différentes techniques expérimentales utilisées pour la caractérisation des conducteurs HTS sont présentées. Les mesures du courant critique de rubans YBCO et Bi-2223 à 4,2 K et sous induction parallèle et perpendiculaire sont exposées dans ce chapitre. Le conducteur YBCO de Super-Power qui a une forte densité de courant critique sous induction parallèle, présente également de très bonnes propriétés mécaniques avec un module de Young de 175 GPa et une limite élastique d'environ 630 MPa. Les conducteurs Bi-2212 d'OST ont un J_c isotrope qui est de l'ordre de 200 A/mm^2 sous 15 T. Récemment cette valeur a été largement augmentée avec les traitements thermiques sous pression.

La résistance de jonction entre les rubans YBCO SP/AMSC a été mesurée à 77 K. Elle est de 33/159 nΩ.cm^2 dans la configuration face à face. Le pas de torsion minimal admissible des conducteurs HTS a été déterminé de façon expérimentale. Il est de 85 mm pour les rubans YBCO SP/AMSC contre 114 mm

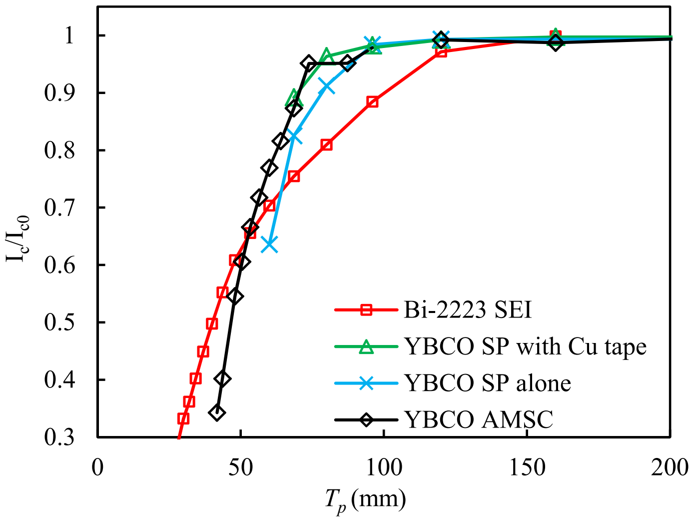

Figure 1.8: Réduction du I_c des rubans HTS soumis à de la torsion. Mesures effectuées a 77 K et sous induction propre.

pour les rubans Bi-2223.

Aux vues de leurs performances électromécaniques les conducteurs YBCO SP et Bi-2212 OST sont des candidats prometteurs pour les aimants d'accélérateurs à haute induction magnétique.

1.4 Chapitre 4 : Les marges opérationnelles des câbles YBCO dans les aimants d'accélérateur à haute induction magnétique

La frontière entre l'état supraconducteur et l'état normal résistif est une surface, appelée surface critique qui dépend de la température, l'intensité et l'orientation de l'induction magnétique, de la densité de courant et de la déformation mécanique. Les mesures expérimentales des performances des conducteurs HTS sont limitées en quantité et ne couvrent pas les diverses conditions environnementales rencontrées dans un bobinage d'aimant. De ce fait un paramétrage de la surface critique, permettant des interpolations et extrapolations est nécessaire. Un nouveau paramétrage de la surface critique des différents conducteurs YBCO et BSCCO étudiés dans cette thèse est proposé dans ce chapitre. Ce paramétrage est ensuite utilisé afin de calculer les marges opérationnelles du dipôle YBCO de 19 T du programme EuCARD. Finalement, un modèle analytique de la réduction du courant critique des rubans YBCO soumis à de la torsion est présenté et comparé avec les mesures effectuées dans le chapitre 3.

1.4.1 Paramétrage de la surface critique des rubans HTS

Un paramétrage précis de la surface critique des conducteurs HTS est nécessaire compte tenu du fait que les caractérisations ne couvrent pas l'intégralité des conditions environnementales rencontrées dans les bobinages d'aimant. Ma formulation novatrice exprimant la dépendance de la densité de courant critique des conducteurs YBCO SP vis-à-vis de la température, l'intensité et la direction de l'induction magnétique est donnée sous la forme :

$$J_c(B,T,\theta) = J_{c,perp}(B,T) + \frac{J_{c,parall}(B,T) - J_{c,perp}(B,T)}{1 + \left(\frac{|\theta - \pi/2|}{e(B,T)}\right)^{g(B,T)}} \tag{1.3}$$

Où $J_{c,perp}$et $J_{c,parall}$ sont respectivement la densité de courant critique sous induction parallèle et perpendiculaire. Ces deux paramètres sont décrits par la théorie d'ancrage des vortex. Le paramètre θ

est l'angle entre l'induction magnétique et le plan de la bande YBCO. Les paramètres d'ajustement e et g de la fonction lorentzienne dépendent de la température et de l'induction. Dans la figure 1.9, Les mesures de la dépendance angulaire de J_c des conducteurs YBCO SP à 4 K sont comparées à l'expression (1.3). Un bon accord est observé sur toute la gamme d'induction et d'orientation.

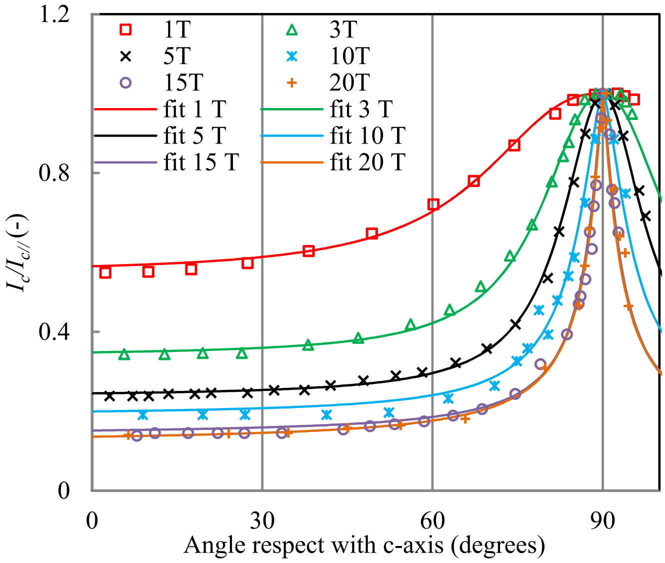

Figure 1.9: L'anisotropie du J_c du conducteur YBCO SP à 4 K. Les mesures (points) sont comparées au paramétrage (ligne).

1.4.2 Les marges opérationnelles des câbles YBCO dans les aimants d'accélérateur

La forte anisotropie de la densité de courant critique des conducteurs YBCO à un fort impact sur la conception des dipôles d'accélérateur : le point critique d'un bobinage en YBCO n'est pas nécessairement celui qui est soumis à la plus forte induction. Le paramétrage de la surface critique des conducteurs YBCO introduit dans la section précédente est utilisé ici afin de déterminer le point critique ainsi que les marges opérationnelles de l'insert YBCO du dipôle 19 T du programme EuCARD.

L'insert YBCO du projet EuCARD

Le programme EuCARD a pour objectif principal de développer les instruments et les technologies de l'avenir des accélérateurs de particules. Une des taches d'EuCARD est la conception et la construction d'un insert en matériaux HTS générant un champ dipolaire de 6 T dans un champ de fond de 13 T produit par un dipôle Nb_3Sn de 100 mm d'ouverture. Plusieurs contraintes reposant sur la conception d'un véritable aimant d'accélérateur (ouverture, qualité de l'induction magnétique...) n'ont pas été prises en considération dans la conception de cet insert. Une densité de courant de 250 A/mm^2 dans le bobinage HTS génère une induction de 6 T. Une vue de la section droite de cet aimant de 19 T est représentée dans la figure 1.10.

Le câble HTS de l'insert

Le conducteur YBCO de la firme SuperPower a été retenu pour cet insert car il allie de fortes densités de courant critique à de hautes propriétés mécaniques. Le câble HTS se constitue de deux conducteurs connectés en parallèle, chacun étant composé de deux rubans YBCO de 12 mm de largeur. Le courant nominal du câble HTS ; large de 12 mm et épais de 0,92 mm ; est de 2,8 kA.

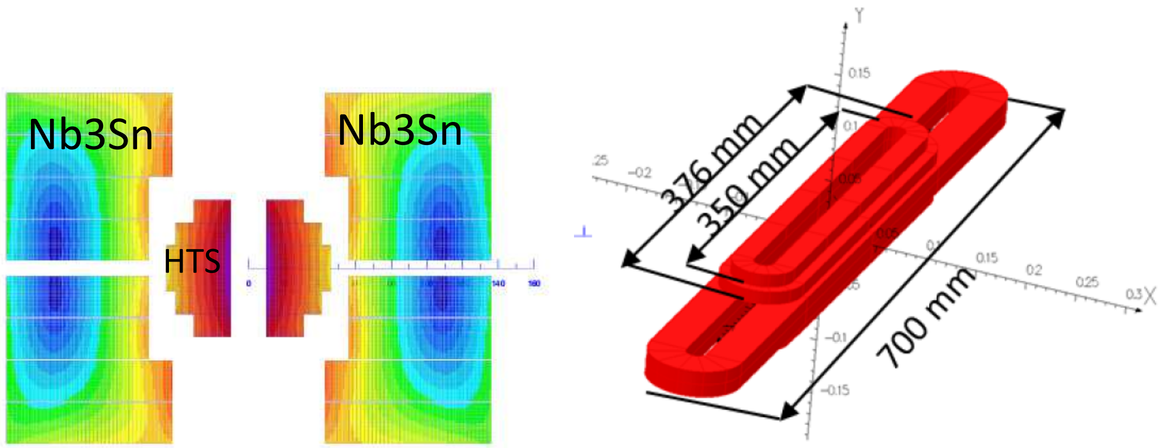

Figure 1.10: Vue en coupe du dipôle YBCO/Nb_3Sn de 19 T du programme EuCARD (gauche). Vue 3D des bobines de l'insert YBCO (droite).

Calcul des marges opérationnelles de l'aimant YBCO

Le point de fonctionnement d'un aimant supraconducteur est toujours choisi avec une certaine marge sur ces performances ultimes. Pour un aimant, il existe principalement trois types de marges :

- la marge en courant critique ;
- la marge le long de la droite de charge ;
- la marge en température.

Pour des raisons de symétries, seulement un quart de la section droite de l'aimant 19 T du programme EuCARD est implémenté dans un logiciel de calculs par élément finis (Comsol). Dans ce modèle, les 4 films YBCO de chaque câble sont considérés et le paramétrage de la surface critique (expression 1.3) permet de calculer la densité de courant critique en tout point de son bobinage. Les marges locales de l'aimant sont définies à l'aide de la densité de courant critique minimum du bobinage. Les câbles étant relativement larges, une forte variation de la densité de courant critique peut avoir lieu à travers leur section. On peut donc également définir des marges globales de l'aimant à partir du courant critique minimum du câble dans le bobinage. Bien évidemment, les marges locales sont moins importantes que les globales. Dans la table 1.1, les marges opérationnelles de l'insert YBCO sont reportées pour une induction centrale de 6 T et 19 T.

Table 1.1: Les marges opérationnelles de l'insert YBCO du programme EuCARD à une induction centrale de 19 T et 6 T.

	B_0=19 T		B_0=6 T	
	Locale	Globale	Locale	Globale
Marge en courant critique (% du I_{nom})	14	30	70	99
Marge le long de la droite de charge (%)	9	18	40	59
Marge en température (T_{op}=4,2 K) (K)	3,5	8,5	>10	>10

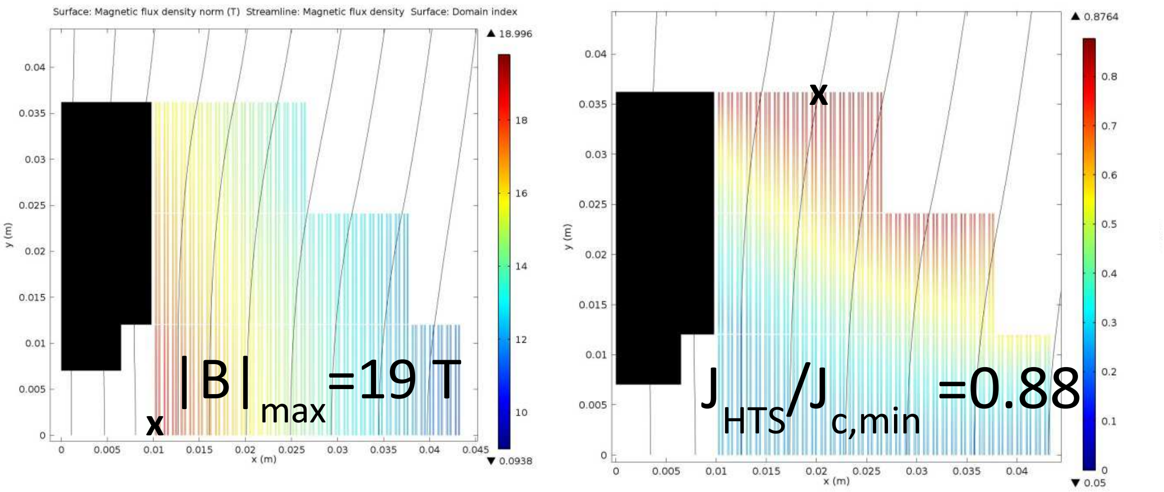

Figure 1.11: Le module de l'induction dans le bobinage HTS au courant nominal (19 T)(gauche). Le ratio entre la densité de courant et la densité de courant critique au courant nominal (19 T)(droite).

1.4.3 Paramétrage de la dépendance du I_c des rubans YBCO à la torsion

Les rubans YBCO sont sensibles à la déformation mécanique axiale. Leur J_c est réduit de façon réversible en dessous de seuils en tension et compression au-delà desquels la réduction est abrupte et irréversible. Ces seuils sont de l'ordre de 0,6% en tension et 2% en compression. Lorsqu'un ruban YBCO est soumis à de la torsion, une certaine distribution de déformation axiale est induite dans le conducteur, elle est exprimée sous la forme :

$$\varepsilon_{tw}(x) = \varepsilon_t(x) + \varepsilon_0 = \frac{2\pi^2}{T_p^2}\left(x^2 - \frac{w^2}{12}\right) \tag{1.4}$$

Dans la figure 1.12, l'expression 1.4 est compilée pour des rubans de 4 mm de largeur soumis à différents pas de torsion. De la distribution de déformation axiale, il résulte une certaine distribution de la densité de courant critique. Une intégration de celle-ci sur la section du conducteur permet d'en obtenir le courant critique. L'expression analytique obtenue est sous la forme :

$$I_c(T_p) = \tau \; w \; J_{c,0\varepsilon_m}\left(1 - \frac{T}{T_e}\right)^k \left(1 - \frac{a}{180}\left(\frac{2\pi^2 w^2}{T_p^2}\right)^2 + \frac{\varepsilon_m^2}{2}\right) \tag{1.5}$$

Plus les conducteurs sont larges, plus ils sont sensibles à la torsion. Dans la figure 1.12, le I_c des conducteurs YBCO de différentes largeurs est rapporté à 4 K et 77 K. La température a un effet relativement faible sur la réduction du I_c. Dans la figure 1.13, les expressions analytiques de la réduction du I_c des conducteurs YBCO soumis à de la flexion ou de la torsion sont comparées aux caractérisations. Les modèles analytiques sont en accord parfait avec les mesures.

1.4.4 Conclusion

Un paramétrage précis de la surface critique des différents conducteurs YBCO et BSCCO étudiés dans cette thèse a été établi. Ce paramétrage, précis sur un large éventail de températures, intensités et directions de l'induction magnétique a été utilisé afin de calculer les marges opérationnelles du dipôle YBCO de 19 T du programme EuCARD. A une induction centrale de 19 T, la marge en courant critique est de 14%, la marge sur la droite de charge est de 9% et la marge en température est de 3,5 K. Un modèle analytique donnant la rétention du I_c des conducteurs HTS en fonction de leur torsion a été développé. Ce modèle, en accord avec les mesures effectuées, met en évidence la plus forte sensibilité des conducteurs les plus larges.

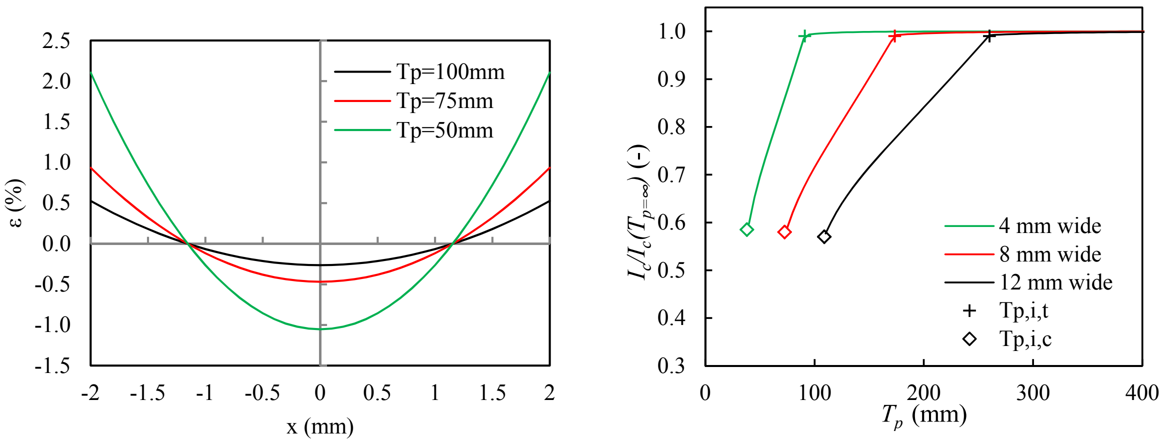

Figure 1.12: Déformation axiale dans un conducteur YBCO soumis à de la torsion (gauche). Réduction du I_c avec la torsion pour des conducteurs YBCO de différentes largeurs (droite).

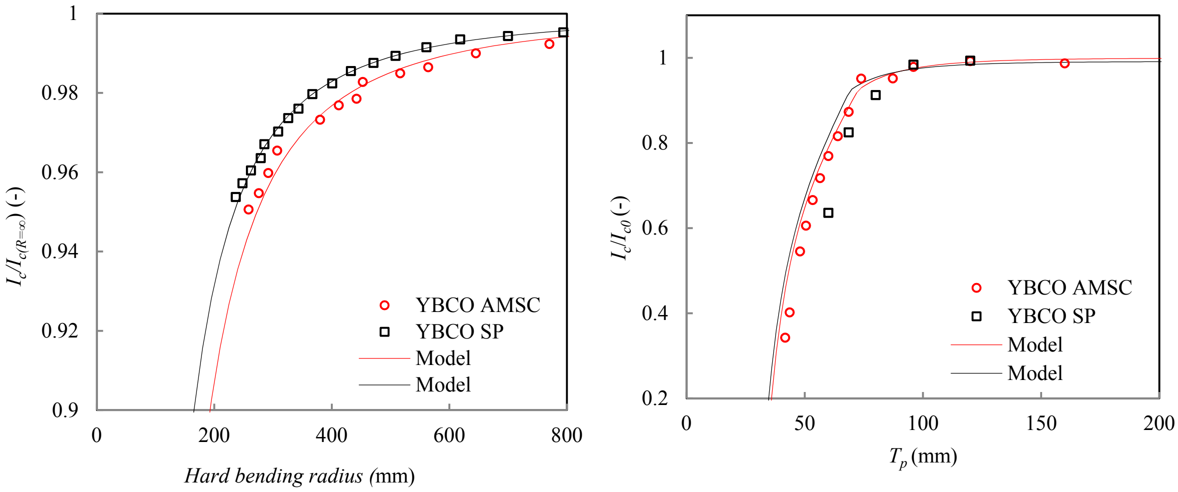

Figure 1.13: Comparaison de la réduction mesurée (points) et calculée (lignes) du I_c à 77 K et en induction propre des conducteurs YBCO soumis à de la flexion dans le plan (gauche) et de la torsion (droite).

1.5 Chapitre 5 : Caractérisation à 4,2 K de câbles YBCO à fort courant

Les aimants supraconducteurs d'accélérateur nécessitent l'emploi de câbles multibrins transposés à fort courant. Le câble Roebel YBCO, ayant un fort potentiel pour les aimants à haute induction opérés à 4 K (20 T), a été à ce jour uniquement caractérisé à 77 K. Dans ce chapitre, le potentiel de ce type de câble est démontré à 4 K. Ce chapitre résume les investigations expérimentales entreprises sur différents câbles Roebel YBCO sous des inductions allant jusqu'à 9,6 T.

1.5.1 Dispositif expérimental et courant critique à 4,2 K

Détails expérimentaux

Dans un câble fort courant d'accélérateur, les brins doivent être transposés afin de limiter les pertes AC et de favoriser une distribution homogène du courant. Les conducteurs YBCO qui se présentent exclusivement sous forme de rubans sont difficilement transposables dans les câbles d'accélérateur. En 2006, le concept de transposition des rubans YBCO dans les câbles Roebel a été démontré. A ce jour, ce type de câble a uniquement été caractérisé à 77 K et en induction propre. La température de fonctionnement des aimants d'accélérateurs à haute induction (20 T) sera autour de 4 K. A cette température, les capacités de transport de courant du câble seront bien supérieures à celles mesurées à 77 K.

Deux types de câbles Roebel ont été mesurés dans la station FRESCA, respectivement produits par General Cable Supraconducteurs (GCS) et Karlsruhe Institute of Technology (KIT). Ces câbles de 12 mm de largeur diffèrent : par leur nombre de brins 15 pour GCS/10 pour KIT, leur épaisseur 0,8/0,6 mm et leur pas de transposition 300/126 mm. Deux câbles de chaque type, d'une longueur de 1,8 m, ont été mesurés dans FRESCA, ils sont nommés respectivement : GCS1, GCS2, KIT1 et KIT2. Les performances des conducteurs YBCO sont connues pour être affectées par le dopage au BaZrO (BZO). À 4,2 K les conducteurs dopés BZO ont des valeurs d'I_c supérieures à faible induction mais aussi une plus forte dépendance sous des inductions plus élevés. Contrairement aux conducteurs du câble GCS, ceux du câble KIT sont dopés au BZO.

Afin d'éviter tout mouvement des câbles Roebel lors de leurs caractérisations, une précontrainte mécanique transverse de 40 MPa a été appliquée. Les rubans YBCO sont quasiment insensibles à la compression transverse uniforme : une réduction marginale du I_c a été signalée pour des contraintes de 600 MPa. L'épaisseur des câbles Roebel n'étant pas homogène les efforts transverses ne sont repris que par une fraction de la section du câble, ce qui engendre une distribution non uniforme des contraintes. La résilience des câbles Roebel à la contrainte transverse a été vérifiée par des mesures préalables à 77 K. Un papier sensible à la contrainte (Prescale Film SH de FujiFilm) a permis d'imprimer la répartition des contraintes dans les câbles Roebel soumis à des efforts transverses. D'après les empruntes (figure 1.14), la surface effective pour reprendre les efforts transverses est estimé à seulement 36% pour le câble GCS et 24% pour le câble KIT. Une précontrainte moyenne de 40 MPa sur les câbles Roebel GCS/KIT implique des contraintes locales d'au moins 111/167 MPa. Le choix de ne pas imprégner les câbles Roebel a été fait afin de prévenir tout risque de délamination des conducteurs YBCO. Les différences de potentiel électrique le long des différents brins des câbles Roebel ont été mesurées à l'aide de nano voltmètres. Afin de mesurer une possible distribution inhomogène de courant dans les brins du câble, l'induction propre du câble KIT a été mesurée le long d'un pas de transposition par l'intermédiaire d'un tableau de 26 sondes à effet Hall.

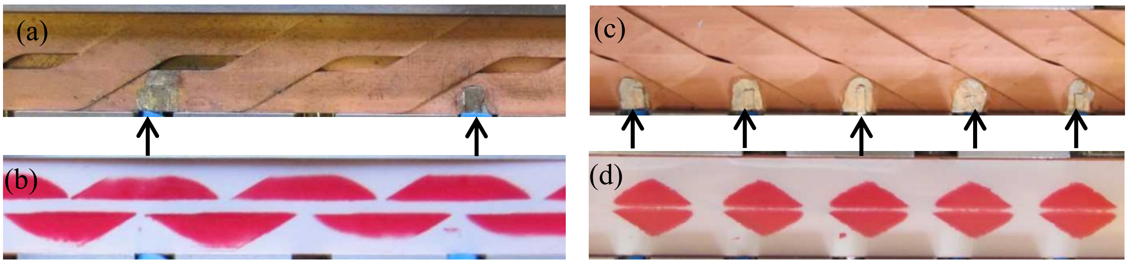

Figure 1.14: Vue de dessus et empruntes sur du papier sensible à la contrainte des câbles Roebel GCS (gauche) et KIT (droite).

Courant critique des câbles Roebel à 4,2 K

Pour la mesure du courant critique des câbles Roebel, le courant de transport a été augmenté jusqu'à ce qu'un champ électrique de 1 μV/cm le long au moins un des brins du câble ait été atteint. Dans la figure 1.15, le I_c des câbles GCS2, KIT1 et KIT2 est rapporté. Sous induction perpendiculaire, il est de l'ordre de 9,9-10,8 kA à 1 T et 2,4-3,4 kA à 9,6 T. Le I_c des différents câbles est moins sensible a l'induction parallèle, il passe de 14 kA sous 1 T à 12 kA sous 8 T. La densité de courant critique des câbles, définie comme le rapport du I_c des câbles et de leur section droite (incluant les vides), est rapportée dans la figure 1.15 en fonction de l'induction externe. A faible champ perpendiculaire, le câble KIT2 présente des valeurs plus élevées de J_{ce} comparées au câble GCS2. Lorsque l'induction est augmentée, le J_{ce} du câble KIT2 a une décroissance plus prononcée : l'écart de J_{ce} entre les deux câbles est progressivement réduit pour devenir nul à 9,6 T. Ces comportements sont pleinement expliqués par le dopage ou non au BZO des conducteurs : les performances électriques des câbles Roebel dépendent des caractéristiques intrinsèques des conducteurs à partir desquelles ils sont faits. Sous une induction perpendiculaire de 9,6 T, le J_{ce} des câbles Roebel est de 364 A/mm^2. Sous une induction parallèle de 6 T, le J_{ce} des câbles GCS2/KIT est respectivement de 1200/1600 A/mm^2.

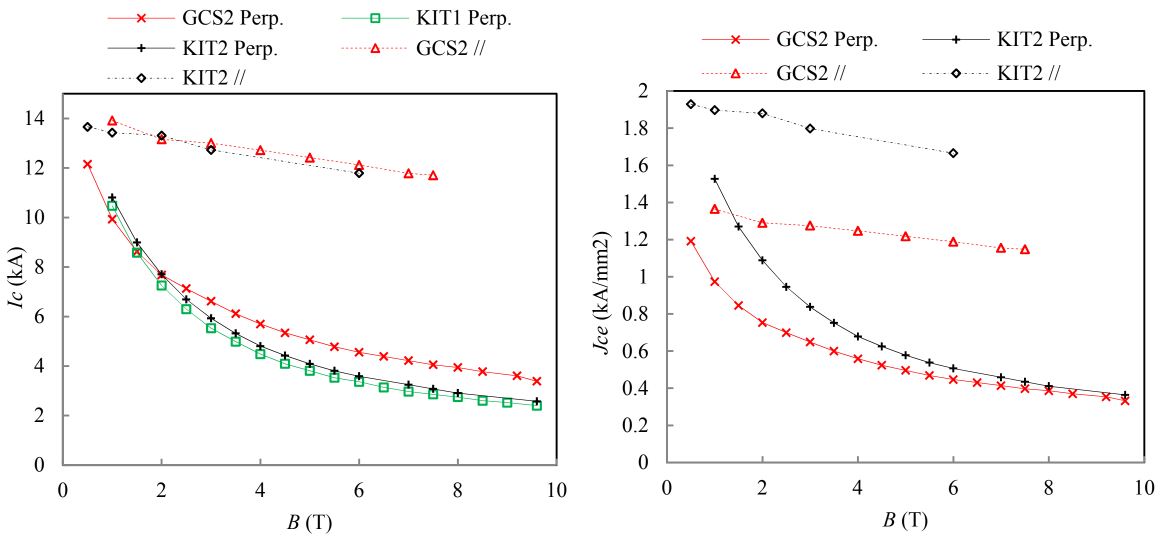

Figure 1.15: I_c (gauche) et J_{ce} (droite) à 4 K des câbles GCS2, KIT1 et KIT2 sous inductions magnétiques perpendiculaire et parallèle.

Résistance électrique des jonction

Les câbles Roebel sont connectés électriquement aux amenées de courant de la station FRESCA par l'intermédiaire de câbles Rutherford en Nb-Ti. La longueur de jonction entre les câbles Roebel et Rutherford est de un (GCS) ou deux (KIT) pas de transposition, correspondant à respectivement 300 mm et 252 mm. La résistance de jonction entre câbles Nb-Ti et Roebel KIT est de l'ordre de 3 nΩ contre seulement 1 nΩ pour les câbles GCS. Cette valeur inférieure de résistance de jonction est expliquée à la fois par une connexion plus longue, mais aussi par une procédure spécifique de nettoyage des oxydes de cuivre pour les câbles GCS.

1.5.2 Résistance de contact interbrins

Dans le câble Roebel, les brins ne sont pas électriquement isolés les uns des autres, ce qui peut donner lieu à des courants interbrins induits. Les courants induits peuvent réduire les performances du câble mais aussi détériorer la qualité de l'induction magnétique d'un aimant d'accélérateur. La magnitude des courants induits est régie par la valeur des résistances de contact interbrins. Une forte résistance de contact limite les courants induits mais ne favorise pas la redistribution de courant en cas de transition d'un brin à l'état résistif. Dans le cadre de ce travail, la résistance de contact interbrins du câble Roebel GCS a été mesurée à 77 K. Le principe de la mesure est de faire circuler un courant entre les brins opposés du câble sur un pas de transposition et de mesurer la différence de potentiel électrique liée.

Pour le câble GCS, une résistance de 94 $\mu\Omega$ a été mesurée entre brins opposés sur un pas de transposition à 77 K et en induction propre. Ce qui correspond à une résistance de contact interbrins de 25 $\mu\Omega$. Cette valeur est deux ordres de grandeur supérieure à celle obtenue pour des connexions soudées ou non entre rubans YBCO SP de 4 mm de largeur. Les brins YBCO des câbles Roebel présentent donc une résistance interne très élevée. Ceci est expliqué par la suppression du cuivre électro-déposé sur les bords du conducteur ainsi qu'une éventuelle délamination de la couche HTS. Le processus de découpe des brins Roebel doit donc être modifié afin d'éviter toute délamination et conserver un bon contact électrique entre le film HTS et le cuivre stabilisateur.

1.5.3 Dégradation du I_c des câbles Roebel

Malheureusement, à un certain point de leurs caractérisations à 4,2 K les performances des câbles GCS1 et GCS2 ont été fortement réduites et ce de manière irréversible malgré une protection active déclenchée à un seuil de 15 mV avec un temps d'intégration de 10 ms. Une dégradation de 27% du I_c du câble GCS1 a eu lieu à un courant de 11 kA et sous une induction parallèle de 6 T. Après de diverses et nombreuses mesures, le I_c du câble GCS2 a été réduit à zéro après un quench se produisant à 13,6 kA et 7 T d'induction parallèle. Afin de prévenir toute dégradation sur les câbles KIT, mesurés à posteriori, un méplat de cuivre (12 mm^2 de section) a été placé au contact des câbles au cours de leur caractérisation dans FRESCA. Les câbles KIT ainsi caractérisés n'ont pas été endommagés. Les câbles GCS ont été endommagés à proximité (8/36 mm) de la jonction basse avec le câble Rutherford. Une inspection visuelle a révélé que la soudure Sn-Pb avait localement fondue pendant le quench (figure 1.16), indiquant une température locale supérieure à 500 K. Certains brins des câbles semblent sectionnés, mais n'expliquent qu'en partie la réduction du I_c observée. Une inspection microscopique de la section longitudinale des câbles (figure 1.16) a révélé un flambement de tous les brins des câbles aux endroits endommagés. Les fortes températures atteintes lors du quench ont engendrées une élongation du câble Roebel. La distribution de contrainte transverse dans le câble Roebel, n'est pas homogène : les portions les plus fines sont exemptes de contraintes. Les câbles Roebel sont donc contraints transversalement de façon discrète, ce qui a autorisé leurs flambements. Les conducteurs YBCO ont un rayon de courbure critique en dessous duquel leur I_c est fortement réduit. Les rayons de courbures atteints dans les zones endommagés des câbles sont en deçà du rayon critique : les performances des câbles ont donc été réduites par les brulures locales mais aussi par les faibles rayons de courbures atteints. Une imprégnation du câble pourrait permettre une distribution plus homogène de la contrainte transverse et ainsi limiter le phénomène de flambement des câbles Roebel.

1.5.4 Délaminage du câble YBCO Roebel

Un délaminage des brins YBCO des câbles Roebel testés dans FRESCA a été observé. Le délaminage peut se produire entre le film HTS et les couches tampons ou entre le film HTS et la couche d'argent. Le délaminage peut avoir deux conséquences principales :

- une réduction du I_c : la section HTS est endommagé par le délaminage
- un découplage électrique du film HTS et des matériaux stabilisant (cuivre, argent..).

En cas de transition à l'état résistif, le film HTS n'étant plus convenablement stabilisé, il peut atteindre des températures susceptibles de l'endommager. La délamination est introduite par la découpe à l'emporte-pièce des brins YBCO des câbles Roebel. Lors de la préparation, du refroidissement et de la caractérisation des câbles, la délamination peut se propager. Le processus de fabrication des brins Roebel doit être modifié de façon à ne plus induire une telle délamination.

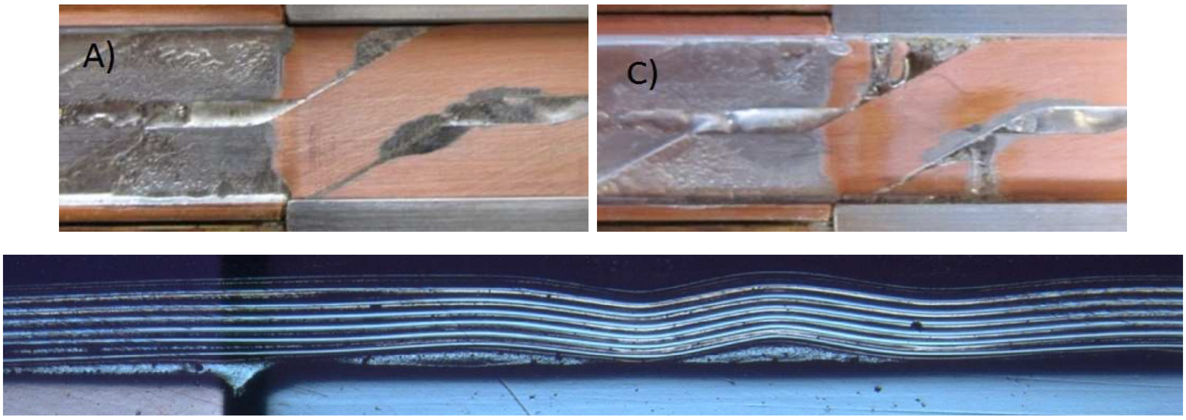

Figure 1.16: Le câble GCS1 avant (A) et après (C) la caractérisation à 4,2 K (haut). Vue longitudinale transverse de la portion endommagée du câble GCS2 (bas).

1.5.5 Conclusion

Mes travaux expérimentaux pionniers ont permis de démontrer le potentiel des câbles Roebel YBCO à 4 K pour des applications dans les aimants d'accélérateur à haute induction. Des densités de courant critique supérieures à 1100 A/mm^2 sous des inductions de 7,5 T ont été mesurées. Des jonctions électriques de faible résistance (1-3 nΩ) entre les câbles Roebel et Rutherford ont été obtenues. Une forte non uniformité des contraintes a été observée dans les câbles Roebel soumis à un chargement transverse. Seulement 26/34% de la section du câble KIT/GCS reprend le chargement transverse. Certains câbles Roebel ont été endommagés lors de leur caractérisation. L'origine des dégradations a été identifiée et des solutions apportées. Une résistance de contact interbrins de 25 $\mu\Omega$ a été mesurée à 77 K sur le câble GCS. Cette valeur élevée, comparée aux résistances de jonctions entre rubans YBCO SP, est due à la résistance interne des brins YBCO des câbles Roebel.

1.6 Chapitre 6 : Distribution du courant dans les câbles HTS

Dans les aimants d'accélérateur, il arrive que les câbles supraconducteurs multibrins transitent dans un état résistif à des courants plus faibles que ceux attendus. L'une des raisons de ce comportement est une distribution de courant non uniforme entre les brins. Dans ce chapitre, les différentes raisons induisant de telles distributions de courant sont identifiées. Au moyen d'un code numérique par éléments finis, le courant critique des brins des câbles Roebel est calculé le long du pas de transposition. Les performances théoriques des câbles Roebel a 4,2 K en sont déduites et comparées aux mesures effectuées dans le chapitre 5. Finalement, un modèle de distribution de courant dans les câbles HTS est introduit et utilisé afin d'identifier les causes de la non uniformité de ce dernier dans les câbles Roebel.

1.6.1 Les raisons de la répartition inégale du courant dans les câbles HTS

Plusieurs raisons peuvent induire une distribution non uniforme du courant entre les brins des câbles supraconducteurs. Certaines ne sont effectives que dans des conditions AC, tandis que d'autres sont effectives à la fois dans des conditions AC et DC. D'une manière générale, toute différence d'impédance ou d'inductance entre les différents brins du câble donne naissance à des courants déséquilibrés. Les principales raisons qui induisent une distribution non uniforme de courant sont les suivantes:

- **Des différences dans l'inductance propre et mutuelle des brins.** Sauf s'ils sont isolés électriquement, les brins d'un câble supraconducteur sont en contact électrique avec leurs voisins. Si les brins ne sont pas torsadés, des courants induits dommageables pour la qualité de l'induction et les performances de l'aimant vont circuler entre les brins supraconducteurs. Afin de limiter ces courants, tous les filaments d'un câble supraconducteur se doivent de présenter la même inductance propre et mutuelle que les autres. Ceci est mis en pratique par le torsadage des brins multifilaments ainsi que la transposition des brins dans le câble. Même avec des câbles parfaitement transposés, un gradient important de la dérivée temporelle de l'induction magnétique le long du câble, peut donner naissance à des courants de couplage.

- **Une distribution non uniforme de résistance de contact.** Les câbles supraconducteurs multibrins sont connectés entre eux ou à des amenées de courant par des jonctions de faibles résistances électriques. A des niveaux de courant faible, le courant circulant dans chaque brin est inférieur au courant critique et les tensions résistives le long du câble sont uniquement produites aux jonctions. Si les résistances de contact de chaque brin sont identiques, cela entraine alors une distribution homogène du courant en conditions établies. Il est techniquement impossible de réaliser un contact électrique parfaitement identique entre les différents brins d'un câble HTS ; d'une part parce que les procédés de soudage ne peuvent pas être aussi strictement maitrisés et d'autre part parce que la résistance électrique interne de contact des conducteurs YBCO peut varier d'un conducteur à l'autre.
- **Une différence dans le courant critique des brins** Une distribution non homogène du courant critique des brins d'un câble supraconducteur entraine de fait des courants déséquilibrés. La distribution non homogène du courant critique peut être intrinsèque aux conducteurs (processus de fabrication) ou extrinsèque (dégradation, induction propre du câble).

1.6.2 Courant critique des brins du câble Roebel

L'induction magnétique propre d'un supraconducteur peut influencer de manière significative ses performances. Dans un câble, les conducteurs qui prennent différentes positions dans la section droite expérimentent différentes inductions : les conducteurs ont donc un courant critique qui dépend de leur position dans le câble. Dans cette section, le courant critique des brins du câble Roebel est calculé en fonction de leur position dans la section droite au moyen d'un code 2D par éléments finis. Le paramétrage de la surface critique des conducteurs YBCO SP (expression 1.3) est implémenté dans le code de calcul. La distribution du courant critique est calculée de façon itérative. Dans la figure 1.17, la carte de l'induction propre du câble Roebel (tel que testé dans FRESCA) ainsi que la distribution de la densité de courant critique sont représentées.

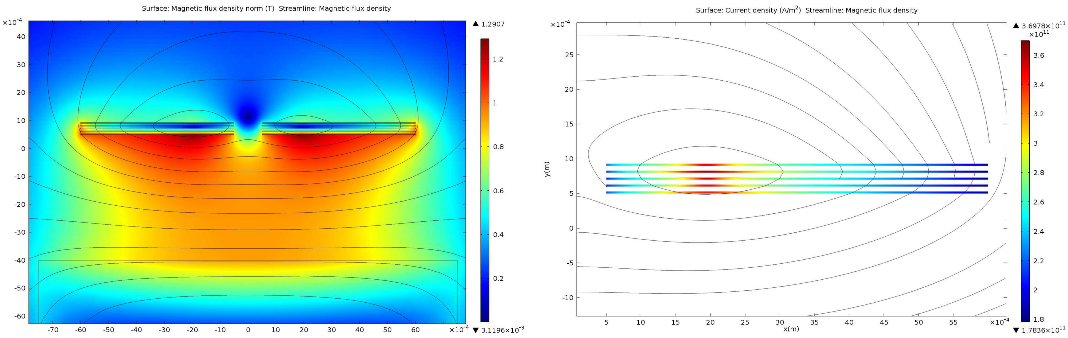

Figure 1.17: Carte de l'induction magnétique propre du câble Roebel KIT (gauche) et la distribution du J_c correspondante (droite).

Une intégration de la densité de courant critique sur la section des conducteurs permet de déterminer le I_c des brins en fonction de leur position dans la section droite. Dans les câbles transposés, chaque brin occupe toutes les différentes positions dans la section droite le long d'un pas de transposition. Il en résulte une modulation du I_c des brins le long du câble. Dans la figure 1.18, le courant critique des brins le long du pas de transposition du câble KIT est présenté pour différents intensités et directions de l’induction magnétique. Les fluctuations du I_c le long d’un pas de transposition sont les plus prononcées pour les faibles inductions perpendiculaires.

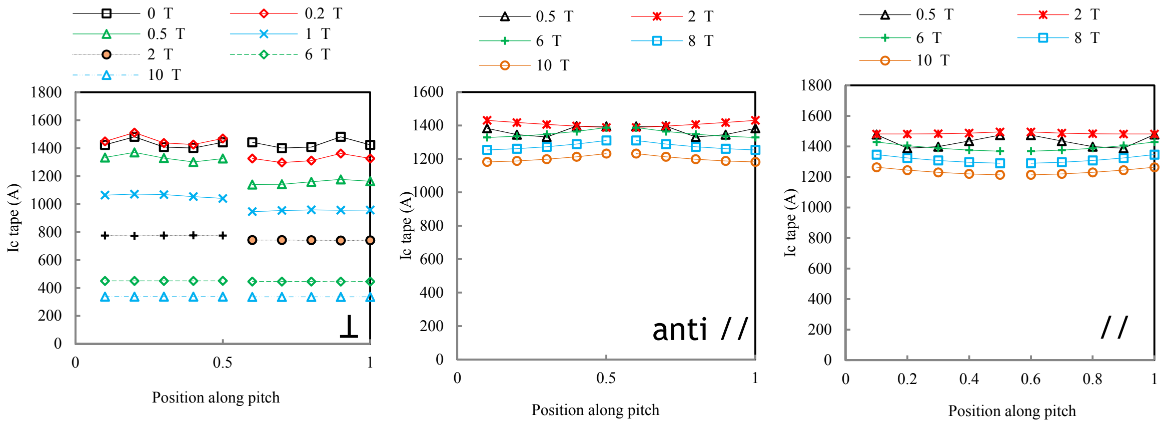

Figure 1.18: Le courant critique des brins du câble KIT le long du pas de transposition soumis à des inductions perpendiculaire (gauche), parallèle (milieu) et anti parallèle (droite).

Les câbles Roebel se composent de 10 à 15 brins transposés et connectés en parallèle. Les brins ont donc le même courant critique sur une échelle supérieure au pas de transposition. Dans l’hypothèse où les brins ne peuvent échanger de courant, le courant critique du câble est donné comme N fois le minimum du I_c d’un brin le long du pas de transposition. Si l’hypothèse où les brins sont connectés avec une résistance de contact nulle, le courant critique du câble est simplement défini comme l’intégration du J_c sur la section du câble. Il convient de noter que le courant critique du câble est supérieur dans l’hypothèse du partage du courant que dans le cas de brins électriquement isolés. Dans la figure 1.19, le courant critique mesuré du câble Roebel KIT sous inductions perpendiculaire et parallèle est comparé à celui calculé. Un bon accord entre les deux valeurs est observé pour l’induction perpendiculaire. Le modèle surestime les performances du câble Roebel sous induction parallèle.

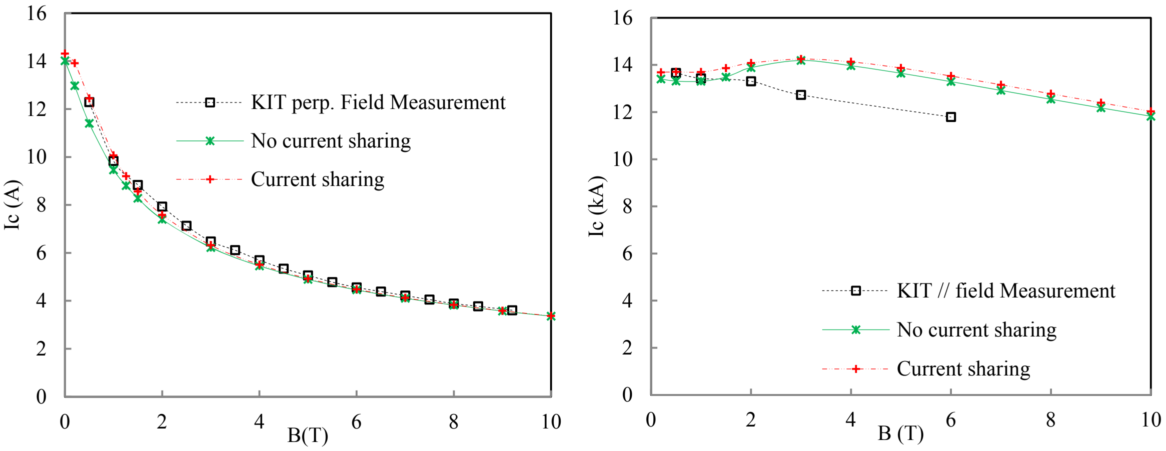

Figure 1.19: Le courant critique mesuré et calculé du câble Roebel KIT sous inductions perpendiculaire (gauche) et parallèle (droite).

1.6.3 Distribution de courant dans les câbles HTS : expériences et simulations

Modèle de distribution du courant dans les câbles HTS

Les brins des câbles Roebel testés dans FRESCA n'étaient pas isolés les uns des autres. Néanmoins, la résistance de contact interbrins était très élevée (25 $\mu\Omega$). Etant donné que les câbles avait des dimensions finies (2 m) et de faible résistance de contact aux connexions avec les câbles Rutherford en Nb-Ti (1-3 nΩ), on peut assumer que les brins étaient isolés les uns envers les autres. On peut alors considérer les différents brins du câble comme des conducteurs électriques connectés uniquement aux jonctions avec les câbles en Nb-Ti (voir figure 1.20). Chaque brin a une résistance propre (R_s) liée au supraconducteur et une résistance de jonction (R_j). Chaque brin a également une inductance propre (l) et une inductance mutuelle (M). Les lois de Kirchhoff sont appliquées à chaque maille et noeud du circuit, il en découle un système d'équations non linéaire qui peut être résolu par la méthode de Newton. Les seules inconnues de ce système d'équations sont les résistances de contact aux jonctions (Rj), le courant critique des brins ayant été calculé dans la section précédente.

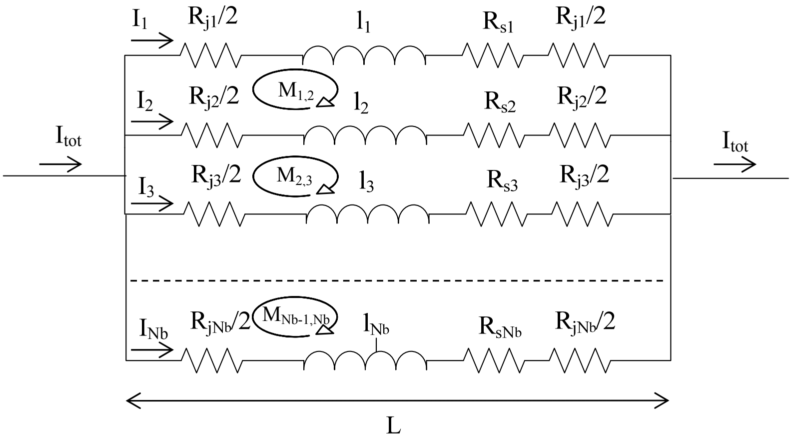

Figure 1.20: Circuit électrique équivalent d'un câble supraconducteur fait de N_b brins isolés.

Distribution de courant dans les câbles Roebel

Au cours de la caractérisation des câbles Roebel, la répartition de courant entre les brins n'a pas été mesurée de façon directe. Uniquement la chute de potentiel électrique le long des brins individuels a été mesurée, la comparaison entre les expériences et les simulations est par conséquent effectuée à travers ce paramètre. Dans le modèle de distribution de courant dans les câbles Roebel, les seules inconnues (résistances de contact des brins) sont ajustées de façon a reproduire les champs électriques mesurés. Dans la figure 1.21 les champs électriques mesurés et calculés le long des brins du câble KIT2 sont reportés en fonction du courant réduit du câble. Une forte non uniformité de résistance de contact des brins du câble Roebel est identifiée comme responsable de la distribution non uniforme du courant.

1.6.4 Conclusion

Lors des mesures des performances des câbles Roebel, une distribution non homogène du courant a été observée. Les possibles raisons induisant une telle distribution sont identifiées dans ce chapitre. Par l'intermédiaire d'un code numérique par éléments finis, les performances des câbles Roebel sont évaluées et comparées aux mesures effectuées. Un bon accord entre les deux est observé. Une modélisation de la

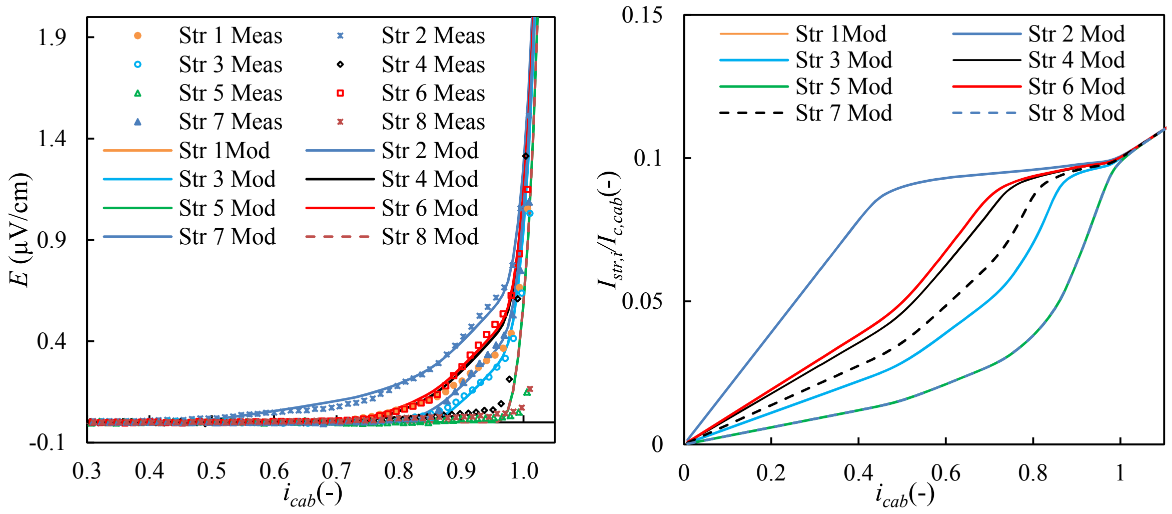

Figure 1.21: Le champ électrique mesuré et calculé le long des brins individuels du câble Roebel (gauche). La distribution de courant calculée dans les brins du câble Roebel (droite).

répartition de courant dans les câbles Roebel permet de mettre en évidence l'origine de la distribution non homogène du courant : la non uniformité des résistances de contact des brins.

1.7 Conclusion générale

Durant ma thèse je me suis concentré sur l'étude de l'implémentation des supraconducteurs à haute température critique dans les aimants d'accélérateur à haute induction. Aux regards des contraintes inhérentes aux aimants d'accélérateurs, les conducteurs YBCO et Bi-2212 ont étés identifiés comme très prometteurs. Ces matériaux qui ont des températures critiques autour de 95 K, présentent des inductions irréversibles et des densités de courant critique très élevées à 4,2 K. A ces températures, ils supplantent les performances des matériaux Nb-Ti et Nb_3Sn et permettent de générer des inductions dipolaires supérieure à 20 T. Dans ce travail, j'introduis un certain nombre de formulations mathématiques décrivant les performances électromécaniques des conducteurs HTS. J'utilise par la suite ces formulations pour déterminer les marges opérationnelles de dipôles en matériaux HTS. Les aimants d'accélérateurs requièrent l'utilisation de câble à fort courant. Je démontre dans ce travail que le câble Roebel fait à partir de bandes YBCO est un concept valable pour les aimants d'accélérateurs. Ces câbles, ont portés des densités de courant critiques supérieures à 1,1 kA/mm^2 sous une induction parallèle de 7,5 T. Les phénomènes de défaillance de ces câbles ont été identifiés et des solutions apportées. Une distribution non homogène du courant dans les brins des câbles Roebel a été attribué, par l'intermédiaire d'une modélisation a une non uniformité des résistances de contact.

Mon travail novateur a permis de développer des outils numériques et expérimentaux universels qui permettent de quantifier et évaluer les performances des câbles HTS pour les aimants d'accélérateur.

Introduction

Particle colliders are the main tool for investigating and understanding the fundamental laws of physics. The CERN Large Hadron Collider (LHC), the largest particle accelerator ever built, is a circular accelerator which steers and collides two counter-rotating protons beams. It has four collision points where detectors are placed to analyze the products emerging from the collisions. In a synchrotron machine an electric field is used to accelerate charged particles and a magnetic flux density is used to guide and focus them around the orbit. In circular accelerators the bending (dipole) flux density determines the final energy of the particles. In relativistic conditions, the relation between the beam energy, E_{beam}(in TeV), the dipole flux density B_d (in T) and the radius of the beam trajectory R_b (in km) is expressed by the following relation:

$$E_{beam} = 0.3\ R_b\ B_d \tag{1.6}$$

The maximum energy that a circular machine with a given geometry can achieve is limited by the maximum strength of the dipole magnetic flux density. There is therefore an interest in the particle physics community in searching for dipole magnets with higher strength. The LHC has a beam trajectory radius of 4.3 km and a collision center-of-mass energy of 14 TeV. Its successful operation enabled CERN to announce in 2012 the discovery of a particle resembling the Higgs Boson, the particle linked to the mechanism that gives mass to elementary particles. This discovery was made possible by the use of superconductivity, a core technology of the LHC. The accelerator employs 1232 large superconducting Nb-Ti dipole magnets operated at a flux density of up to 8.3 T in a bath of superfluid helium at 1.9 K. Energies higher than that achieved with the LHC require magnets made from superconductors with higher upper critical flux density. Nb_3Sn is an option for magnets operated up to about 14 T. The level of energies of the type being discussed for a potential energy upgrade of the LHC machine - 33 TeV- would require the use of high temperature superconductors (HTS).

Three technical HTS are available today: YBCO, Bi-2212 and Bi-2223. At low temperature YBCO conductors present both irreversible flux density and current density in excess of those measured in Bi-2212 and Bi-2223 conductors. In addition, YBCO can be used as reacted conductor, which makes its use for applications simpler than Bi-2212, which requires heat treatment at high temperature and in oxygen atmosphere after cabling and winding. The level of currents required for application to accelerator magnets, which is above 10 kA at the nominal operating temperature and flux density, excludes the use of single strands. The high current and high current density required can be achieved with cables having several strands connected in parallel.

The main objective of my work has been the study of HTS cables for high current/high current density applications, starting from the analysis and selection of suitable conductors, through the characterization of their intrinsic (e.g. critical surface, strain sensitivity and irreversible strain) and extrinsic (e.g. cabling degradation) properties, with the final objective of validating 10 kA-range cables based on HTS material for high flux density magnets.

In chapter two, the different constraints laying on superconducting accelerator magnets and their design are exposed. Starting from the 2-D electromagnetic design of dipoles and taking into account the performance of HTS conductors, a semi-analytical formula providing an estimate of the short sample flux density in HTS iron-less accelerator dipoles is derived. Different concepts of high current HTS cables are reviewed and the most relevant for application to high flux density accelerator magnets are presented.

In chapter three, several experimental techniques used for characterizing HTS conductors are introduced. The critical current of YBCO and Bi-2223 tapes at 4 K under parallel and perpendicular flux density is measured using purpose built samples holders. A complete review of the strain sensitivity of HTS materials is presented, and the measured critical current retention of HTS tapes under torsion is discussed.

In chapter four, expressions that describe the critical current density of HTS conductors as a function of flux density strength, flux density orientation, temperature and strain are introduced. Analytical models that provide the allowable twist and bending radius of YBCO tapes as a function of strain are elaborated and compared with measurements. The accurate expressions are then used to compute the margins of the winding pack of a 19 T dipole made with a YBCO cable. The study reveals that the peak flux density orientation is more critical than the peak flux density value.

In chapter five, two topologies of YBCO high current cables are characterized at 4.2 K and in flux densities of up to 9.6 T: the Roebel cable and the twisted pair cable. The twisted pair cable was proposed as a new type of electrical transmission cable operating in low fields. However its topology is similar to the stacked cable that is a promising candidate for high flux density application. Roebel cables for application to magnets were characterized in liquid helium under parallel and perpendicular flux densities. These are the first measurements ever performed at 4.2 K and with high currents. The Roebel cables reached critical currents of up to 12 kA with engineering current density in excess of 1.1 kA/mm2 at 7.5 T. These measurements demonstrate the potential of Roebel cables for high flux density magnets. During measurements two out of four Roebel cables were irreversibly damaged. The mechanism of failures is detailed and explained.

Multi-strand HTS superconducting cables may quench at current values that are lower than expected. One of the most likely reasons for this behaviour is non-uniform current distribution among strands. In chapter six, the different reasons for unbalanced current distributions are identified and models of current distribution are introduced. In a transposed cable, conductors occupy different positions in the cable cross sections along the transposition pitch. They experience different self-flux densities along the pitch length and their critical current is therefore not constant. The performance of HTS strands in transposed cable is calculated by means of finite element models. The derived cable performances are then compared to the measured ones. Finally a model of current distribution is elaborated and used for interpreting the results of the measurements. Proposals for improving the quench behaviour of Roebel cables are presented and discussed.

Chapter 2

Superconducting accelerator magnet: state of the art and perspective for HTS materials

In this chapter an introduction to superconducting accelerator magnets is provided. The constraints pertaining to these magnets are outlined and their basic design detailed. Based on the 2D electromagnetic design of dipoles and the performance of HTS conductors, semi-analytical formula allowing to estimate the ultimate flux density in HTS accelerator dipoles based on sector coils are derived. The ultimate performance of YBCO and Bi-2212 coils are estimated. The magnet cross sectional area is briefly discussed and a baseline value of current density in coil pack is determined. One of the constraints lying on accelerators superconducting magnet is the use large current capacity cable. A review of high current HTS cable concepts is performed in the second part of this chapter. Regards on their electromechanical properties, the promising candidates for application to high flux density accelerator magnets are selected.

2.1 Design of superconducting accelerator dipole

In particle accelerators, the first function of magnets is to guide and steer the particle, i.e. to keep it in orbit in a circular accelerator or to just bend in a transfer line. The second main function is focusing the beam, thus providing it with the necessary stability in the plane perpendicular to the trajectory. These two functions are ensured by respectively the arc dipoles and the arc quadrupoles. The arcs magnets represent most of the accelerator layout. In LHC 1232 arc dipoles and 360 arc quadrupoles are in operation [1]. The luminosity of a collider is the ratio between the production rate of events and the cross section of the beam [2]. To increase this ratio, the quadrupoles that are just before the collision points focus the beam strongly. This set of quadrupoles features an aperture significantly larger than the lattice quadrupoles, and requires a large flux density gradient. The magnets that are used to steer and focus the beam close to interaction points are named interaction magnets [3]. The other important function of magnets is, in general terms, to assure the stability of the beam in the transverse space. This is accomplished by correctors: quadrupoles, sextupoles and octupoles of much smaller size and flux density compared to the arc and interaction magnets.

2.1.1 Constraints on the design of superconducting accelerator magnet

The design of superconducting magnets is subject to a number of constraints: the most important are reported and detailed in this section.

Aperture

High energy particle colliders are filled with a large number of particles that are then accelerated for few hours to the final collision energy. The periodic accelerating electrical field collects the particles into circulating bunches: in the LHC at nominal current, there are 2808 bunches, each consisting of 1.15 10^{11} particles, circulating in each of the two rings [2]. The particles travel in an ultra-high vacuum environment, of the order of 10^{-7} bar whereas superconducting magnets are operated in liquid helium at pressure of about 1 bar. A vacuum pipe is installed in the coil aperture to allow the flow of particles. A small number of particles are unstable; these particles exit the reference trajectory and hit the surrounding materials leading to heat generation and possible radiation damage. The interaction of these particles with the magnet winding is undesirable, so they must be intercepted by a beam screen. The aperture of this screen is set for LHC to be at least 10 times the RMS transverse beam size [2]. The beam, the beam screen and the vacuum pipe have to fit in the bore of the magnets, leading to a minimum bore aperture of arc magnets of about 40 mm. The bore aperture of a superconducting magnet is kept as small as required since the cost, the cold mass and the stored magnetic energy rise with magnet dimensions. Close to interaction regions, particle beam has a larger RMS transverse dimension in order to enhance the collision luminosity: magnets with larger aperture are therefore required [2]. The aperture of LHC arc and interaction magnets are respectively 56 mm and 70 mm [2].

Flux density quality

The design of superconducting accelerator magnets is largely determined by the optimal distribution of compact superconductors around the beam aperture. In fact, in contrast to classical electromagnets, the flux density in a superconducting accelerator magnet is mainly produced by the current in the conductor, rather than the magnetization of an iron yoke. The coil shape is optimized to maximize the bore flux density and achieve acceptable flux density quality, as described later. The large forces that are experienced by the coil (several tens to hundreds of tons per meter) cannot be reacted by the winding alone, and hence the force is transferred to a structure that guarantees mechanical stability and rigidity.

The use of high current cables

Superconducting accelerator magnets are wound from cable made of superconducting strands bundled together. The most obvious consequence of using cables instead of single strands is the reduction of the magnet inductance. **The use of multi-strand cables presents also many advantages:**

- **The number of turn in the magnet is reduced**

  Large scale superconducting magnets require large amount of superconducting material. For example an LHC main dipole requires more than 20 km of Nb-Ti strand. This quantity is one order of magnitude larger than the typical superconductor unit length. By using multi strand cable instead of single conductor, one can wind a magnet with a single unit length of cable and a limited number of turns: this facilitates the winding process.

- **Reduction of quench protection time constant**

  Superconductors in magnets are submit to a spectrum of disturbances. The bigger the device, the more likely are releases of energy and the more varied the character of the disturbances. The immediate consequence of a disturbance is a local rise in temperature. This temperature rise may be huge even for small disturbances because the specific heat of materials at 4.2 K is very small. For temperature excursion exceeding the so called current sharing temperature, some of the transport current in the filaments will spill over to the normal-conducting matrix/substrate. If the extra heat generated oversteps the heat removed into the surroundings, the temperature will exceeds the critical temperature; a normal zone is created within the coil winding. The resistance of the superconductor in the normal state is a few order of magnitudes higher compared with that in superconducting state. The large magnetic energy stored in the winding, is progressively discharged in the normal zone. The normal zone must spread to avoid high temperature generation. The diffusion of this normal zone is characterized by the normal zone propagation velocity (NZPV). At high temperatures, such as 77 K for HTS material, the temperature margin is in principle sufficiently low to cause a fast normal zone propagation. On the other hand, the operating current at these high temperatures is low, and the NZPV is severely hindered by the lack of driving force (I^2R) and by the large heat capacity of the materials. At low temperatures, by contrast, the heat capacity is low: the operating current, and Joule heating, can be high enough to increase the NZPV. On the other hand, the large temperature margin (in HTS) tends to reduce the NZPV. Recent experiments on small-scale coils built with Bi-2212 and operated at 70-90% of I_c up to 8 T have shown an NZPV as small 0.5 cm/s [4]. The use of high current cables help to improve the protection of a superconducting coil as the current can be removed more rapidly. The quench detection and protection of HTS magnet is very delicate and not yet mastered. More details about HTS magnets protection can be found in [5].

- **Lower voltage power supply requirement**

  In operating conditions, superconducting electromagnets are operated with DC ramp rates of few tens of amps per second. Reduction of magnet inductance reduces the voltage requirement of the power supply.

- **Voltage to ground insulation**

  In case of fault, the magnetic energy of superconducting magnets is discharged in a dump resistor with a current ramp rate of up to a few kA per second. Reduction of magnet inductance helps to keep voltage to ground requirement to an achievable value in the range 1-10 kV. This voltage requirement holds for insulation to ground of the winding and for the associated instrumentation.

- **Higher reliability**

  One of the main issues in manufacturing superconductor is to get a conductor without local defects over long unit lengths. Assembling conductors into multi-strand cable presents the advantage of sharing the current of possibly damaged strands. Superconducting cable is therefore more reliable than conductor made of a monolithic strand.

The use of cable in superconducting magnets also presents some disadvantages:

- **Flexibility on multipole minimizations**

  When coils are wound with cable, the coil will not exactly match the optimum analytical magnetic design, thus producing non-negligible multipoles. The dimension of the cable imposes an additional constraint on the magnetic optimisation.

- **Dynamic flux density distortion**

  In accelerator magnet superconducting multi-strand cables are submitted to time dependent flux density. Apparition of current coupling between strands with long time decays results in dynamic distortion of flux density. Coupling currents are proportional to the flux density time variation and inversely proportional to the contact resistance between strands. High contact resistance values suit for diminution of coupling current. On the other hand, for electrical stability of the cable, current sharing between different strands is required. This calls for careful optimization.

- **Cryogenic operational cost**

  From room temperature, current is carried to magnets through resistive or partially resistive current leads. Both conduction and joule heating in the leads induce thermal load on the cryogenic system. The use of high current cable increases the thermal load and therefore the cryogenic operational cost. High Temperature Superconducting (HTS) current leads have become, in the last few years, a valid choice for the powering of superconducting magnet systems. Their potential for reducing the heat load to the cryogenic environment makes them attractive mainly for large scale superconducting accelerators, operating at liquid helium temperature. In a machine made out of many magnets operated at the same current (as for LHC), the number of current leads is reduced by connecting magnets in series strings. The heat load to the helium bath induced by the 13 kA HTS current leads of the LHC was measured to be lower than 1 W per lead [6].

- **Accommodation of rectangular shape conductor**

  Superconductors in the form of wires are easy to accommodate into transposed cable. Some HTS superconductors are only available in form of tapes that are much more difficult to assemble into transposed multi-strand cable.

2.1.2 Design of superconducting dipole

In the previous section a few of the many constraints pertaining on the design of an superconducting accelerator magnets have been exposed. In this section, a simplified magnetic layout of arc dipole that cancel the first non-desired harmonic of flux density is introduced and then used to estimate performance of HTS magnets.

Ideal current distribution to generate pure dipolar flux density

The prime purpose of the electromagnetic design is to obtain a multipolar flux density with the quality demanded by beam physics requirements. Several ways can be found to generate perfect multipolar flux densities required by high energy physics accelerator magnets.

Two uniform current density cylinders with opposite current polarity generate a perfect dipolar flux density in the region of current overlap, i.e. in the internal current-free region. More generally, the uniform dipolar flux density may be generated by a constant current density with a geometry given by opposite intersecting ellipses as depicted in figure 2.1. The non-circular aperture of such coils is a drawback, in addition the shape of the coil is not easily approximated with superconducting cable.

As an alternative, a perfect dipolar flux density can be generated by a shell of current, of constant thickness, in which the volume current density is maximum at the midplane and vanishes toward the pole region with a $J(\phi) = J_0 \cos\phi$ dependence. In this case the inner region can be perfectly circular. A $J(\phi) = J_0 \cos\phi$ not only generates a perfect dipolar flux density, but is the most efficient current distribution, i.e. any other distribution requires more total current (Ampere turns) to generate a given central flux density [1].

In practice, the $\cos\phi$ current distribution cannot, however, be technically realized with a cable and a single power supply. Therefore, the magnetic design aims at an approximation of the ideal current distribution with shells or blocks of constant current density. These two approximations are namely the sector coil and the block coil layout (see figure 2.1). The design of these two coil layouts is detailed in the next subsections.

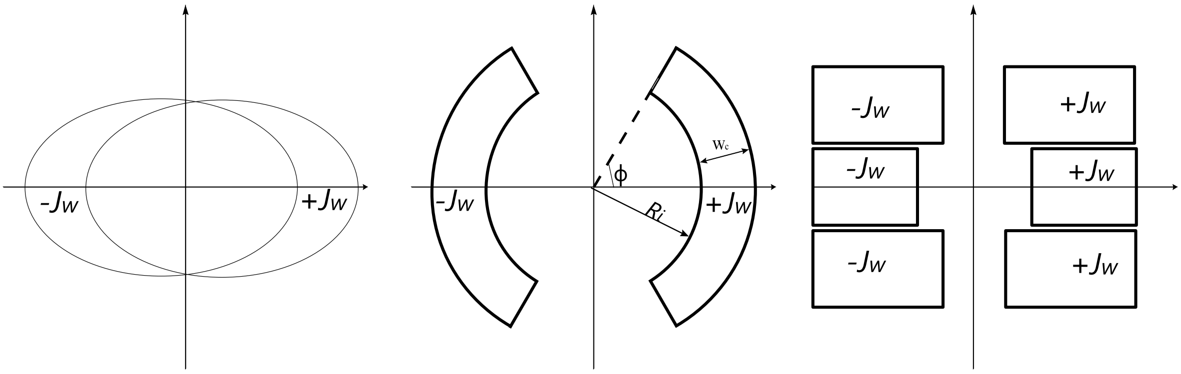

Figure 2.1: Cross section of accelerator dipole: intersection of ellipse (left), the simplified sector coil cancelling the first non desired flux density harmonic (middle), and the block coil (right).

Sector coil

In sector coil, the $\cos\phi$ ideal current distribution is approximated by sector shells of constant current density, with spacers. The cables are arranged around the circular aperture to form a roman arch. The cable cross sections have generally a keystone angle to accommodate the formation of the arch. A typical cross section of sector coil is presented in figure 2.2. For the specific case of a four-fold symmetric coil layout, as shown in figure 2.1, the skew multipoles and the even normal cancel out and the equation for the multipoles (B_n) reads:

$$B_n(\phi) \propto \sin(n\phi) \tag{2.1}$$

The magnitude of the multipoles is decreasing with order (n), so the highest priority is to cancel out the low order multipoles, typically B_3 to B_{11}. With one-sector per quadrant, one can only set one multipole to zero, e.g. B_3 with $\phi = 60°$.

By segmenting the sectors using insulating wedges, and using two (or more) nested layers (see figure 2.2) more multipoles could be set to zero. To cancel out the first five multipoles three sectors at least are required. When the coil is built with a cable, the actual thickness of the cable imposes an additional constraint. The coil will not exactly match the analytical solution, thus producing non-negligible multipoles. Additional sectors are required to deal with this constraint. The LHC arc dipoles, for example, are made of 6 sectors per quadrant arranged into two layers [2]. The bore flux density (B_0) of a sector coil dipole is expressed as:

$$B_0 = \frac{2\mu_0}{\pi} w_c \; J_w sin(\phi) \tag{2.2}$$

where w_c is the coil width, J_w is the current density and ϕ is the extend of the sector coil as depicted in figure 2.1.

Block coil

In block coil, the $\cos\phi$ ideal current distribution is approximated by rectangular block of constant current density, with spacers. The blocks are formed by the winding of the cable around an island. Typical cross section of block coil dipole is depicted in figure 2.2. The block coil configuration is sometimes chosen to manage the mechanical stress on conductors and has been mainly used for high flux density Nb_3Sn demonstrator dipoles [7][8]. As for sector coil, specific block coil geometries cancel the undesired flux density harmonics [9].

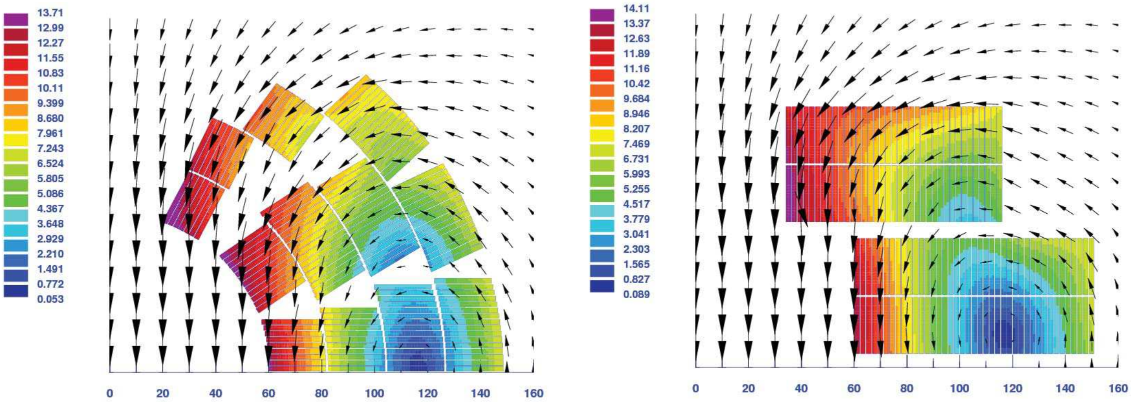

Figure 2.2: Flux density map inside the cross section of a 13 T dipole. Solution based on the sector coil (left) and block coil (right) studied in the framework of EuCARD [10].

Hybrid and graded magnets

The flux density map inside the thickness of a sector and a block coil is strongly non-uniform: the flux density is systematically lower towards the outer radius of the coil as depicted in figure 2.2. With regard to this observation, two different options allow to enhance the performance of a magnet: the grading and/or the hybriding of the coils. These two solutions are both applicable either in block coil and sector coil configuration, but they are presented here only for sector coils.

- The grading of magnet consist in an increase of the outer layer current density in the way to enhance the central flux density. Two options could be used for grading a magnet: the first one is to use different power supply for the different layers, the second one consists in changing the cable cross section between the different layers. The last solution presents less complexity and is used in LHC arc dipoles [2]. It must be pointed out that grading reduces the coil thickness at the expense of an increase in mechanical stress on the conductor.

- Every superconductor has a flux density limitation (B_{irr}) beyond which it can no longer transport current. Superconductors with high B_{irr} are expensive and to manage the cost of an high flux density magnet, one can use different superconductors in the magnet cross section. In an hybrid magnet, the superconductor with the highest B_{irr} is placed at internal layer where the flux density is the highest. The superconductor with the lowest B_{irr} is placed at outer layer where the flux density is the lowest. A Nb-Ti/Nb_3Sn hybrid demonstrator accelerator dipole has already been tested [11].

Iron yoke

An iron yoke surrounding a coil winding has the main function of closing the magnetic circuit: it shields the surrounding environment from the inner magnetic flux density and induces higher peak and bore flux density for the same current density. A typical 5% enhancement of bore flux density for a 13 T dipole is observed by the use of iron yoke [10]. The iron contribution to central flux density is non-linear and starts to saturate for flux densities above about 2 T. In this chapter, magnets are considered without iron yoke.

Stresses in superconducting dipoles

The mechanical design of superconducting magnets has to deal with two main issues: first, a mechanical structure must be designed that limits the deformations of the coil due to electro-magnetic forces (figure 2.3); secondly, the stress arising inside the coil must be carefully analysed to avoid insulation creep or superconductor degradation [12]. The YBCO conductors have shown to withstand transverse stress of up to 150 MPa without significant I_c degradation [13]. The BSCCO materials present reduction of performances at lower stress of about 100-120 MPa [14]. The coil cross-section must be carefully designed to match the mechanical limits of the superconductor. To estimate the mechanical stress in the dipoles, the simplified sector coil layout is used: the coils is of inner radius R_i, radial width w_c and an angular extension $\phi = 60°$ (thus canceling the first allowed flux density harmonic B_3), fed by a uniform current density J_w. The equation for the azimuthal compressive stress σ_ϕ on the coil mid plane can be evaluated through balancing the forces acting on an infinitesimally small coil element not considering the shear effect. Integrating the differential equation given by the force balance, one can get [12]:

$$\sigma_\phi(r) = \frac{\mu_0\sqrt{3}J_w^2}{6\pi\ r}\left[2r^3 + R_i^3 - 3r^2(R_i + w_c)\right] \tag{2.3}$$

Where r is the radial position. The azimuthal stress increases quadratically with J_w. In figure 2.4 the azimuthal stress at coil mid plane is depicted for different coil thicknesses producing 20 T of central flux density with coil aperture of respectively 30 mm and 60 mm. For the 30 mm aperture dipole, a peak stress of 155 MPa is observed in a 72 mm thick coil whereas a value of 210 MPa is reached in a coil of the same thickness but with an aperture of 60 mm: lower stresses are observed for windings that are either thick or feature a small aperture.

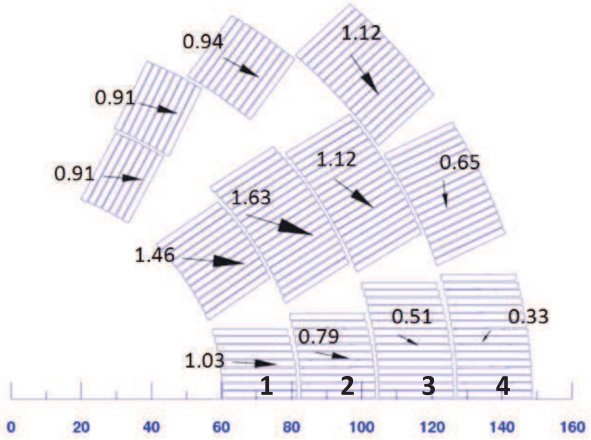

Figure 2.3: The electromagnetic forces distribution (MN/m) in the cross section of the sector coil layout of the EuCARD Nb_3Sn dipole [10].

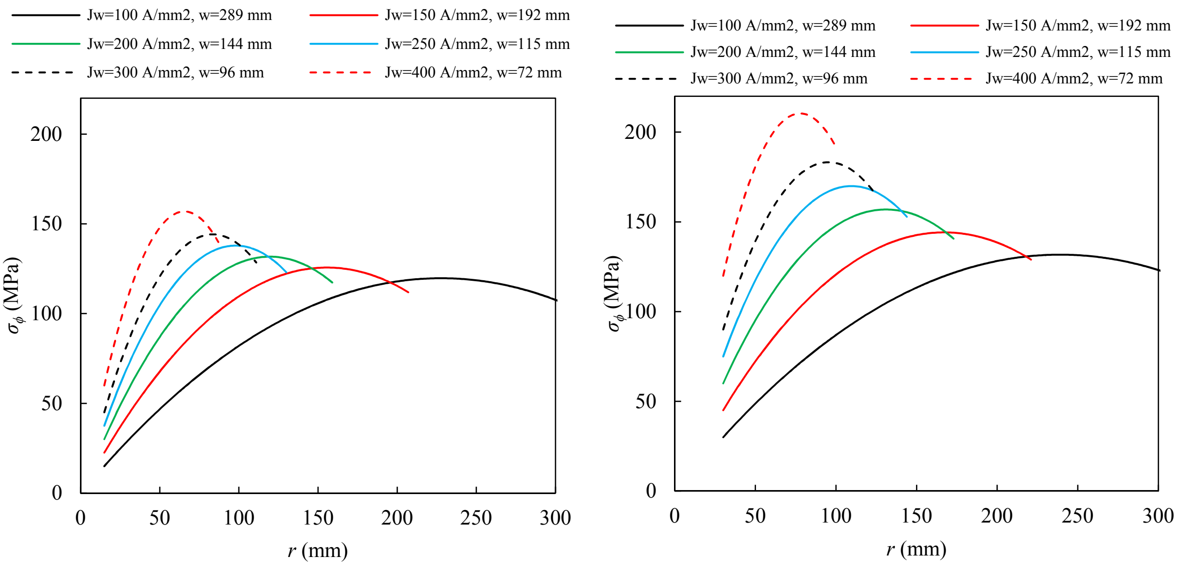

Figure 2.4: The azimuthal stress on the mid plane of a 30 mm aperture (left) and of a 60 mm aperture (right) 20 T dipole as a function of the radial position r.

2.2 Performance and cross sectional area of HTS dipole

A deeper understanding of particle physics requires higher collision energy and/or higher luminosity. The increase of these parameters means, by keeping the actual LHC layout, higher flux density of the arc dipoles and/or higher gradient (or coil aperture) for the interaction quadrupoles. The most relevant parameters of superconductors for magnet application are the engineering critical current density (J_{ce}) and the irreversible flux density (B_{irr}). The engineering critical current density is the ratio of the critical current (I_c) to the cross sectional area of the conductor. The critical current (I_c) is defined as the current above which a substantial electrical field is generated parallel to the transport current (see chapter 3). The B_{irr} is the flux density at which the I_c become null. Both these parameters are temperature dependent see chapter 4 for more details. The ultimate performance of a superconducting magnet is reached as soon as any local winding J_{ce} value is reached. Magnet performances are therefore limited by the intrinsic properties of superconductors. A review of the HTS magnet performance is performed in this section followed by an estimate of the ultimate performance of a dipole based on the use of HTS.

2.2.1 Review of performances of HTS solenoids and dipoles

After the discovery of high-temperature superconductors in 1986 [15], their potential application in high-field magnets was generally recognized. Many projects were launched to develop and construct high flux density NMR magnets. This resulted in 2011 of the generation of a record 35.4 T by an hybrid HTS solenoid [16]. Trends in the central flux density and winding current density achieved in HTS solenoids are reported in figure 2.5. During the same period, the application of HTS materials to accelerator like magnets has been limited, with a record flux density of 2.6 T at a temperature of 18 K being reported [17]. The performance of the most significant HTS solenoids and dipoles are reviewed in this section.

Performance of HTS Solenoids

Almost all the HTS solenoid coils that have been made are demonstrators that take place as insert in resistive, hybrid or superconducting magnet. The bore flux density of these magnets is increased by a few tesla by the presence of the HTS insert. Key parameters of the most significant HTS inserts are presented in table 2.1. The first significant HTS insert was developed by Hitachi in 2000 [18]: a 5.4 T contribution of the HTS insert was added to the 18 T of the LTS outsert to create a new 50 mm bore 23.4 T LTS/HTS high flux density magnet that was operated for 1.5 years. This Bi-2212 coil meets the average current density target of 72-112 A/mm^2 in the winding. In 2004 the NHMFL/OST 5 T insert was the first to reach the 25 T central flux density benchmark [19], with a resistive magnet providing 20 T background magnetic flux density. The current density in the Bi-2212 winding was moderate (69-89 A/mm^2) compared to YBCO insert built later on. A YBCO insert tested at NHMFL in 2009 reached a winding current density of 459 A/mm^2 at 33.8 T (2.8 T from the HTS) [20]. This was nearly four times the winding current density of the best BSCCO insert coil, while this insert operates in significantly higher magnetic flux density. A second insert build the same year at NHMFL produced 7.8 T in the background flux density of 19 T with a current density of 274 A/mm^2 [21]. These two inserts demonstrated the potential of YBCO conductors in high flux density application. To explore the limits of layer wound YBCO coils in a high flux density environment (above 30 T), a series of small insert coils was built and characterized at the NHMFL [16][20]. One of the coils repeatedly reached 35.4 T at 1.8 K using a YBCO tape wet wound with epoxy and nested in a 31 T background magnet (see figure 2.6). The coil outer diameter was 38 mm, the inner one 14 mm and at full flux density (35.4 T), the coil operated at a winding current density of 308 A/mm^2. The coil was quenched safely several times without I_c degradation. Quench protection of the coil was achieved by closely monitoring layer voltages, used to trigger a trip of the power supply and transfer the stored energy to a dump resistor circuit as soon as a threshold voltage value was reached.

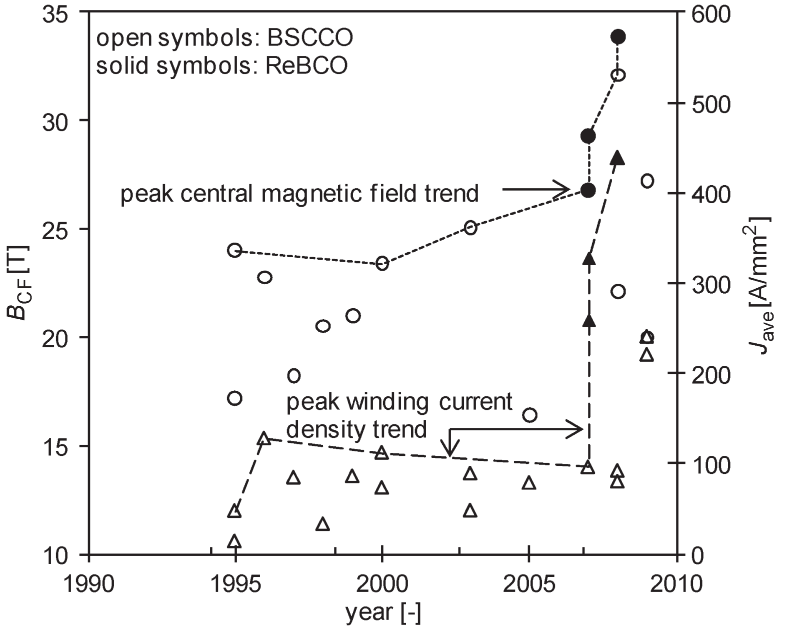

Figure 2.5: Trends in the central flux density (circles) and winding current density (triangles) achieved in HTS solenoids at 4.2 K (plot from [22]).

Table 2.1: Review of the HTS solenoids performance at 4.2 K.

Central flux density (T)	Flux density from HTS (T)	J_w (A/mm^2)	Bore diameter (mm)	Material	Year	Lab.	Ref.
35.4	4.2	308	14	YBCO	2011	NHMFL	[16]
33.8	2.8	459	25	YBCO	2009	NHMFL	[20]
26.8	7.8	274	19	YBCO	2009	NHMFL	[21]
25	5	69-89	41	Bi-2212	2004	NHMFL	[19]
23.4	5.4	72-112	16	Bi-2212	2000	Hitachi	[18]
16.9	5.4	59	50	Bi-2223	2005	KIT	[23]

Performances of HTS dipoles

The application of HTS materials to accelerator dipole has been limited. The few relevant HTS dipoles built are presented in this section and the main parameters are reported in table 2.2. A 3 T proof-of-principle dipole magnet for accelerator applications, based on YBCO tape was designed, built, and tested by a consortium under the lead of Danfysik (see figure 2.6) [17]. The magnet was designed to have a straight, circular bore with a good flux density region of 25 mm of radius, and a magnetic length of 250 mm. A total length of 2.5 km YBCO-based copper stabilized conductor supplied by SuperPower, was isolated with 0.025 mm of epoxy and subsequently wound into 14 saddle coils and 4 racetrack coils with a cosine theta like configuration. The coils were impregnated with epoxy and mounted between a support of stainless steel and a collar made from aluminium. Due to production errors in the impregnation process, four coils did not live up to the test requirements and had to be removed from the magnet when going to high excitation levels. This resulted in a lower magnetic flux density than the design value. The maximum attained flux density with the reduced number of coils but with added iron poles inside the aperture was 2.60 T, which was reached at a temperature of 18 K and a current of 126 A. A 1 m long dipole magnet made of 1G Bi-2223 tapes, fabricated and tested by NSRRC and HTS-110 Ltd [24], was successfully operated for 72 h at the central flux density of 1.26 T at 45 K. A series of pancake racetracks coils wound with a 17 strand Bi-2212 Rutherford cable were manufactured and tested at LBNL [25][26]. Measurements were performed at 4.2 K on subscale coil standing alone. Over the 10 subscale coils tested the maximum quench current occurred at 1.1 T of peak flux density instead of the 2.6 T expected. The twisting of filaments was shown to induce additional I_c degradation with respect to non-twisted filaments. Witness samples and cables reacted during the same heat treatment than coils, exhibited better performance. The temperature homogeneity in the coil pack during the heat treatment was identified as a critical issue of Bi-2212 conductors.

Table 2.2: Review of the HTS dipoles performance.

Central flux density (T)	Temperature (K)	J_w (A/mm^2)	Magnetic length (mm)	Material	Year	Lab.	Ref.
2.6	18	-	250	YBCO	2012	Danfysik	[17]
1.9	4.2	68	400	Bi-2223	2002	IHEP	[27]
1.1	4.2	232	300	Bi-2212	2010	LBNL	[25]
1.3	45	86	1000	Bi-2223	2012	HTS-110	[24]

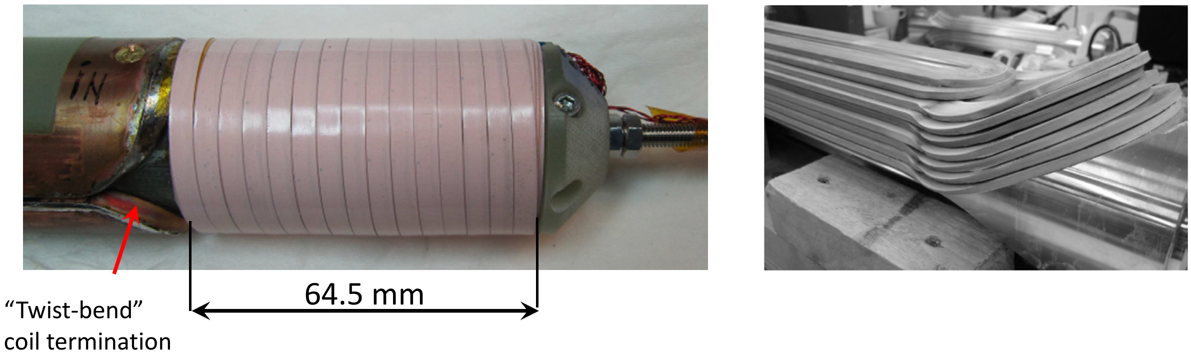

Figure 2.6: The YBCO insert solenoid that produced 4.2 T in a 31.2 T background flux density [16] (left). The YBCO dipole that reach 2.6 T of central flux density at 18 K [17] (right).

2.2.2 Ultimate bore flux density of HTS dipoles

The LHC magnets are built with the alloy compound Nb-Ti which has an intrinsic flux density limitation of about 11 T at 4.2 K and 13 T at 1.9 K [28]. For dipoles operated at 1.9 K, this leads to an operational bore flux density of 9 T [29]. The 4 T difference between material intrinsic flux density limitation and magnet bore flux density is explained by both a higher flux density intensity in coil winding compared to bore and an operation margin of about 20%. To overstep this 9 T flux density limitation, one has to use superconductors with higher B_{irr} values. The inter metallic compound Nb_3Sn exhibit B_{irr} value of 23 T at 1.9 K [30]. The technology of superconducting magnets made with Nb_3Sn was demonstrated with the design, construction and operation of a number of prototypes [7][8][11][31] and a record bore flux density of 16 T [7].

A more substantial gain in bore flux density is expected with HTS materials since their B_{irr} at low temperature is beyond 100 T [32][33]. In this section, based on the 2D electromagnetic design of dipoles and the performance of HTS conductors, semi-analytical formula allowing to estimate the bore flux density at short sample limit ($B_{0,ss}$) in HTS ironless accelerator dipoles based on sector coils is derived. The formula is then applied to 30 mm aperture YBCO and Bi-2212 sector coil dipoles.

Critical point of coils made from HTS conductor with anisotropic J_c

The ultimate bore flux density of a dipole, denoted short sample flux density ($B_{0,ss}$), is reached as soon as any location of the coil rise the local J_{ce} value. For non-graded magnet made from isotropic superconductor, the first point to hit the critical surface is the one that see the peak flux density (B_p). In sector coil, the peak flux density is located on the edge of the coil at a radial position that depends on coil thickness. For magnets made from HTS conductors with anisotropic I_c (YBCO and Bi-2223 tapes) the first point to reach the J_{ce} is no longer necessarily the one with the peak flux density: the critical point has to be found with regards to both the flux density strength and orientation. Each superconductor has its own I_c anisotropy therefore, even with the same coil layout the location of critical point is conductor dependent.

Simplified J_{ce} parameterization

In order to estimate the performance of HTS magnets, performances of superconductors have first to be parametrized. The different HTS materials considered here are YBCO and Bi-2212. The J_{ce} of Bi-2212 and YBCO conductors is temperature and flux density dependent [34]. The J_{ce} of YBCO tapes is in addition flux density orientation dependent, as depicted in figure 2.7. These two HTS materials have a critical temperature (T_c) exceeding 89 K and could therefore be operated at 77 K (the temperature of liquid nitrogen at 1 bar). At 77 K the I_c of the different conductors is not exceeding 400 A in self flux density [35][36], a substantial gain in term of both I_c and B_{irr} is observed by lowering the operating temperature down to 4 K [35][36][34]. A marginal increases of YBCO tapes I_c is observed by lowering the temperature from 4.2 K to 1.9 K (see chapter 3). The HTS magnets are considered in this thesis to be operated at 4.2 K.

J_c anisotropy of YBCO conductors

The critical current density (J_c) of YBCO tapes is dependent on flux density orientation. Two flux density orientations with respect to the wide face of the tape are of specific interest: the parallel and the perpendicular flux density. The lowest values of J_c are observed in the perpendicular flux density at 4.2 K, whereas the largest ones are observed in parallel flux density regardless of temperature. The J_c anisotropy of YBCO conductors at 4.2 K is depicted in figure 2.7. At high flux density, the J_c of YBCO tapes is highly sensitive to small deviation from the parallel orientation: at 20 T, a deviation of 5° from parallel orientation decreases the J_c by a factor 2. More details about J_c anisotropy are given in chapters 3-4.

In sector coil dipoles, the flux lines at inner coil radius are mostly perpendicular to the conductors, as depicted in figure 2.2. In block coils even if the flux density is parallel to conductors at innermost layers, its takes all the orientations in the winding pack. The ultimate bore flux density of bloc and sector dipoles made only from YBCO coils is estimated by considering the conductor J_c in perpendicular flux density.

When a YBCO dipole made of bloc coils is nested in the bore of an LTS dipole, the flux lines are almost parallel to all the HTS conductors (see figure 4.8). This assumption is almost true if the bore flux density generated by the outsert LTS coils is superior to the one produced by the HTS coils. For YBCO insert dipole made from block coils, the ultimate bore flux density is estimated through the conductor J_c in parallel flux density.

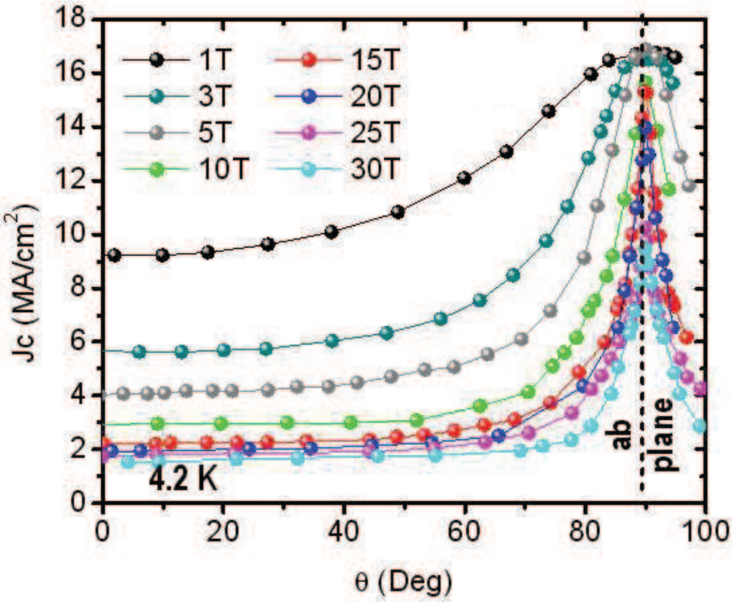

Figure 2.7: The J_c anisotropy of YBCO SuperPower conductors at 4.2 K [37]. The orientation refers to the c-axis of crystals. The 90° orientation corresponds to flux density parallel to tape plane.

$J_{ce}(B)$ parameterization

The engineering critical current density (J_{ce}) of HTS and LTS conductors at respectively 4.2 K and 1.9 K are presented in figure 2.8. The LTS materials are operated at 1.9 K since a substantial benefit of J_{ce} is observed compared to 4.2 K [28][30]. The J_{ce} of HTS materials is weakly affected by flux density intensity, thanks to a high value of B_{irr}. The J_{ce} performances of the different HTS superconductors can be described with an accurate expression that has a small number of fitting parameters. Note that J_{ce} parameterization will be discussed in much more detail in chapter 4. The flux density dependency of J_{ce} in HTS materials is expressed as:

$$J_{ce}(B) = (\frac{r_0}{B^s} - Bd) \tag{2.4}$$

Where r_0, s and d are fitting parameters. In this expression, B is the modulus of flux density for Bi-2212 conductors. For YBCO conductors, B is either the parallel or the perpendicular flux density, depending on the orientation considered. The $J_{ce}(B)$ dependence (depicted in figure 2.8) is accurate with respect to the reported measurements for all materials and thus over the full flux density range.

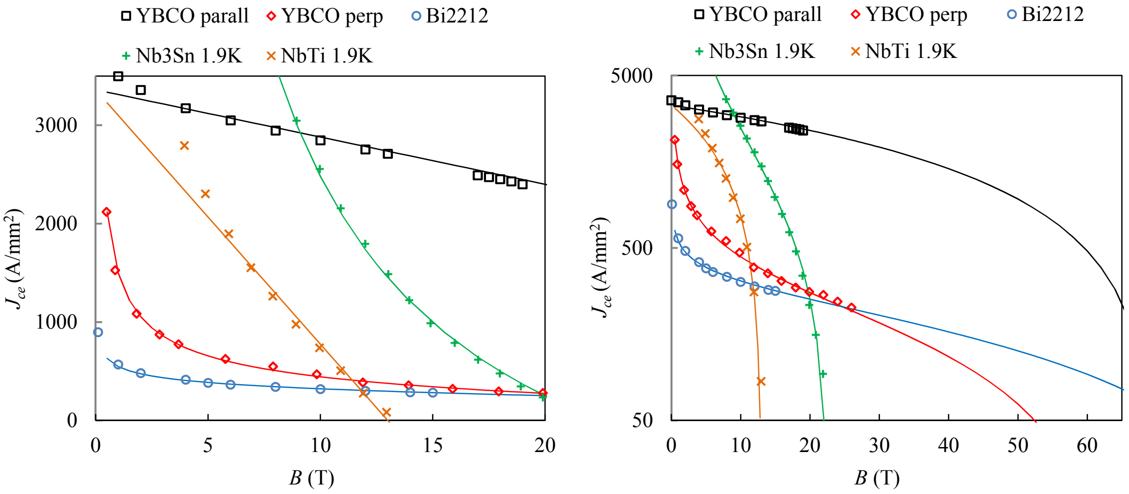

Figure 2.8: J_{ce} parameterization versus reported measurements for HTS and LTS conductors. Up to 20 T (left) and up to 65 T in a log scale (right).

Ultimate bore flux density ($B_{0,ss}$) of an HTS dipole

The $B_{0,ss}$ of an HTS dipole can be expressed as a function of the superconductor performance and coil layout. For a sector coil dipole, the bore flux density (B_0) and the peak flux density (B_p) are expressed as [38]:

$$B_0 = \frac{B_p}{\lambda} = \gamma_0 \; w_c \; J_w \tag{2.5}$$

where γ_0 is characterizing the coil layout. For the simplified dipole layout ($\phi = 60°$) considered here the bore flux density is expressed through $\gamma_0 = \sqrt{3}\mu_0/\pi = 6.93\ 10^{-7}$ [38]. Both B_0 and B_p are proportional to J_w and the coil thickness w_c. They are independent of the magnet aperture. The parameter λ that represents the ratio between B_p and B_0 has been numerically evaluated by [38] for an aperture of 30 mm: from a value of 1.45 at a coil thickness of 4 mm the ratio tends to unity in a hyperbolic way with increasing thickness. For a 40 mm thick coil the ratio is already 1.04. The following expression can be used to fit numerically computed values:

$$\lambda = 1 + \frac{c\ R_i}{w_c} \tag{2.6}$$

where $c = 0.07$ [38]. In any superconducting magnet, the superconductor is diluted in the coil: void fraction and insulation reduce the winding pack engineering current density (J_w) compared to the engineering current density flowing in the superconductor (J_e). The winding current density is expressed as:

$$J_w = KJ_e \tag{2.7}$$

where K is the dilution factor defined as the ratio between the sum of strands cross section and insulated cable cross section. Regardless of superconductors, a typical dilution factor of 0.8 is used in this section. The $B_{0,ss}$ is reached when the peak flux density hits the critical surface ($J_e = J_{ce}$). The $B_{0,ss}$ of HTS dipoles can therefore be expressed as:

$$B_{0,ss} = \frac{1}{\lambda}\left(\frac{\gamma_0 w_c \lambda K r_0}{1 + \gamma_0 w_c \lambda K d}\right)^{\frac{1}{s+1}} \tag{2.8}$$

The $B_{0,ss}$ of a 30 mm aperture HTS dipole is depicted in figure 2.9 as a function of the coil thickness. In the same figure, the $B_{0,ss}$ of Nb-Ti and Nb_3Sn coils are also reported using expressions from [38]. Asymptotic values of $B_{0,ss}$ for Nb-Ti and Nb_3Sn dipoles are reached respectively at flux densities of 11 T and 20 T. Up to coil thickness of 200 mm the $B_{0,ss}$ produced by HTS coils doesn't saturate. The performances of Nb_3Sn dipoles are overstepped by respectively YBCO and Bi-2212 dipoles for coils thickness of 75 mm and 105 mm. A 165 mm thick YBCO or Bi2212 sector coil produce a flux bore flux density of 28 T. If the YBCO is considered in the parallel flux density orientation, large flux density is generated even for thin coils: a 30 mm thick coil produces the central flux density of 29 T. In comparison, a Nb-Ti coil of the same thickness produces a flux density of 9.5 T. The $B_{0,ss}$ of dipoles is strongly dependent on the dilution factor K. For protection reasons, especially for YBCO conductors, the dilution factor (K) must be lowered compared to the 0.8 value considered here [5]. Lower values of $B_{0,ss}$ are therefore expected.

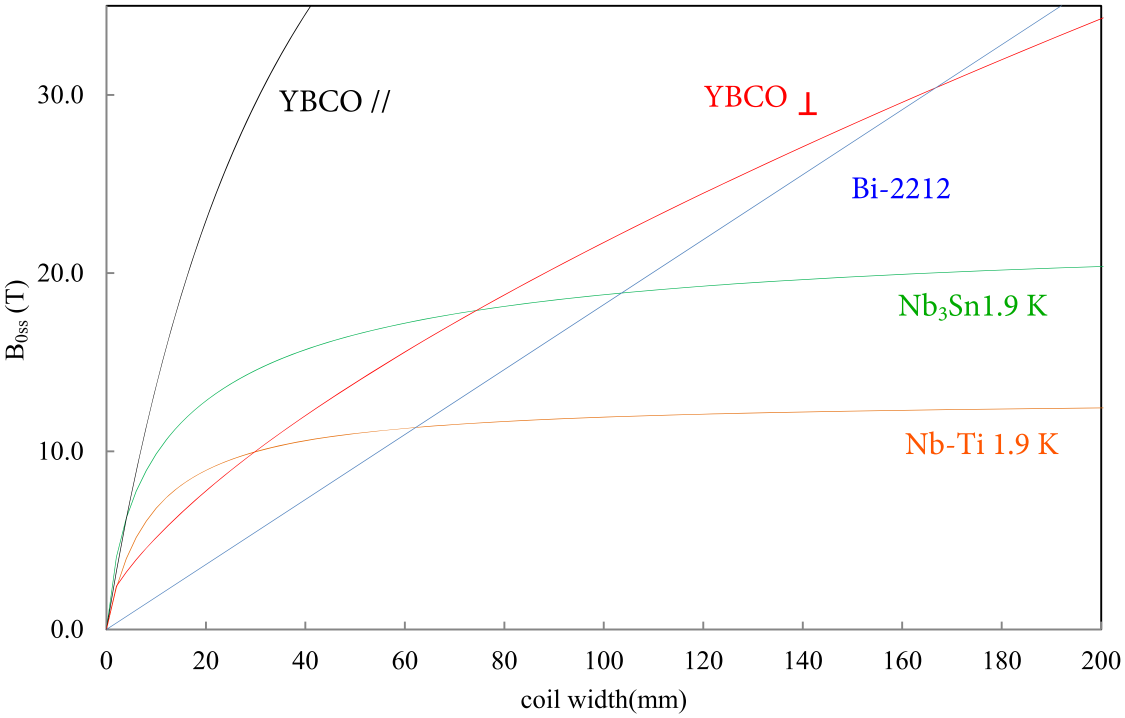

Figure 2.9: The $B_{0,ss}$ of HTS and LTS 30 mm aperture dipoles as a function of coil thickness.

2.2.3 Cross sectional area of a 20 T HTS dipole

In the design of superconducting magnet, the coil cross sectional area has to be managed since HTS superconducting materials are expensive. Superconductors with high B_{irr} are more expensive than superconductors with low B_{irr}. The actual price of HTS materials is at least two orders of magnitude higher compared to Nb-Ti. It is expected that the price of YBCO conductors will reduce in the next decade thanks to scaling up of the production. The price of BSCCO conductors is not foreseen to reduce greatly since it is driven intrinsically by the cost of the silver matrix. In this section, the cross sectional area of HTS dipole that generate 20 T is regarded as a function of the winding current density.

Magnet cross sectional area

The cost of a magnet can be considered to be proportional to it winding cross sectional area. The winding cross sectional area (S_m) of a sector dipole ($\phi = 60°$) is expressed as:

$$S_w = \frac{2\pi w_c}{3}(2R_i + w_c) = \frac{2\pi B_0}{3\gamma_0 J_w}\left(2R_i + \frac{B_0}{\gamma_0 J_w}\right) \tag{2.9}$$

In the thick coil limit ($w_c \gg R_i$), the cross sectional area reduces to:

$$S_w = \frac{2\pi}{3}\left(\frac{B_0}{\gamma_0 J_w}\right)^2 \tag{2.10}$$

Within the thick coil approximation the magnet cross sectional area, is inversely proportional to the square of J_w. To manufacture a 20 T dipole, one can use HTS coils or hybrid HTS/LTS coils. The last solution is preferred since it minimize the cross sectional area of the expensive HTS conductors. In the hybrid HTS/LTS dipole, the HTS sector coil generates 5 T, the other 15 T are produced by Nb_3Sn and Nb-Ti coils (as in the design proposed in [39]). The winding cross sectional area of a full HTS and an hybrid HTS/LTS 20 T dipole (aperture of 30 mm) is reported in figure 2.10 as a function of J_w. The magnet cross sectional area of the full HTS dipole in the limit $w_c \gg R_i$ is also depicted. It should be noted than S_w of the full HTS dipole is weakly dependent of the aperture, due to large thickness to aperture ratio. The HTS cross sectional area of the hybrid dipole is at least 5 times lower compared to the full HTS one. For J_w above 300 A/mm^2 a weak and quasi linear decrease of S_w is observed for both dipoles. For J_w lowered below 200 (100) A/mm^2 a strong increase is observed in the full HTS (hybrid) dipole.

2.2.4 The winding current density threshold (J_{wt})

To manage the cross sectional area of an HTS dipole, a minimum winding current density of $J_{wt} = 150 - 200$ A/mm^2 can be considered as being a practical threshold value. Lower current density will nevertheless allow to produce high flux density but at the expanse of thick coils and large quantity of HTS conductors. The J_{wt} value is half that of the generic current density (J_w =400 A/mm^2) used in Nb-Ti and Nb_3Sn accelerators magnets [29]. The J_{ce} of present HTS materials at 20 T and 4.2 K are above this threshold. For YBCO materials in parallel flux density orientation, a comfortable J_{ce} of 1400 A/mm^2 is reported (but it is only 350 A/mm^2 in the perpendicular orientation). For isotropic Bi-2212 materials the reported J_{ce} is about 330 A/mm^2. Large improvements of the J_{ce} of Bi-2212 conductors (factor 2-5) may be achieved by over pressurised heat treatment (10-100 bar). In magnets the winding current density (J_w) is always lower than the engineering current density (J_e) since conductors are diluted in the cable and the cable is diluted in the winding.

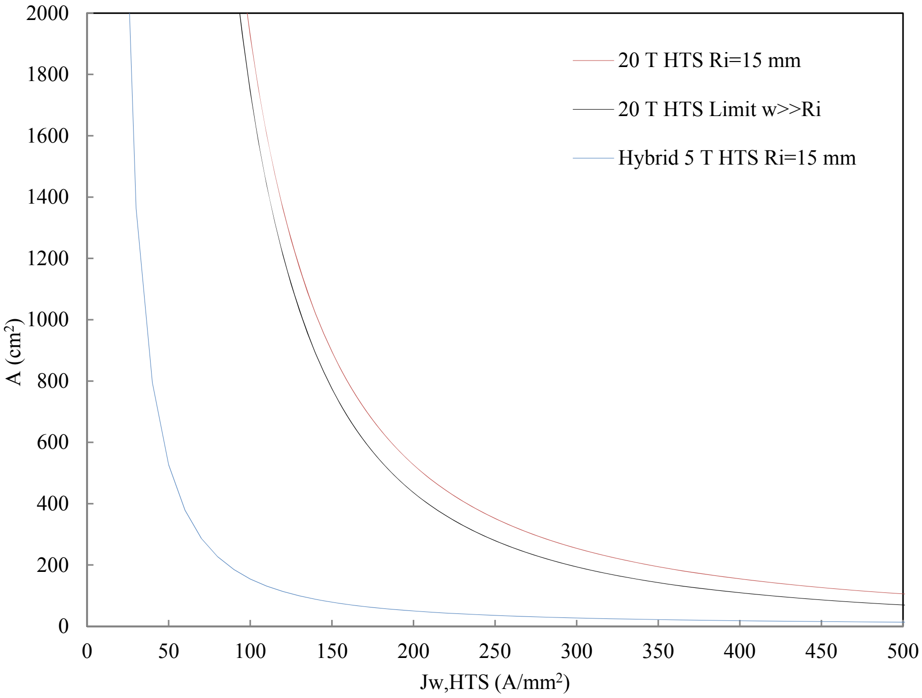

Figure 2.10: The winding cross sectional area of a 20 T full HTS and an hybrid HTS/LTS dipole (30 mm aperture) as a function of J_w. In the hybrid dipole, the HTS coils produce a flux density of 5 T.

2.3 Superconducting cable

Accelerator magnets require superconductors with both high engineering critical current density (J_{ce}) and long unit length that are bundled together to form multi strands cable with high transport current capacity. Over the last 50 years, several thousand of accelerator magnets made from Nb-Ti Rutherford cable have been manufactured [2][40][41][42]. Rutherford cables that have a rectangular cross section are made from some tens of round strands arranged in two layers. The superconductors Nb-Ti, Nb_3Sn and Bi-2212 in the form of round wires are applicable to Rutherford cable. The superconductors YBCO and Bi-2223 present good performance only in the form of tapes. In view of their rectangular cross section, they are not easily formed into the Rutherford cable. However, they can be formed into Roebel cable, a cable topology that was introduced more than 100 years ago [43] originally dedicated for AC loss reduction in generators. The strands in Roebel and Rutherford cables are transposed. Some others non-transposed cable concepts are also reviewed in this section: the stacked cable where the HTS tapes are stacked on top of each other and the former cable where the tape conductors are helically wound around a former. The superconductor properties are shortly reviewed before considering the different HTS cable concepts.

Among the different high current HTS cable concepts, a few will be selected for application to high flux density dipoles with regards to their current density as a function of the J_{wt} threshold.

2.3.1 Superconductor properties

Superconductors applicable into accelerator magnets are in the form of wires or tapes. Wires are preferred if applicable since they have isotropic properties and are easily bundled into transposed cable. Cabling process induces strain into conductors. All superconductors except the ductile Nb-Ti material [44] have strong I_c reduction with tensile strain above a threshold of about 0.2-0.6%. The Nb-Ti wires are produced by the co-extrusion of Nb-Ti rods stacked in a copper matrix down to a typical wire diameter of 0.8 - 1 mm. The high strain sensitivity of Nb_3Sn and Bi-2212 materials doesn't allow the direct drawing of conductors into their final dimensions. For these materials, the precursors of the superconducting phase are embedded in the wire and the wire is then drawn to it final dimension before reaction.

The grain alignments play a major role in J_c of YBCO and Bi-2223 conductors. In YBCO conductors good J_c values are only obtained for well textured films produced by epitaxial growth. A progressive loss of texture is observed with an increase of film thickness, limiting it to about only 1-2 μm. The YBCO film lays over the width of coated conductor (4-12 mm). The typical thickness of YBCO tapes is ranging between 0.05 and 0.4 mm. The coated conductors don't require heat treatment after magnet winding. The Bi-2223 conductors are in the form of tapes produced by rolling of round shape wire produced by the Powder in Tube (PIT) process. The rolling increases the grain connectivity and therefore the J_c. Bi-2223 tapes are most often already reacted for magnet application but they could also be reacted once the magnet is wound. The typical width of Bi-2223 tapes is ranging between 2 and 4.4 mm with thickness between 0.1 and 0.4 mm. More details on the manufacturing process of HTS conductors is reported in chapter 3.

Two routes are available to use superconductors in magnets: the wind and react route (W&R) and the react and wind route (R&W).

- In the W&R route, the precursor elements of superconductor are embedded in the conductor. The conductor is then assembled into the cable and/or the magnet. Finally the formation of superconducting phase from precursors is performed with the help of an appropriate heat treatment. By this process the superconductor does not experience strain exceeding the strain threshold. This route is used for the Nb_3Sn, Bi-2212 and sometimes for the Bi-2223 conductors. Too large plastic strain during cabling can lead to conductor internal structure modification and a possible J_c degradation after heat treatment.
- In the R&W route the superconductors are used already reacted during the cabling. This route is used for YBCO and Bi-2223 conductors. Obviously in the R&W route one have to manage the level of strain during cabling to avoid J_c degradation of the conductors.

To reduce the hysteresis loss, superconductors are made of many tiny filaments embedded in a resistive matrix [45]. Two different types of AC losses are presents at the scale of filaments in superconductor: hysteresis losses [45] and inter filament coupling losses [46]. Both these losses are not suitable for flux density quality and thermal stability. Standard industrial production yields filament sizes as low as 5-10 μm, which is mandatory for reducing the flux density perturbations induced by persistent current magnetization.

In the range of wire diameters of interest, 0.5-1 mm, Nb-Ti filaments of 1-2 μm seem to be a practical lower limit. Lower filaments size reduce the J_c. Furthermore, fine and closely spaced filaments tend to couple with each other, either through direct contact or because of electrical proximity [47]. In Bi-2212 wires several studies have reported improvement of J_c capacity with a reduction of filament size due to increased Ag interface area [48][49]. A trend that is interrupted with the onset of filament sausaging or filament non-uniformity that is exacerbated with smaller wire size. The filament diameter has to be optimized with regards to the hysteresis losses, to the J_c, but also to the cost. The various parametric studies that have been carried out indicate optimum filaments size in Bi-2212 wires ranging between 13 μm and 19 μm [48][49]. The measurements of intra-strand coupling losses in Bi-2212 strands, have indicated bridging among filaments [50]. The obtained effective filament diameter describing the hysteresis loss property indicated that almost all filaments in strands were strongly connected to each other. In order to limit the hysteresis losses in coated conductors, striation of the film has been performed [51]. The J_c was strongly reduced and the filaments were strongly coupled since they were not twisted.

Interfilament coupling losses are reduced by twisting the filaments. Eddy current losses occurring in the resistive matrix are reduced by the use of a resistive matrix. For the ductile Nb-Ti materials twisting filaments down to a pitch 25 mm for 0.8 mm diameter strands is not a big issue. The pitch is applied to the filaments by twisting the wire. The long current ramp for most of accelerator magnets means that an AC strand design is not required, leading to very small levels of inter filaments losses. Twisting Nb_3Sn conductors is more delicate and typical twist pitch of 15-100 mm are usual. A strong reduction of I_c with twisting filaments of BSCCO conductors has been reported. Therefore most of BSCCO conductors are untwisted. The bridging of filaments in Nb_3Sn and Bi-2212 strands suppress part of the gain in coupling losses. Main geometrical features of practical superconductors are listed in table 2.3.

Table 2.3: Main geometrical features of practical superconductors.

Superconducting material	Nb-Ti	Nb_3Sn	Bi-2212	Bi-2223	YBCO
Conductor shape	Round	Round	Round	Rectangular	Rectangular
Diameter (mm)	0.8-1.1	0.7-1.2	0.7-1.2	-	-
Width (mm)	-	-	-	2-4	4-12
Thickness (mm)	-	-	-	0.2-0.4	0.05-0.4
Number of filaments	4500	1500	600	120	-
Typical filament diameter(μm)	6	15	20	20	-

2.3.2 Rutherford cable

Rutherford type cable was developed in the early 1970′s at Rutherford Appletown Laboratory in the UK [52]. The Rutherford cable is made of some tens of round strands, twisted together and then shaped into a flat, two-layer cable. Rutherford cables have a typical width of 4-30 mm and a thickness of 0.8-3 mm. The cross section of Rutherford cable could be rectangular or trapezoidal and can also include a resistive core foil between the two strand layers (see figure 2.11). Rutherford cables with rectangular/trapezoidal cross section are used in block/sector coils. For sector coils, the cable trapezoidal cross section help to form a roman arch around the circular beam pipe. Trapezoidal cables are commonly name keystoned cables. The keystone angle is the angle between the two large faces of the cable. In manufacturing Rutherford cable, large plastic deformations are induced; especially at the cable edges where strands have to pass from the top layer to the bottom layer of the cable or inversely. The plastic deformations induced during Rutherford cabling are exceeding the threshold strain values of Nb_3Sn and Bi-2212 materials. These materials can therefore only be used with the W&R route. In order to compare easily Rutherford cables made from different numbers of strands and with different strand diameters, some further cable parameters are introduced. The packing factor that represents the voids fraction in the transverse cross section of the cable is expressed as:

$$P_f = \frac{N_b\ \pi\ D^2}{4\ (w_m\ t_m - A_{core})\ \cos\alpha} \tag{2.11}$$

Where D is the strand diameter, A_{core} is the core cross section N_b is the number of strands in the cable, w_m and t_m are respectively the cable average width and average thickness. The pitch angle α is defined as the angle between strands longitudinal axis and cable longitudinal axis. The transposition pitch of the cable is defined as the length over which each strand makes a full transposition. The transposition pitch is somehow linked to the pitch angle and cable width through the expression:

$$T_p = 2\ w \tan\alpha \tag{2.12}$$

Figure 2.11: Schematic view of Rutherford cable [53] (left). Cross section of a Bi-2212 Rutherford cable [54] (right).

Nb-Ti and Nb_3Sn Rutherford cable

Rutherford cables made of Nb-Ti strands have been extensively used in accelerator magnets for the different colliders RHIC, LHC, HERA and Tevatron [2][40][41][42]. In the LHC, the insulation of Nb-Ti Rutherford cable is permeable to liquid helium in order to enhance the thermal stability of the cable. Magnets made from Nb-Ti Rutherford cable are reliable and the technology is considered as being mature. The application of the brittle Nb_3Sn conductors in Rutherford cable is delicate. The Nb_3Sn has so far only been used in a few tens of demonstrator magnets [11][7][8][55][56][57]. The Nb_3Sn cable is impregnated with epoxy to manage the stress distribution. Impregnated Nb_3Sn coils exhibits a initial and progressive training of performance up to a current plateau of about 90-95% of short sample limit: the formation and propagation of epoxy cracks due to the large electromagnetic forces is liable to trigger a quench. The epoxy impregnation doesn't allow a direct contact between the strands and liquid helium: the thermal stability of the coil is not enhanced by helium.

Bi-2212 Rutherford cable

Bi-2212 round shape superconductor is highly sensitive to strain and can only be used in the form of Rutherford cable via the W&R route. Moreover, large plastic deformations in the cabling process may induce cracks in the weak silver matrix that lead to Bi-2212 leakages during heat treatment. The leakages have been observed to appear randomly and only in the flat surface and not at cable edges.

Several Bi-2212 Rutherford cables have been manufactured over the last 20 years [54][58][59][60]. In 2004 Hasegawa et al. [60] manufactured and tested Rutherford cables of 20 and 30 strands made from respectively 1 mm and 0.8 mm diameter wires. The two cables exhibit the same I_c of 12 kA at 4.2 K and in self-field. At 6 T the critical current density was 230 A/mm^2. They observed that the largest factor affecting the I_c degradation was strand diameter. The transposition pitch didn't seem to play a role in I_c degradation. Barzi at al. [54][59] report a I_c reduction less than 20% for packing factors of up to 90%.

The major issue of Bi-2212 conductors is the delicate final heat treatment performed under oxygen gas at temperature of 880°C. A strong J_c dependence on heat treatment has been reported [49]: homogeneous temperature (within 1°C) and good oxygen circulation in the winding pack are required for an optimum reaction of the precursor powders. The conductor performance has also been reported to be length dependent [61]: high J_c is achieved in short length, smaller one in long samples. This is ascribed to the formation of gas bubbles in the melt precursor powder during heat treatment. The gas bubbles limit the grain connectivity and therefore limit the critical current. An optimization of both precursor composition and heat treatment will hopefully solve this issue. By increasing the pressure of heat treatment to up to 100 bar and keeping the partial oxygen pressure of 1 bar the I_c of Bi2212 wires has been almost doubled in recent experiments [62]. This achievement is very promising for high flux density applications.

Table 2.4: Review of the performances of Bi-2212 Rutherford cable.

Number of strands	Strand diameter (mm)	I_c (4 K s.f) (kA)	J_{ce} (4 K s.f.) A/mm^2	I_{quench}/I_c (%)	Year	Lab.	Ref.
20	1	12	583	-	2004	Showa	[60]
30	0.8	12	583	-	2004	Showa	[60]
25	0.8	7.3	471	90	2011	FNAL	[54]
21	0.91	5.2	304	56	2008	FNAL	[59]
19	1	3.7	201	53	2008	FNAL	[59]
18	0.81	3.6	119	90	2000	Showa	[58]

Typical parameter values of Rutherford cable

A survey of the various Nb-Ti, Nb_3Sn and Bi2212 Rutherford cables produced reveals similar parameter values for: the number of strands, the packing factor, the cabling angle and the strand diameter (see table 2.5). Large differences are observed concerning the I_c degradation induced by cabling: from less than 5% for the mature Nb-Ti technology [63], the reduction is up to about 10%-20% for Nb_3Sn conductors [64] and up to 15%-90% for Bi-2212 conductors.

Table 2.5: Typical parameter values of Rutherford cables made from Nb-Ti, Nb_3Sn and Bi2212 conductors.

	Nb-Ti	Nb_3Sn	Bi-2212
Number of strands	24-36	27-51	18-30
Strand diameter (mm)	0.5-1.2	0.5-1	0.6-1
Cable width (mm)	4.5-15.1	9-20	8-13
Cable mid-thickness (mm)	0.5-0.8	0.5-1.5	0.6-1.1
Keystone angle (°)	1-1.3	0-1.2	0
Cable transposition pitch(mm)	73-112	78-150	70-130
Pitch angle (°)	14-17	14-17	13-17
Packing factor (%)	80-90	90	81-89
I_c reduction due to cabling (%)	<5	10-20	15-90
Ref.	[63][65][66]	[11][7][8][55][56][57]	[58][59][54][60]

2.3.3 Roebel cable

The concept of continuously transposed cable made of tape conductor was introduced by Ludwig Roebel in 1912 to reduce AC-losses in high current copper cables of generators [43]. Such continuously transposed cables are commonly named Roebel cables. The Roebel cable are made of strands with rectangular cross section transposed without twist and arranged into two stacks. The planar geometry of strands and the schematic view of strands arrangement in the Roebel bar is depicted in figure 2.12. Over a transposition pitch, the planar geometry is based on respectively two longitudinal straight segments and two transition segments. This typical shape is called a meander shape. The topology of Roebel and Rutherford cable is similar except that the first is made from tape conductors and the second from round wires.

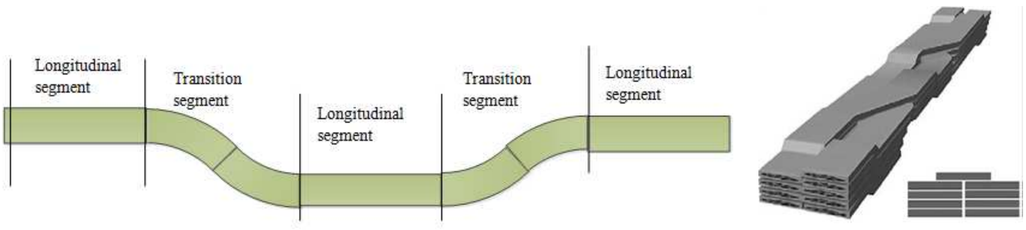

Figure 2.12: Schematic view of the different sections of a meander shape tape conductor(left). Schematic view of Roebel cable [67](right).

The first superconductor applied to Roebel cable was Nb-Ti in the toroidal field coils of the Large Coil Task (LCT) [68]. The low strain sensitivity of this material allowed a direct winding of the conductor without strain limitation. The strain sensitive YBCO and Bi-2223 tape conductors were applied to Roebel cable via the R&W route more recently [69][70][67][71]. The meander shape tape conductor of Roebel cable can be formed by bending rectilinear YBCO/Bi-2223 conductors or by pre-shaping YBCO tapes.

Roebel cable from rectilinear conductor (RRC cable)

Only few Roebel cables have been manufactured from rectilinear YBCO conductor [69]. To produce the meander shape, a force is applied to the tape in transition segments. A short transition segment length was observed to generate arching of the tape. The arching of tapes was minimized by application of longitudinal tension. The cables produced were mechanically unstable without longitudinal tension to the conductor: once formed they must be bound with superimposed tape. The mechanical instability of this cable is ascribed to the high aspect ratio of the cross section of coated conductors (typically 10-200) and the high mechanical strength of the substrate. The rectilinear YBCO conductors are considered to be difficult to use in Roebel cables.

In 2004, a 5 strands Bi-2223 RRC cable with a transposition pitch of 570 mm has been used to wind a solenoid with an inner diameter of 200 mm [70]. The Bi-2223 tapes were 0.2 mm thick and 1.85 mm wide, with an I_c value of 24 A at 77 K and in self flux density. Since fragile Bi-2223 tapes cannot be handled as easily as copper wires a dedicated cabling technology was developed at Siemens which makes cabled Bi-2223 conductors in lengths greater than 100 m available. Lengths up to 160 m of 13-strand cabled conductors were manufactured semi-automatically using the cabling machine. Multifilamentary Bi-2223 tape with a cross section of 3.5 x 0.25 mm^2 presented a critical current at 77 K and in self flux density of 52 A [67]. The transposition pitch of the cable was approximately 3 m. The cable reached a critical current of 400 A at 77 K. A 31 m long RRC cable made of 13 strands (4.02 x 0.3 mm^2) with a transposition pitch of 3.5 m has been used in a double pancake test coil [71]. The coil operated at 30 K reached a cable critical current of 1.8 kA.

The limited in-plane bending capability of BSCCO and YBCO tapes, regarding I_c degradation, leads to a large transposition pitch of the RRC cables.

Minimum transposition pitch of RRC cable

In RRC cables, meander shape geometry is obtained by the in plane bending of rectilinear conductor. The maximum of axial strain induced by the bending is observed at the tape edges. The minimum transposition pitch ($T_{rp,min}$) of a RRC cable is defined as the pitch for which the strain at tape edges reaches the irreversible strain threshold (ε_{irr}). The Bi-2223 (YBCO) conductors have a typical ε_{irr} value of 0.38(0.6)%.

The minimum transposition pitch of RRC cable is expressed as:

$$T_{rp,min} = w\left((N_b-1)\left(\frac{1}{\varepsilon_{irr}+1}\right)\sqrt{1-\left(\frac{1-\varepsilon_{irr}}{1+\varepsilon_{irr}}\right)^2}+\frac{2}{\varepsilon_{irr}}\sqrt{1-\left(1-\frac{W\varepsilon_{irr}}{w}\right)^2}\right) \tag{2.13}$$

Where W is the width of the cable, w and N_b are respectively the width and the number of strands. The minimum transposition pitch is proportional to the conductor width and increases with the number of tapes in the cable. In figure 2.13, the minimum transposition pitch of a 15 strands RRC cable as a function of ε_{irr} is depicted for different conductors width. For $\varepsilon_{irr} = 0.5\%$ the minimum transposition pitch of a 15 strand Roebel cable is equal to $T_{rp,min} = 453 * w$, i.e. 1.8 m for a 4 mm wide conductor. For application into magnets the transposition pitch of Roebel cable must be lower than the coil magnetic length. The achievable transposition pitch of RRC cables is too high for practical applications.

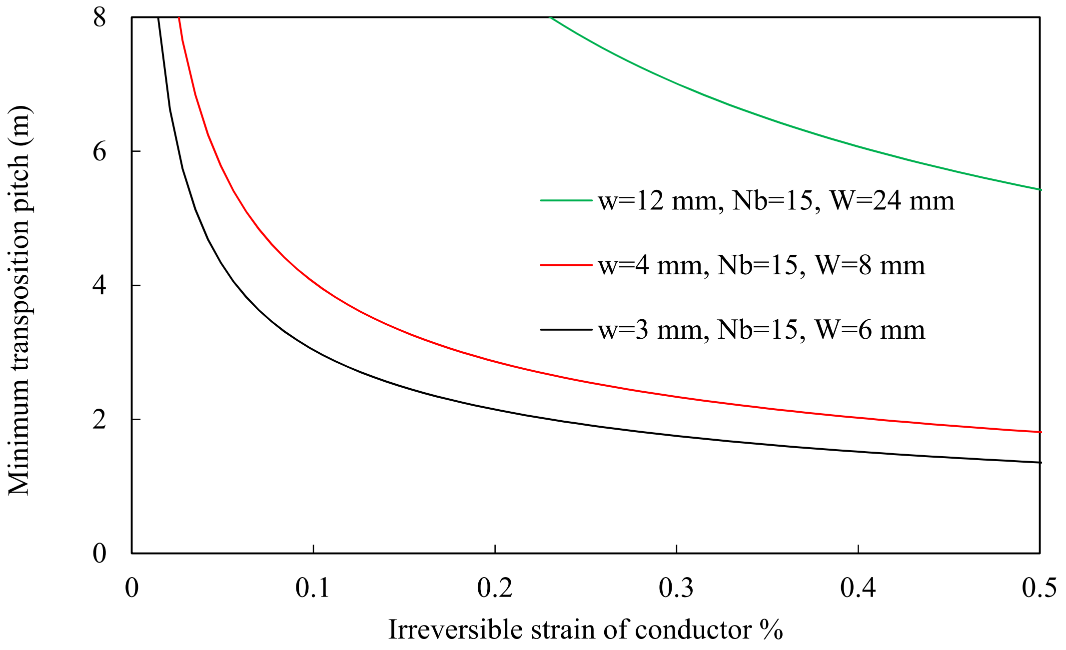

Figure 2.13: Minimum transposition pitch ($T_{rp,min}$) of RRC cables as a function of the conductor ε_{irr} threshold.

Roebel assembled coated conductor cable (RACC cable)

Edgewise bending of coated conductor has been considered not feasible for application into Roebel geometry since the transposition pitch allowed is rather long and the mechanical stability of the cable is not ensured. A solution based on the pre-shaping of coated conductors into the Roebel meander tape was demonstrated in 2006-2008 [72][73]. Only coated conductors are suitable for applying this technique. Rectilinear coated conductors are mechanically punched to form meander tape that are shaped with a precision punching process, see figure 2.14. The strands Precision punching process provides very sharp cutting edges with minimum damage to the coated layers. A cross section of a punched YBCO tape is depicted in figure 2.14. In the punching of the tape, a portion of the expansive raw material is lost. In addition the punching opens the silver cap and potentially exposes the HTS layer to moisture and delamination. However, no delamination of the copper stabilizer has been reported by the Roebel manufacturer. Between two consecutive longitudinal segments a remaining gap of few mm is created to allow easy cabling. Short lengths of cable (1-2 m) can be made manually, but longer lengths require the use of an automated device [74]. The longest Roebel cable produced to date is 27 m long [75]. The packing factor of Roebel cable is defined as:

$$P_f = 1 - \frac{2w}{W} \tag{2.14}$$

Where W is the width of the cable and w is the width of meander tape. In Roebel cables, relatively high P_f of about 90% are achieved. The reported critical currents of RACC cables at 77 K and in self flux density are depicted in table 2.6 [76][77][78][75][79]. The depreciation of the current due to cable self flux density, as computed by [80] has been found to range between 19% and 66%. It is correlated to the number of strands in the cable and the anisotropy of HTS conductors.

Figure 2.14: Cross section of a punched YBCO conductor [73] (left). At the right: top view of a meander YBCO tape conductor with a 126 mm transposition pitch (top). Top view of a 15 strand YBCO Roebel cable with a transposition pitch of 300 mm [81] (bottom).

Table 2.6: Main parameters of RACC cables.

Ref.	[77]	[76]	[75]	[75]	[75]	[78]
Laboratory	KIT	KIT	GCS	GCS	GCS	FNAL
Cable width (mm)	12	12	12	5	5	12
Number of strands	16	45	15	9	5	15
Length (m)	0.45	1.1	5	0.5	0.7	2.6
Transposition pitch (mm)	190	188	-	-	300	300
Strand width (mm)	5	5	5	2	2	5
Cable I_c measured (1μV/cm) (kA)	1.02	2.29	1.10	0.31	0.20	1.01
Sum of individual strands I_c (kA)	1.47	6.73	1.95	0.43	0.25	1.62
I_c reduction due to self flux density (%)	30	66	44	28	19	38

Mechanical properties of Roebel cable

Coated conductors are resistant to tensile load by themselves but the punched out sections of the meander structures required for RACC cables weaken their mechanical properties. The I_c stress sensitivity of HTS Roebel cable has been investigated by [82] at 77 K and in self flux density. A 15 strand Roebel cable made from 5 mm wide meander tapes was submit to axial stresses. The meander tapes were punched from a 12 mm wide YBCO conductor from SuperPower. An irreversible I_c degradation was found to occur above 700 MPa in the raw 12 mm wide YBCO SP tape. For the 5 mm wide meander tape the irreversible I_c degradation was found to occur at 146 MPa. Finally the irreversible I_c degradation of the cable occurs at 113 MPa. This value is only 21% of the strength of the 12 mm wide YBCO conductor. When submitted to uniaxial strain, stress concentration at the elbow [83][82] lowers the electro-mechanical properties of meander tapes. From a mechanical point of view, the shape of meander tapes requires optimizing [83].

AC losses in Roebel cable

The dominant AC losses in YBCO strands are the magnetization losses caused by the magnetic flux density perpendicular to the cable width [79]. These losses are reduced by cutting the tapes into strands because at large applied flux density amplitudes the AC losses are proportional to the strand width [84][45]. Moreover, the Roebel structure provides the transposition necessary to eliminate the coupling losses [46]. In addition, the lower width-over-thickness aspect ratio of the cable contributes to the reduction of the AC losses because of the increase of the penetration flux density [85]. There are different options to further reduce the AC losses. One is applying striations to the strands and somehow twisting them (to make the striation effective), which has not been developed yet; a second option is to reduce the width of the cable; the third is to increase the cable thickness by increasing the number of strands [79]. The measured transport losses do not depend on the frequency, indicating that the coupling losses are very small. The magnetization AC losses per unit cycle and cable volume are strongly reduced by the use of Roebel cables [79][86].

2.3.4 Stacked cable

The easiest way to bundle HTS tapes in a high current cable is to stack them on top of each others. Stacked cable have been widely used in HTS solenoids, however flux couplings created in the loop circuits among the parallel superconducting tapes generate significant losses. The magnetic flux coupling can been reduced by twisting the cable. The details about untwisted and twisted stacked cable are reported in this section.

Untwisted Stacked cable

Untwisted stacked cable have been widely used in HTS demonstrator solenoid [18][87][88]. The cables are usually made of 2-3 conductors. To provide mechanical reinforcement, especially for the BSCCO conductors, a tape of high strength material is co wound with the conductor [18][19][89][90]. The current density in such cable is relatively high at the expense of no transposition. The packing factor of this cable is equal to unity if no stabilizer strips are interleaved between the HTS tapes. The untwisted stacked cables suffer from flux couplings created in the loop circuits among the parallel superconducting strands. A concept of balanced loops circuit between the different coils of the HTS dipole of the EuCARD program was introduced [88]. The transposition is performed between the upper and the lower midplane pancakes (see figure 2.15), leading to an effective transposition pitch of few hundred of meters. The two main drawbacks of this transposition technique are the very long transposition pitch and a possible misalignment of upper and lower coils leading to unbalanced loops.

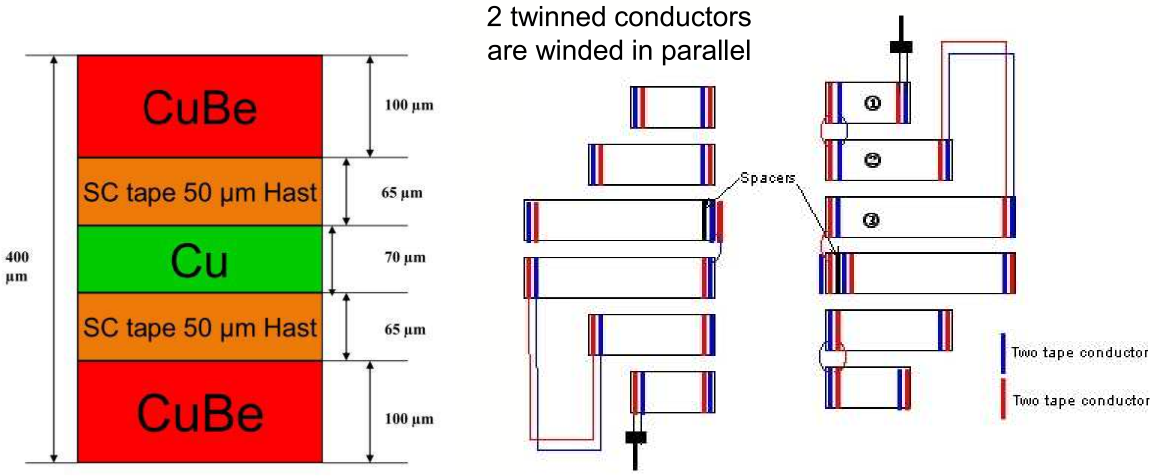

Figure 2.15: The EuCARD YBCO conductor made of two 12 mm wide SuperPower tapes [88] (left). In the cable, EuCARD conductors are not transposed. The two conductors of the cable are transposed between the upper and lower midplane pancakes (plot from [88]) (right).

Twisted stacked cable

In some applications, the level of AC losses must be small. The twisting of stacked cable allows to reduce the magnetic flux coupling. The twisted stacked cable consists of housing a stack of HTS conductor in a helical groove made in a former (see figure 2.16). The cable has isotropic behaviour with respect to the external flux density since HTS tapes are twisted. These cables present high mechanical performances but relatively low packing factor (10-60 %).

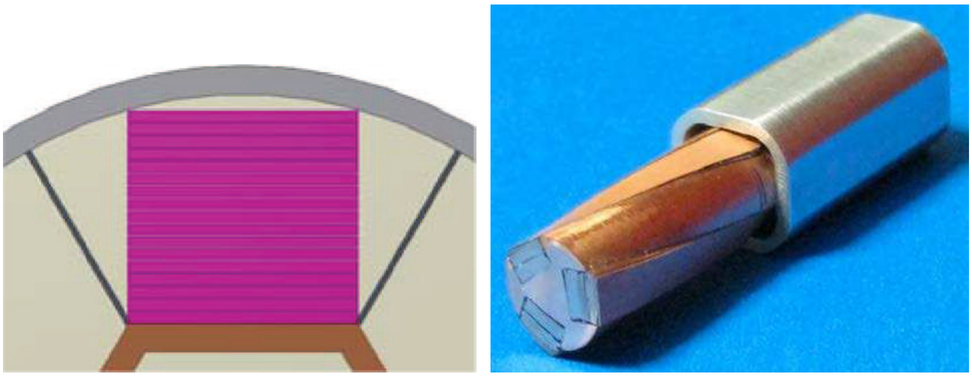

Figure 2.16: Twisted Stacked cable in conduit

2.3.5 Former cable

Following the observation of no irreversible degradation in critical current of YBCO conductors under axial compressive strain of up to 2%, a new method of producing coated conductor cabling for use in low AC loss and high-field magnet applications was introduced [91]. The coated conductors are spiral-wound around a former with a relatively small diameter. The cable flexibility was demonstrated by bending a 6.5 mm diameter cable over a radius as small as 125 mm [92], which did not reduce the critical current. A longitudinal view of a former cable made of a single coated conductor is presented in figure 2.17. In the same figure a cross section of a former cable made of 40 tapes wound in eight layers is depicted. Different former cable prototypes were tested at 4.2 K and 76 K (see table 2.7). At 76 K the different prototypes were tested in self field and a record I_c value of 4.6 kA was measured on a 39 strands cable. At 4.2 K the measurements were performed in flux density of up to 20 T. A record I_c value of 5.1 kA was measured in a 52 strands cable at a flux density of 19 T with a current density of 117 A/mm^2. This J_{ce} value is below the threshold current density of J_{wt}=150 A/mm^2.

Table 2.7: Performances of YBCO former cables at 76 K and 4 K.

Number of tapes	Former diameter (mm)	Temperature (K)	External flux density (T)	I_c (kA)	J_{ce} (A/mm^2)	Year	Ref
12	5.5	76	0	1.23	36	2011	[92]
24	5.5	76	0	2.28	61	2011	[92]
39	5.5	76	0	3.72	70	2012	[93]
39	8.40	76	0	4.6	56	2012	[93]
15	5	4.2	12	2.6	80	2012	[93]
12	5	4.2	20	0.9	26	2012	[93]
40	5	4.2	20	4.1	76	2012	[93]
52	5	4.2	19	5.1	117	2012	[93]

The packing factor of former cable strongly depends on the number of strands and the diameter of the former: packing factor is increased for a small former radius and for a large number of tapes. The former cable method provides a very flexible conductor, but provides low overall current density, and could result in poor utilization of the HTS tapes. The J_{ce} of the former cable seems to be too low for application in high flux density accelerator magnet windings, but could be very promising for bus bars and current transfer lines.

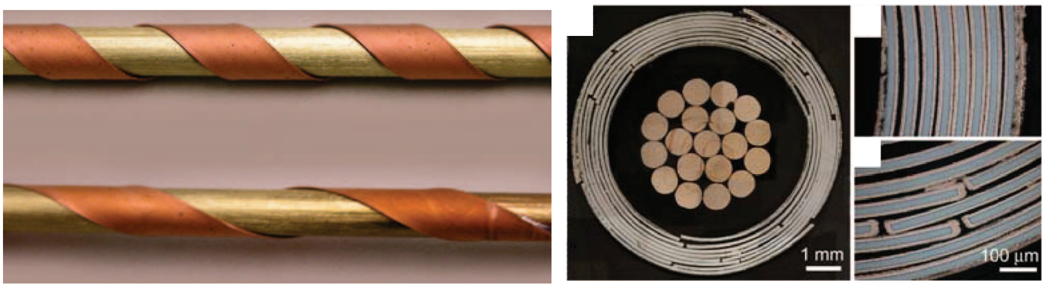

Figure 2.17: A longitudinal view of two single strand former cables (plot from [91]) (left). A cross sectional view of a 40 strands former cable (plot from [93])(right).

2.4 Choice of HTS cable concept for high flux density magnet

For application in a high flux density magnet, HTS cable must present both high engineering current density and good mechanical properties. In table 2.8 a comparison of the main aspect of the different HTS cable concepts is summarized. These cover the packing factor, the cabling, the mechanical properties and the engineering critical current density. With regard to these aspects, the Bi-2212 Rutherford cable, the YBCO stacked cable and the Roebel YBCO cables appear as promising candidates for application to high flux density magnets. The packing factor of the YBCO former cable is to low for an efficient use of the expensive YBCO tapes in high flux density magnets.

Table 2.8: Comparison of main HTS cable concept parameters and properties.

Cabling method	Rutherford	Stacking Not Twisted	Stacking Twisted	Roebel	Former
Conductor geometry	wire	tape	tape	tape	Tape
Packing factor (%)	0.8-0.95	1	0.5	0.95	0.2-0.5
Cabling	known	easy	easy	complex	easy
HTS Materials applicable	Bi-2212	YBCO	YBCO	YBCO	YBCO
Conductor I_c anisotropy (in respect of the background flux density)	NO	YES	YES	YES	YES
Cable I_c anisotropy (in respect of the background flux density)	NO	YES	NO	YES	NO
$J_w > 150$-200 A/mm^2 @ 20 T	YES	YES	NO	YES	NO
Mechanical strength of conductor	low	high	high	medium	high

2.5 Conclusion

The design constraints laying on superconducting accelerator magnets are introduced in this chapter. Based on the 2D electromagnetic design of dipoles and the performance of HTS conductors, semi-analytical formula allowing to estimate the ultimate bore flux density in HTS accelerator dipoles based on sector coils is derived. A 110 mm thick Bi-2212 coil produces an ultimate bore flux density of 20 T. With YBCO conductors, the same flux density is achieved with a thinner coil: 90 mm. For insert YBCO block coils nested in LTS coils, the ultimate flux density is roughly estimated by considering the I_c of YBCO tapes in parallel orientation. In this specific case a large bore flux density is generated even with thin coils e.g. 19 T for a 30 mm thick coil.

Accelerator magnets require the use of large current cables. The different high current HTS cable concepts are reviewed in this chapter. In view of their electromechanical properties, the Rutherford Bi-2212 cable, the YBCO stacked cable and the Roebel YBCO cable concepts appear as promising candidates for application to high flux density accelerator magnets.

Chapter 3

Performances of HTS conductors

The goals of this thesis require extensive experimental work to analyse the performance level of the present generation of HTS conductors under the various conditions encountered in superconducting magnet windings. In this chapter, the experimental techniques of superconductor characterization are introduced. The electro-mechanical properties of different YBCO, Bi-2223 and Bi-2212 conductors are investigated and reviewed at 4.2 K and in flux density of up to 12 T. The splice resistance of these conductors and their I_c *retention with torsion is measured at 77 K and in self flux density. Electrical and mechanical properties of YBCO and Bi-2223 conductors were measured in the superconducting laboratories at CERN (Bd.163 and Bd.288). Properties of Bi-2212 conductors are extracted from data in the literature.*

One of the principal relevant parameters of a superconductor is the critical current (I_c). Critical current reflects the macroscopic current transport capability of the superconductor. During operation of accelerator magnets, conductors placed in the winding are submitted to various combinations of flux density intensity and direction, temperature and strain. The critical current of HTS conductors is dependent on all of these parameters. For the proper use of HTS materials in accelerator magnets, one has to know their intrinsic properties with respect to those parameters. The electrical properties of HTS conductors have been investigated experimentally under conditions reproduced in the laboratory, and the results are presented in this chapter.

3.1 Physical origin of I_c

In this section the physical origin of critical current in superconductors is introduced. Many physical models have been proposed to explain the physical origin of the critical current. In LTS materials, the model based on flux creep theory was shown to be the most appropriate to describe the temperature, flux density and I_c strain dependency. It will be shown in next chapter that this theory is also the most appropriate for HTS conductors despite the fact that they do not obey the BCS theory [94]. In the flux creep theory [95], the current carrying capability of a type II superconductor is determined by the pinning of the flux-line lattice. Above the flux density B_{c1}, flux-lines, each of magnitude $\phi_0 = h/2e$, penetrate the superconductor. A repulsive interaction between neighbouring flux-lines leads to a uniform distribution of flux-lines into a lattice as described in the theory of Abrikosov [96]. The lattice parameter of vortices decreases with flux density. At flux density of B_{c2} the vortices are in very close vicinity, the superconductor is fully penetrated and a second order transition to normal state occurs. The mutually repulsive forces between vortices give rise to a net force per unit of volume which is proportional to the flux density and flux density gradient. The force arising from fluxoid concentration is thus equivalent to the Lorentz force acting on a macroscopic current density. The force acting on vortices will create motion if the latter are not pinned to the material. Practical superconductors contain many inclusions of normal material or secondary superconducting phase. These inclusions act as pinning centres for fluxoids. If the transport current is too large, the pinning force is overcome by the force acting on fluxoids. Fluxoids start to move and the electric field generated along the slab induces power dissipation. By considering a pinning potential energy which has minima at pinning sites Anderson and Kim [95][97] introduced the flux creep model. The energy required (W_p) for a flux line to get out from this state of minimum energy is reached by thermal activation. The presence of a macroscopic transport current density (J) affects the relative energy depth at pinning sites. From the Maxwell-Boltzmann statistics and an activation energy in the form $W_p(J) = W_0\ ln(J/J_c)$ the electric field generated parallel to the macroscopic current in the superconductor can be expressed as:

$$E = E_c \left(\frac{J}{J_c}\right)^n \tag{3.1}$$

where n refers to the n-value of the material and reflects the shape of the transition between superconducting and normal states. The critical current density J_c is defined as the current density for which the electrical field (E) generated along conductor equal the electrical field criterion E_c. Practical HTS conductors are made of many superconducting grains connected through a percolation path. Grains have different individual critical properties and orientation and thus with a certain distribution depending on manufacturing process. The distribution of critical properties over the grain affects the conductor transition to normal state. Conductors with a large distribution undergo a smoother transition as compared to conductors without such a distribution. Therefore the n value for practical conductors also reflects the non-uniformity of grain critical properties. The thermal activation of flux line movement results in a de-pinning flux density called irreversibility flux density (B_{irr}). Beyond this threshold, the material is still in the superconducting phase but can no longer transport macroscopic current in a non-dissipative way. In cuprate superconductors (YBCO and BSCCO) the CuO_2 layers of HTS crystals and their vicinities are strongly superconducting and the layers with CuO chains and their vicinities are weakly superconducting. This induces anisotropy of superconducting properties in these crystals: the weakest superconducting properties are observed for flux density oriented parallel to the c-axis of the crystal, the strongest for flux density oriented in the ab plane of the crystal. When cuprate superconductors are in the form of tapes, the crystal anisotropy is transposed to a macroscopic anisotropy since material is textured. For HTS conductors in form of wire, no specific ordering of crystal is observed and a macroscopic isotropy is observed. The irreversible field H_{irr} and upper critical field H_{c2} of HTS and LTS materials are schematically depicted in figure 3.1. For HTS tape conductors, these two parameters are field orientation dependent.

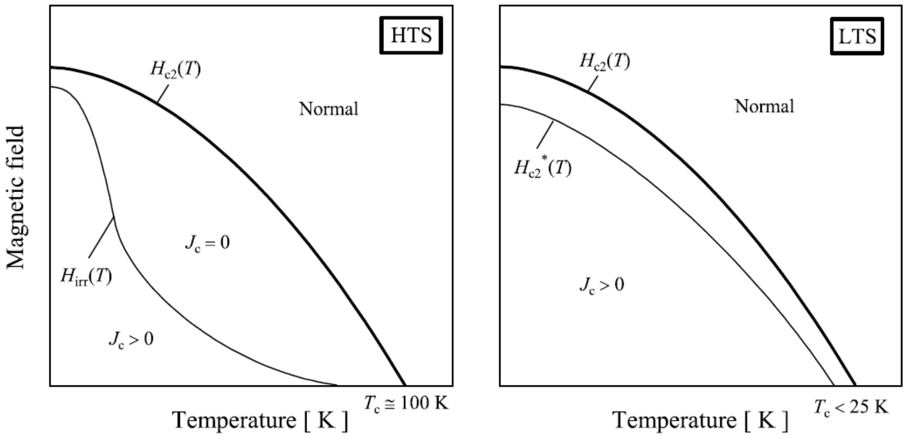

Figure 3.1: H_{irr} and H_{c2} for HTS (left) and LTS materials (right) as a function of the temperature (plot from [98]).

3.2 Experimental techniques

To characterize the electrical properties of HTS conductors, the conditions encountered in the winding of magnets have to be reproduced in the laboratory. Generation of homogeneous high flux density in a test facility is limited to a small volume: dimensions of samples are therefore limited. The flux density anisotropy of HTS conductors in the form of tapes requires measurements in at least the configurations with the smallest and the largest I_c (more details in sections 3.5 and 4.2). These two configurations correspond respectively to flux density oriented perpendicular and parallel with respect to the tape wide face. In test stations, samples are generally thermalized with the help of a helium bath at atmospheric pressure, corresponding to a temperature of 4.2 K. This temperature is the most likely working temperature of future HTS accelerator magnets. In magnet windings, superconductors experience stress and strain: behaviour under such mechanical solicitation must be characterized. This section reports on the different experimental protocols for I_c characterization.

3.2.1 I_c determination

The I_c can be measured by two experimental protocols. The magnetization protocol consists in applying a variation of external magnetic flux density to a superconducting sample. Shielding currents are induced in the sample and the magnetization of the sample is measured using pick up coils. Based on the critical state model introduced by Bean [45], the critical current of the sample is determined. This contactless method gives the local J_c of the sample and can be performed on small samples.

The transport current protocol is more representative of what is happening to a superconductor in a magnet. A macroscopic transport current flows in the superconductor and the electrical potential difference over a certain length of the sample is recorded. Experimentally I_c is defined as the transport current at which a threshold voltage is reached along the conductor in a reversible way. To compute the I_c value from measurements, the threshold voltage value could be either defined as a resistive criterion or electrical field criterion. For HTS and LTS conductors electrical field criterion is the most common, with the usual value of respectively 1 μV/cm and 0.1 μV/cm. One has to specify the range over which the n value is computed. In this thesis it is done for data in the range between 0.1 μV/cm and 2 μV/cm, except if specified.

There are three main routes to measure the I_c dependence on temperature and flux density by transport current protocol:

- **current ramping**: current is ramped at fixed background flux density and temperature.
- **flux density ramping**: background flux density is ramped at fixed current and temperature.
- **temperature ramping**: temperature is ramped at fixed current and background flux density.

In this thesis the I_c of HTS sample/cable was characterized by ramping the transport current at fixed magnetic flux density and temperature.

3.2.2 Generation of homogeneous flux density

The I_c of all HTS materials is flux density strength and temperature dependent. In addition for HTS conductors in form of tapes the I_c is also flux density orientation dependent. These three parameters are inter-dependent: the I_c characterization must be performed in a combination of them. To generate homogeneous flux density in the laboratory two magnet layouts are commonly used: solenoid with a bore in the order of 50-200 mm or dipole magnet that can be a split pair or of the accelerator type. For YBCO and Bi-2223 conductors the minimum and maximum of I_c at 4.2 K are reached for respectively perpendicular and parallel flux density with respect to tape plane. The different ways to characterize HTS samples under combination of flux density intensity and orientation in the laboratory are exposed here.

I_c measurements in solenoid

The aperture of a superconducting solenoid for sample characterization is generally in the order of 50-200 mm. The most common way to characterize HTS samples in a solenoid is to place them straight across the aperture diameter with the transport current direction perpendicular to the flux density. The total sample length, not exceeding the aperture diameter, includes the connections to resistive current leads. A scheme of a sample mounted in the bore of a solenoid is depicted in figure 3.2. A minimum contact area at splice is necessary to prevent the sample from overheating: for HTS tapes, the typical connection length is in the range of 8-20 mm. In the vicinity of the electrical junction, the current is still shared between the resistive matrix/shunt and superconducting filaments/layer leading to power dissipation. After the current transfer length, the current has fully penetrated the superconducting filaments/layer and the I_c could then be measured. The lengths required for electrical junction (D_1) and the current transfer length (D_2) reduce the effective length for I_c measurements (D_m) to about 10-30 mm for a 100 mm aperture solenoid, see figure 3.2. It should be noted than the current transfer length is conductor and temperature dependent. The flux density orientation with respect to the tape plane can be tuned by a rotation of the sample. In most experimental set-ups the orientation of samples is fixed at room temperature but some devices allow a direct increment of orientation during characterization [99].

The I_c properties of HTS conductors are non-uniform even within the same unit length and the conductor performance is limited by the weakest point of its length. As an illustration, the I_c variation along a 95 m long unit length of YBCO AMSC conductor is depicted in figure 3.3. The I_c is measured over 1 m long section at 77 K and in self flux density. The minimum I_c is measured to be 122 A, the maximum 174 A and the average 145 A. A standard deviation of 6.2% is observed over the 95 m unit length. The standard deviation depends on the section length over which measurements are done.

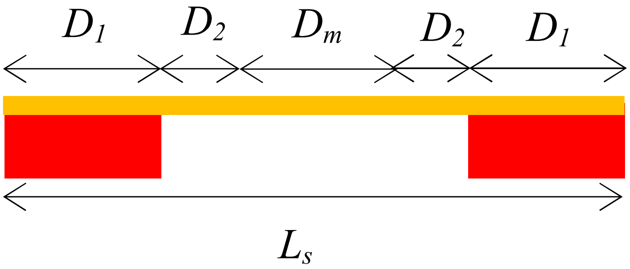

Figure 3.2: Illustration of the sample length (L_s) and the effective length for I_c measurements (D_m).

For magnet applications, long lengths of conductor are required. The minimum I_c of the conductor will be the limiting factor. Therefore for qualification tests, measurements performed on long length samples are preferred. In addition, for long samples the ratio of signal to noise is much higher compared to short ones. The I_c measurement on long samples is possible with the help of the Barrel sample holder (inspired from the VAMAS sample holder [100]). The HTS sample (wire or tape) is helically wound around the barrel. The background flux density is almost perpendicular to the macroscopic current and oriented parallel to tape plane. The sample is soldered to resistive current leads at top and bottom of the barrel. The measurement of I_c with HTS barrel can be done over a length of up to about 5 m.

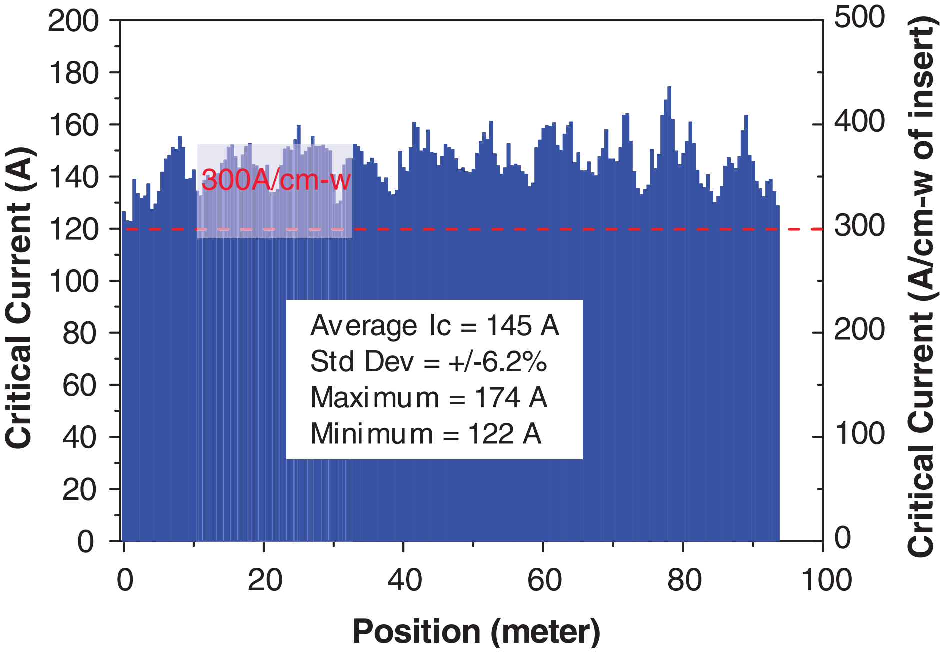

Figure 3.3: Illustration of I_c variation at 77 K and in self flux density along a spool of YBCO AMSC. A standard deviation of 6.2% is observed for measurements performed over 1 m long section.

I_c measurements in a dipole

For I_c measurements performed in the aperture of dipole magnets, the effective length of measurements could be as long as the magnetic length of the coils. Most of dipoles used for HTS characterization are of split pair type that produces homogeneous flux density (10-15 T) over a length of 100-200 mm. At CERN the FRESCA test station generates, with an accelerator like dipole, a homogeneous flux density of up to 9.6 T over a length of 600 mm. This station was used in the framework of this thesis to characterize

HTS high current cables. The FRESCA test station will be described in more details in chapter 5. When tested in dipole, the orientation of external flux density with respect to HTS sample is easily tuned by a rotation of the test station insert. Dipole magnets generate much lower flux density, about 10-15 T in comparison with solenoids and the record 45 T in DC mode of the NHMFL coil [101].

3.2.3 Thermalization of samples

The low cost operation of HTS materials at liquid nitrogen temperature (77 K at 1 bar) makes them attractive for power transmission application. For accelerator magnet applications, the HTS conductors will be operated at 4.2 K since their performances are strongly enhanced by lowering the temperature. The samples characterized in this thesis were immersed in liquid helium bath at 4.2 K. The bath temperature was regulated by means of the gas vapour pressure. The high specific heat of liquid helium compared to that of metals a 4.2 K help to keep a uniform and constant temperature in the sample. The HTS samples may also have been thermalized by conduction in vacuum or gas flow, but in these two techniques, the temperature stability during measurements at high current is difficult to maintained.

3.2.4 Feeding sample with transport current

In I_c test stations, current leads carry the transport current from the power supply (room temperature) to the HTS sample. Both conduction and joule heating of the leads induce thermal load on the cryogenics. Current leads are optimized to minimize the thermal load on the cryogenics for a certain current range: the station has therefore a current limitation. The performances of samples sometimes exceed the current capacity of the station. The temperature and field range of measurements are therefore limited.

The high current capability of coated conductors may be reduced by a reduction of conductor width. The conductor is chemically etched only at the central part where the voltage taps are attached. The width of the tape is maintained to it original value in the connection region to maximize the contact area and therefore minimize the contact resistance. A width reduction down to 50-100 μm has been reported by [102]. In view of the large non uniformity of J_c that may be present across coated conductors width, this characterization technique is not necessarily representative of the original conductor performances.

3.2.5 Reproduction of axial strain

In a magnet winding, superconductors are exposed to large axial and transverse strains induced by the Lorentz forces, magnet pre-stress and thermally induced stress. Most superconductors (except the Nb-Ti type) are known to be highly strain sensitive. The I_c dependence on uni-axial strain could be characterized with different approaches. In the first one, the sample is free hanging during cooling and a pulling force is applied at cold. Only axial tensile regime can be explored with this protocol. To explore the behaviour of conductors in tension and compression a device was developed by Walters et al.[103] (see figure 3.4). The superconducting wire or tape to be investigated is soldered to a thick coiled spring. The strain is applied to the conductor by twisting one end of the spring with respect to the other. To allow large strains without plastic deformation, copper alloy is used for the spring. The spring supports the sample mechanically against the Lorentz force produced during the measurements and long samples can be measured in standard high-field solenoid magnets. Few Walters springs type apparatus were developed to investigate the strain dependence of HTS materials [104][105][106]. To perform measurements on HTS tapes in perpendicular flux density, based on the same approach, a device named U-Spring was developed by [107](see figure 3.4). The sample (20 mm) was soldered to the bottom leg of a U shape. Compression or tension was created in the conductor by moving the two legs of the U. To investigate the I_c anisotropy of HTS tapes under various strain solicitations, the springboard device was introduced by Van der Lan et al. [108] and Sunwong et al. [109]. The HTS sample soldered to a springboard made of copper alloy was placed in split pair dipole (see figure 3.4). By acting on the legs of the springboard, compression or tension is created in the sample. By rotating the full insert, the orientation of flux density with respect to tape plane was modified.

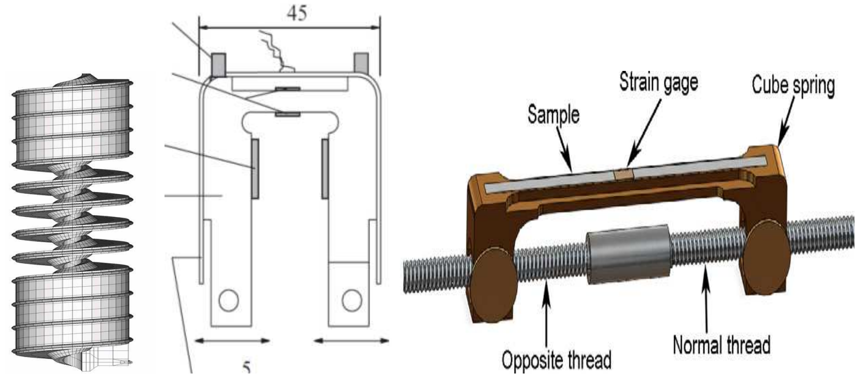

Figure 3.4: The apparatuses used to characterized the strain sensitivity of HTS materials: the Walters spring [103] (left), the U-shape [107](figure from [98]) (middle) and the springboard [108] (right).

3.3 HTS conductors

For application into accelerator magnets, HTS materials must be available in form of conductors with long unit lengths and good electro-mechanical properties. BSCCO conductors were the first to fulfil these requirements and are therefore referred to as first generation (1G) of HTS conductors. More recently coated conductors fulfil these requirements; they are referred to as second generation (2G). Over the different commercially available 1G and 2G conductors, five have been selected: two coated conductors, two Bi-2223 tapes and one Bi-2212 wire. The fabrication process and mechanical properties of these conductors are introduced in this section.

3.3.1 Grain alignment and oxygen stoichiometry

Oxygen stoichiometry plays a major role in the different cuprate superconductors: the critical temperature, the I_c and the B_{irr} depend on the oxygen content. In figure 3.5, the critical temperature of $YBa_2Cu_3O_x$ conductor is depicted as a function of the oxygen content. The T_c is 89 K at x=7, but it progressively reduced to T_c=70 K for x=6.7 [110]. The T_c of BSCCO conductors presents similar oxygen content dependence [111].

Any practical HTS superconductor is made of many grains connected through grain boundaries. A high alignment of the superconducting plane at grain boundaries has been observed to enhance the transport current capacity of cuprate superconductors. In figure 3.5, the J_c of BSCCO and YBCO conductor is depicted as a function of the grain boundary angle. The J_c is increased by an increase of the grain alignment. In YBCO conductors, a good grain alignment is achieved by the epitaxial growth of YBCO crystals on a well textured substrate or buffer layer. By increasing the film thickness, a reduction of texture leads to a progressive reduction of J_c. This is depicted in figure 3.5 for different fabrication processes.

3.3.2 Fabrication process

Two coated conductors are commercially available: the first one from the firm SuperPower (SP) [112], produced by the IBAD technique, is 4 mm wide. The second one from the firm American Superconductors (AMSC) [113], produced by the RABiTS technique, is 4.4 mm wide. The Bi-2223 tapes commercially available are produced by the Japanese company Sumitomo [114] and by the European company Bruker [115]. The last conductor studied is the Bi-2212 wire from Oxford instruments Superconducting Technology [116] which has a 0.8 mm outer diameter [116]. The Bi-2212 conductor is not superconducting when delivered, a specific and complex heat treatment under oxygen atmosphere must be performed after magnet winding in order to react the precursor powders of superconducting phase. The main specifications of the HTS conductors are presented in table 3.1.

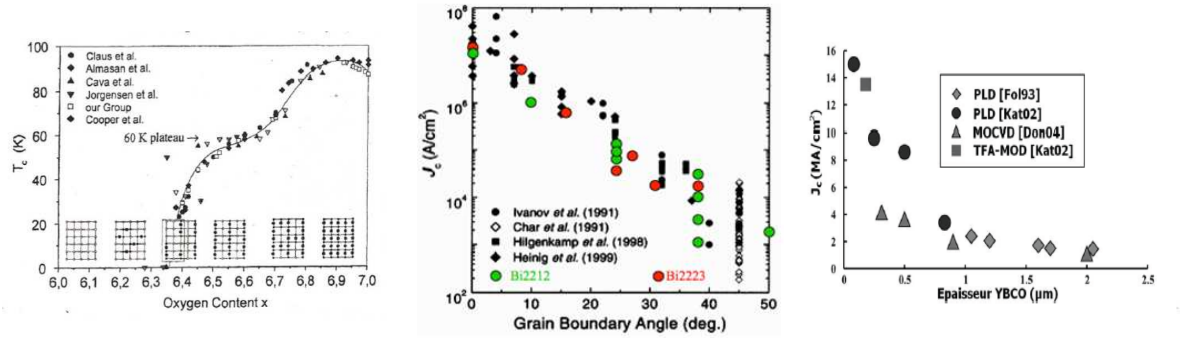

Figure 3.5: The T_c of YBCO as a function of oxygen content (left). The J_c in HTS conductors as a function of the grain boundary angle (middle). The J_c in coated conductors as a function of the film thickness (right)

Table 3.1: Main parameters of HTS conductors.

Manufacturer	**SuperPower**	**AMSC**	**Sumitomo**	**Bruker**	**OST**
HTS material	YBCO	YBCO	Bi-2223	Bi-2223	Bi-2212
Denomination	YBCO SP	YBCO AMSC	Bi-2223 SEI	Bi-2223 BHTS	Bi-2212 OST
Conductor shape	tape	tape	tape	tape	wire
Width (mm)	4	4.4	4.5	3.95	-
Thickness (mm)	0.095	0.44	0.36	0.21	-
Diameter (mm)	-	-	-	-	0.8
HTS section (mm^2)	0.004	0.004	0.29	0.24	0.15
Filling factor %	1	0.2	18	30	30
Stabilizer material	Hastelloy/ Copper	Ni-W/ Cu alloy	Ag/ Ag alloy/ Cu alloy	Ag/ Ag alloy	Ag/ Ag alloy
Minimum bending radius (mm)	6	30	30	25	-
I_c guaranteed @77K and in self field (A)	90	85	180	85	-
I_c expected @4.2 K and in self field (A)	1370	1350	1100	460	900
Expected ratio of I_c at 4.2 K and at 77 K in self field	12	14	6	5.2	-

YBCO conductor from SuperPower (YBCO SP)

The coated conductors from the firm SuperPower Inc. [112] consist of MgO biaxially textured buffers made by ion beam assisted deposition (IBAD) on high-strength Hastelloy substrates followed by REBCO (RE = Y, Sm, Gd or a mixture of them) Metallo-Organic Chemical Vapor Deposition (MOCVD). The high-strength non-magnetic Hastelloy C276 tape substrate is 50 μm thick (can be 100 μm). The IBAD MgO buffer stack includes 5 layers between the metal substrate and HTS layer in order to make it robust in the MOCVD HTS film deposition at a temperature of 850° C [117] (see figure 3.6). The first layer is alumina which mainly serves as a diffusion barrier. The second layer is yttria serving as a seed layer to help IBAD MgO nucleation. The third layer, IBAD MgO is the key layer that forms biaxial texture by IBAD. The fourth layer is homo-epitaxial MgO (HE-MgO), which makes the IBAD MgO robust and improves the texture, and the fifth layer is the LMO cap layer to provide a good match with HTS layer. The HTS layer deposit by the MOCVD technique is 1 μm thick. Texture of film progressively reduces for thicker film. Via sputtering, a 2-3 μm thick silver cap layer is formed around the coated conductor. This silver cap acts as electrical contact and protection against moisture. A final 20 μm thick copper (can be 0-100 μm), deposited by electroplating, surrounds the tape. The copper layer act as a stabilizer since resistivity of Hastelloy substrate is very high (1050 $n\Omega.m$ at 77 K). The standard width of coated conductors from SuperPower is 3 mm, 4 mm and 12 mm. A SuperPower coated conductor cross section is depicted in figure 3.7. The I_c of 4 mm wide conductor has been measured to be 122 A and 1400 A at temperatures of respectively 77 K and 4 K in self-field.

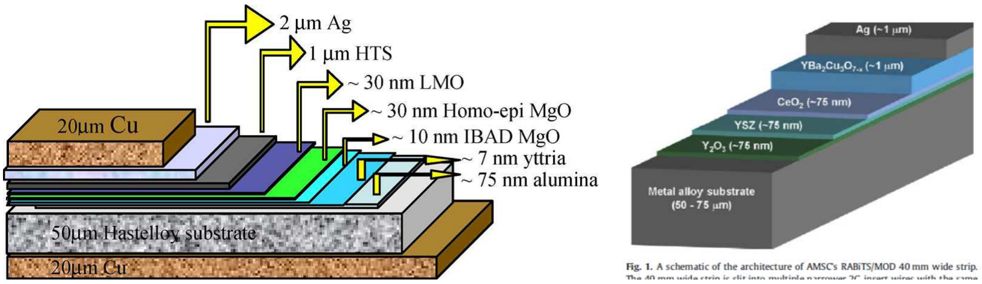

Figure 3.6: Schematic view of the cross section of YBCO SP (left) and YBCO AMSC (right) coated conductors.

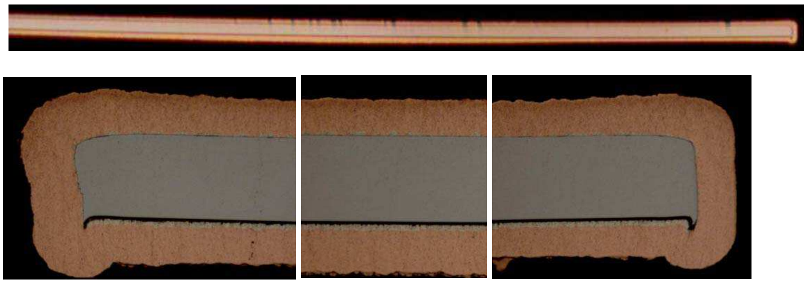

Figure 3.7: Cross section of YBCO SP conductor.

YBCO conductor from AmericanSuperconductor (YBCO AMSC)

The YBCO conductor manufactured by AMSC [118] consists of a Ni alloy substrate produced by the Rolling Assisted Biaxially Texture route (RABiTS). The YBCO AMSC conductor is made from a 75 μm thick (could be different) magnetic Ni-5 at.%W substrate. The use of the non-magnetic alloy Ni-9 at.%W have been recently reported but conductors made from this alloy are still under development [119]. Buffer layers and the superconductor are then deposited on the RABiTS tape. The buffer stack consists of a Y_2O_3 seed layer, a YSZ barrier layer and a CeO_2 cap layer, deposited by high-rate reactive sputtering [120]. YBCO precursor films are slot-die coated onto buffered substrates to reach a film thickness of 0.8 μm (see figure 3.6). The YBCO precursor consists of a nominally stoichiometric metal trifluoroacetate-based (TFA) solution. The Metal Organic Deposition (MOD) film is pyrolyzed at temperatures 600° C in a humid, oxidizing atmosphere to remove the organic components, leaving a film consisting of a mixture of metal oxides and metal oxy-fluorides, which is reacted to an epitaxial YBCO film by pulling the tape through a reel-to-reel furnace at 800° C in a flowing O_2-H_2O environment. The processed YBCO strip is capped with a 3 μm Ag layer and then O_2 annealed. The 4 mm wide YBCO insert strip (could be different) is then laminated between two metallic stabilizer strips with the edges sealed by solder fillets. The strip material depends on application and can be stainless steel, copper or copper alloy. This last provides low resistivity with high mechanical strength and is dedicated to high flux density magnets. The thickness and width of the strips are respectively 160 μm (can be different) and 4.4 mm. The I_c of this conductor measured in self field is respectively 112 A and 1350 A at 77 K and 4 K. A YBCO AMSC coated conductor cross section is depicted in figure 3.8.

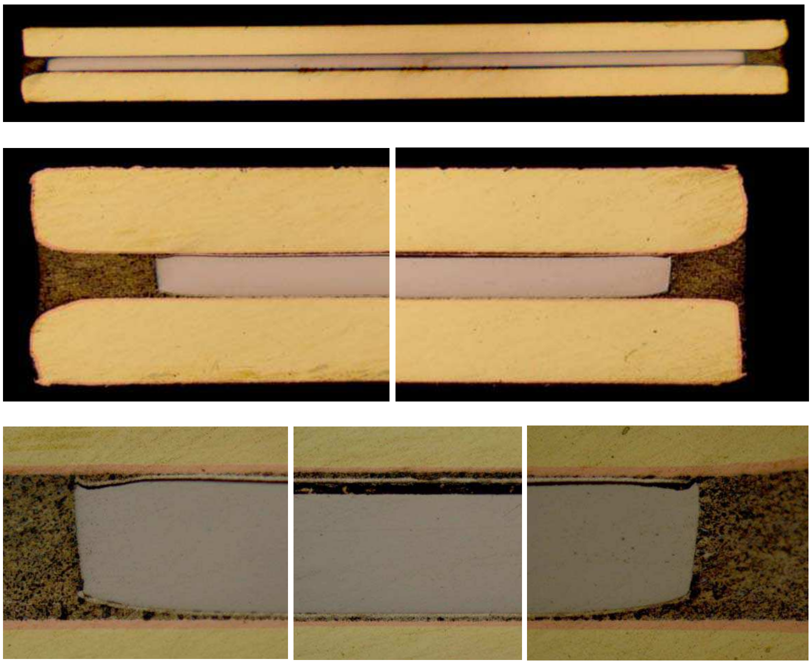

Figure 3.8: Cross section of YBCO AMSC conductor.

Fabrication of BSCCO conductors

BSCCO conductors considered here are produced by the so-called powder-in-tube method (PIT). The ceramic precursor powder is packed in silver rods and then drawn and stacked inside a silver or silver-alloy tube. Depending on the final number of filaments, and their size and number, a second round of drawing and stacking may be performed. The final conductors identified as single stacked or double stacked refer to this stage of manufacturing. The final steps of manufacturing differ between conductor suppliers: this will be introduced in the following section. The heat treatment of conductors that reacts the precursor powders into the superconducting phase is performed at high temperature in partial oxygen pressure. Oxygen diffuses through the silver matrix during heat treatment and thereby allows the formation of the desired superconducting phases. Whereas the ceramic carries the current when superconducting, the matrix provides mechanical strength, electrical stability and environmental protection. One of the significant issues quoted as current limiting factors for Bi-2223 round shape conductors is misalignment of grains. Wire rolling increases drastically the J_c: Bi-2223 conductors are therefore supplied in the form of tapes.

Bi-2223 conductor from Sumitomo (Bi-2223 SEI)

Bi-2223 conductor from Sumitomo is a 3-ply conductor: the superconducting Bi-2223 tape is co laminated with two thin metallic tapes. The HTS insert, which has a rectangular cross section 4.2 mm x 0.2 mm, is produced by the controlled overpressure sintering process (CT-OP). Conductors have 81 filaments embedded in a silver alloy matrix. The significant issues quoted as current limiting factors for Bi-2223 conductors are incomplete phases, misalignment of grains, porosity and unhealed micro-cracks induced by intermediate rolling, all resulting in a defective grain-connectivity and inter-linked via complex mechanisms during the overall processing [121]. The CT-OP sintering has enabled significant progress in Bi-2223 tape resulting in the enhancement of critical current by over 60% and approximately doubling mechanical properties and anti-ballooning property. A variety of reinforcing metallic tapes are available: 50 μm thick heat-resistant copper alloy tapes are dedicated for electromagnet applications for which both robustness and low normal resistance are required. The copper reinforcing tape is highly alloyed to maintain its mechanical strength after the soldering process. Bi-2223 SEI conductor exhibits I_c values of respectively 1063 A and 190 A at 4 K and 77 K in self-field. A Bi-2223 SEI conductor cross section is depicted in figure 3.9.

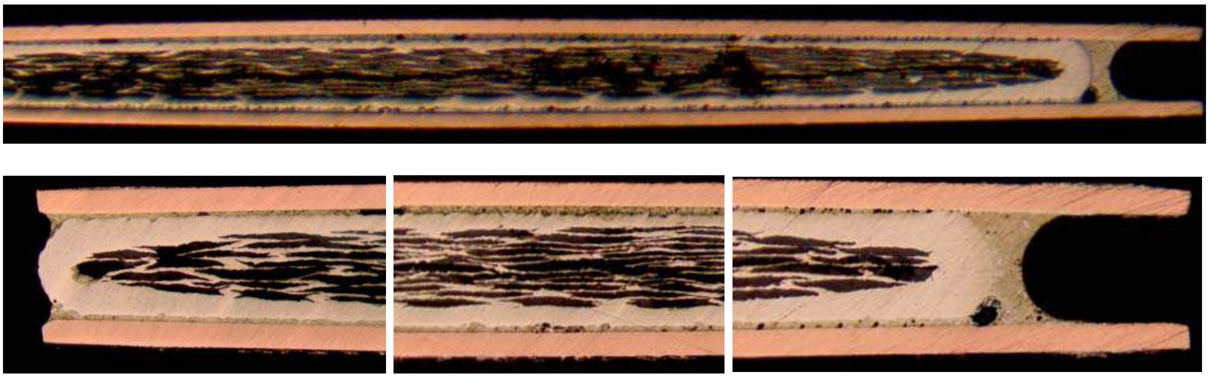

Figure 3.9: Cross section of Bi-2223 SEI conductor.

Bi-2223 conductor from Bruker (Bi-2223 BHTS) (No longer available)

The Bi-2223 tape produced by Bruker is 4.2 mm wide and 0.2 mm thick. This conductor is produced by the PIT route and has 121 filaments embedded in a Ag /AgMg matrix. The filling factor is 30 % and the twist of filaments is 6 mm or longer. The usual production unit is 1500 m long. The minimum critical bending radius of this conductor at 77 K is 25 mm. Bi-2223 BHTS conductor exhibits I_c values of respectively 464 A and 85 A at 4 K and 77 K in self-field. A Bruker tape cross section is shown in figure 3.10.

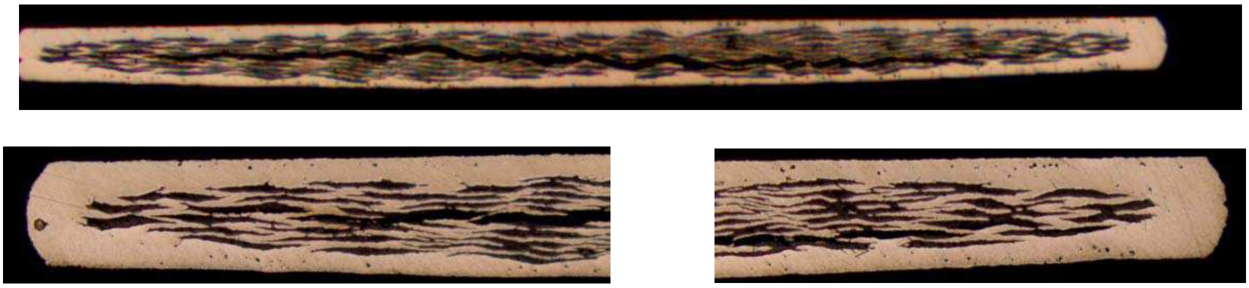

Figure 3.10: Cross section of Bi-2223 BHTS conductor.

Bi-2212 conductor from Oxford instruments (Bi-2212 OST)

Bi-2212 conductor from Oxford instruments Superconducting Technology (OST) presents a round cross section of 0.8 mm outer diameter(could be different). This conductor is produced by the double-stacked PIT route. After the second stacking, the conductor is drawn to the final diameter. Silver has a relatively low Young modulus (less than 80 GPa) and a low tensile yield strength (20 MPa). The Mg-Ag alloy, that is chemically compatible with the Bi-2212 phase is used as external sheath material to improve the mechanical properties. The conductor presents 18 x 45 filament that are 14 μm in diameter [122]. Bi-2212 conductors require a partial-melt heat treatment that can be executed after coil winding (W & R route). A typical Bi-2212 heat treatment cycle in oxygen and the resulting J_c from different heat treatments are depicted in figure 3.12. By increasing the gaz pressure during heat treatment, the J_c of Bi-2212 samples at 4.2 K was doubled recently [49] [62]. Groove-rolled multifilamentary wires has shown a J_c increased by a factor of about 3 with respect to drawn wires prepared with the same Bi-2212 powder and architecture [123]. A Bi-2212 OST conductor cross section is depicted in figure 3.11.

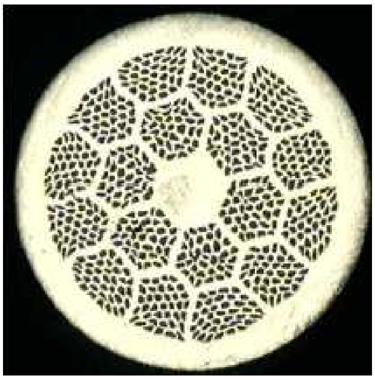

Figure 3.11: Cross section of Bi-2212 OST conductor.

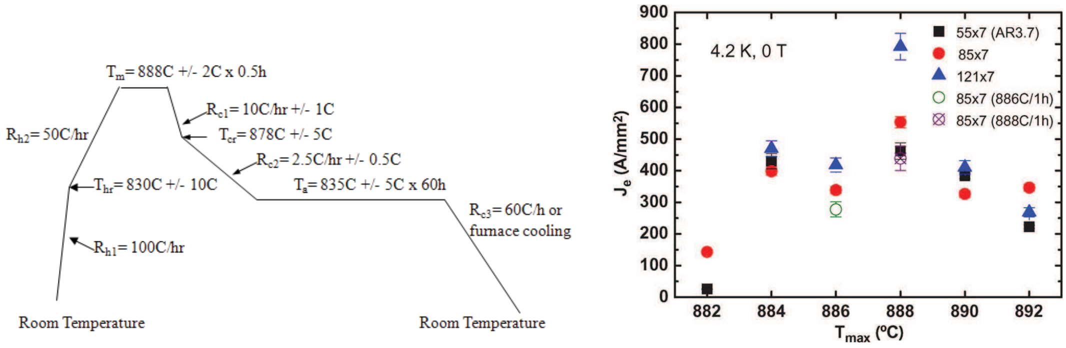

Figure 3.12: Summary of Bi-2212 OST heat treatment cycle used in [61](left). The J_c (4.2 K, 0 T) of Bi-2212 wires as a function of the maximum of temperature reached during heat treatment (for 0.5 h and 1 h) [49] (right).

3.3.3 Mechanical properties of HTS conductors

During the operation of high flux density magnets, conductors are subjected to large Lorentz forces. The I_c dependence on strain of HTS conductors is well established. The transcription of mechanical stresses into I_c degradation passes by the knowledge of conductor mechanical properties. The HTS cuprates have very weak mechanical properties, therefore the rigidity and strength of conductors is fully given by the matrix/substrate. The coated conductors YBCO SP and YBCO AMSC are made from an high strength substrate that represents respectively 50% and 40% (could be different) of the cross section. In these conductors the HTS film is respectively only 1% and 0.5% of the tape section. The silver/silver alloy matrix of Bi-2223 BHTS and Bi-2212 OST conductors represents 70% of the cross section. The other 30% are the HTS filaments. Silver has a low yield strength limit and a weak modulus: these two parameters are enhanced by alloying it with magnesium. In Bi-2223 SEI conductor, high strength copper alloy laminations are soldered around the HTS/Ag insert. The laminations enhance the mechanical properties of the conductor. The different mechanical properties of HTS conductors are given in table 3.2. Over the different HTS conductors the YBCO SP presents the highest mechanical properties with a Young's modulus of 175 GPa and a yield strength of 628 MPa. These two values depend on the amount of copper present in the tape cross section. The tensile stress in YBCO SP conductors as a function of axial strain is depicted in figure 3.13. The mechanical properties of some materials entering in the composition of HTS conductors have also been reported [124][125][13].

Table 3.2: Mechanical properties of HTS conductors at 77 K.

	Yield strength (MPa)	Young modulus (GPa)	Yield strain (%)	Ref.
YBCO SP	628	175	0.36	[124]
YBCO AMSC	212	132	0.16	[124]
Bi-2223 SEI	312	91	0.54	[126]
Bi-2223 BHTS	210	75	-	[127]
Bi-2212 OST (300 K)	126	70	0.34	[128]

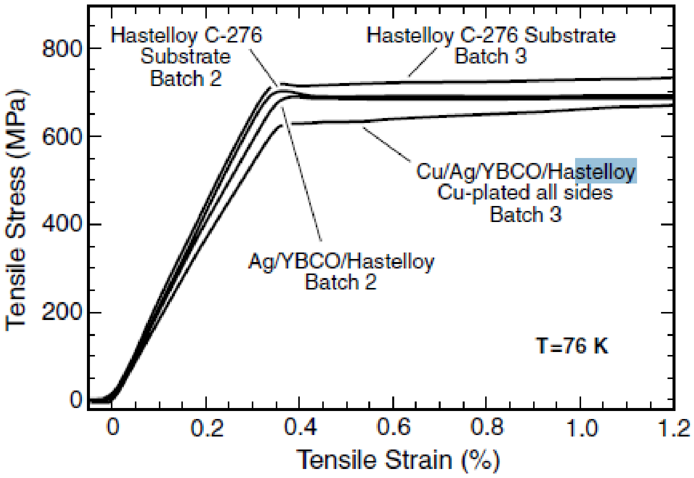

Figure 3.13: The tensile stress in YBCO SP conductor as a function of the tensile strain at 76 K (plot from [124]).

3.4 Measurements of the I_c dependence on flux density

In this section the facilities and the specific sample holders used to perform I_c measurements on YBCO SP, YBCO AMSC, Bi-2223 SEI and Bi-2223 BHTS tapes at 4.2 K are introduced. The measurements are presented, discussed and compared with reported data. Properties of Bi-2212 OST conductors are extracted from data in the literature.

3.4.1 Conductor I_c test facility

I_c test station Nb.4 and Nb.2 of CERN Bd. 163

For the I_c measurements of single tapes at 4.2 K two CERN test stations (Bd. 163), named respectively test station Nb.2 (TS2) and Nb.4 (TS4), have been used. The first station was used for perpendicular flux density measurement; the second one for parallel flux density measurement. The test station setup is shown schematically in figure 3.14. These two stations were used to perform the acceptance tests of virgin and extracted Nb-Ti strands for the main LHC dipole and quadrupole production [129]. The cryostat is a conventional double bath system divided in two parts by a plate made of insulating material (λ -plate). The liquid helium in the upper bath is always at 4.2 K whereas the lower bath can be cooled down to 1.9 K by pumping on a toroidal heat exchanger. The 100 mm aperture Nb_3Sn/Nb-Ti hybrid solenoid is located in the lower bath with the sample. The magnets installed in TS4 and TS2 differ in maximum flux density achievable. At 4.2 K a maximum flux density of 12 T can be generated in bore of TS4 and 11 T for TS2. The flux density homogeneity of TS4 magnet was measured to be better than 0.2 % over the relevant volume, where the strand samples are placed. The magnetic flux density value was calibrated beforehand by a NMR probe: the total uncertainty on the flux density is 3 mT. The temperature is controlled by means of two Cernox and one germanium probes, which are located in low-field zones. In such a way, the temperature readings on both Cernox probes are not affected by the applied magnetic field. The germanium probe, much more flux density sensitive but known for its precision and long-term stability, is thus used to check the reliability of the Cernox probes before the magnetic flux density is ramped up. The overall uncertainty on temperature reading is +/-7 mK. In TS2 stable DC power supply (batteries) providing up to 800 A supplies the current to the HTS sample through bronze current leads. For TS4 a 4 kA class power supply from Kenpower is used. The sample current is measured with zero-flux current transformer by a Keithley 2000 multimeter [130] with an overall uncertainty of respectively 0.01 A and 0.02 A for TS2 and TS4. In both stations the sample voltage is measured using Keithley 1890 nanovoltmeter [130] with uncertainty and accuracy of respectively 10 nV and 1 nV. A Labview routine [131] controls both the magnet and the sample power supply and records at the same time the measurements. The HTS samples were protected against over voltage by a POTAIM card (CERN equipment developed in house). The threshold value and integration time for over voltage protection were set respectively to 1 mV and 100 ms for all measurements carried out. Over the many samples characterized none have been damaged during measurements.

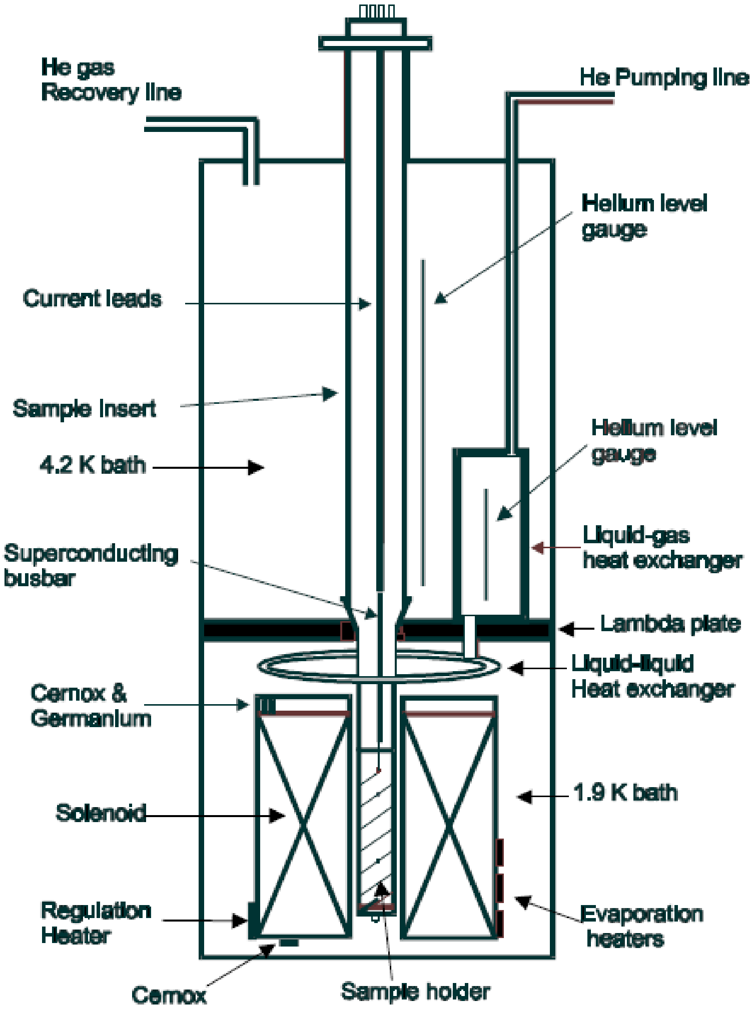

Figure 3.14: Schematic overview of the TS4 and TS2 cryostats, containing the sample holder and the magnet.

Accuracy of I_c measurements with TS4

The I_c measurement repeatability and reproducibility of TS4 has been reported to be better than respectively 1% and 1.5% [129]. The I_c measurements performed with station TS4 was compared to other institute measurements: a reference LHC Nb-Ti strand sample of diameter 0.8 mm helically wound on a Barrel was circulated between the institutes INFN, UNIGE and CEA. The measurements were performed with the current ramping protocol up to flux density of 12 T in liquid helium bath with pressure close to 1 bar. The electrical field criterion of $0.1\mu\mathrm{V/cm}$ was used to compute the sample I_c. Since measurements were not exactly performed at the same temperature, the I_c values were scaled to the reference temperature of 4.22 K by means of the well-known extrapolation:

$$I_{cc} = I_{cme}\frac{T_c - 4.22}{T_c - T_{me}} \tag{3.2}$$

Where I_{cc} is the critical current at 4.22 K, I_{cme} is the critical current measured at the temperature T_{me} and T_c is the critical temperature as given by Lubell [132]. The measurements performed over the different laboratories are compared in figure 3.15: the I_c values agree within 1.2% up to 5 T. At higher flux densities discrepancy between measurements is observed, nevertheless the agreement remains within 2.2%. The same discrepancy was observed for I_c computed using the 1 μV/cm criterion. The n-value of the circulated sample is reported in figure 3.16. Good agreement between the different institute measurements is observed. The measurements performed at CERN in test station Nb.4 are therefore reliable.

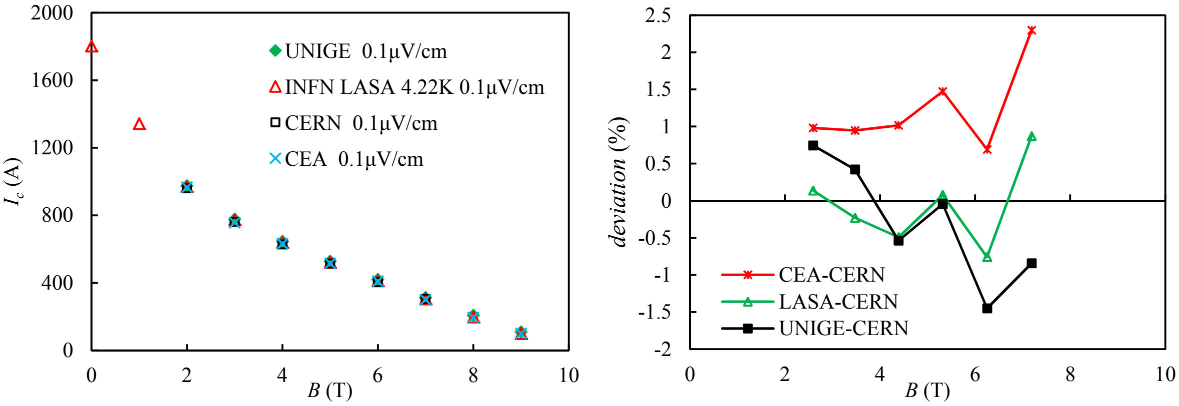

Figure 3.15: The I_c measurements performed in the framework of EuCARD program on a Nb-Ti sample circulated in different laboratories. The I_c is computed using the 0.1 μV/cm electrical field criterion and the temperature is corrected to 4.22 K (left). The I_c deviation at 4.22 K using the 0.1 μV/cm electrical field criterion (right).

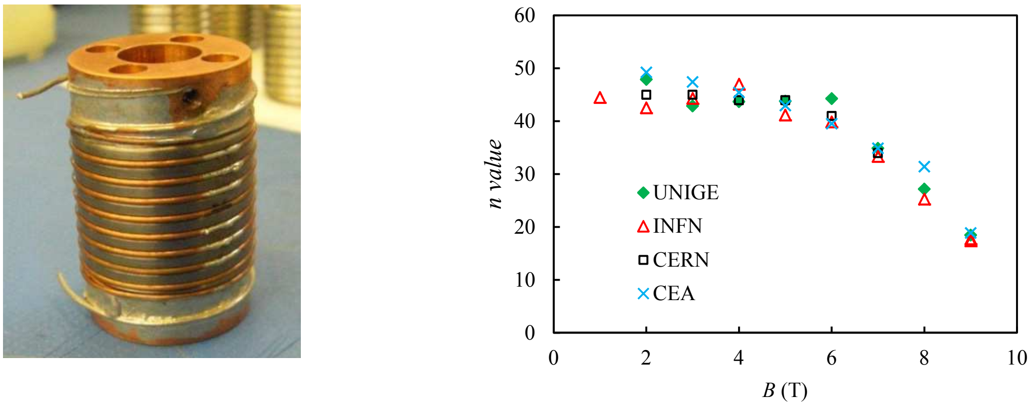

Figure 3.16: The Nb-Ti sample circulated in different laboratories (left) and the n-value computed (right).

3.4.2 Sample holders for HTS tape conductors

To characterize the I_c of the different tape conductors at 4.2 K, three specific sample holders were developed. Two of them allow measurements under parallel flux density orientation, the third in perpendicular flux density. The design of the different sample holders that fit in the test station TS2 and TS4 is detailed in this section.

The HTS Barrel Sample Holder (TS4)

The HTS Barrel sample holder, inspired from the VAMAS sample holder [100], was developed and used to measure I_c of about 1 m long YBCO SP samples exposed to parallel flux density. The HTS Barrel that fits in TS4 consists in a 40 mm long stainless steel cylinder with an external diameter of 31 mm (see figure 3.17 left). Copper end-rings (10 mm high) are bolted to each end of the barrel. They act as electrical connection between the current leads and the sample. The tape (1040 mm long) is first helically wound on the barrel under tension (20 N) and then soldered to the copper terminals. A helical groove was machined in the stainless steel central piece to fit the width of YBCO SP conductor. This groove allows a better mechanical supporting of the tape. The barrel enables of 5 or 6 turns of HTS conductor. The HTS side of the conductor faces with the copper terminals to lower the electrical contact resistance. The soldering of the joints is done with eutectic Sn-Ag at a temperature of 230° C. Voltage taps were used to cover the 2 and 4 central turns where the current was fully flowing in the HTS layer. A sample ready for a test is shown in figure 3.17 left. The HTS Barrel was made to characterise YBCO SP conductors. The I_c measurements under parallel flux density of YBCO AMSC, Bi-2223 SEI and Bi-2223 BHTS conductors was ensured by the HTS Flatened Barrel.

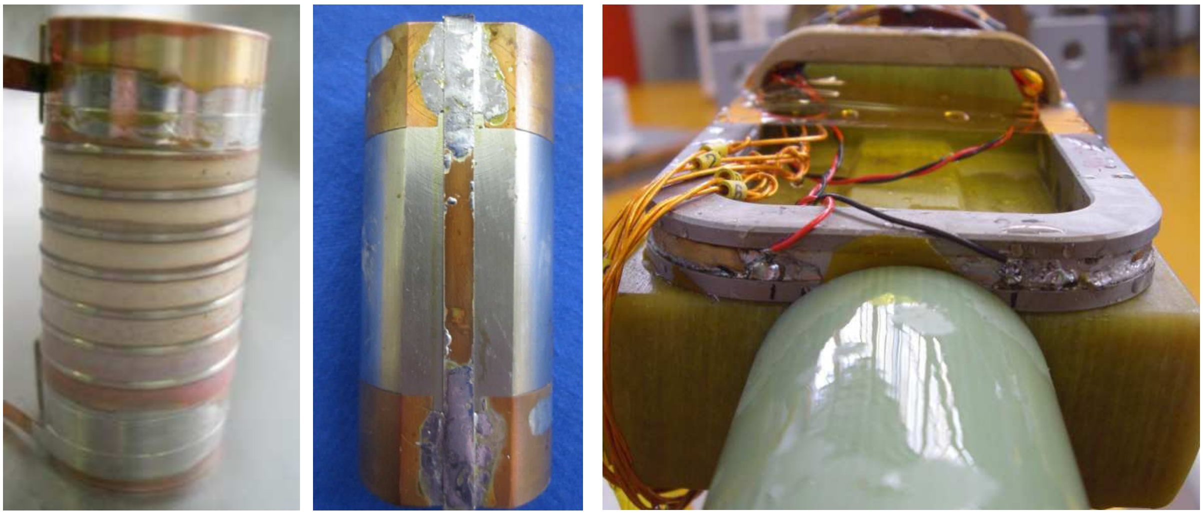

Figure 3.17: YBCO SP conductor mounted on the different sample holders: HTS Barrel that fits in TS4 (left), HTS Flattened Barrel that fits in TS4 (middle) and U-Shape that fits in TS2 (right).

The HTS flattened Barrel Sample Holder (TS4)

The performances of YBCO AMSC, Bi-2223 SEI and Bi-2223 BHTS conductors in parallel flux density were measured using the HTS flattened sample holder. The HTS flattened Barrel that fits in TS4 consists in a HTS Barrel where a 15 mm wide face was machined out over the height of the Barrel, see figure 3.17 middle. The HTS sample is placed straight along the flat surface and soldered to the two copper terminals over a distance of 10 mm. The voltage taps are placed symmetrically around the mid-length of the tape and are 15-20 mm distant. No current sharing was observed in the instrumented portion of the tapes, indicating a current transfer length of less than 20 mm at 4.2 K. In the HTS Flattened barrel the current is parallel to the external magnetic flux density.

The U-Shape Sample holder (TS2)

To measure YBCO SP conductor performances under perpendicular flux density a stainless-steel device named U-Shape [133] was developed to fit in TS2 (see figure 3.17 right). The HTS tape is housed in a copper plated groove and soldered along its whole length (320 mm). Two Nb-Ti wires soldered to the HTS tape in the legs of the U-Shape act as current leads. The transition between U-Shape legs (vertical parts) and head (horizontal part) is made with constant curvature radius of 19 mm. This radius only allows the measurements of YBCO SP conductor. The length of tape exposed to the perpendicular flux density is 36 mm. Voltage taps, placed in the perpendicular flux density location are 20 to 30 mm distant.

3.4.3 Measurements at 4.2 K

The I_c measurements were performed at a temperature of 4.2 K and in background flux density of up to 12 T. The current was ramped in samples with rates of 12 A/s and 20 A/s. The measurements were carried out at both increasing and decreasing flux density to check a possible hysteresis. At each flux density, the measurement was performed twice for each ramp rate in order to ensure the reproducibility. The measurements are presented in this section.

Measured I_c of YBCO SP conductor

The YBCO SP samples were extracted from two different spools (SP-1 and SP-3) with unit length of 100 m. The provided conductors were measured at 77 K and in self field by the manufacturer: the mean I_c value is 102 A for spool SP-1 with a standard deviation of about 4% and 122 A for spool SP-3.

Parallel flux density

Three YBCO samples from SuperPower (SP-1a, SP-1b and SP-3a) were measured in parallel flux density via the HTS Barrel sample holder. Two samples were from spool SP-CERN-20100108-1 (SP-1), the last one was from spool SP-CERN-20100108-13 (SP-3). The measurements are reported in figure 3.18. For SP-1 samples, the I_c measured was about 1300 A in self-flux density and 970 A at 12 T. A quasi linear current decrease is observed between these two flux densities, with a slope of -50 A/T.

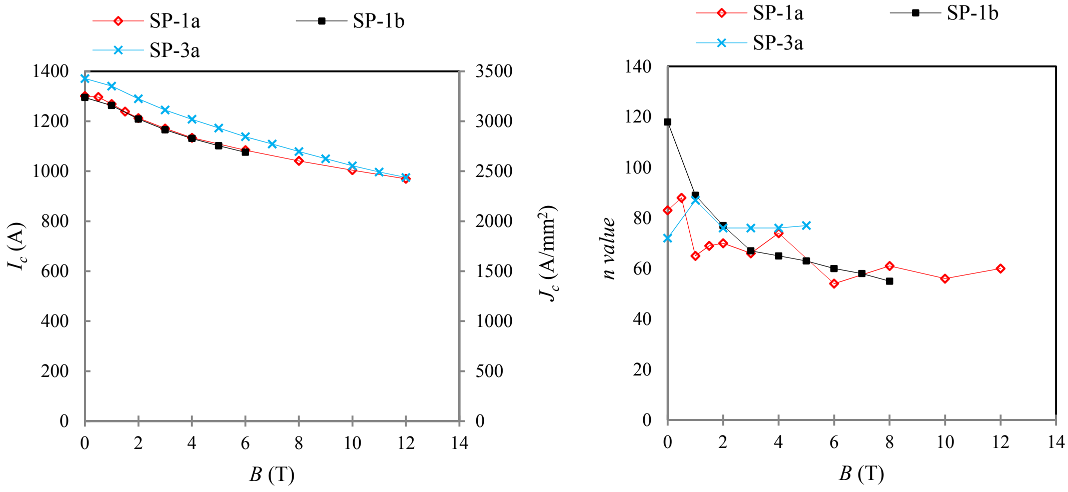

Figure 3.18: I_c (left) and n-values (right) of YBCO SP conductors at 4.2 K as a function of parallel flux density.

The SP-3a sample presents an I_c 6 % higher in self flux density (1370 A) but the difference disappears progressively by increasing the magnetic flux density - it vanishes at 12 T. The n value of the samples measured is presented in figure 3.18. The n value at 4.2 K is about 80 in self-field and 60 at 12 T.

Perpendicular flux density

Three samples from spool SP-1 (SP-1c, SP-1d, SP-1e) and one from spool SP-3 (SP-3b) were measured in perpendicular flux density with the U-Shape sample holder. The current limitation of TS2 confines I_c measurements to flux densities above 1 T. The measurements are presented in figure 3.19, a good uniformity between the different samples is observed. At 1 T the I_c is about 840 A. The I_c decrease is rapid up to 6 T where an I_c value of 298 A is observed. From 6 T to 11 T the decrease is more gentle from respectively 298 A to 192 A.

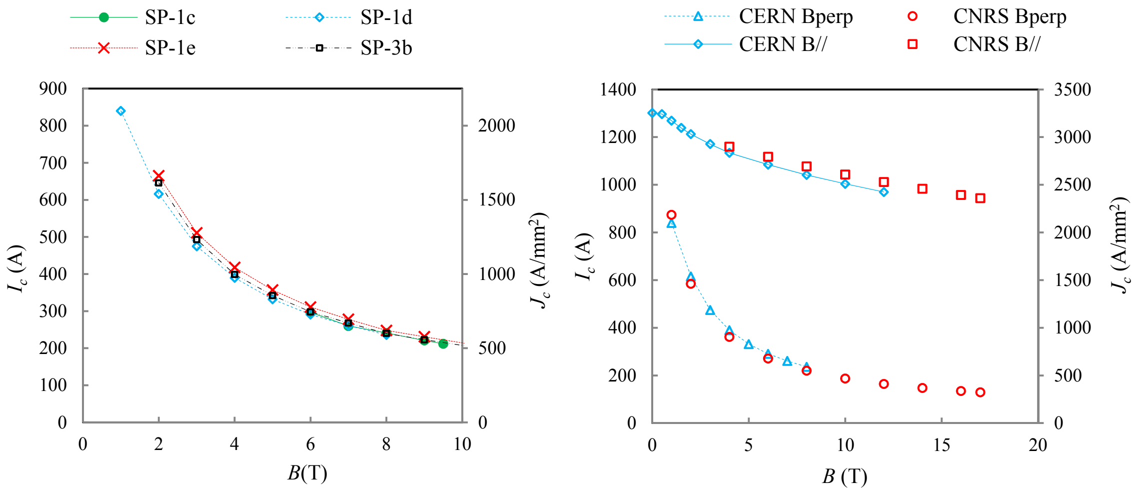

Figure 3.19: The measured I_c of YBCO SP conductor in perpendicular flux density at 4.2 K (left). Comparison of measurements performed at CERN and CNRS [134] on YBCO SP samples from the same spool under parallel and perpendicular flux density at 4.2 K (right).

Discussion

A sample extracted from the spool SP-1 was characterized at CNRS Grenoble in perpendicular and parallel flux densities of up to 17 T [134]. The sample was mounted straight across in the 160 mm flux density aperture of a 20 T resistive solenoid. The CNRS measurements are compared to those carried out at CERN in figure 3.19. Good agreement is observed in perpendicular flux density. For parallel flux density, a small discrepancy (3%) which is equivalent to the standard deviation of I_c reported by the manufacturer is observed. No hysteresis behaviour was observed in YBCO SP conductors and the noise to signal ratio was low for both sample holders.

Measured I_c of YBCO AMSC conductor

An YBCO AMSC coated conductor extracted from a 150 m unit length was characterized in parallel flux density on the HTS flattened barrel. The I_c of the sample was measured to be 112 A at 77 K and in self flux density, well above the 85 A minimum I_c performances ensured by the manufacturer. The measurements performed at 4.2 K in increasing and decreasing flux density are reported in figure 3.20. The sample I_c at 4.2 K in self-field was measured to be 1354 A. By increasing the flux density up to 0.4 T the I_c was slightly increased to 1379 A. Then, for higher flux density, the I_c decreases quasi linearly with a slope of -23.3 A/T down to a final I_c value of 1109 A at 12 T. The I_c with increasing and deceasing flux density are identical. In figure 3.20, the electric field along YBCO sample as a function of current is depicted at flux density values of 2 T, 6 T and 10 T. A complete superposition of increasing and decreasing flux density measurements is found: no hysteresis is observed. Some additional measurements were performed at 1.9 K at flux density of 0 T, 0.5 T and 1 T (see figure 3.20). An increase of I_c of about 0.4-1.5% was observed with respect to the values measured at 4.2 K. This is easily explained by the high T_c and B_{irr} of this conductor. At 4.2 K, the n-value in self flux density is 58, it is 36 under a flux density of 12 T. The n value data set is approximated by a linear flux density dependency of -0.75 per Tesla.

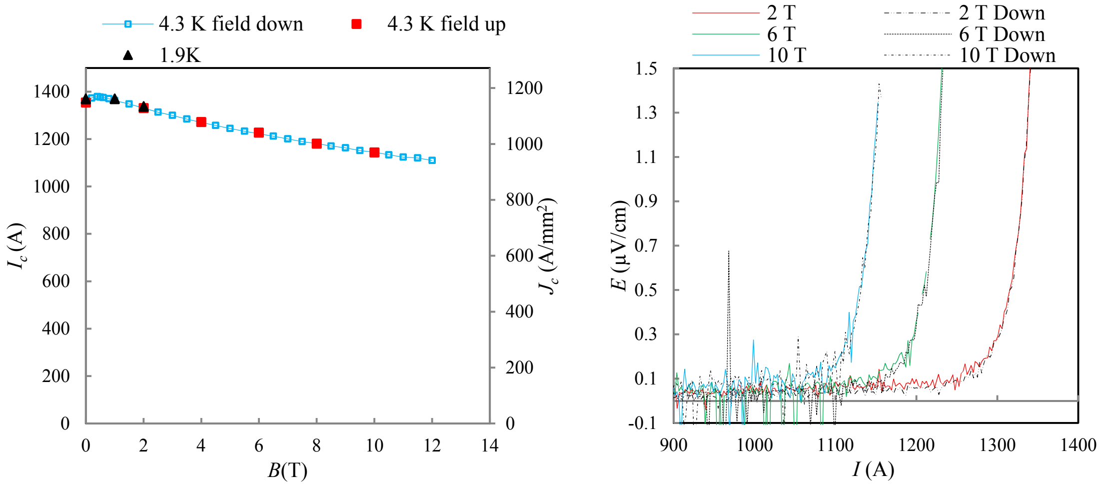

Figure 3.20: The I_c of YBCO AMSC conductor in parallel flux density at 4.2 K and 1.9 K (left). The electrical field as a function of the current for increasing and decreasing flux density at 2 T, 6 T and 10 T (right).

Measured I_c of Bi-2223 SEI conductor

The Bi-2223 SEI conductor was measured on the HTS flattened Barrel by progressively increasing the flux density up to 12 T and then decreasing it down to 0 T. The measurements are reported in figure 3.21. During the sample integration in the station, a large loop of voltage tap wire with respect to the samples was formed. The noise to signal ratio was quite important: the computation of the n-value was not possible and the I_c was determined with a 10 μV/cm electrical field criterion. By increasing flux density, the I_c is progressively increased from 1063 A at 0 T to 1095 A at 0.5 T. Between 0.5 T and 1.5 T a plateau of I_c value is hold. Then by increasing flux density above 1.5 T, the I_c is decreased down to 798 A at 6 T and 674 A at 12 T.

Between increasing and decreasing flux density measurements, a large hysteresis was observed: I_c values are measured to be higher for decreasing flux density compared to increasing flux density. The maximum of hysteresis is observed at 5 T with a 133 A deviation. In self flux density the deviation is 98 A. In decreasing flux density, a plateau of I_c value between 0.5 T and 1.1 T is observed. The hysteretic behavior exhibited by the sample, also observed by [135], is related to the flux motion at the boundaries of weakly linked grains [136].

In figure 3.21, the reported I_c of Bi-2223 SEI tapes measured at 4.3 K in parallel and perpendicular flux densities of up to 28 T [135] are compared to measurements performed at CERN. For increasing parallel flux density, a perfect match between measurements is observed. The different magnetic history doesn't allow to compare the related measurements in decreasing flux density.

In perpendicular flux density the hysteresis behaviour of I_c is also observed. By increasing flux density, the I_c rapidly decreases from 1100 A in self field to 500 A at 4 T and then more quietly down to 380 A at 25 T.

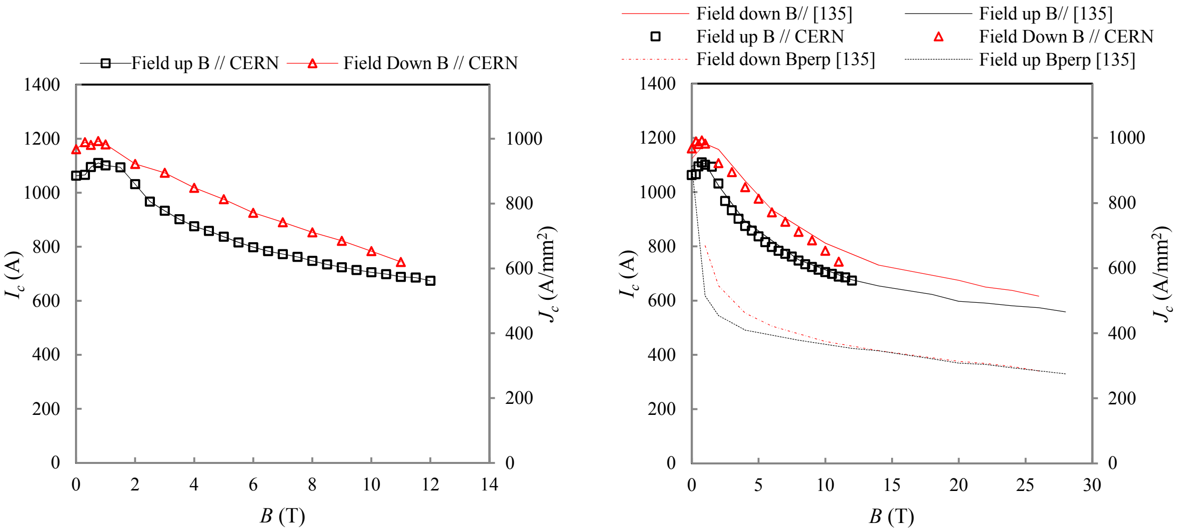

Figure 3.21: The measured I_c of Bi-2223 SEI conductor in increasing and decreasing parallel flux density at 4.2 K (left). I_c measured and reported data [135] in increasing and decreasing parallel flux density (right).

Measured I_c of Bi-2223 BHTS conductor

The Bi-2223 BHTS conductor was measured on the HTS flattened Barrel in increasing flux density of up to 12 T. The measurements are reported in figure 3.22. The I_c in self flux density is 464 A and decreases rapidly to 281 A at 4 T. At 12 T the I_c is 217 A. The n-value is ranging between 38 at self flux density and 28 at 12 T. The electrical field along the Bi-2223 BHTS sample as a function of the current is depicted in figure 3.22 for various flux densities. Despite the relatively small distance between the voltage taps (2.8 cm), the sample exhibits low values of noise to signal ratio.

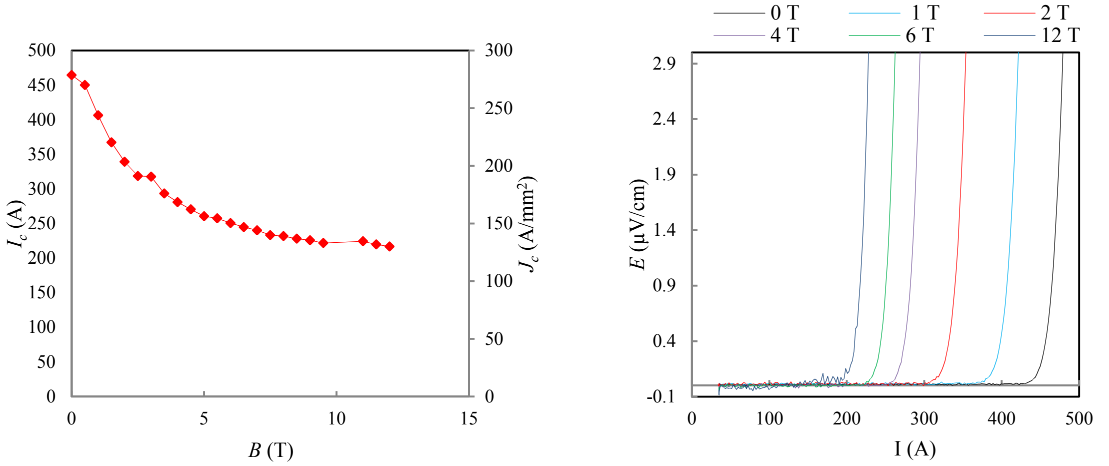

Figure 3.22: The I_c of Bi-2223 BHTS conductor at 4.2 K in parallel flux density (left). The electrical field along the Bi-2223 BHTS sample as a function of current at different flux densities (right).

Reported I_c of Bi-2212 OST conductor

Reported J_c measurements [34] of Bi-2212 conductor (0.8 mm in diameter) at temperature ranging between 4.2 K and 24 K are depicted in figure 3.23. The J_c sharply decreases with increasing flux density up to 2 T and then more quietly. At 4.2 K the I_c is 450 A in self flux density and 175 A at 15 T, corresponding to a critical current density of respectively 900 A/mm^2 and 350 A/mm^2.

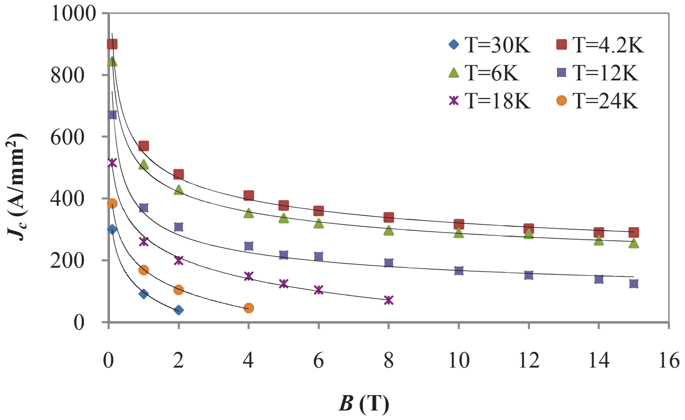

Figure 3.23: The reported I_c of Bi-2212 OST conductor as a function of magnetic flux density, plotted at different temperatures (plot from [34]).

3.5 Angular dependence of I_c in YBCO and Bi-2223 conductors

In the winding of accelerator magnets, flux density takes various orientation with respect to the HTS conductor tape plane. A detailed knowledge of the angular I_c dependence of these conductors is required to estimate with accuracy the magnet performances.

3.5.1 I_c Anisotropy of YBCO conductors at 77 K

The I_c anisotropy of coated conductors has been widely studied at 77 K. The generic shape of the I_c anisotropy at this temperature is marked by a sharp I_c peak at parallel flux density orientation ($\theta = 90°$), typical of the intrinsic pinning and a second reduced peak close to perpendicular flux density orientation ($\theta = 0°$), due to pinning at columnar defects, such as dislocations or columnar arrays of nanoparticles.

3.5.2 I_c Anisotropy of YBCO conductors at 4 K

The shape of the anisotropy at 77 K and at 4 K differs: the cusp-like peak at parallel flux density orientation ($\theta = 90°$) is observed at both temperatures but the local maximum at the perpendicular flux density orientation ($\theta = 0°$) is only observed at 77 K. The low temperature flux pinning mechanisms differ significantly from those at high temperature due to the smaller vortex core size and the reduced thermal fluctuation effects that allow operation of weaker pins that become thermally depinned at higher temperature.

At 4.2 K, in contrast to 77 K [99], all tapes have qualitatively a similar shape of anisotropy. However the peak of I_c around the ab plane (θ=90°) for $BaZrO_3$ (BZO) doped samples is broader that for undoped samples as depicted in figures 3.24-25. This is positive news for magnet construction because it shows that strong pinning enhancement by methods such as BZO addition do affect beneficially the $I_c(\theta,B)$ at 4 K and fields up to 30 T (figure 3.25) [137][37][138][139][140].

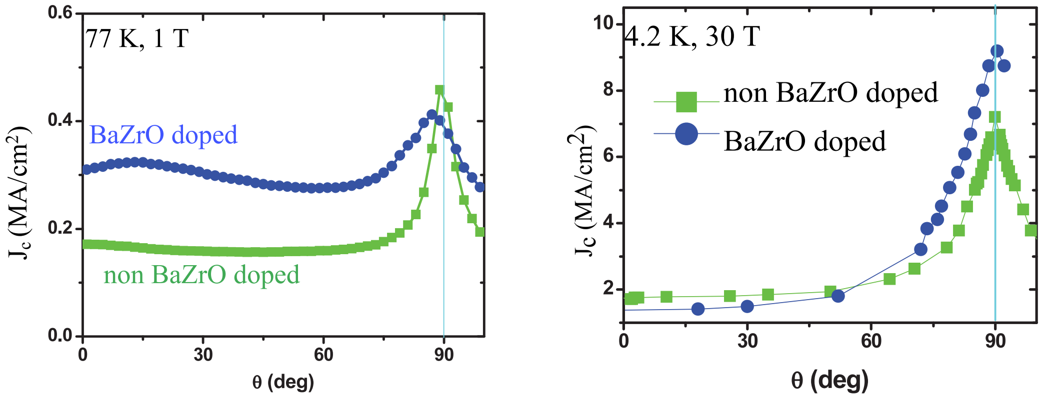

Figure 3.24: The J_c anisotropy of YBCO SP conductors with different pinning centers at 77 K and 1 T (left) and at 4.2 K and 30 T (right) (plots from [99]). BZO stands for $BaZrO_3$ doped samples.

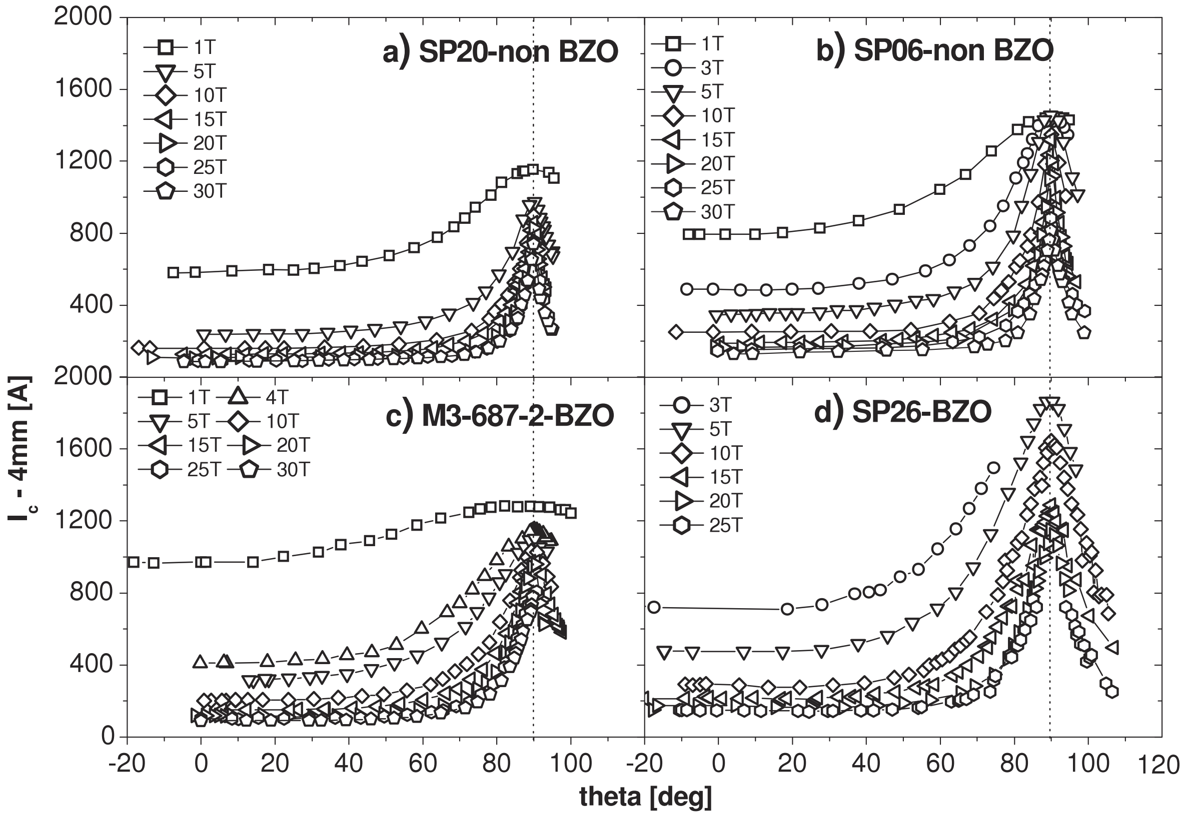

Figure 3.25: The I_c anisotropy of YBCO SP conductor at 4 K with and without $BaZrO_3$ (BZO) inclusions (plot from [137]).

3.5.3 The I_c anisotropy of Bi-2223 SEI conductor at 77 K and at 4 K

In figure 3.26, the I_c of Bi-2223 SEI tapes as a function of the flux density orientation with respect to the tape plane is depicted at 77 K and 4 K. The highest I_c is observed at any flux density in parallel orientation. The lowest I_c is observed in perpendicular orientation. The peak of I_c around the parallel orientation is due to the intrinsic pinning associated with the Cu-O planes.

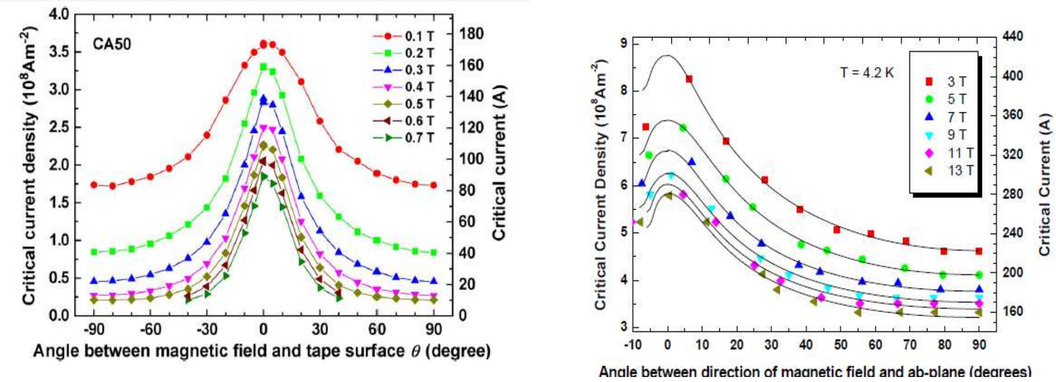

Figure 3.26: The I_c of Bi-2223 SEI tape as a function of the flux density orientation with respect to the tape plane at 77 K (left) and 4 K (right) (plots from [141]).

3.5.4 Ratio of I_c in parallel and perpendicular orientations at 4.2 K

The knowledge of the I_c anisotropy of YBCO and Bi-2223 tape conductors is far from being complete and is conductor dependent. At 4.2 K, for any HTS tape conductor, the maximum and minimum of I_c are observed in respectively the parallel and the perpendicular flux density orientation. Measurements in these two orientations already give useful information for the coil design. The amplitude of the anisotropy is defined as the the ratio of the I_c in parallel and perpendicular flux density orientations. In figure 3.27, this ratio for YBCO SP, YBCO AMSC, Bi-2223 BHTS and Bi-2223 SEI conductors is depicted as a function of external flux density. The I_c ratio of YBCO conductors increases quasi linearly with flux density. At 4 T the ratio is already 3.2 and 4.9 for respectively YBCO SP and YBCO AMSC conductors. At 10 T the ratio is respectively 5.6 and 8.9. The I_c ratio of Bi-2223 conductors is much lower. It increases rapidly from unity in self flux density to a value of about 2 at 1 T. At higher flux densities the I_c ratio is progressively reduced to 1.57 for Bi-2223 BHTS conductor at 10 T and 1.99 for Bi-2223 SEI conductor at 12 T.

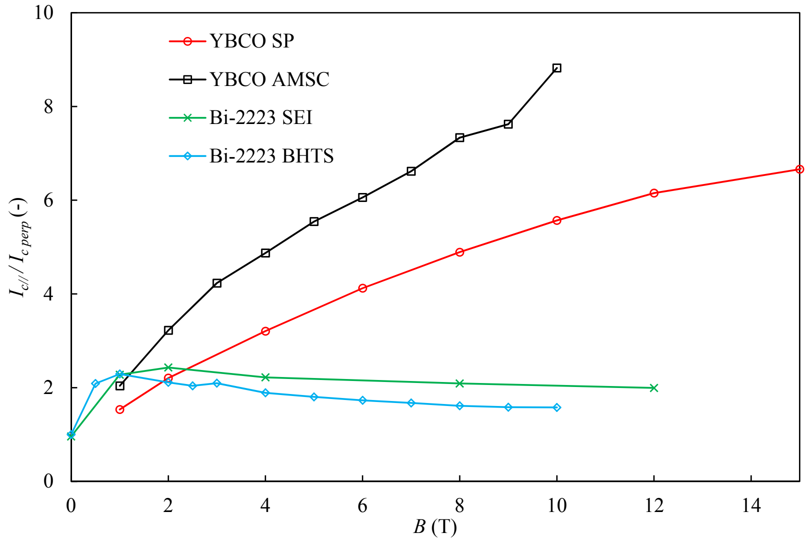

Figure 3.27: The ratio of the I_c in parallel and in perpendicular flux density for YBCO SP, YBCO AMSC, Bi-2223 SEI and Bi-2223 BHTS conductors at 4.2 K.

3.6 Measurements of resistance of splice between HTS tape conductors

High flux density accelerator magnets will require large quantity of conductors exceeding the typical unit lengths today available of HTS materials [118][142]: splice between HTS conductors will therefore be required. The basic properties that ensure the reliability of an HTS splice are low electrical resistance and high mechanical strength [143]. Low joint resistance can be achieved for BSCCO tapes by removing the silver sheath and directly joining the superconducting filaments of the two tapes together via high pressure pressing and sintering [144]. Although this process is relatively complicated and requires additional heat treatment, contact resistance is reported to be as low as $10^{-12}\Omega$ to $10^{-15}\Omega$, which facilitates the use of this method in producing NMR and MRI magnets that employ the persistent current mode [145]. Similarly, directly joining the HTS films of coated conductors through the silver layer has been reported to provide low contact resistance [146][147]. These two processes that consist in removing a part of the matrix to make HTS filaments/films in closer vicinity are not of practice for accelerator magnets where in situ splicing will be required. In addition the mechanical strength of the splice produced by these techniques is low. Therefore the direct splicing of HTS tapes via intermediate solder material is the preferred solution.

At the splice location, the current has to flow through different resistive interfaces and materials to be transferred from the HTS filaments/film of the first conductor to that of the second. The resistance of a splice is composed of two mains contributions: the internal resistance and the conductor interfacing resistance. The use of solder for splicing ensures low interfacing resistance value. The internal resistance is intrinsic to the conductor internal structure and is governed by the resistivity of the matrix materials but also by the resistance of internal interfaces. The measurement of HTS splice resistance is required since the internal interface resistances are difficult to predict.

In the first part of this section the resistance of YBCO SP, YBCO AMSC, Bi-2223 SEI and Bi-2223 BHTS splices is characterized at 77 K and in self field. Then measurements reported on YBCO SP splices at 4 K under magnetic flux density are reviewed. The mechanical strength of YBCO splice is then briefly discussed.

3.6.1 The lap joint layout

There are several different configurations for splicing HTS tapes such as: lap joints, butt joints, praying hands joints, and shim joints where normal metals or superconducting materials are overlapped between two adjacent HTS tapes. This study has been limited to the common lap joint type, in which one HTS tape is laid flat over the second HTS tape (see figure 3.28). The two conductors are interfacing over a distance D_0.

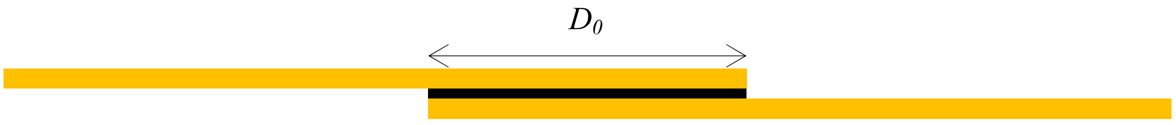

Figure 3.28: Longitudinal schematic view of a lap joint. The two conductor are soldered over an interfacing distance D_0.

Different types of lap joints

Bi-2223 tapes present a symmetric cross section: a unique type of lap joint can be manufactured. The YBCO tapes have an asymmetric geometry, as depicted in figure 3.29. The HTS film lays at one side of the highly resistive substrate. Three types of lap joint could therefore be made from YBCO conductors:

- **The face to face lap joint (FF)** in which no substrate is in between the two HTS films.
- **The back to back lap joint (BB)** in which the HTS films are placed as far as possible from each other with two substrates in between.
- **The face to back lap joint (FB)** in which the HTS tapes are positioned such that only one substrate is in between the HTS films.

For YBCO lap joint, the lowest resistance is achieved in the face to face configuration, but in a magnet FB or BB configuration lap joint could be necessary. The three lap joint configurations were therefore characterized at 77 K and in self field.

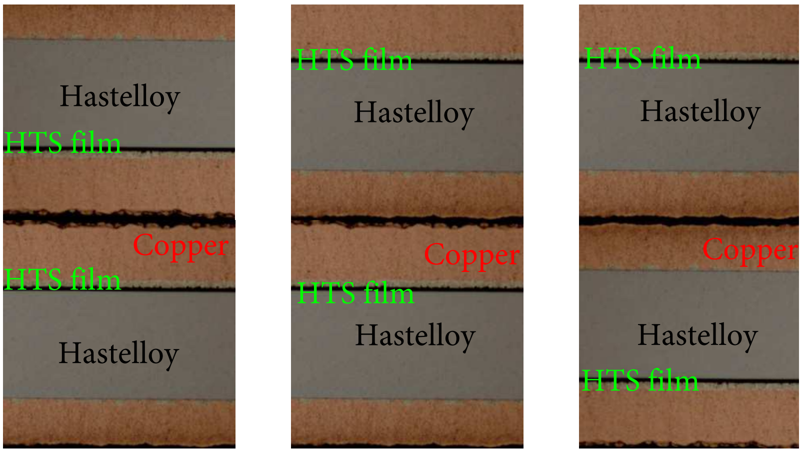

Figure 3.29: Cross section of the different lap joint configurations of YBCO SP conductors. The Face to Face (FF) lap joint (left), the Face to Back (FB) lap joint (middle) and the Back to Back (BB) lap joint (right).

Splicing temperature and selection of solder material

Splicing temperature limitation

The choice of the solder used to perform the splice is constrained by the maximum temperature that the conductor could withstand without I_c or structure degradation. The I_c properties of HTS materials are closely related to the oxygen stoichiometry [110]. The laminations in YBCO AMSC and Bi-2223 SEI conductors are soldered to the HTS tape. To avoid delamination, a splicing temperature lower than the melting point of these solders must be respected.

The splicing temperature of lap joints made from YBCO SP conductor must be lower than 250° C [148]. To safeguard against possible delamination of the tape structure, the AMSC conductor should not be exposed to 165° C for more than 3 minutes and to 155° C for more than 20 minutes [149]. For lap joints made from Bi-2223 SEI conductors the manufacturer recommends the use of Sn-Pb solder at temperatures below 200° C [150]. For Bi-2223 BHTS conductors no specifications have been given by the manufacturer for the splicing temperature, but for conservation of oxygen stoichiometry it should not be envisioned to exceed 250° C.

Solder material and chemical flux

The choice of a solder has to be made considering the splicing temperature, the electrical resistivity and the mechanical strength. For splicing at temperature lower than 240° C few solders can be selected: $Sn_{63}Pb_{37}$, $Sn_{96.5}Ag_{3.5}$, $In_{52}Sn_{48}$ and In_{100}. The properties of these solders are reported in table 3.3. The $Sn_{60}Pb_{40}$ and $Sn_{96.5}Ag_{3.5}$ solders, commonly used in many industrial splicing applications, have either low resistivity and high mechanical strength. If applicable, soldering with one of these two solders is preferred. If the splicing temperature is limited to below 180°C, the solder $In_{52}Sn_{48}$ is preferred to In_{100} since it has a much higher tensile strength value.

If the splicing process is performed in atmosphere, undesirable oxides may be created at conductor surfaces. Oxides are highly resistive and the use of flux limits their formation. The flux must be chosen with regards to the splicing temperature, the materials of tape face and the solder [151]. Too chemically aggressive fluxes must be avoided since they could reduce irreversibly the I_c of HTS conductors.

Table 3.3: Electrical and mechanical properties at 300 K of solders used for splicing HTS tapes.

	Melting temperature (° C)	Electrical conductivity (10^6 S/m)	Tensile strength (MPa)
$Sn_{96.5}Ag_{3.5}$	222	9.57	36.5
$Sn_{63}Pb_{37}$	183	6.67	51.7
In_{100}	157	1.39	1.9
$In_{52}Sn_{48}$	118	6.79	11.9

3.6.2 Resistivity of materials

Resistivity of soft solders at 77 K and 300 K

The resistivity of solders used to perform the splice between HTS conductors were measured at 77 K and in self-field. Since the conductors are in the form of tapes, solders in the form of foils are preferred. The tapes of solder are free of flux. The solder resistivity was measured on 450 mm long samples. A transport current was circulated in samples and the voltage drop along a 250 mm long central portion was recorded. The cross sectional area of samples was not modified by the presence of the instrumentation. The measured resistivity at 77 K and 300 K of the different solders is presented in table 3.4. At 77 K it is ranging between 14 and 100 $n\Omega.m$. The Sn-Ag alloy presents the lowest resistivity. A large deviation between the resistivity of Sn-Ag solder from two different manufacturers is observed, this is ascribed to a different alloy weight ratio. The Sn-In alloy has the highest resistivity at 77 K (100 $n\Omega.m$).

Table 3.4: Measured resisitivity of soft solder at 77 K and 300 K in self flux density.

Solder alloy	Supplier	Resistivity at 77 K ($n\Omega.m$)	Resistivity at 300 K ($n\Omega.m$)
Sn-Ag (96.5-3.5%)	Indium Corporation [152]	14	121
Sn-Ag (96.5-3.5%)	LucasMilhaupt [153]	23	119
Sn-Pb (63-37%)	Fransor industie [154]	49	141
Sn-In (48-52%)	Vitta [155]	100	183

Resistivity of conductor components at 77 K and in self field

As stated earlier, part of the splice resistance is arising from the conductor internal resistance. The resistivity of the different materials entering in the composition of the HTS conductors was measured at 77 K. The measurements are presented in table 3.5. For the YBCO conductors one should note the high resistivity of Hastelloy and NiW5% substrates, respectively 1029 $n\Omega.m$ and 258 $n\Omega.m$ [156]. The electroplated copper of YBCO SP was measured to be 2 $n\Omega.m$. This value is in agreement with the residual-resistivity ratio of 100 (at 4.2 K) reported by [157]. The laminations of Bi-2223 SEI and YBCO AMSC have been peeled off and measured to be respectively 7 $n\Omega.m$ and 24 $n\Omega.m$ at 77 K. These different values are in good agreements with reported data, as depicted in table 3.5. The resistivity of Ag and Ag-Mg (Bi-2223 SEI and Bi-2223 BHTS conductors) were not measured. The reported resistivity at 77 K are respectively 2 $n\Omega.m$ for Ag and 20 $n\Omega.m$ for Ag-Mg.

Table 3.5: Measured and reported resistivity at 77 K and 300 K of materials in HTS conductors.

Conductor	Material	Measured resistivity (this work)		Reported resistivity	
		77 K ($n\Omega.m$)	300 K($n\Omega.m$)	77 K ($n\Omega.m$)	Ref.
YBCO SP	electroplated copper	2	17	3	[157]
YBCO SP	Hastelloy	1029	1053	1100	[158]
YBCO AMSC	NiW5%	258	320	268	[156]
YBCO AMSC	Brass laminations	24	45	26	
Bi-2223 SEI	Cu alloy lamination	7	25	6	

Resistivity of materials at temperatures below 77 K

The temperature dependence of the resistivity of the different materials entering in the composition of HTS conductors is depicted in figure 3.30. The resistivity of Hastelloy and Brass is almost independent of temperature. Except from these two, resistivity of materials is strongly reduced by lowering the temperature. The electrical resistivity of soft solder used for HTS conductors splicing is also strongly reduces with temperature.

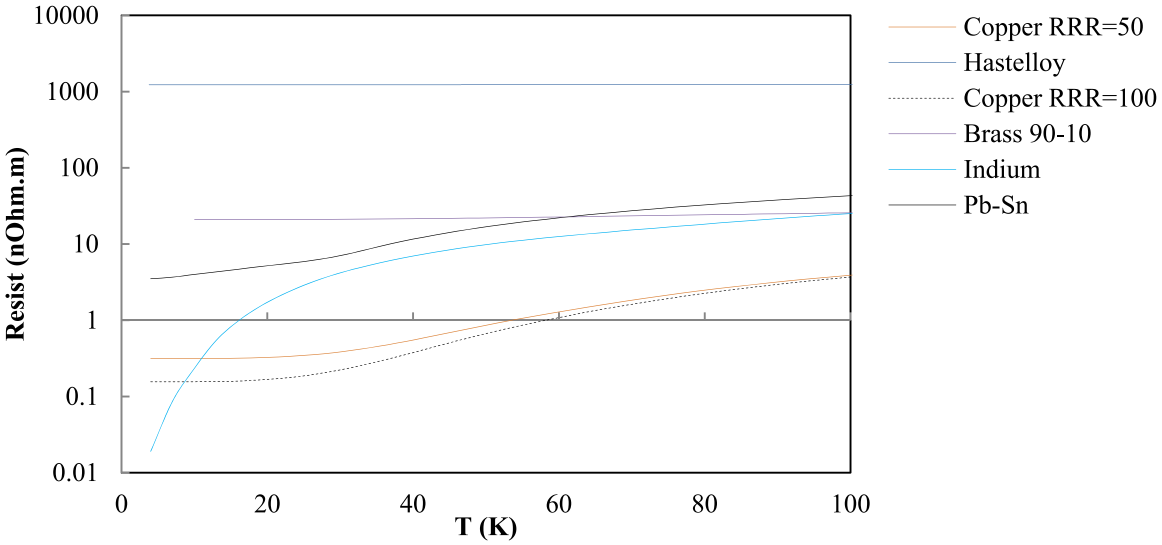

Figure 3.30: Resistivity of the materials entering the composition of HTS conductors as a function of temperature between 4 K and 77 K [159].

3.6.3 Electrical resistance of lap joint made of HTS conductors at 77 K and in self field

The electrical resistance of lap joint made of HTS conductors was measured at 77 K and in self field. This section reports on the experimental details and on the measurement results.

Lap joint preparation

The splice preparation influences strongly the achieved splice resistance. For the samples preparation, reasonable care was taken to ensure consistency during lap joint fabrication. Each conductor surface was first rubbed mechanically to remove oxide. Then surfaces were cleaned with ethyl alcohol, prior to soldering. Lap joints were prepared by using a fixture that consists of two aluminium blocks with a groove that matches exactly the width of conductors. A tape of solder was sandwiched between two fluxed conductors. The sample was heated to the desired soldering temperature via heaters, inserted in the aluminium blocks (two per block). Once the ribbon solder melted, a constant transverse pressure of about 10 MPa was applied via bolts and Belleville spring washers. The temperature plateau was held for 3 minutes and then the heaters were turned off. The sample was cooled down to room temperature by natural convection. The length of lap joints produced ranged from 7.5 mm to 43 mm. A summary of the different lap joints manufactured is reported in table 3.6. In figure 3.31, a cross-sectional micrograph of the different splices is depicted. The solder fills all the space in between the conductors: the solder layer is 5-15 μm thick. It should be noted than the cross sections of Bi-2223 SEI and Bi-2223 BHTS conductors are not rectangular: the tapes are thicker at mid-width compare to edges, resulting in larger thickness of solder layer at edges. This is due to the conductor manufacturing process (rolling).

Table 3.6: Details of the various HTS lap joints manufactured.

Conductor	Lap joint Type	Solder	D_0 (mm)	Number of Samples made
YBCO SP	FF	Sn-Ag	7.5-41	24
YBCO SP	FF	Sn-Pb	14-31	8
YBCO SP	FB	Sn-Ag	7.5-43	14
YBCO SP	FB	Sn-Pb	15-22	6
YBCO SP	BB	Sn-Ag	10.5-37	16
YBCO SP	BB	Sn-Pb	26-43	6
YBCO AMSC	FF	Sn-In	19-20	2
YBCO AMSC	FB	Sn-In	24-28	2
YBCO AMSC	BB	Sn-In	21-26	2
Bi-2223 SEI	-	Sn-Pb	20-25	2
Bi-2223 BHTS	-	Sn-Ag	19-27	2
Bi-2223 BHTS	-	Sn-Pb	20-41.5	18

Instrumentation and experimental protocol

To measure the electrical resistance of a lap joint, current is passed from one HTS conductor to the second one. A pair of voltage taps that span the entire lap joint is used to measure the electrical potential drop. Voltage taps are placed at locations 10 mm distant from the ends of lap joint to ensure a complete transfer of current into the superconducting filaments. The measurements are performed at 77 K and in self-field. A DC power supply (TDK-8 V 600 A [160]) and a precision digital multi-meter (DMM-PXI-1010 [161]) are used respectively for current source and voltage measurement. The samples are ramped at current ramp rates of 1 A/s and splice resistances are determined as the slope of voltage versus current.

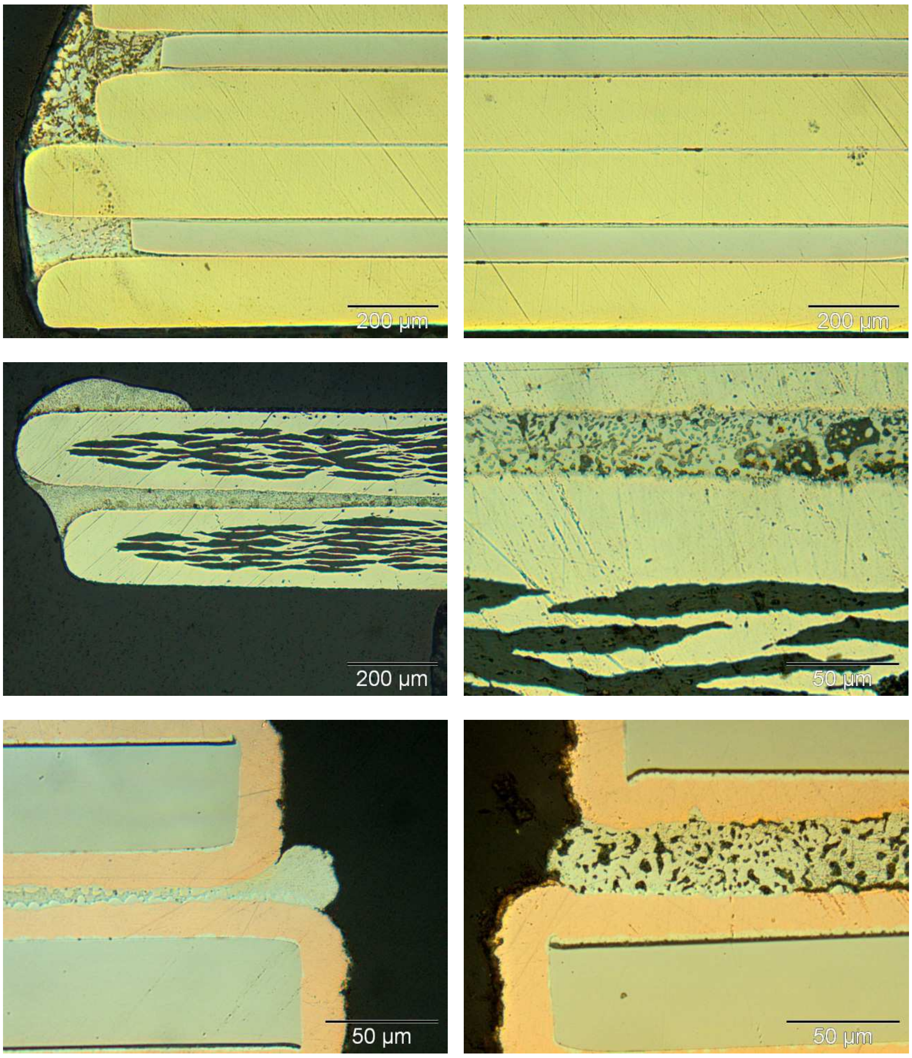

Figure 3.31: Cross section view of lap joints made from HTS conductors. From top to bottom : YBCO AMSC (top), Bi-2223 SEI (middle), YBCO SP with Sn-Ag (bottom left) and YBCO SP with Sn-Pb (bottom right).

Measurements

In a lap joint, the electrical resistance in the longitudinal direction is many orders of magnitude lower than that in the transverse direction: the transfer of current from one conductor to the other one is uniform along the splice. The lap joint resistance (R_s) that is inversely proportional to its length (D_0) is expressed as:

$$R_s = \frac{S_c}{wD_0} \tag{3.3}$$

Where w is the conductor width and S_c is the splice resistivity. S_c depends on conductor internal and interfacing resistance. For the different lap joints produced, the measured S_c values are depicted in figure 3.32. The mean and standard deviation of S_c are reported in table 3.7.

Table 3.7: Splice resistivity of the various lap joints manufactured.

Conductor	Lap joint Type	solder	S_c mean (nΩ.cm^2)	S_c StDev. (nΩ.cm^2)	S_c StDev. (%)	Nb. Samples (-)
YBCO SP	FF	Sn-Ag	33	5	15	24
YBCO SP	FF	Sn-Pb	63	22	35	8
YBCO SP	FB	Sn-Ag	884	111	13	14
YBCO SP	FB	Sn-Pb	851	55	6.5	6
YBCO SP	BB	Sn-Ag	1186	189	16	16
YBCO SP	BB	Sn-Pb	1283	119	9.3	6
YBCO AMSC	FF	Sn-In	159	3	1.8	2
YBCO AMSC	FB	Sn-In	2006	94	4.7	2
YBCO AMSC	BB	Sn-In	3402	52	1.5	2
Bi-2223 SEI	-	Sn-Pb	37	4	11	2
Bi-2223 BHTS	-	Sn-Ag	14	2	15	2
Bi-2223 BHTS	-	Sn-Pb	14	5	33	18

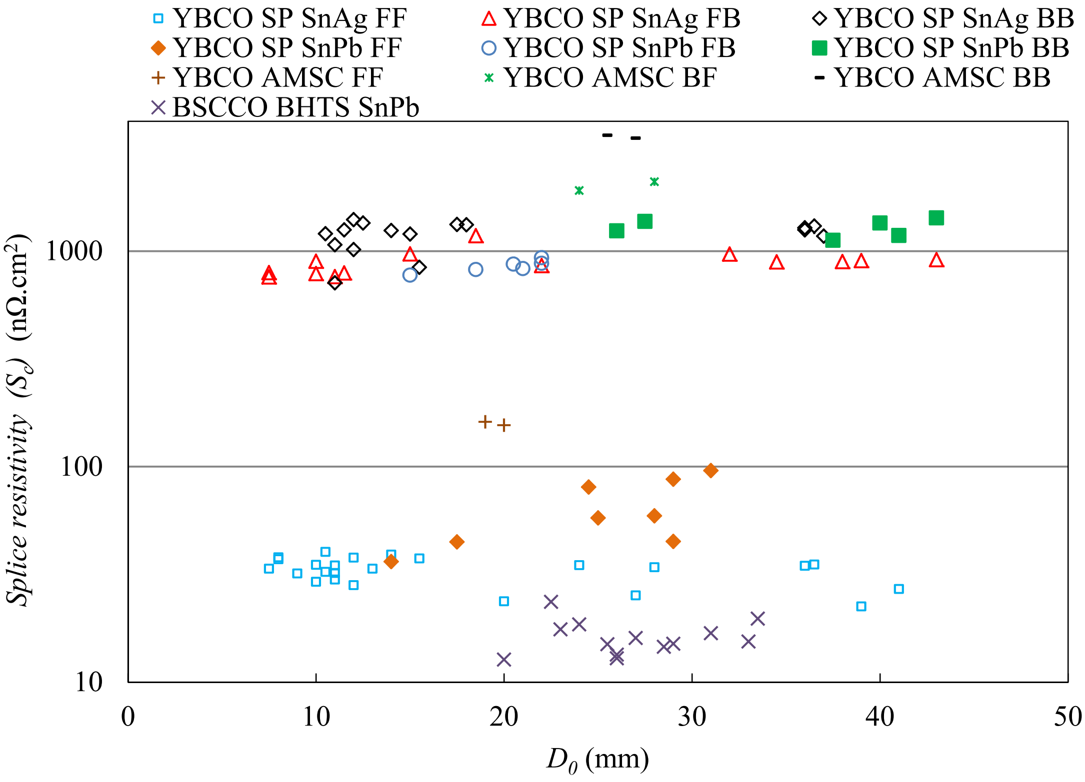

Figure 3.32: The S_c of lap joint made from YBCO SP, YBCO AMSC, Bi-2223 SEI and Bi-2223 BHTS conductors at 77 K and self field.

Lap joint resistivity of YBCO conductors

The splice resistivity of YBCO SP face to face (FF) lap joint made from Sn-Pb solder was measured to be 63 nΩ.cm^2 at 77 K in self flux density, slightly more than the 40-50 nΩ.cm^2 reported by the manufacturer [151]. The presence of voids induces a reduction of the cross section of the Sn-Pb solder, as seen in figure 3.31. By using Sn-Ag solder, no voids were observed and the S_c was reduced to 33 nΩ.cm^2.

High S_c values of YBCO SP lap joints were measured in respectively the back to face (BF) and back to back (BB) configurations: respectively 851 nΩ.cm^2 and 1283 nΩ.cm^2. In these configurations the use of Sn-Ag solder instead of Sn-Pb has no specific benefit on lap joint resistance, since its major contribution is the conductor internal resistances.

YBCO AMSC lap joint made with Sn-In solder presented S_c values of 159 nΩ.cm^2, 2006 nΩ.cm^2 and 3402 nΩ.cm^2 in respectively the FF, FB and BB configurations. The value in the FF configuration is similar to the 168 nΩ.cm^2 value reported by [143] and is 4.8 times higher than for YBCO SP splice made with Sn-Ag. This is attributed to both thicker and more resistive stabilizer strips.

Influence of conductor batch on the lap joint resistivity of YBCO SP conductors

For YBCO conductors the internal resistance of the conductor plays a major role in the splice resistance. A large variation of splice resistivity was reported for face to face lap joint made from YBCO SP conductors from different batches [157][5]. Over a study performed on four batches, the highest S_c value was measured to be 1000 nΩ.cm^2 whereas the lowest one was in accordance with the manufacturer data (50 nΩ.cm^2) [5]. This large variation was ascribed to be due to large differences in the interface resistance between the silver and YBCO layer from batch to batch.

Different current paths in the FF and BB YBCO lap joints

In YBCO lap joints, the S_c in the BF and BB configurations has been measured to be at least one order of magnitude higher than for the FF configuration. This large difference is easily explained by the presence of both highly resistive substrate and buffer layers in between the HTS films. In the FF configuration, from the HTS film the current has to cross only a thin silver shunt (2-3 μm) and then the stabilizer to exit the conductor (20 μm for YBCO SP conductor and 75 μm for YBCO AMSC conductor). In the BB configuration, there are two current paths. In the first one, named the substrate path, from the HTS film, current flows through the buffer layers, the substrate, the silver cap and finally the stabilizer. In YBCO tapes, the substrate does not extend over the full conductor width: at the tape edges, a low resistivity material is present (copper for YBCO SP conductor and Sn-Pb for YBCO AMSC conductor). The edges of the tape provide a second current path, around the substrate. Schematic views of the different current paths in the FF and BB configuration are depicted in figure 3.33. The direct current path is depicted with a red arrow, the substrate path with blue arrow and finally the around substrate path with green arrow. The around substrate path presents a lower cross section than the substrate path but with a much lower resistance, since the buffer layers and substrates of YBCO conductors are highly resistive [162][163].

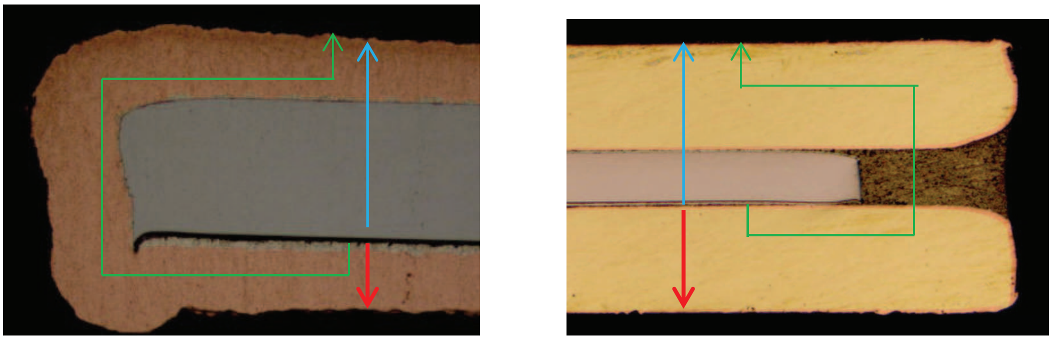

Figure 3.33: The current paths in YBCO conductor for the different joint configuration. YBCO SP (left) and YBCO AMSC (right). The direct current path is depicted with a red arrow, the substrate path with blue arrow and finally the around substrate path with green arrow.

Lap joint resistivity of Bi-2223 conductors

The Ag/Ag-Mg matrix of Bi-2223 conductors is low resistive and the area of interface between the matrix and the HTS filaments is large since the filament dimension is small. One can expect low S_c values of lap joints made from these conductors. The S_c of Bi-2223 BHTS lap joints (Sn-Ag and Sn-Pb), was measured to be as low as 14 nΩ.cm^2. This S_c value is half the one measured on YBCO lap joints in the FF configuration. The S_c of Bi-2223 SEI lap joints was measured to be 37 nΩ.cm^2, in accordance with the 40 nΩ.cm^2 reported by the manufacturer [150]. This higher S_c with comparison to the one of Bi-2223 BHTS lap joints is explained by the presence of resistive laminations in the Bi-2223 SEI conductor that have a contribution of 18 nΩ.cm^2 to the splice resistivity.

3.6.4 Lap joint resistance as a function of interfacing length at 77 K

Based on the mean values of S_c reported in table 3.7, the lap joint resistance as a function of splice interfacing distance (D_0) is computed in figure 3.34 for the different HTS tape conductors. To achieve a splice resistance lower than 20 nΩ, the minimum distance of overlapping is respectively 39 mm, 180 mm, 42 mm and 18 mm for YBCO SP, YBCO AMSC, Bi-2223 SEI and Bi-2223 BHTS conductors.

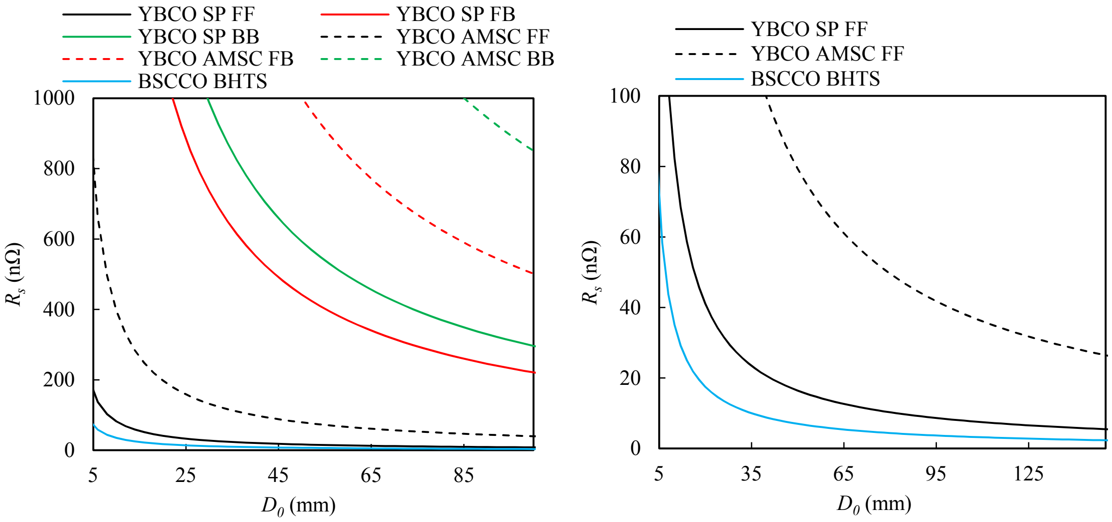

Figure 3.34: The lap joint resistance (R_s) as a function of interfacing length (D_0 see figure 3.28) for the different joint configuration (left). The lap joints resistance as a function of D_0 for Bi-2223 and YBCO conductors in the FF configuration (right).

3.6.5 Lap joint resistivity of YBCO SP conductors at 4 K under flux density

In magnets, joints will be operated at 4.2 K in the presence of background flux density. The flux density has a well-known influence on the resistivity of metals. This effect, named the magneto-resistance, leads to an increase of the resistivity with increasing flux density. In the design of splices, the effect of magneto resistance has to be taken into account. In this section the physical origin of magneto resistance is briefly introduced and then the reported splice resistivity of YBCO SP conductors at 4.2 K under flux density are reviewed.

Magneto resistance

Electrical magnetoresistance describes the fractional change in electrical resistance of metals or alloys in the presence of a magnetic flux density. It is typically positive for many metals, which corresponds to an increase in electrical resistance in the presence of increasing background magnetic flux densities [164].

The change of the electrical resistance in a magnetic flux density is due to the interaction of the magnetic flux density with the conduction electrons, which leads to a change in their scattering. The Lorentz force acting on the electrons causes their trajectories to bend around the magnetic lines of force between scattering events [165], thus creating a higher probability of scattering and, as a result, a higher electrical resistance. This effect is small when the electron mean free path is low but may dominate the resistance if the electron mean free path is large, as it is the case for many conductors at cryogenic temperatures.

Lap joint resistivity at 4.2 K under flux density

The resistivity at 4.2 K of FF YBCO SP lap joints in flux density of up to 18 T is depicted in figure 3.35 [157]. As expected, the splice resistivity increases with increasing flux density in both the perpendicular and the parallel orientation. Starting from a splice resistivity of 32 nΩ.cm^2 in self flux density, the splice resistivity is erratically increased up to 40-50 nΩ.cm^2 at 18 T. The resistivity of the lap joint was measured beforehand to be 58 nΩ.cm^2 at 77 K and in self-field. By lowering the temperature to 4.2 K, the splice resistivity was reduced by a factor 1.8. This reduction is consistent with the significant decrease of resistivity of copper, silver and Sn-Pb solder. The measurement of R_s at 77 K in self flux density is roughly representative of its value at 4 K and high flux densities.

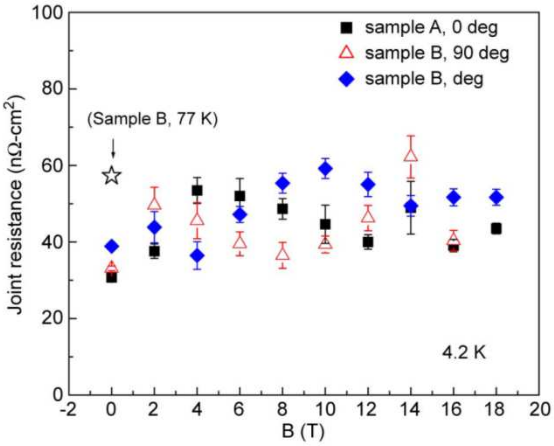

Figure 3.35: The resistivity of YBCO SP lap joints at 4.2 K as a function of magnetic flux density (plot form [157]).

3.6.6 Mechanical strength of lap joint

In magnet winding, HTS splice will encounter large stresses induced by electromagnetic forces. The dependence on axial mechanical stress of the YBCO SP lap joint electrical resistance was investigated by [151] at 77 K and in self field. The lap joints (Sn-Pb) made in the FF configuration were 25.4 mm long. The normalized splice resistance and the conductor I_c were measured as a function of uni axial stress (see figure 3.36). Both I_c and R_s of YBCO SP lap joints were found to be quasi independent of axial stress up to 650 MPa where the I_c starts to reduce. This stress corresponds to the yield stress of single conductor: the effective mechanical strength of the YBCO lap joints is determined by the strength of the superconductor, not the lap joint itself.

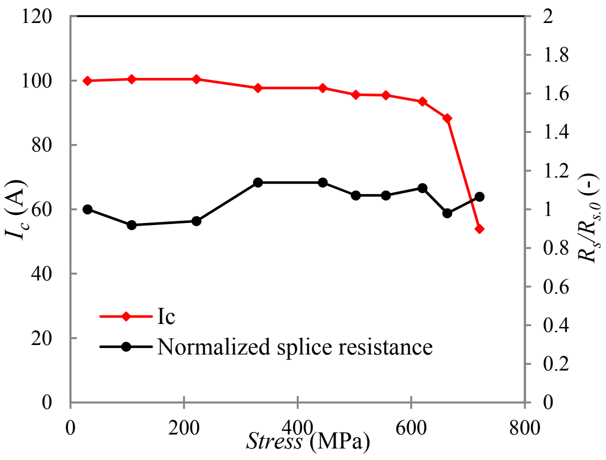

Figure 3.36: The electromechanical properties of YBCO SP lap joint (Sn-Pb) in the FF configuration at 77 K and in self flux density (right). The I_c and R_s of the lap joint are reported as a function of the mechanical stress (data from [151]) (right).

3.7 Axial strain and transverse stress dependence of the I_c of HTS conductors

The development of high flux density superconducting magnets requires not only a conductor that is capable of carrying sufficient critical current density (J_c) at high magnetic flux density, but also one that is sufficiently robust mechanically in order to withstand the very large Lorentz forces associated with high magnetic flux density generation and the transient local forces generated by thermal stresses following a quench. The I_c of HTS conductors have been reported to be reduced in the presence of uni-axial strain, torsion and transverse strain. In this section, the I_c sensitivity of HTS conductors to strain is reviewed.

3.7.1 Uni-axial strain dependence of I_c

The I_c dependence of YBCO/Bi-2223 tapes and Bi-2212 wires on uni-axial strain has been widely reported in tensile and compressive regime [166][167][168][109][169][170]. The performances of such conductors are reversibly modified by increasing the uni-axial strain up to a threshold strain limit named irreversible strain (ϵ_{irr}). Above ϵ_{irr} an abrupt and irreversible drop of I_c is generally observed. The reversible strain dependency is ascribed to the intrinsic dependence of ceramics grains and grains boundary to strain [171]. The variation in distance between the apical oxygen and the CuO_2 planes with strain and the change in tetragonality with pressure are likely causes of the change in T_c [172][173][174]. Cuprates Bi-2223, Bi-2212 and YBCO have very weak mechanical properties. The mechanical behaviour of coated conductors is governed by the stronger substrate/matrix materials [124]. The irreversible I_c degradation, occurring beyond ϵ_{irr} is ascribed to the yielding of the matrix materials inducing fracture in the ceramic current paths. The irreversible tensile strain of Bi-2223 and Bi-2212 conductors is relatively low, typically 0.3-0.4%. The weak electromechanical behaviour of the Ag/Ag-Mg matrix of BSCCO conductors remains one of the key limits to their implementation in high flux density applications.

YBCO conductors

A reversible change in the J_c of YBCO conductors with axial strain was observed in 2003 [166]. The decrease of J_c was limited in magnitude to about 5% at 0.47-0.62% of tensile strain. This observation was ascribed to an improved grain-to-grain alignment in superconducting films when deposited on a metal substrate with ceramic buffer layers. A possible reversible strain effect in the limited elastic strain regime of early materials was most likely masked by the multiplicity of current paths that results from the granularity of the materials and their rather poor grain alignment. The reversible strain effect on I_c was clearly linked to the uniaxial pressure dependence of T_c in single crystals of YBCO [172]. The change in T_c with pressure oriented along the a-axis and the b-axis of crystals is respectively $\frac{dT_c}{d\varepsilon_a} = 230\ K$ and $\frac{dT_c}{d\varepsilon_b} = -220\ K$. The change along the c-axis is less pronounced: $\frac{dT_c}{d\varepsilon_c} = 18\ K$.

Axial strain dependence of I_c in self field

The I_c strain dependency of YBCO SP and YBCO AMSC in self field have been reported at 76 K [167]. In the reversible strain regime, the strain dependence of I_c has a parabolic shape with maximum close to null strain. If compared with YBCO SP (IBAD) conductors, the I_c of YBCO AMSC (RABiTS) conductor is more sensitive to strain. The strain sensitivity of coated conductors manufactured by IBAD on 100 μm thick Hastelloy substrate was investigated by [175] at temperatures ranging from 40 K to 80 K. The measurements are reported in figure 3.37. The strain sensitivity of the tape is observed to be stronger for temperatures closer to T_c. In addition the strain at which the maximum of I_c occurs was observed to be temperature dependent: it reduces when the temperature is lowered.

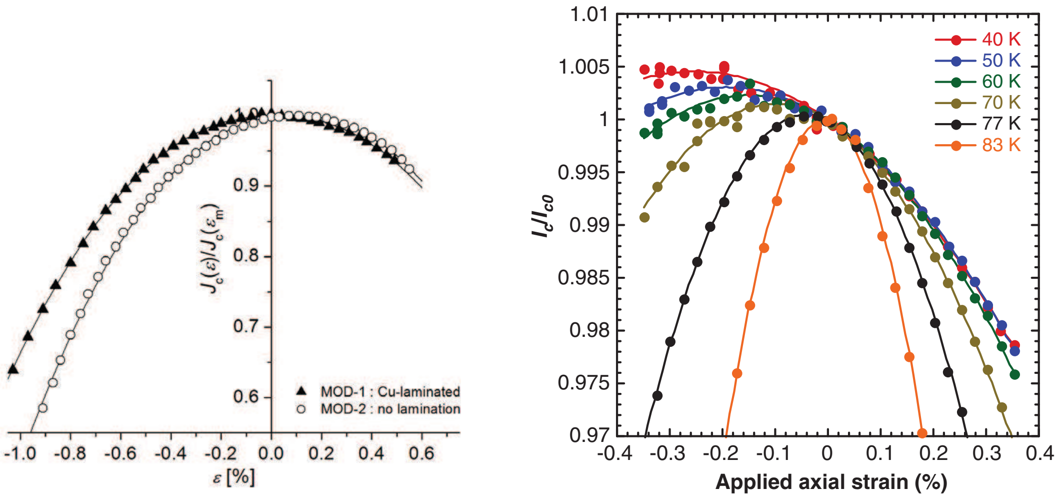

Figure 3.37: Dependence of the superconducting current density on applied axial strain in a copper laminated MOD-RABiTS sample at 76 K [167] (left). The temperature I_c strain dependency of a IBAD YBCO sample between 40 K and 83 K [175] (right).

Axial strain dependence of I_c in external flux density

In the presence of external flux density, the strain dependence of I_c in coated conductor depends on the REBCO layer composition, as illustrated in figures 3.38-39. In weak perpendicular flux densities, the I_c in (Y-Sm)BaCuO [108] conductors presents two peaks at strain of about -0.35% and 0.45%. The relative magnitude of peaks increases with flux density up to 0.25 T where a maximum is reached. As the flux density increases above 0.25 T, the magnitude of the peaks decreases. At a flux density of about 3 T the peaks are no more present. The strain dependence of I_c get stronger as the flux density increases. This suggests that different pinning mechanism are present in coated conductor. In GdBaCuO conductors at 76 K, the two peaks of I_c are not observed (see figure 3.39): pining mechanisms are composition dependent.

In parallel flux density, GdBaCuO and (Y-Sm)BaCuO samples didn't present the two peaks of I_c. The strain dependence of I_c follow a parabolic law. A reduced strain sensitivity of the I_c of YBCO conductors was measured recently at 4 K and in flux density of 14 T [176].The striking reduction in the sensitivity to strain of YBCO conductors at this temperature and flux density is due to the fact that the material is very far away from the critical surface [47].This reduced strain sensitivity of YBCO conductors at 4 K over large axial strain range holds significant promise for their application in high-field magnets.

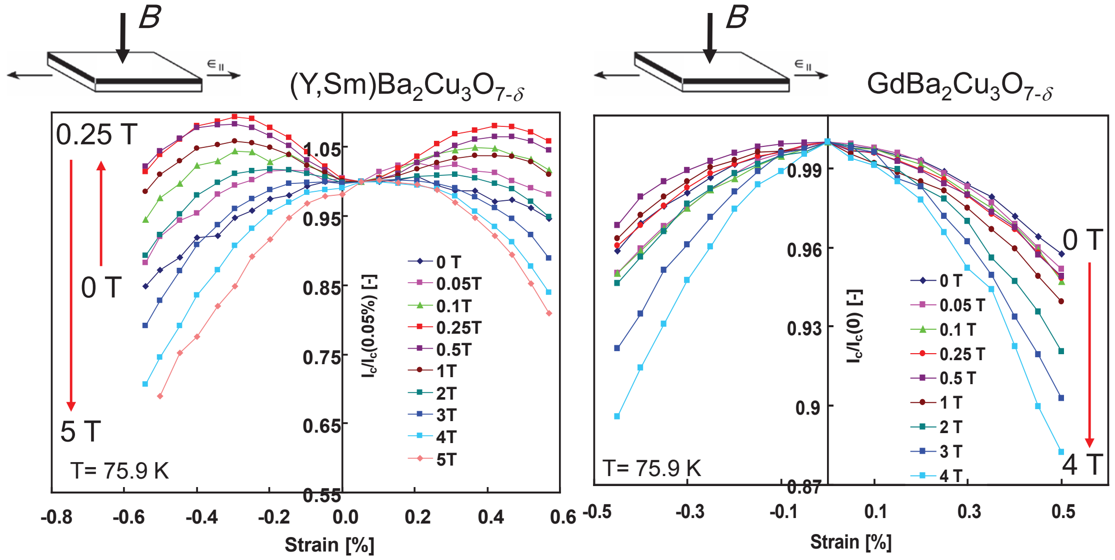

Figure 3.38: The I_c strain sensitivity of (Y-Sm)BaCuO (left) and GdBaCuO (right) conductors produced by SuperPower in perpendicular flux density at 75.9 K. The (Y-Sm)BaCuO sample shows a double peak shape, not the GdBaCuO sample [177].

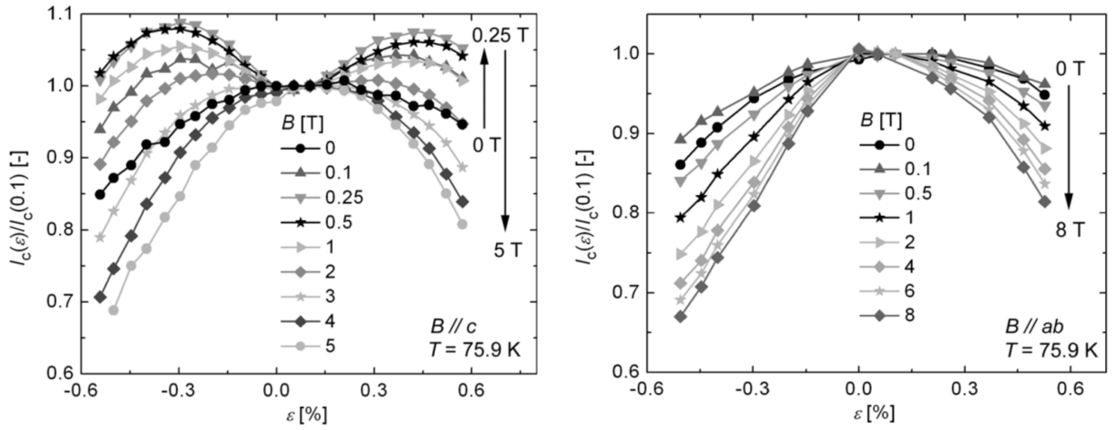

Figure 3.39: The I_c anisotropy of (Y-Sm)BaCuO conductor at 75.9 K under perpendicular (left) and parallel (right) flux density orientation [108].

Axial strain orientation dependence of I_c

The deposition of YBCO film by the MOCVD route results in a twinned superconducting film that is oriented with the [100] and [010] directions along the tape axis. An anisotropic in-plane reversible strain effect on the I_c in IBAD-MOCVD (Y-Gd)BCO coated conductors was discovered by [178]. The maximum strain sensitivity of the I_c occurs when the applied strain is aligned with the [100] and [010] directions of the superconducting film. The I_c becomes almost insensitive to strain when the strain is aligned with the [110] direction. This effect has been directly correlated to the uniaxial pressure dependence of the critical temperature.

Bi-2223 tapes and Bi-2212 wires

A reversible reduction of I_c with strain in Bi-2212 wires and Bi-2212 conductors was observed recently [169][170][109]. Between -0.08% and 0.38%, Bi-2223 SEI conductors exhibited a linear and reversible decrease of I_c with strain at 65 K and 76 K [169]. The slope of the decrease has been observed to be steeper for temperature closer to T_c. At 4.2 K the strain sensitivity of Bi-2223 SEI conductors was measured by [109] (reported in figure 3.40). Authors correlate the reversible effect of strain on the performance of Bi-2223 tapes with the dependence of critical temperature on pressure.

For Bi-2212 OST conductor at 4.3 K, a reversible strain effect on I_c in the tensile regime has been observed [170]. In tension, up to 0.3% strain, a decrease of about $\frac{dI_c}{d\varepsilon} = -2.7\%$ per percent strain was reported in flux density of 16 T. A linear increase in T_c with pressure has been measured in Bi-2212 crystals, when uniaxial strain is applied along the a or b axis [179]. The intrinsic reversible strain effect on I_c did not appear under axial compressive strain (except after strain cycling). A two-component model was proposed that suggests the presence of mechanically weak and strong Bi-2212 components within the filaments. The model identifies the weak component to be the fibrous network of Bi-2212 grain colonies that generally run in the middle section of a filament, and the strong component to be the dense grain colonies adjacent to the Ag matrix. In figure 3.39, an illustration of dependence of I_c on axial compressive and tensile strains in Bi-2212 conductor according to the modified descriptive strain model is depicted.

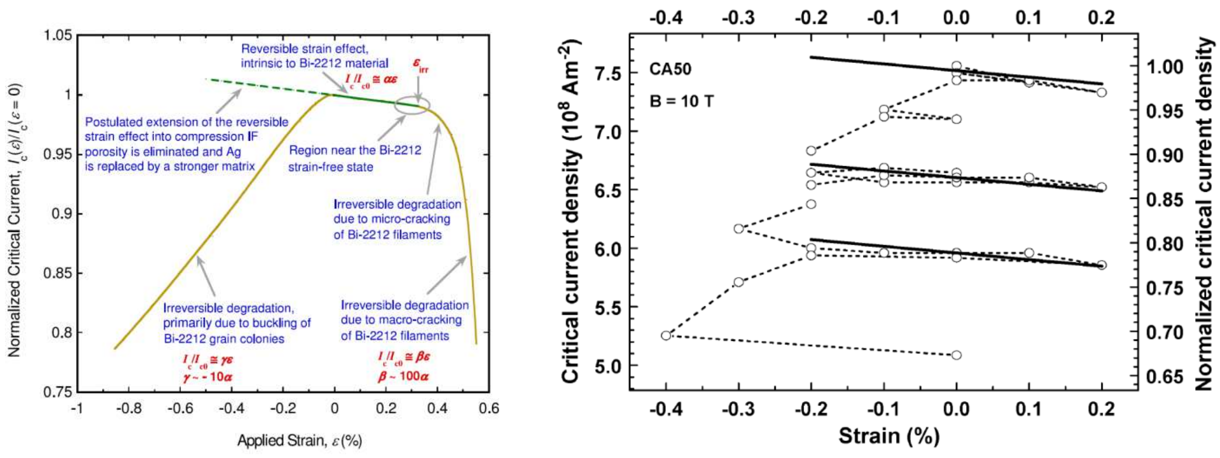

Figure 3.40: Illustration of the dependence of I_c on axial strain in Bi-2212 conductor according to the modified descriptive strain model [170] (left). Critical current density as a function of strain for Bi-2223 SEI tape at 4.2 K and perpendicular flux density of 10 T [109] (right).

3.7.2 Transverse stress dependence of the I_c of HTS conductors

In magnet applications, the Lorentz force and the pre-stress applied to the winding pack produce a hoop stress that induces axial tensile strain and transverse compressive stress in the conductors. The sensitivity to transverse stress of HTS conductors has to be known since it is a key design factor of high flux density magnets.

YBCO tapes

The measurement at 76 K of IBAD and RABiTS coated conductors under transverse compressive strain was reported by [180][13]. Small I_c reduction of about 1-2% was observed when the stress was increased up to 150 MPa in RABiTS samples [13][180]. The IBAD conductors stressed up to 100 MPa have shown the same order of I_c reduction [180].

The effect of fatigue cycling was investigated on IBAD and RABiTS conductors [180]: the coated samples were submitted to a fatigue test of 20 000 cycles. The load was cycled between the maximum stress (100-150 MPa) and near zero at a frequency of 1 Hz. The effect of fatigue cycling on IBAD conductor is depicted in figure 3.41: no I_c reduction was observed either in IBAD and RABiTS samples.

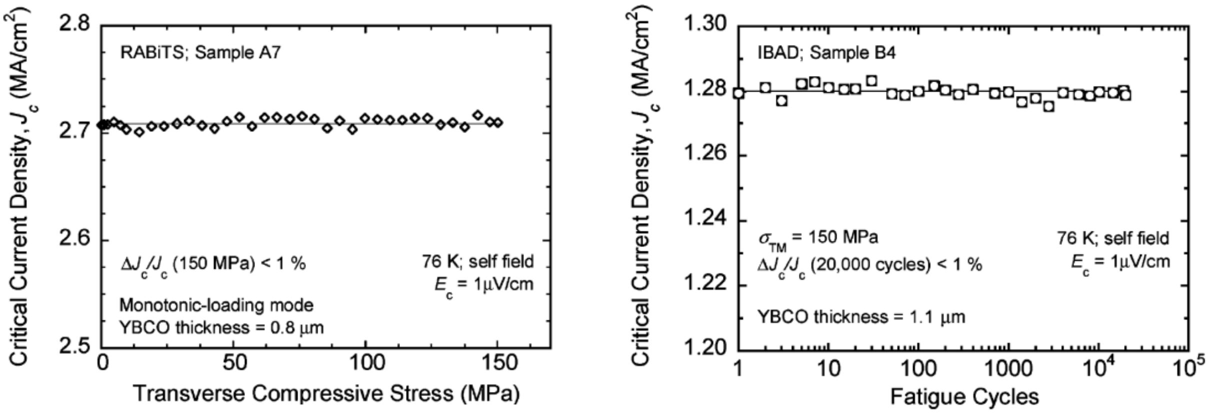

Figure 3.41: Dependence of I_c on transverse compressive stress of up to 150 MPa in YBCO RABiTS conductors [180](left). Dependence of I_c on cycled transverse compressive stress in YBCO IBAD [180](right).

Bi-2223 tapes

The transverse compressive stress dependence of I_c in Ag alloy sheathed Bi-2223 tapes has been studied at 77 K [14]. Three samples with different thickness were submitted to compressive stress of up to 150 MPa. A 5% I_c degradation was observed at stress of respectively 109 MPa and 70 MPa in the thickest and thinnest samples. The thinner silver sheath provides a lower protection for the superconductive core compared to the thick tape. The sausaging phenomena are more likely at the interface of the Ag/superconducting core in the thinner tape.

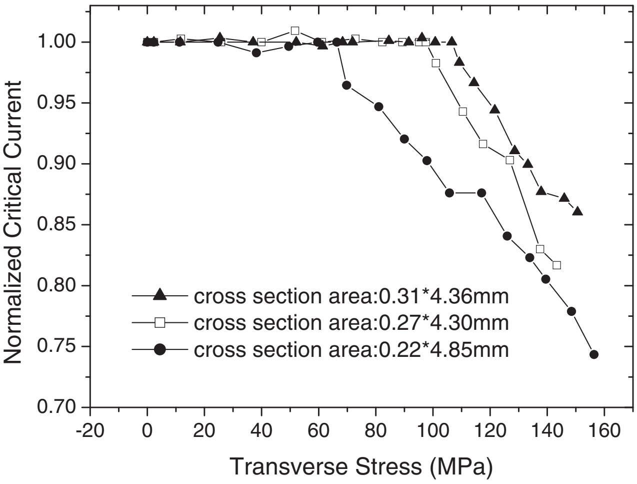

Figure 3.42: Dependence of I_c on transverse compressive stress of up to 150 MPa in Bi-2223 tapes of different thickness [14].

3.8 I_c dependence on twist pitch and bending radius

During the winding of magnet, HTS conductors are subjected to torsion, bending, tension or even a combination of them. A good understanding of the behaviour of HTS tapes under these mechanical solicitations is of key importance for the definition of the allowable bend and twist during cabling activity.

3.8.1 I_c dependence on out of plane bending radius

During the winding of accelerator magnet, the bending radius of HTS conductor could be severe, especially in the magnet heads. The allowable minimum bending radius of YBCO conductor is mainly given by the distance of the HTS film from the neutral axis. The I_c reduction with bending radius of YBCO SP conductors 95 μm thick was investigated at 77 K and 4 K [181]. Given the asymmetry in the cross section of YBCO tape, tests were run both with YBCO film under tension and compression.

When the YBCO film is under tension, critical current reduction is significant at both 77 K and 4 K for radius lower than 12 mm. A 95% retention of original I_c is observed at a radius of 10 mm. When the YBCO film is in compression, the I_c of conductor is not affected down to a bending radius of 4 mm.

The reduction with bending radius of the I_c of Bi-2223 BHTS conductors start to be significant at radius lower than 30 mm as reported in figure 3.43.

3.8.2 I_c dependence on twist pitch

YBCO and Bi-2223 conductors are both available in the form of tape with large aspect ratios, typically 10 to 200. In some applications, they are subjected to torsion. This is the case of the twisted-pair cables [182], which are being developed for application to electrical transfer lines in the LHC machine. Prototype twisted-pair cables with twist pitch of 400 mm were characterized at cryogenic temperatures, in background flux densities of up to 9.6 T, and showed good performances [183][184]. The behaviour of HTS tapes under torsion is of key importance for the definition of the allowable twist during cabling activity. The strain sensitivity of these materials used in the react and wind route can induce large I_c reduction, and the management of the associated reductions depends on the comprehension of the phenomenon. Several measurements have been reported on the reduction of I_c with twist pitch of HTS tapes [185][186][187][188]. The twist pitch influence on the I_c of YBCO SP, YBCO AMSC and Bi-2223 SEI conductors has been investigated at CERN at 77 K with a purpose-built set-up. In chapter 4 a model

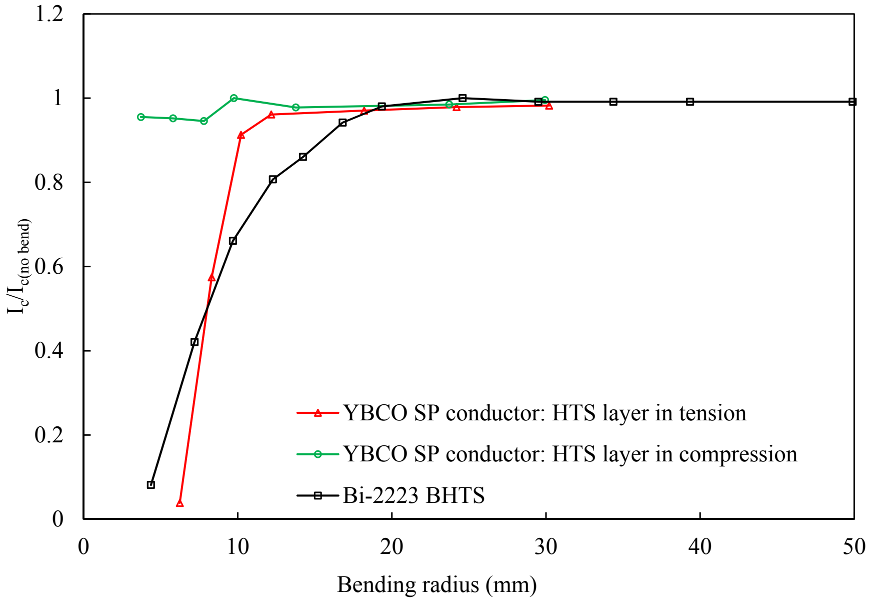

Figure 3.43: The I_c reduction with out of plane bending radius of YBCO SP conductor [181] and Bi-2223 BHTS conductor [127] at 77 K.

of YBCO conductors reduction of I_c with twist pitch is introduced. The experimental details and the measurements are reported in this chapter.

Experimental details

Measurements of the I_c reduction induced by torsion in YBCO and Bi-2223 tapes were carried out at CERN with a purpose built set-up. The HTS samples were clamped in rotating copper chucks 260 mm distant. A picture of the set-up is shown in figure 3.44. At one end of the tape, all degrees of freedom were blocked, whereas at the other end the rotational and longitudinal translation degrees of freedom were released. The tape was twisted by applying the desired angle of twist at room temperature. Motivation for applying the twist at room temperature is to reproduce the process of cabling [183]. Two voltage taps were soldered on the HTS tape at 240 mm distance. The presence of the voltage taps did not perturb locally the twist of the samples. The I_c was measured according to the electric flux density criterion of 1 μV/cm. The I_c at 77 K and in self-field of the sample was first measured before loading (I_{c0}). The sample was then twisted applying progressively decreasing twist pitches, and each time the I_c was measured at 77 K. The I_c values obtained after loading were normalized to I_{c0}. The measurements are reported in figure 3.45. The data acquisition system and power supply used were the same as those used for the measurements of lap joint resistance.

The irreversible twist pitch (Tp_i)

In self-flux density, the I_c dependence on axial strain of YBCO and Bi-2223 tapes has a reversible behaviour up to a maximum strain value (ε_{irr}). Above ε_{irr} the current percolation path is modified, and an irreversible drop of I_c is observed. The irreversible twist pitch (Tp_i) of HTS tape conductor is defined as the twist pitch at which the tensile strain at tape edge reaches ε_{irr} (see chapter 4). For pitch longer than Tp_i no irreversible degradation of I_c is observed. For smaller pitches irreversible degradation of J_c are observed at tape edges.

Figure 3.44: The mock up used to apply twist pitch on HTS conductor: an artist view (top) and a Bi-2223 SEI sample with a twist pitch of 45 mm (bottom).

Measurements

From the measurements reported in figure 3.45, we can derive that the twist pitch corresponding to a 95% I_{c0} retention is 114 mm for Bi-2223 SEI and 80-90 mm for YBCO SP and YBCO AMSC conductors. These values match the irreversible twist pitch of the conductors. The reduction of I_c for shorter twist pitches is pronounced: the twist pitch corresponding to a 70% I_{c0} retention is 60 mm for Bi-2223 SEI, 65 mm for YBCO SP and 57 mm for YBCO AMSC conductors. Application of a uniform twist in a YBCO SP conductor is difficult because of the high aspect ratio of the conductor cross section. During twisting, the conductor tends to form a network of bands with large torsion, oriented at 45 degrees from the longitudinal direction of the tapes. To ensure uniform twist, the coated conductor was twisted together with a 0.2 mm thick copper strip. This is representative of the cabling process in the twisted-pair YBCO cables [183]. For all conductors most of the reduction of I_c occurs at pitches lower than Tp_i. The major part of the I_c reduction with pitch arises from the irreversible reduction of I_c with strain (see chapter 4).

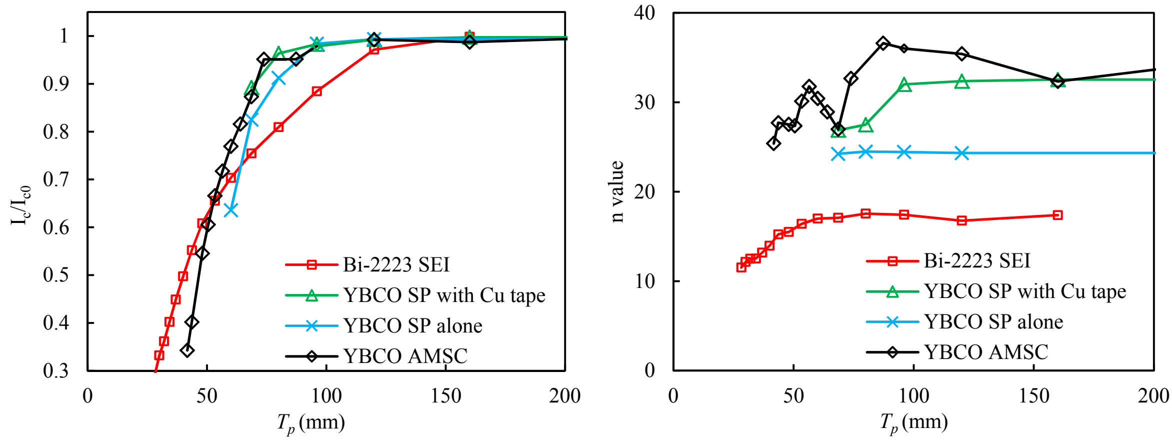

Figure 3.45: The measured normalized I_c dependence (left) and the n value (right) as a function of the twist pitch for YBCO SP, YBCO AMSC and Bi-2223 SEI conductors at 77 K and in self flux density.

3.9 Choice of HTS conductor for high flux density magnet

The development of high flux density superconducting magnets requires not only a conductor that is capable of carrying sufficient engineering critical current density (J_{ce}) at high magnetic flux density, but also one that is sufficiently robust mechanically to withstand the very large Lorentz forces associated with high magnetic flux density generation. The J_{ce} of the different YBCO and Bi-2223 and Bi-2212 conductors under perpendicular and parallel flux density are reported in figure 3.46 and compared with the winding current density threshold (J_{wt}) of 200 A/mm^2 (see chapter 2).

The J_{ce} of YBCO SP conductor at 4.2 K and 20 T is in excess of the 200 A/mm^2 threshold in either the parallel and perpendicular flux density orientation. The J_{ce} of others HTS tape conductors studied are below this threshold. The generation of high flux density (20 T) with dipole made from the Bi-2223 SEI, YBCO AMSC or Bi-2223 BHTS conductors is possible at the expanse of thick coils.

The YBCO SP conductor exhibits good mechanical properties with a Young's modulus of 175 GPa and a yield strength of about 630 MPa. YBCO SP conductors are resilient to transverse stresses exceeding 150 MPa and present minimum bending radius as small as 6 mm.

The J_{ce} of Bi-2212 conductor is isotropic, in excess of 200 A/mm^2 at 20 T and has recently been increased by a factor 2-5 in J_{ce} in over pressure processed samples. The round shape of this conductor facilitate its application in Rutherford cable. The weak electromechanical behaviour of the Ag/Ag-Mg matrix of Bi-2212 conductors remains one of the key limits to their implementation in high flux density applications. Impregnation of coils and magnetic optimisation may reduce the stress encountered by the conductor. The irreversible tensile strain of Bi-22212 OST wire is about 0.38 %.

In view of their electromechanical performances, both YBCO SP and Bi-2212 OST conductors are promising candidates for application in high flux density accelerator magnets.

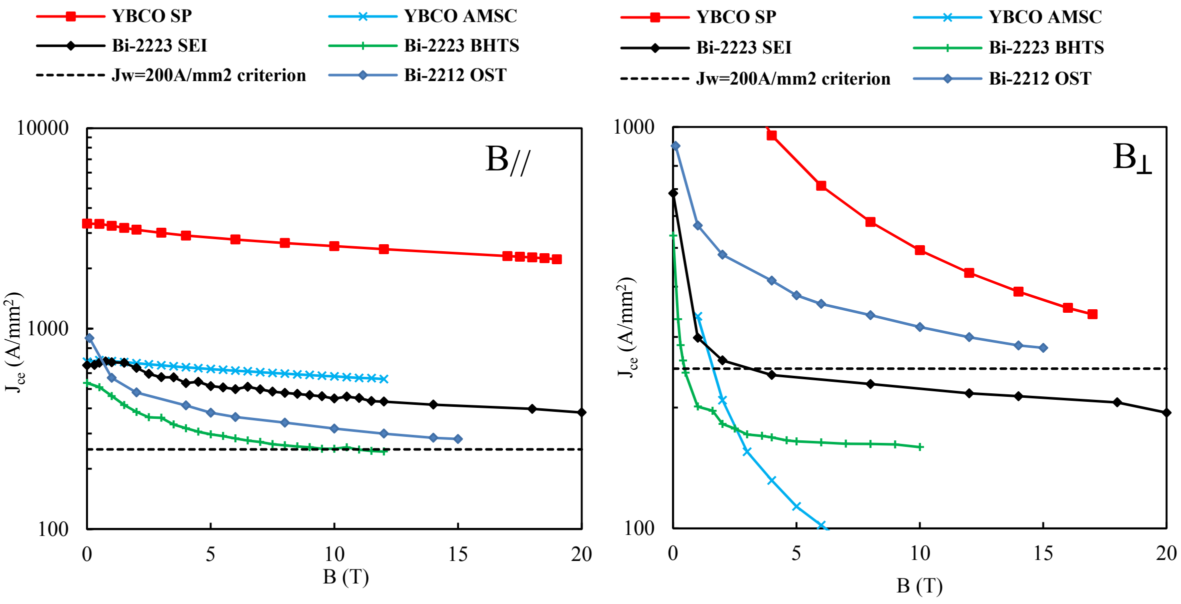

Figure 3.46: The J_{ce} of YBCO, Bi-2223 and Bi-2212 conductors in parallel (left) and perpendicular (right) flux density. The winding current density threshold J_{wt} =200 A/mm^2 is shown as a dotted line.

3.10 Conclusion

In this chapter, the electromechanical properties of HTS conductors are reviewed. The manufacturing processes and the main characteristics of HTS conductor candidates for application to high flux density magnets are introduced. The results of the I_c measurements of YBCO SP, YBCO AMSC, Bi-2223 SEI and Bi-2223 BHTS conductors at 4.2 K in flux densities of up to 12 T are presented.

The J_{ce} of YBCO SP conductor at 4.2 K and 17 T is in excess of 2300 A/mm^2 and 300 A/mm^2 in respectively the parallel and perpendicular orientation. This conductor exhibits good mechanical properties with a Young's modulus of 175 GPa and a yield strength of about 630 MPa. The I_c dependence of HTS conductors on axial strain and transverse stress has been reviewed in this chapter. The YBCO SP conductor that presents an irreversible axial tensile strain of 0.6% is insensitive to transverse stresses of up to 150 MPa and hold its high performances at bending radius as small as 6 mm. The minimum bending radius of the other HTS tape conductors is in the range 25-30 mm. The minimum allowable twist pitch of HTS tape conductors is determined in this chapter: 85 mm for 4 mm wide YBCO SP conductor and 114 mm for Bi-2223 tapes.

Accelerator magnets will requires splices between HTS conductors. The basic properties that ensure the reliability of an HTS splice are its electrical resistance and mechanical strength.

Splice resistivity of YBCO and Bi-2223 conductors was measured at 77 K and in self flux density. In the case of direct facing of YBCO films a splice resistivity of 33 nΩ.cm^2 was achieved with YBCO SP conductors. With BSCCO conductors, splice resistivities of 14-37 nΩ.cm^2 were measured. A splice resistance lower than 20 nΩ, is achieved for a YBCO SP lap joint with interfacing length longer than 39 mm (FF configuration).

The engineering critical current density of the different HTS conductors studied are compared with a reference winding current density of 200 A/mm^2, value considered in the previous chapter as the limit for the cross section of accelerator magnets. Only the YBCO SP and Bi-2212 OST conductors show performances above this threshold for flux densities of up to 20 T. These two conductors are therefore promising candidates for application in high flux density accelerators magnets.

Chapter 4

YBCO cable in high flux density dipole : operational margins and allowable mechanical deformation

The J_c measurement performed on HTS samples are limited in number and do not extend over the various conditions encountered in magnet windings. The optimal use of HTS conductors requires practical expressions describing the J_c dependence on flux density strength, flux density orientation, temperature and strain. Such expressions should allow accurate interpolations, extrapolations and scalings of conductor performance. In this chapter, a $J_c(B,T)$ parameterization is provided for YBCO SP, YBCO AMSC and BSCCO OST conductors. The J_c anisotropy of YBCO conductors is parameterized and the impact of this anisotropy on accelerator magnet design is illustrated with the calculation of the operational margins of a YBCO dipole. The design of a YBCO coil has to consider the electromechanical limitations of the conductor. Analytic models of the I_c dependence of YBCO tape on bending and twisting is introduced and used to derive the minimum bending radius and twisting pitch that the conductor can withstand.

4.1 Parameterization of the J_c dependence on temperature and flux density in parallel and perpendicular flux density

Accurate $J_c(B,T)$ parameterization is required to enable an efficient use of HTS materials in high flux density magnets. In annex 1 an extensive review of the most significant J_c parameterizations for HTS conductors is performed. The most appropriate fit for recent HTS materials has been selected and a self-consistent formula of J_c dependence on temperature and flux density elaborated. This is expressed as:

$$J_c(B,T) = \frac{C_0\left((1-t^{m_1})^{m_2}\right)^{n_1}}{B}\left(\frac{B}{B_{irr}}\right)^p\left(1-\frac{B}{B_{irr}}\right)^q \tag{4.1}$$

with

$$B_{irr}(T) = B_{irr,0}(1-t^{m_1})^{m_2} \tag{4.2}$$

where $t = T/T_{cf}$ is the reduced temperature with T_{cf} the critical temperature and B_{irr} is the irreversible flux density. $B_{irr,0}$ is the irreversible flux density at zero degree and external flux density. The $J_c(B,T)$ parameter values need to be optimized in regards of data set. A method which uses a step-by-step approach instead of globally solving all parameters simultaneously is used. The details of a similar routine applied to LTS materials was reported by [189]. The criterion used to optimize J_c parameterization will infer the final result [190]:

- The optimization based on absolute value of J_c percentage error minimization preferentially fits those data at high flux density and temperature. This may not be suitable for a single pinning mechanism parameterization.
- The optimization based on J_c root-mean-squared preferentially fits those data at low flux density and low temperature. This may not be suitable for a single pinning mechanism parameterization.
- A pinning force density (F_p) can be defined as the critical value of the Lorentz force per unit volume $F_p = J_c\ B$. The optimization based on F_p root-mean-squared preferentially fits favour the data close to $F_{p,max}$ (maximum of pinning force) regardless of the temperature. This method is preferred in the determination of p and q, since the exponents describe the pinning force curve.

The optimization based on F_p root-mean-squared is choose here since we are interested in an accurate description over a large range of temperatures. Based on the J_c data sets from [5][112][36][36][34], J_c parameterization for YBCO SP, YBCO AMSC and Bi-2212 OST conductors in parallel and perpendicular flux densities are provided according to expressions (4.1) and (4.2). The parameters values are reported in table 4.1. The J_c fits provide good accuracy with respect to reported measurements over the full temperature and flux density range of data sets. A small deviation is observed at low flux density. The self flux density has a strong reducing effect on the J_c of HTS materials. A self-flux density correction that takes into account the flux density anisotropy of the material and the experimental details should ideally be applied. This was not done here since the experimental details required to perform such correction have not been reported. Nevertheless, the validity of the fit proposed is demonstrated over the different materials for both perpendicular and parallel flux density orientations.

The parameters values reported in table 4.1 are based on the performance of YBCO and Bi-2212 conductors produced between 2008 and 2010. The performance of HTS conductors is increasing year by year. The parameters values presented in table 4.1 will become obsolete and a simple actualisation with regard to contemporary measurements will be required.

Table 4.1: Parameter values to be used in the J_c(B,T) parameterization (eq. (4.1)(4.2)) of YBCO SP, YBCO AMSC and Bi-2212 OST conductors.

Conductor	YBCO SP		YBCO AMSC		Bi2212 OST
Data set	[5]	[112]	[36]	[36]	[34]
Flux density orientation	parallel	perp	parallel	perp	-
p(-)	0.63	0.9	0.9	0.35	0.8
q(-)	1.72	3.01	2.5	1.8	1.6
T_{cf}(K)	88	89	92	92	92
m_1(-)	2.06	2.27	2.2	1.2	1.32
m_2(-)	1	1	0.4	1	1

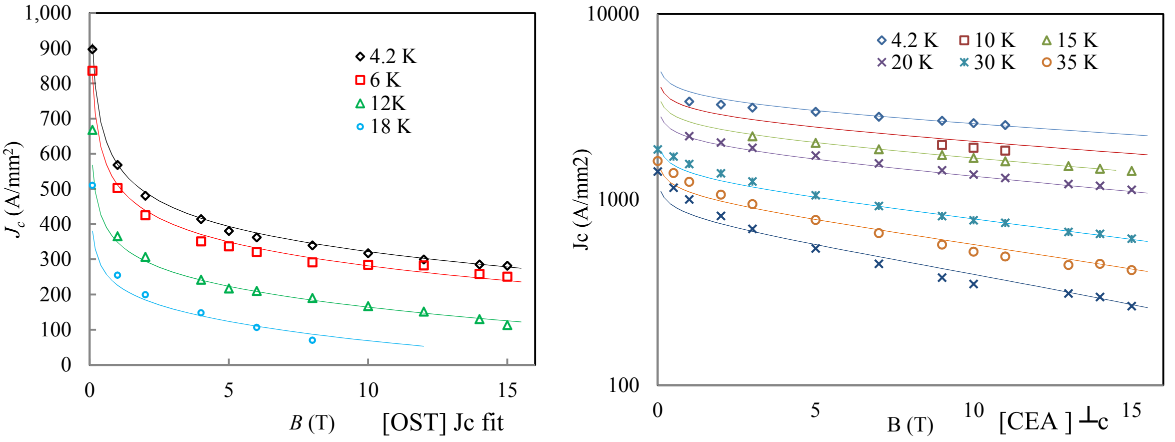

Figure 4.1: The J_c data versus the parameterization for Bi-2212 OST conductor (data from [34])(left) and YBCO SP conductor in parallel flux density (data from [5]) (right).

4.2 Paramaterization of the J_c anisotropy of YBCO conductors

The YBCO coated conductor is very promising for high flux density magnet applications because of its high current carrying capability, high irreversibility flux density and high mechanical strength especially in the versions made on high strength Hastelloy substrates. However, a key part of the coil design depends on knowing the detailed angular dependence of the critical current density (J_c) so that the coil can be optimized with confidence. At low temperature, the anisotropy of YBCO conductors is in the form of a cusp-like peak around the parallel flux density orientation, with no c-axis peak at any magnetic flux density. The low temperature flux pinning mechanisms in YBCO are significantly different from those at high temperature due to the smaller vortex core size and reduced thermal fluctuation effects that allow operation of weaker pins that become thermally depinned at higher temperatures. The intrinsic pinning due to the modulation of superconducting order parameter along the c-axis may be responsible for the strong cusplike $J_c(\theta)$ near the parallel flux density orientation at low temperature. Indeed, the coherence length along c-axis, which is about 0.2 nm at 0 K, is comparable to the distance between the strong CuO_2 superconducting layers, allowing the CuO charge reservoir layers to serve as correlated ab-plane pinning centers, as earlier envisaged by Tachiki and Takahashi [191]. The anisotropy of YBCO SP conductors was reported in chapter 3. In this chapter, a short review of the different models of J_c anisotropy is performed and an empirical expression is proposed for YBCO SP conductors.

4.2.1 Review of J_c anisotropy models

Different models have been tried to explain the J_c anisotropy in HTS conductors. The most relevant are reported here.

The Tinkham and Lawrence-Doniach models

The Tinkham [192] and Lawrence-Doniach models [193], derived directly from the Ginzburg-Landau theory [194], were originally developed to describe the anisotropy of the critical field (H_c). The Tinkham and Lawrence-Doniach models express the critical field (H_c) in the form:

$$\left(\frac{H_{c2}(\theta)\cos(\theta)}{H_{c2//}}\right)^2 + \left(\frac{H_{c2}(\theta)\sin(\theta)}{H_{c2per}}\right)^i = 1 \tag{4.3}$$

where $i = 1$ for Tinkham model and $i = 2$ for Lawrence-Doniach model. To describe the J_c anisotropy of HTS materials, these two models were modified [195] by an unjustified substitution of H_c by J_c as follow:

$$\left(\frac{J_{c2}(\theta)\cos(\theta)}{J_{c2//}}\right)^2 + \left(\frac{J_{c2}(\theta)\sin(\theta)}{J_{c2per}}\right)^i = 1 \tag{4.4}$$

The modified Lawrence-Doniach model was shown to be accurate with respect to experimental data at temperatures close to T_c. The shortening of coherence lengths with decreasing temperature below the value of the interplanar distances renders the model inapplicable at low temperatures. The modified Tinkham model assumes very weak coupling between the superconducting planes of a layered superconductor and is not expected to be accurate close to T_c where strong Josephson couplings between the superconducting CuO_2 planes are present. However as the temperature decreases, the coupling progressively vanishes making the modified Tinkham model applicable. Nevertheless these two models are not able to describe the J_c cusp-like anisotropy of YBCO SP conductors at 4.2 K.

The Long model

The J_c angular dependence of YBCO was predicted by Long [196] by assuming anisotropic populations of pining sites in c-axis and ab-plane with normal and Lorentz distributions. The vortex finds a path through the film following the main pinning sites in the ab direction (spacer layers between the CuO planes or stacking faults) and the c direction (dislocations, twins or nanorods). In the case of Lorentz distribution of pinning sites, the dependence of J_c on orientation is given as:

$$J_c(\theta) = \frac{J_{c0}\Gamma}{\cos^2\theta + \Gamma^2\sin^2\theta} \tag{4.5}$$

Where Γ is the anisotropy ratio of the material. The angular dependence of J_c given by the Thinkam and Long models are depicted in figure 4.2.

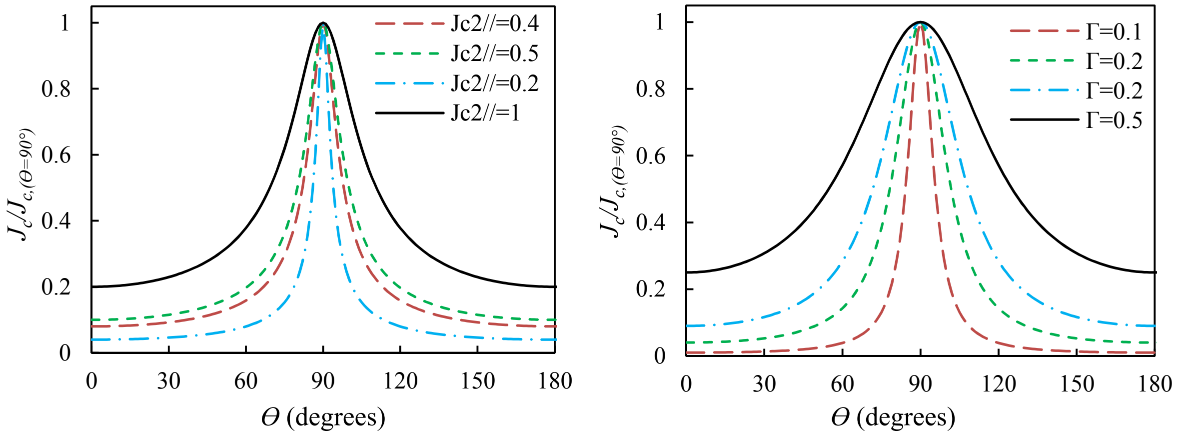

Figure 4.2: The normalized J_c angular dependence given by the Thinkham model (with J_{c2per}=5) (left) and by the Long model (right).

4.2.2 Empirical $J_c(\theta)$ fit for YBCO SP conductors

The different models reviewed are not able to describe the $J_c(\theta)$ anisotropy of YBCO SP conductors at 4.2 K. I introduce here an empirical and accurate formulation that modulates the J_c of YBCO SP conductors between its value in perpendicular and parallel flux density:

$$J_c(B,T,\theta) = J_{c,perp}(B,T) + \frac{J_{c,parall}(B,T) - J_{c,perp}(B,T)}{1 + \left(\frac{|\theta-\pi/2|}{e(B,T)}\right)^{g(B,T)}} \tag{4.6}$$

Where $J_{c,perp}$ and $J_{c,parall}$ are respectively the critical current density in parallel and perpendicular flux density orientation. The parameter $\theta - \pi/2$ is the angle between the flux density and the YBCO tape plane. The fitting parameters e and g are temperature and flux density dependent. The J_c angular dependence of YBCO SP conductor at 4.2 K is shown in figure 4.3 [37], along with a fit according to equation 4.6. The data are fitted over the entire angular range and thus at all the different values of flux density. The flux density dependency of parameters e and g are given by:

$$e(B) = e_0 - e_1\ B \tag{4.7}$$

$$g(B) = g_0 + g_1 exp(-g_2\ B) \tag{4.8}$$

The J_c anisotropy of YBCO SP materials have also been reported at 77 K and 70 K [197]. The measurements at 70 K and 77 K are well described by expression (4.6), as depicted in figure 4.3. The empirical expression introduced here to describe the J_c anisotropy of YBCO SP conductors is robust over an extended temperature and flux density range.

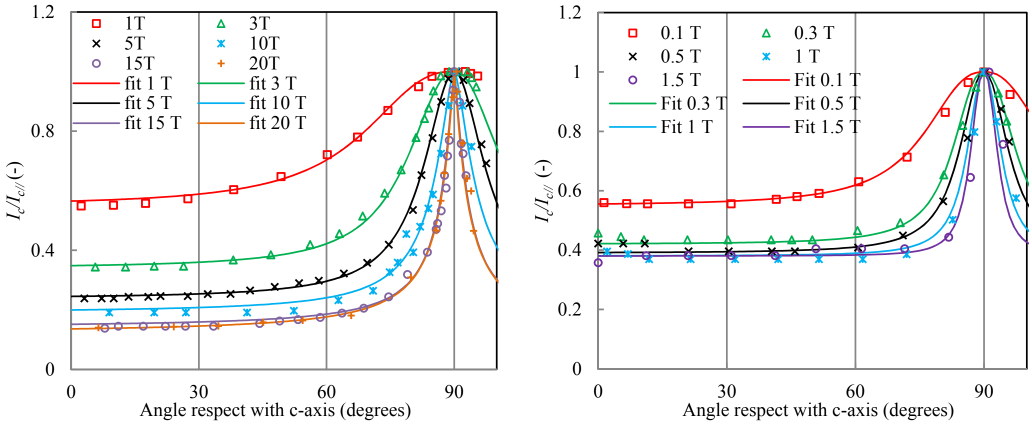

Figure 4.3: The normalized J_c angular dependence of YBCO SP conductor at 4.2 K (data from [37]) (left) and at 77 K (data from [197]) (right). Data (markers) are compared with expressions (4.1) and (4.2) (lines).

4.3 The operational margins of YBCO cables in magnet

The J_c anisotropy of YBCO conductors has a strong impact on the design of accelerator dipole magnets. The flux density perpendicular to the surface of a tape has a much stronger reductive effect on the critical current density than the parallel flux density. The critical point of a magnet made from YBCO conductor is therefore not necessarily at the peak flux density location. Based on the EuCARD HTS dipole insert, the key aspects of magnet design using anisotropic YBCO materials are introduced and the insert operational margins are computed.

4.3.1 The HTS insert of the EuCARD program

To illustrate the impact of the J_c anisotropy of YBCO conductors on magnet design, the HTS dipole of the European program EuCARD [198] is considered in this section. The HFM EuCARD program studies the design and the realization of a HTS insert of 6 T operated at 4.2 K nested in a Nb_3Sn dipole of 13 T [10]. The EuCARD program has as primary goal to develop instruments and technologies for future particle accelerators, therefore several constraints needed in the design of a real accelerator magnet have not been considered in the design of this HTS insert: e.g. flux density quality is not taken into account. The HTS magnet will fit the 100 mm bore aperture of the Nb_3Sn dipole. As the insert should not transfer any load on the Nb_3Sn magnet during operation, all the magnetic loads and deformations have to be supported by the insert itself. A schematic cross section view of the Nb_3Sn and HTS dipoles is depicted in figure 4.4. In order to reach the expected bore flux density of 6 T the engineering current density over the HTS winding needs to be 250 A/mm^2.

Table 4.2: The main characteristics of Nb_3Sn and HTS dipoles of the EuCARD program.

	HTS	Nb_3Sn
Contribution to bore flux density (T)	6	13
Outer diameter (structure) (mm)	99	904
Magnetic length (mm)	250	730
Cable width/thickness (mm)	12.1/0.92	21.41.9
Cable current at nominal bore flux density (kA)	2.8	10.9

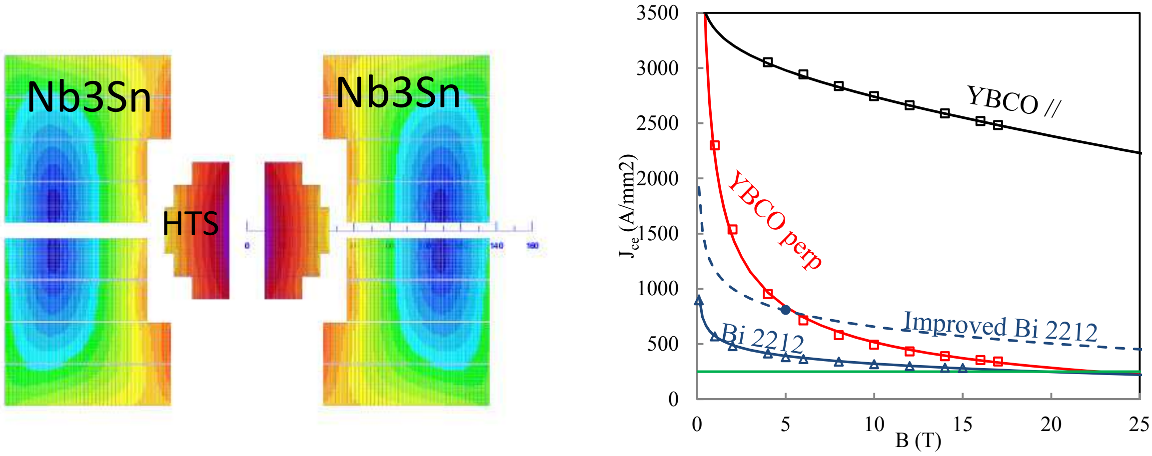

Figure 4.4: Cross section view of the Nb_3Sn and HTS dipoles of the EuCARD program (left). The engineering critical current density (J_{ce}) of YBCO SP [134] and Bi-2212 OST conductors [181][62](right). The J_{ce} of YBCO conductors is presented here for 4 mm wide and 0.095 mm thick tape.

The HTS cable for the 6 T insert

The YBCO and Bi-2212 conductor options were studied in the early stages of the project. The engineering critical current density (J_{ce}) of this two materials is depicted as a function of the flux density in figure 4.4. Up to 20 T, the performances of YBCO materials are over the baseline of 250 A/mm^2 for both the parallel and the perpendicular flux density orientation. The performances of short samples Bi-2212 wires reported in 2010 are just above the current density baseline with a value of 270 A/mm^2 at 15 T. A delicate heat treatment in oxygen atmosphere after coil winding is required for Bi-2212 conductors. In 2005 a J_{ce} of 740 A/mm^2 was reported in Bi-2212 OST wires at 4.2 K and 5 T, but the strands suffers from serious leaks of Bi-2212 through the outer sheath during heat treatments. Since 2007, OST has modified their fabrication process and nearly eliminated the leakage, but the post-2007 wires have always shown lower J_{ce} by more than 30%. Recently a great increase in the J_{ce} was achieved by over pressuring the samples during the heat treatment [62]. The J_{ce} was almost doubled compare to the 2007 generation of wires, being 804 A/mm^2 at 4.2 K and 5 T. The extrapolated performance of OST wires with improved heat treatment is also depicted in figure 4.4. Groove-rolled multifilamentary wires has showed a J_c increased by a factor of about 3 with respect to drawn wires prepared with the same Bi-2212 powder and architecture [123].

The YBCO conductor made in the IBAD route (high strength Hastelloy substrate) was selected with SuperPower as supplier. This conductor presents: high engineering critical current density, high mechanical properties and doesn't require delicate heat treatment after magnet winding. The outsert Nb_3Sn magnet will be operated at the nominal current of 10.9 kA. To limit the self and the mutual inductance of the insert, the HTS cable current must be in the range of few kA. To fulfil this requirement, the HTS cable is made from 4 of the widest YBCO SP tapes, i.e. 12 mm wide. The HTS cable is 12.1 mm wide and 0.92 mm thick and is made from 2 HTS strands stacked on top of each other as depicted in figure 4.5. Each HTS strands consist in 2 YBCO SP tapes soldered through a 70 μm thick copper layer. The soldered YBCO tapes are then interleaved between two 100 μm thick copper alloy tapes, as depicted in figure 4.5. An insulation film of 30 μm is deposited at each side of the strands: the two strands of the cable are insulated from each other. They are in electrical contact only at splice to current leads. The winding current density of 250 A/mm^2 necessary to generates a bore flux density of 6 T correspond to a cable current of 2.8 kA.

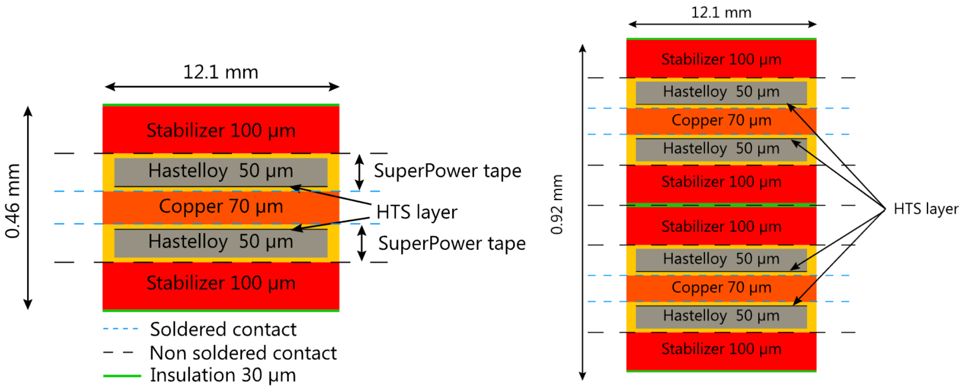

Figure 4.5: Schematic cross section view of the HTS strand (made of 2 YBCO SP tapes) (left) and the HTS cable (made of 4 YBCO SP tapes) (right) of the insert dipole of the EuCARD program.

The magnetic design of HTS insert

The design of this HTS insert is mainly driven by the mechanical structure: an external tube of 3 mm with pads is used to maintain forces. The insert consists of 6 pancakes of three different types (see figure 4.6 and table 4.3). The mid plane pancakes are longer (750 mm) than the upper and lower ones (350 mm) in order to reduce the peak flux density problems in the coil heads and to limit the conductor length. In the different pancakes, the first conductors are placed at a horizontal distance equal to 10 mm from the centre: the conductor will experience a minimum bending radius of 10 mm. The number of conductors per pancakes have been set in order maximize the coil cross section. The pancake length and the number of conductor turns per pancake is reported in table 4.3. In order to either enhance the magnetic flux density and limit the perpendicular flux density in respect with YBCO conductors a ferromagnetic piece (iron) placed in coil apertures has been considered, see figure 4.7. The iron pole permits a 14% increase of the insert central flux density (from 5.7 T to 6.52 T at a cable current of 2.8 kA). The iron pole concentrates the flux density lines which limits the peak flux density on the coil. The different pancakes are connected in serial and the strands that are not transposed in the cable are transposed between the top and bottom mid pancakes. The inductance of individual strand is therefore balanced over the magnet winding.

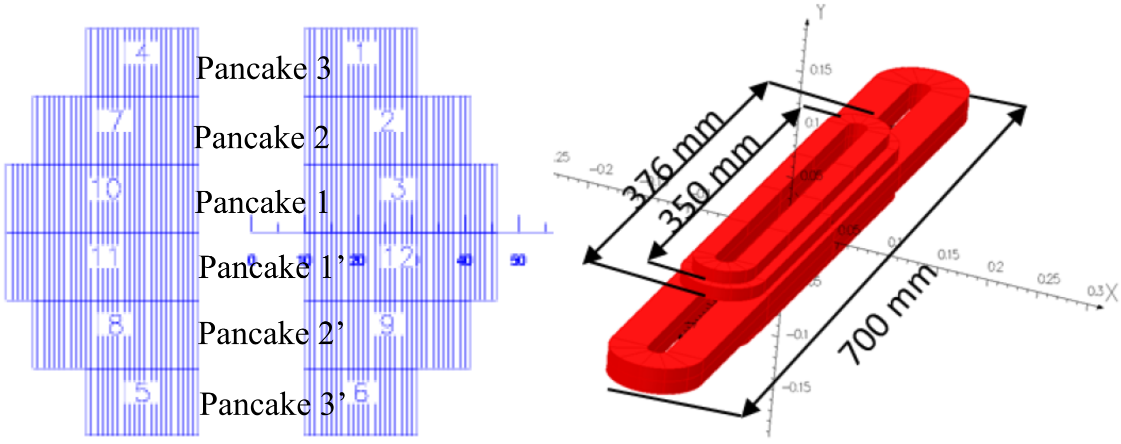

Figure 4.6: The cross section view (left) and the 3D view of the HTS insert (right).

Table 4.3: The main characteristics of the pancakes of the HTS insert.

Pancake ID (see figure 4.6)	3-3’	2-2’	1-1’
Pole width (mm)	20	20	20
Pancake length (mm)	350	376	750
Number of turns (mm)	35	61	73
Cable length (mm)	23	42	101

The 2D FEM model

The HTS coil has a length of 750 mm and a outer diameter of 99 mm, in a first approximation it is considered as infinitely long such that there is no magnetic influence of the heads at the magnetic center. This approximation allows to study only a 2D cross section of the magnet with current density flowing perpendicular to the cross section. For reasons of symmetry, only a quarter of the coil cross section needs to be considered, with appropriates boundary conditions, in the commercial software Comsol [199]. Each individual YBCO SP tapes is considered and is represented by its superconducting layer with a thickness of 50 μm (instead of 1 μm in reality) and a width of 12 mm. All other components such as substrate (Hastelloy), buffer layers, stabilizers and insulations are meshed as vacuum because their influences to the magnetic flux density are negligible. In the model, the flux density component B_x is the perpendicular flux density with respect to the tape conductor plane and B_y is the parallel flux density. The Nb_3Sn coil and its iron yoke and iron pole are implemented in the model, as depicted in figure 4.7. All the non magnetic mechanical pieces of the magnet are meshed as vacuum.

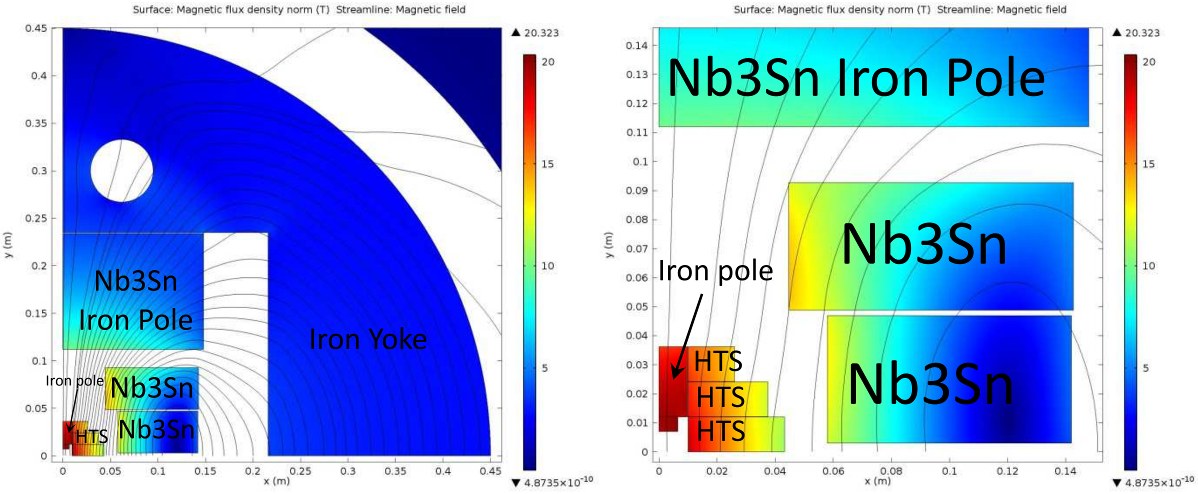

Figure 4.7: The 2D FEM model of the dipoles of the EuCARD program. General view of magnet cross section (left) enlarged view of the LTS and HTS coils (right). In these plots, the different YBCO layers are not depicted.

4.3.2 Minimization of B_x by the use of iron pole

In YBCO tapes, the flux density perpendicular to the surface of a tape, has a much stronger reductive effect on the critical current density than the parallel flux density. In order to reduce the B_x component, a ferromagnetic piece (iron) is placed in coil apertures, see figure 4.7. The two upper pancakes are wound on the iron pole. The flux density lines are concentrated in the iron pieces which limit the B_x component on the coils. The iron piece also has a substantial benefit on the bore flux density (B_0). The drawback of this solution is the highly nonlinear distortion of the flux density in the bore as a function of the cable current.

In figure 4.8, the perpendicular flux density with respect to YBCO conductor is depicted at the bore flux density of 19 T with and without the HTS iron pole. Without the iron pole, a maximum B_x value of 3.3 T is observed in the external turns of the top pancake. The presence of the iron pole reduces the maximum value to 3.1 T. The shape of the iron piece could be optimized to reduce as much as possible the B_x component on the coil. It should also be noted than the Nb_3Sn magnet also makes a small contribution to B_x in the HTS coil.

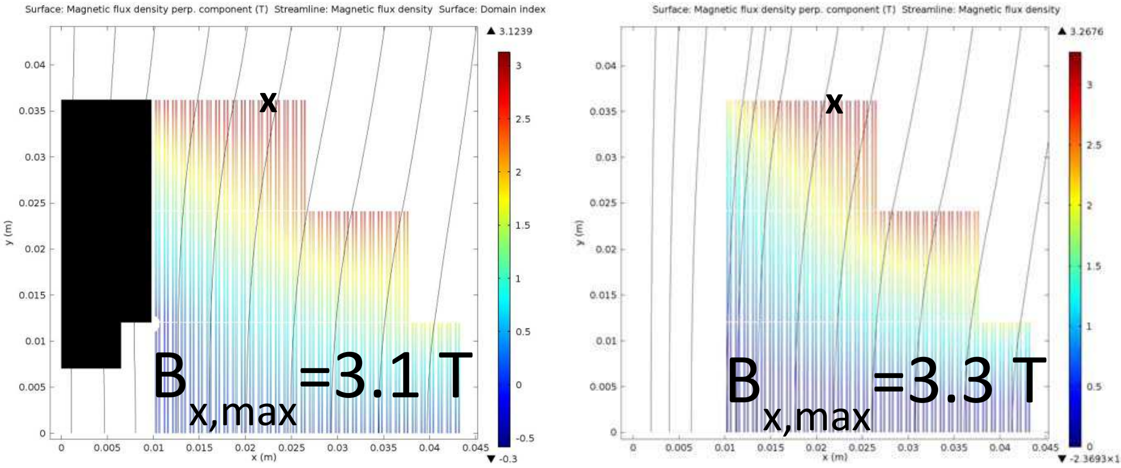

Figure 4.8: The B_x component in the HTS winding at the bore flux density of 19 T, with iron pole (left) and without the iron pole (right).

4.3.3 The flux density distribution

The flux density distribution in the HTS winding is studied for two operating configurations: in the first configuration the HTS insert operates alone, creating a bore flux density of 6.5 T. In the second configuration the HTS and Nb_3Sn coils are operated together, creating a bore flux density of 19.3 T. The modulus and the orientation of the flux density in the HTS winding are depicted for these two configurations in respectively figure 4.9 and figure 4.10. The distribution of the magnitude of the flux density strongly differs: in the stand alone configuration at the coil midplane (y=0) it decreases from 6 T at the innermost conductor (x=10 mm) to 1 T at the outermost conductor (x=43 mm). At B_0=19 T, the magnitude of B at the coil midplane (y=0) decreases from approximately the bore magnetic flux density value (B_0=19 T) at the innermost turn to 13 T at its outermost turns. At B_0=6 T the angle between flux lines and the conductor tape planes takes all the orientation between zero and 180°. At B_0=19 T the flux lines became almost parallel to every YBCO conductor with a maximum deviation of 13° from the parallel orientation at the outermost turns of the top pancake, as depicted in figure 4.10.

4.3.4 The electromechanical forces and stresses on coil pack

The mechanical design of superconducting magnets has to deal with two main issues: first, a mechanical structure limiting the deformations of the coil due to electro-magnetic forces must be designed; secondly, the stress arising inside the coil must be carefully analysed to avoid insulation creep or superconductor degradation. In this section the forces and stresses in the HTS coils are estimated.

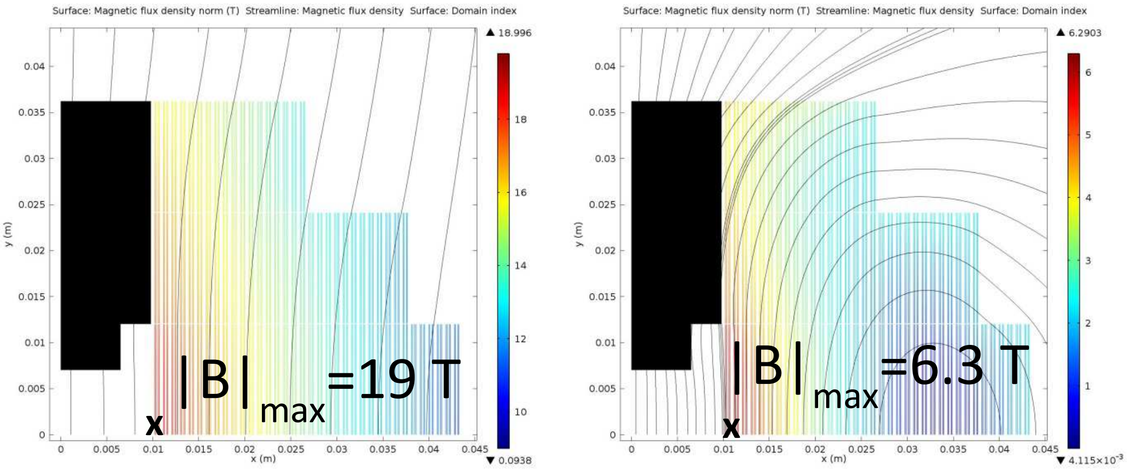

Figure 4.9: The modulus of flux density in the HTS winding at the bore flux densities of 19 T (left) and 6 T (right) with the iron pole.

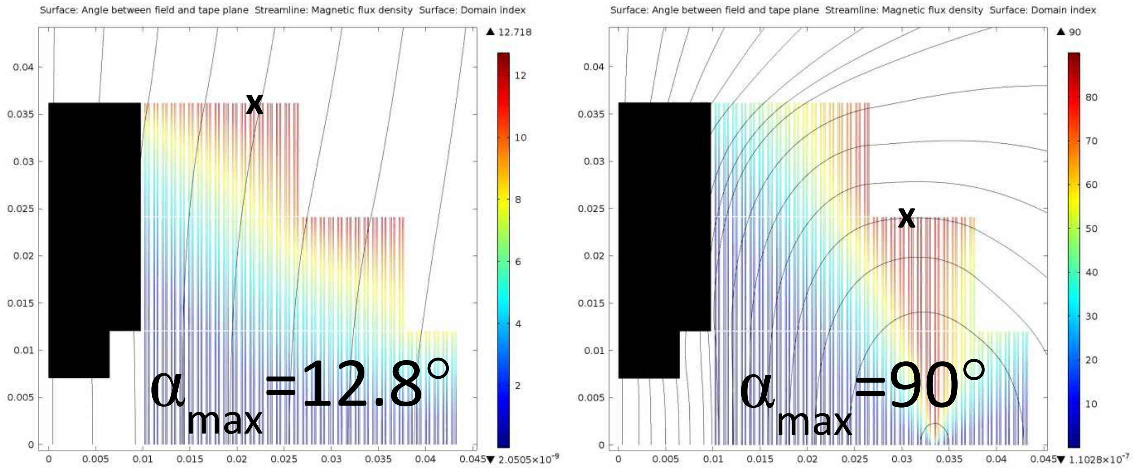

Figure 4.10: The deviation (α) of the flux density with respect to the YBCO tape planes (bottom) at the bore flux density of 19 T (left) and 6 T (right) with the iron pole.

Magnetic forces and stresses in HTS coil

In figure 4.11 the distribution of the Lorentz force in the HTS winding is depicted at B_0=19 T and B_0=6 T. The sum of the Lorentz force acting on each HTS pancakes are reported in table 4.4 at the bore flux density of 6 T and 19 T. At B_0=19 T the sum of the Lorentz forces acting on the midplane pancake (pancake 1) is the largest with a value of 1449 kN/m in the x direction. This is easily explained by both a higher number of turns and a higher flux density. At B_0=6 T, the sum of the Lorentz forces in the x direction is reduced to 163 kN/m. In the y direction, the sum of the Lorentz forces is much lower at B_0=19 T (B_0=6 T) being -45(-41) kN/m.

In each pancake, an estimation of the transverse stress on the conductor further away from the magnetic centre can be obtained by dividing the horizontal component of the force by the width of the cable (see table 4.5). This estimate assumes perfect sliding between the various interfaces. At B_0=19 T, the maximum of transverse stress is observed in the mid pancakes with a value of 121 MPa. The pancakes

2 and 3 (see figure 4.6) present smaller values with respectively 101 MPa and 62 MPa. The YBCO SP conductors have been shown to withstand without significant I_c degradation transverse stress of up to 150 MPa [13]. When the bore flux density is 6 T, the stresses values can be considered only as indicative, as for example, they do not consider the build-up and reversal of magnetic forces along the x direction, as depicted in figure 4.11.

Table 4.4: The electromechanical forces on the HTS coil pack.

	B_0=19 T		B_0=6 T	
	F_x (kN/m)	F_y (kN/m)	F_x (kN/m)	F_y (kN/m)
Pancake 3	741	-112	107	-104
Pancake 2	1209	-118	141	-107
Pancake 1	1449	-45	163	-41

Table 4.5: The electromechanical transverse stresses on the conductors further away from the centre at B_0=19 T and B_0=6 T.

	B_0=19 T	B_0=6 T
	σ_x (MPa)	σ_x (MPa)
Pancake 3	61.7	8.9
Pancake 2	100.7	11.7
Pancake 1	120.7	13.6

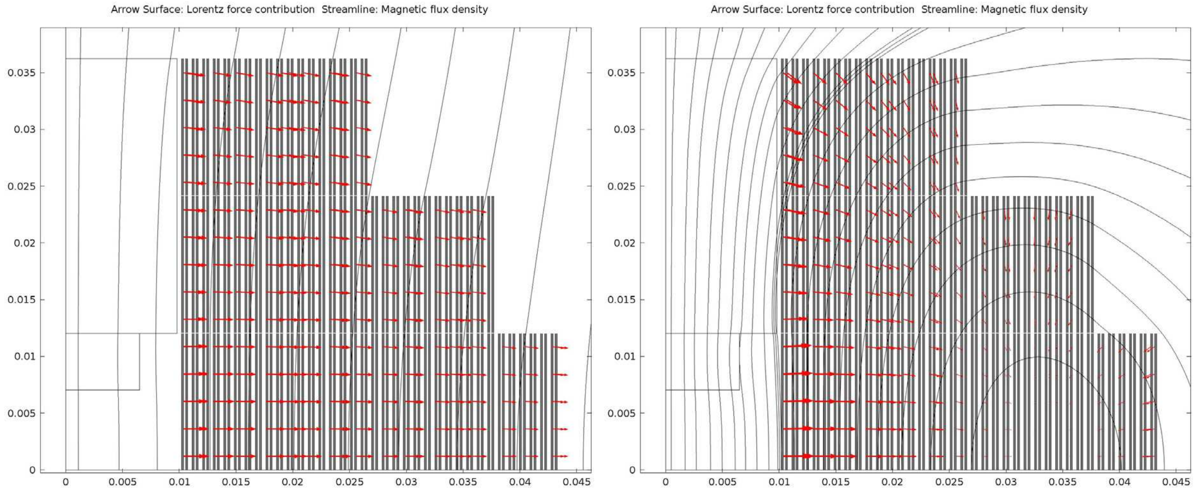

Figure 4.11: The distribution of the Lorentz force in the HTS winding at B_0=19 T (left) and B_0=6 T (right). The scale factor of the arrows differs between the two plots.

Magnetic forces and stresses in LTS coil

The stray flux density of the HTS insert as an impact on the peak flux density of the Nb_3Sn coil. When the Nb_3Sn dipole is operated alone at the nominal current of 10.9 kA (without the HTS iron pole), the peak flux density in the Nb_3Sn coil is 13.7 T and is located at the innermost turn of the top double pancake. At B_0=19 T (with the HTS iron pole) the location of peak flux density is unchanged but is slightly increased to 14.02 T. The HTS stray flux density has therefore a minor effect on the peak flux density in the Nb_3Sn coil. The sum of the Lorentz force acting on each LTS double pancakes are reported in table 4.6 at the bore flux density of 13 T and 19 T. For each double pancake, the sum of the Lorentz forces in the x direction is almost the same at B_0=19 T and B_0=13 T. The sum of the Lorentz forces in the y direction are increased between B_0=13 T and B_0=19 T, by respectively 9 % and 25 % in the top and mid plane double pancake. This is easily explained by the increase of the B_x component in the LTS pancakes induced by the stray flux density of the HTS insert.

Table 4.6: The electromechanical forces on the Nb_3Sn coil pack.

	B_0=19 T		B_0=13 T	
	F_x (kN/m)	F_y (kN/m)	F_x (kN/m)	F_y (kN/m)
Top double pancake	4576	-3934	4620	-3597
Midplane double pancake	3200	-859	3540	-656

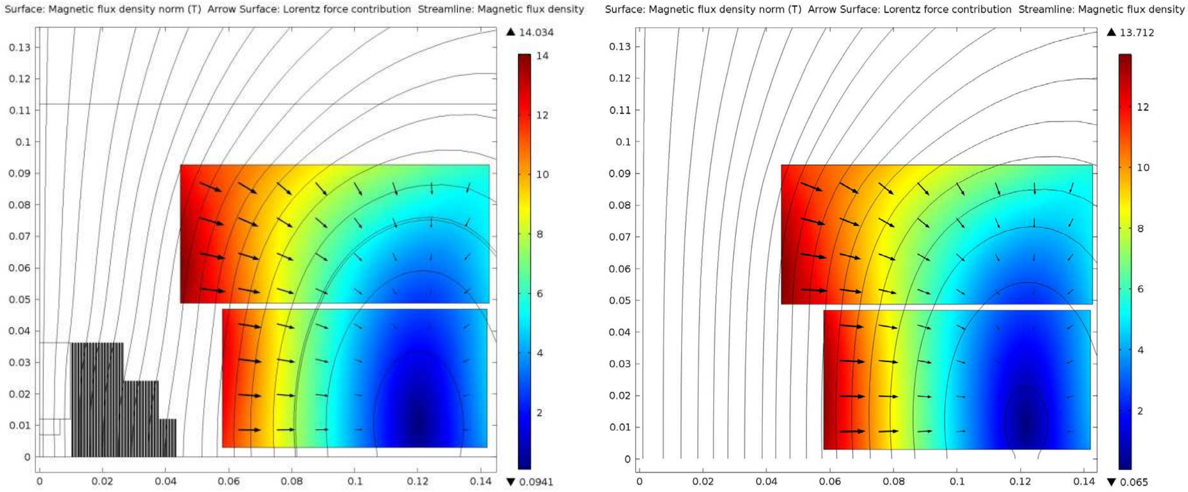

Figure 4.12: The norm of the flux density and the Lorentz forces in the LTS winding at B_0=19 T (left) and B_0=13 T (right).

4.3.5 Operational margins of YBCO cable

Despite all the effort to work at the highest current density, the operating point of a superconducting magnet must be chosen to be well below the critical current density of the material (see figure 4.13), i.e. with proper margins that ensure stability at the operating point [1]. The typical metrics used for operating margins are:

- **The critical current margin**

  The critical current margin is defined as the difference between the cable quench current (I_q) and the cable operating current (I_{op}). The critical current margin gives the level of tolerance allowable on the cable I_c.

- **Margin along the loadline**

  The margin along the loadline gives the maximum flux density the magnet will produce if the current is increased up to the quench. There are three ways to increase the bore flux density above 19 T: the first is to increase only the flux density generated by the outsert, the second is to increase at the same time the flux densities generated by the insert and the outsert and the third is to increase only the flux density generated by the insert. Only the last scenario is considered here:

from the B_0=19 T, the current of HTS dipole is ramped up while the current of the Nb_3Sn is keep at the value of 10.9 kA.

- **Temperature margin**

  The temperature margin is defined as the difference between the operating temperature (T_{op}) and the quench temperature (T_q). Different sources of power dissipation could lead to a winding temperature increase: sudden internal energy release (conductor motion), AC losses, highly resistive joints or beam interaction with magnet winding. The increase of the coil temperature with these events depends on parameters that are difficult to control and cannot be easily predicted. For the calculation of the temperature margin, the magnet is energized to the nominal bore flux density at 4.2 K and the temperature is swept up to the quench.

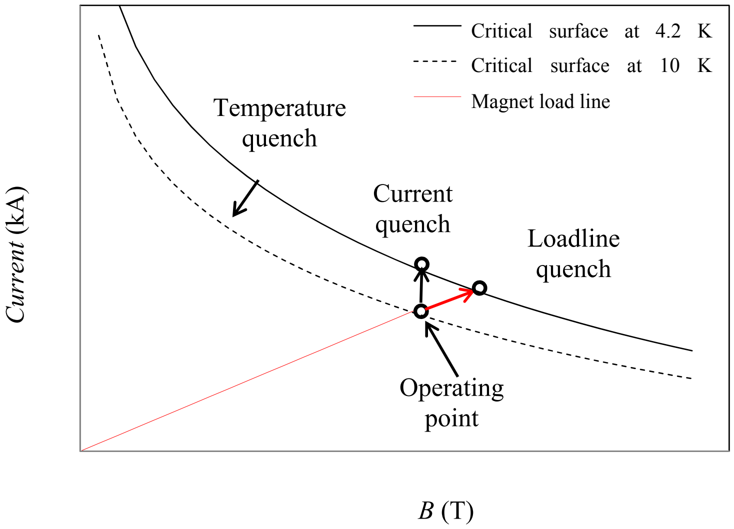

Figure 4.13: A schematic view of the HTS load line where the different types of margins: critical current, temperature, load line and flux density are graphically depicted.

The local and the overall margins

The cable of the HTS insert is 12 mm wide and made from 4 YBCO tapes. Across the width of the HTS cable, non-uniform distributions of the modulus and the orientation of flux density are observed (see figures 4.9-10). Within individual pancakes the YBCO tapes are not transposed in the cable: the electrical and magnetic boundary conditions are therefore not the same across the conductor width, inducing a specific J_c distribution. Assuming a homogeneous current distribution in the HTS film (J_{HTS}), the local margins are defined as the points where any local J_c is in excess of J_{HTS}. The overall margins are defined as the points where any cable I_c is in excess of the cable current. Obviously the local margins are smaller than the overall margins. The J_c anisotropy of YBCO SP conductor is implemented in the 2D FEM model and the local and overall margins of the HTS insert are calculated in the following sections. A summary of the local and overall current, load line and temperature margins is reported in table 4.7.

Table 4.7: Summary of the local and overall current, load line and temperature margins of the EuCARD YBCO insert.

	B_0=19 T		B_0=6 T	
	local	overall	local	overall
Current margin (% of I_{nom})	14	30	70	99
Load line margin (HTS ramp up) (%)	9	18	40	59
Temperature margin (T_{op}=4.2 K) (K)	3.5	8.5	>10	>10

The current margin

The local current margin ($I_{m,loc}$) and the global current margin ($I_{m,ov}$) are defined as :

$$I_{m,loc} = A_c(J_{c,min} - J_{HTS}) \qquad I_{m,ov} = min \int (J_c - J_{HTS}) dA_c \tag{4.9}$$

where A_c is the cross section of the HTS cable, $J_{c,min}$ is the minimum of the critical current density over the HTS winding and J_{HTS} is the uniform current density flowing in the HTS film. The ratio of J_{HTS} and J_c at B_0=19 T and B_0=6 T is depicted in figure 4.14. The maximum value of the ratio is 0.88 for B_0=19 T and 0.59 for B_0=6 T. The minimum of the conductor J_c is observed in the top pancakes at both bore flux density. The overall current margin of the HTS cable at different location in the coil is reported in figure 4.15. The conductor in the top pancakes presents the lowest overall current margin, the conductors in the midplane pancakes the largest. For B_0=19 T the outermost cable of the top pancakes presents the smallest overall current margin with a value of 836 A. The different current margins of the HTS insert are reported in table 4.8.

Table 4.8: The local and overall current margins of the YBCO insert at B_0=19 T and B_0=6 T.

	$I_{m,loc}$ (A)	$I_{m,loc}$ (% of I_{nom})	$I_{m,ov}$ (A)	$I_{m,ov}$ (% of I_{nom})
B_0=19 T	392	14	836	30
B_0=6 T	1978	70	2772	99

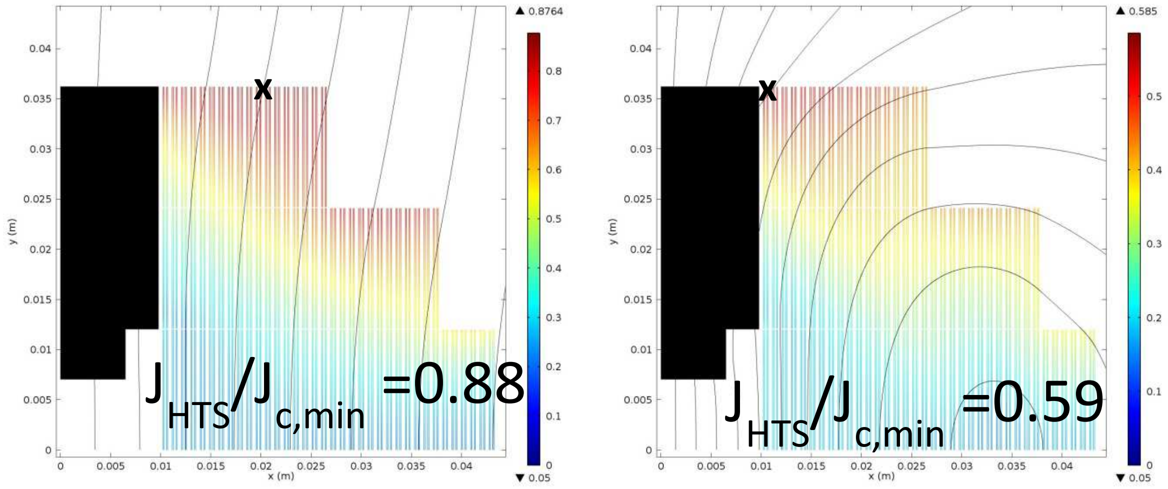

Figure 4.14: The ratio of the current density in the HTS layer and the critical current density at the bore flux density of 19 T (left) and 6 T (right).

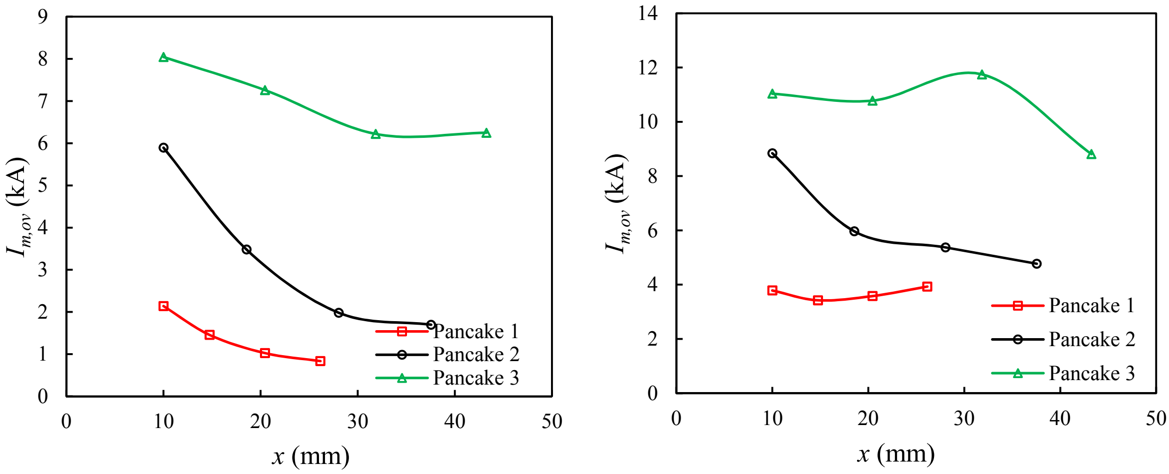

Figure 4.15: The overall current margin of the cable at different x-location in the HTS coil at B_0=19 T (left) and B_0=6 T (right).

The load line margin

To compute the load line margin, the current in the HTS cable is swept up to the local and the overall quench current at which respectively local and global current margins are null. In figure 4.16, the local and overall cable current margins are depicted as a function of the HTS cable current for the HTS insert operated alone and for the HTS insert operated with the LTS coil at a current of 10.9 kA. When the LTS and HTS coils are operated together, the local current margin is zero at a HTS cable current of 3.04 kA, corresponding to a bore flux density of 19.6 T. The overall current margin is zero at a HTS cable current of 3.34 kA corresponding to a bore flux density of 20.2 T.

Table 4.9: The load lines margins of the YBCO insert operated alone or together with the LTS magnet at a current of 10.9 kA.

	$I_{q,loc}$ (kA)	Local load line margin (%)	$I_{q,ov}$ (kA)	Overall load line margin (%)
HTS operated with LTS	3.04	9	3.34	18
HTS operated alone	3.92	40	4.45	59

The temperature margin

To compute the temperature margin, the HTS and LTS coils are energized to the cable current of respectively 2.8 kA and 10.9 kA at an initial temperature of 4.2 K. The temperature is then swept up to the local ($T_{q,loc}$) and the overall ($T_{q,ov}$) quench temperature at which respectively the local and the overall current margins are null. The overall and local current margin of the HTS cable as a function of the temperature are reported in figure 4.17 for B_0=19 T. The local and overall margins temperature are respectively 3.5 K and 8.7 K.

Table 4.10: The temperature margins of the YBCO insert operated at B_0=19 T and B_0=6 T.

	$T_{q,loc}$ (K)	Temperature margin (K)	$T_{q,ov}$ (K)	Temperature margin (K)
B_0=19 T	7.7	3.5	12.9	8.7
B_0=6 T	>14	>10	>14	>10

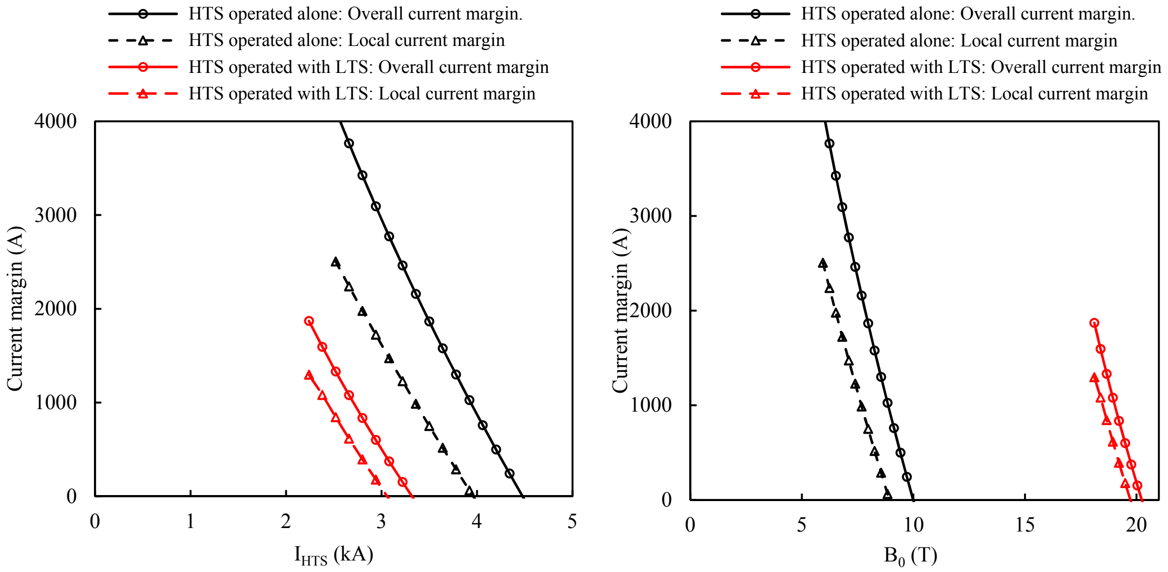

Figure 4.16: The current margins as a function of the HTS cable current (left) and the current margins as a function of the bore flux density (right).

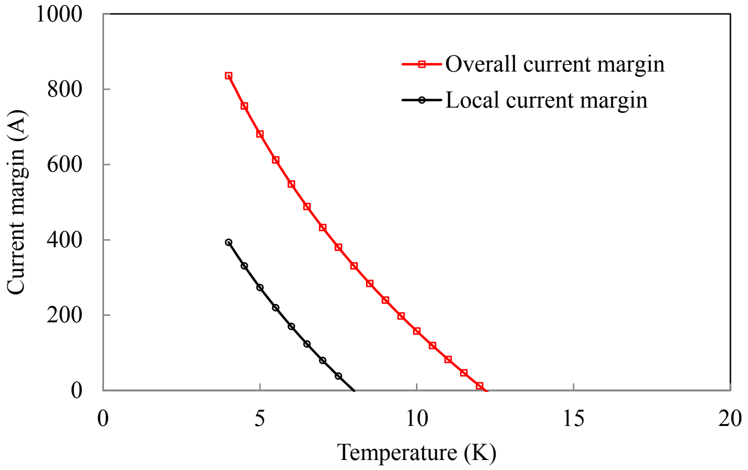

Figure 4.17: The overall and local current margin of the HTS cable as a function of the temperature at B_0=19 T.

4.4 Determination of the allowable bending radius and twisting pitch of YBCO conductors

Coated YBCO conductor is in the class of react and wind conductors: the fully reacted YBCO film is formed during the conductor fabrication process. The total strain that can tolerated without damage the conductor is limited to the irreversible strains $\varepsilon_{irr,c}$ and $\varepsilon_{irr,t}$ in respectively compression and tension. The sources of strain on the conductor include the strain of cabling and coil winding in addition to the thermal strain of cool-down to operating temperature and the strain from the electromagnetic loads during operation. The cabling and winding strains reduce the amount of operating strain that can be applied before the irreversible strain limit is reached. In a first part of this section, parameterizations of the J_c dependence on axial strain of YBCO conductor are introduced. Then the strain distribution in the YBCO film is estimated for conductor bending and twisting. The uni-axial strain dependence of the critical current density is then integrated over the conductor section and analytical expressions that describe the conductor I_c as a function of the twist pitch and bending radius are provided. These expressions are then used to determinate the minimum allowable pitch and radius of YBCO conductors.

4.4.1 Parameterization of the J_c dependence on axial strain of YBCO conductor in self flux density

The J_c dependence on uni-axial strain of YBCO conductors in self, perpendicular and parallel magnetic flux density was reported in chapter 3. The strain dependence of J_c is complex: it is flux density (intensity and orientation [108][178][171]), strain orientation and composition dependent [178]. In this section only the uni-axial strain dependency of J_c in self flux density is parameterized. In self flux density, the performances of YBCO conductors are reversibly modified by increasing the uni-axial strain up to a threshold strain limit named irreversible strain (ε_{irr}). Irreversible reduction of J_c has been observed for strain below the irreversible compressive strain $\varepsilon_{irr,c}$ and in excess of the irreversible tensile strain $\varepsilon_{irr,t}$. In the irreversible strain regime, the J_c is rapidly reduced to zero. The typical value of $\varepsilon_{irr,t}$ for YBCO SP and YBCO AMSC conductors is respectively 0.7% and 0.5%. The compressive irreversible strain $\varepsilon_{irr,c}$ have been reported to be ranging between -1 and -2%. The ε_{irr} values are temperature constant. The strain dependence of J_c is first parameterized in the reversible strain regime ($\varepsilon_{irr,c} < \varepsilon < \varepsilon_{irr,t}$).

Dependence on axial strain in the reversible regime

The J_c strain dependence of YBCO conductors in self flux density ($J_{c,s.f}$) in the reversible strain range ($\varepsilon_{irr,c} < \varepsilon < \varepsilon_{irr,t}$) is well described by the empirical power-law:

$$J_{c,s.f}(\varepsilon, T) = J_{c0,\varepsilon_m} \left(1 - \frac{T}{T_e}\right)^k \left(1 - a(T)\left[\varepsilon - \varepsilon_m(T)\right]\right)^2 \tag{4.10}$$

where the parameter a express the strain sensitivity of the material. The parameter ε_m is the strain at which J_c is maximum with a value J_{c0,ε_m} at 0 K. Parameters k and T_e express the temperature dependence of the critical current density (see appendix A). The exponent 2 of the right term was set by [167] as a fitting parameter with value of about 2.1-2.2. The value 2 provides a satisfactory fit and an easy analytical integration of expression 4.10 over the HTS domain. One should notice that expression 4.10 is similar to the one introduced by Ekin [200] for Nb_3Sn conductors. The ε_m parameter has been observed to be temperature dependent with no correlation to the null residual thermal strain [201][175][108]. The YBCO sensitivity to strain is observed to be reduced by lowering the temperature [175]. The temperature dependence of parameter a and ε_m are expressed in the form:

$$a(T) = a_0 + a_1\ \exp\left(a_2\ T\right) \tag{4.11}$$

$$\varepsilon_m(T) = -\varepsilon_{m0} + \varepsilon_{m1}\ T \tag{4.12}$$

where a_0, a_1, a_2, ε_{m0} and ε_{m1} are fitting parameters. The $J_{c,s.f}$ strain dependency of YBCO for temperature between 40 K and 83 K [175] is shown in figure 4.18 along with a fit according to equation 4.10. The data are well fitted over the entire strain range and thus at all temperatures. The parameters values of equation 4.10 for YBCO SP and YBCO AMSC conductors are reported in table 4.11.

Table 4.11: Parameters values of the $J_{c,s.f}$ strain sensitivity of YBCO SP and YBCO AMSC conductors.

	YBCO SP	YBCO AMSC
J_{c0,ε_m} (A/mm^2)	3997	648
T_e (K)	98	94
k (-)	1.64	1.45
a_0 (-)	1000	1200
a_1 (-)	4.3e-4	4.3e-4
a_2 (-)	0.201	0.201
ε_{m0} (%)	0.23	0.44
ε_{m1} (-)	5.1e-5	5.1e-5
$\varepsilon_{irr,c}$ (%)	-2	-2
$\varepsilon_{irr,c}$ (%)	0.7	0.5

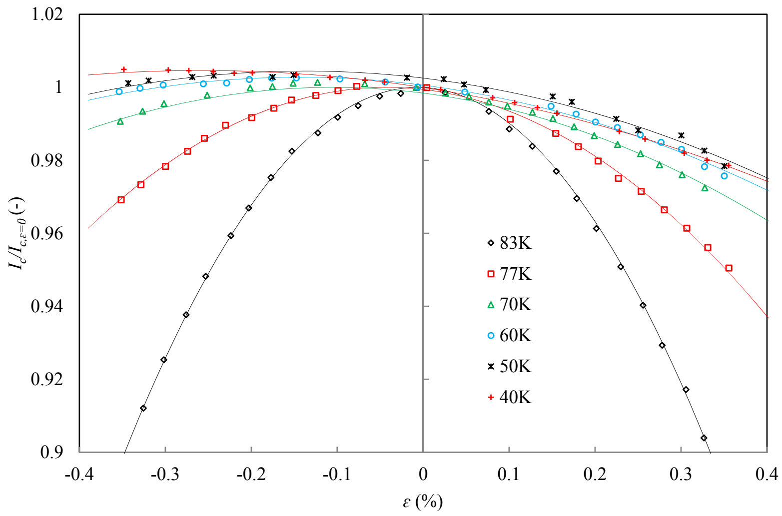

Figure 4.18: The J_c of YBCO IBAD conductors in self flux density as a function of the axial strain: measurements [175] (markers) and compared with equation 4.10 (lines).

Dependence on axial strain over the reversible and the irreversible regimes

The $J_c(\varepsilon)$ parameterization proposed here describes the intrinsic reduction of J_c with strain in the reversible regime but also the sudden and irreversible reduction of J_c beyond $\varepsilon_{irr,t}$ and below $\varepsilon_{irr,c}$:

$$J_{c,s.f}(\varepsilon,T)=\begin{cases}0 & \text{for } \varepsilon<\varepsilon_{irr,c}\\ J_{c0,\varepsilon_m}\left(1-\frac{T}{T_e}\right)^k\left(1-a(T)\left[\varepsilon-\varepsilon_m(T)\right]\right)^2, & \text{for } \varepsilon_{irr,c}\leq\varepsilon\leq\varepsilon_{irr,t}\\ 0 & \text{for } \varepsilon>\varepsilon_{irr,t}\end{cases} \tag{4.13}$$

This fit is accurate in the reversible regime but tends to underestimate the measurements in the beginning of the irreversible regime. The real transition between reversible and irreversible regimes is not as sharp as modelled here.

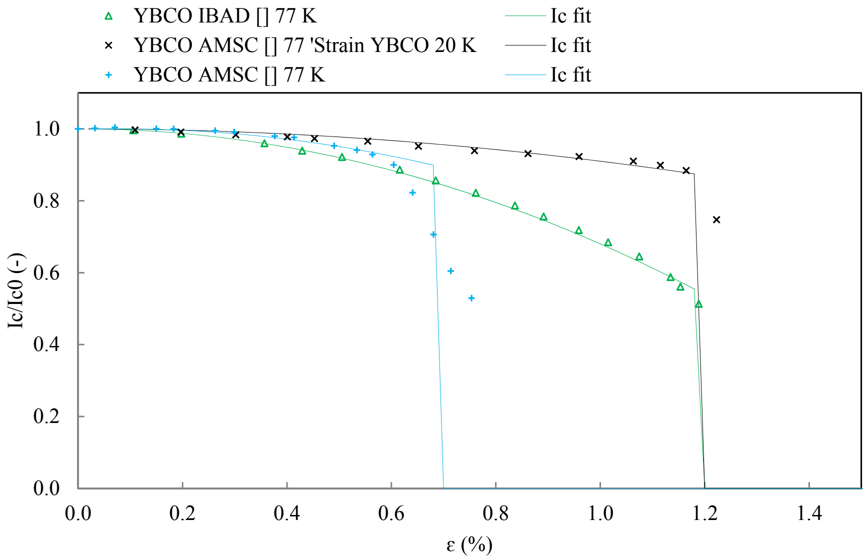

Figure 4.19: The YBCO J_c dependence on axial strain in the reversible and irreversible regimes. The measurements [175] (markers) are compared with equation 4.13 (lines).

4.4.2 Axial strain induced by bending and twisting

To make up coated conductors, YBCO compound is mechanically coupled to various materials including the substrate, the silver shunt and reinforcement cladding. Estimation of the real shear strain occurring in the cuprates is not straightforward. In addition, the J_c sensitivity of HTS conductors to shear strain have not been reported. The main assumption of this work is that the cabling-winding activity induces only longitudinal axial strain. The HTS film in YBCO conductors has a very large aspect ratio (4000-12000) with a thickness of about 1 μm: it can therefore be considered as a surface. An axial stress (σ) applied on a HTS tape induce a uniform strain distribution within the tape cross section. The strain is given by : $\varepsilon_t=\frac{\sigma}{E}$ where E is the modulus of elasticity. When submitted to bending or torsion, specific strain distributions are induced in the tape cross section. These strain distributions are introduced in the next sections.

Axial strain induced by edge and face bending

The YBCO conductors are in the form of tapes with large aspect ratio of about 10 to 200. One can distinguish therefore the edge bending and the face bending. These two bending are also frequently named respectively hard and easy bending due to the difference in moment of inertia of the cross section.

The tapes are bent to a radius of curvature R at the neutral axis. For edge bending, the neutral axis is at the conductor mid width, for reasons of symmetry. For the usual case of equal thickness of stabilizing copper on both sides of the conductor, the YBCO composite conductor is nearly symmetric about the metallic substrate. Since the YBCO layer and buffer layers are relatively thin, the neutral axis for face bending is therefore located near to the conductor mid thickness, as depicted in figure 4.20. Applying the standard treatment of bending in thin beams, the strain in the YBCO film for edge bending (ε_{eb}) and face bending (ε_{fb}) is expressed as:

$$\varepsilon_{fb}(R) = \frac{y}{R} \qquad \varepsilon_{eb}(R) = \frac{x}{R} \tag{4.14}$$

where x/y is the distance to the neutral axis for edge/face bending and R is the curvature radius of the conductor neutral axis (see figure 4.20). For face bending, all location of YBCO film are equidistant from the neutral axis ($y = cst.$), the strain is therefore uniform in the HTS film. The YBCO film is deposited on only one side of the substrate: the bend strain is tensile or compressive depending on whether the YBCO film is toward the outside radius or the inside radius. For edge bending, the strain distribution across the tape width is linear, with the outside radius in tension and the inside radius in compression. The maximum strain occurs at the tape edges ($x = \pm w/2$) and is equal to $\varepsilon_{eb,edge} = \pm w/(2\ R)$. The strain at tape mid width is null ($\varepsilon_{eb,x=0} = 0$). The strain distribution across the conductor width is depicted in figure 4.20.

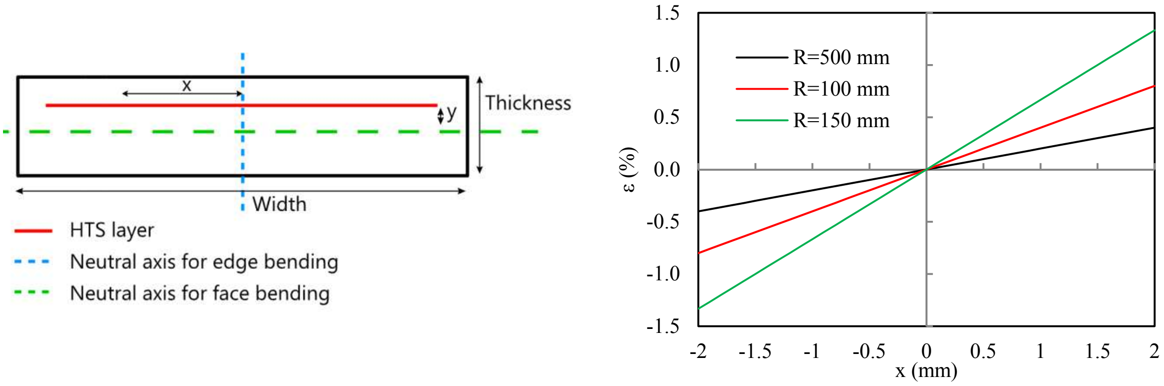

Figure 4.20: Schematic illustration of YBCO conductor cross section with the neutral axis for edge and face bending (left) and the axial strain induced in a 4 mm wide conductor by edge bending (right).

Axial strain induced by twisting

For torsion the YBCO film is assumed to be at the conductor mid thickness ($y = 0$). When a torsion angle (ψ) is applied to a thin rectangular tape of the length L as shown in figure 4.21, a longitudinal chord parallel to the z-axis at the distance x from the z-axis elongates to the length L'. The twist pitch T_p of the YBCO tape is defined as the length over which the YBCO tape is transposed ($T_p = 2\pi L/\psi$). The chord length L' is expressed as a function of the twist pitch as [202]:

$$L' = \sqrt{L^2 + \left(\frac{2\pi x L}{T_p}\right)^2} \approx L\left[1 + \frac{1}{2}\left(\frac{2\pi x}{T_p}\right)^2\right] \tag{4.15}$$

Therefore the tensile axial longitudinal strain (ε_t) of the chord due to torsion is obtained as:

$$\varepsilon_t(x) = \frac{L' - L}{L} = \frac{2\pi^2 x^2}{T_p^2} \tag{4.16}$$

In pure torsion the tape does not have a net force in the longitudinal direction. The integrated longitudinal force (and thus strains in the elastic regime) over the tape cross-section should be zero. To fulfil this requirement a uniform compressive strain ε_0 is established in the tape:

$$\varepsilon_0 = -\frac{1}{w}\int_{-w/2}^{w/2} \varepsilon_t(x)dx = -\frac{\pi^2 w^2}{6T_p^2} \tag{4.17}$$

The longitudinal strain induced by pure torsion (ε_{tw}) is the summation of the tensile strain ε_t and the shortening compressive strain ε_0. The longitudinal strain ε_{tw} is given as a function of the distance x by:

$$\varepsilon_{tw}(x) = \varepsilon_t(x) + \varepsilon_0 = \frac{2\pi^2}{T_p^2}\left(x^2 - \frac{w^2}{12}\right) \tag{4.18}$$

figure 4.21 shows the ε_{tw} in a 4 mm wide tape at different twist pitches. The strain is compressive in the central region and tensile in the edge regions of the conductor.

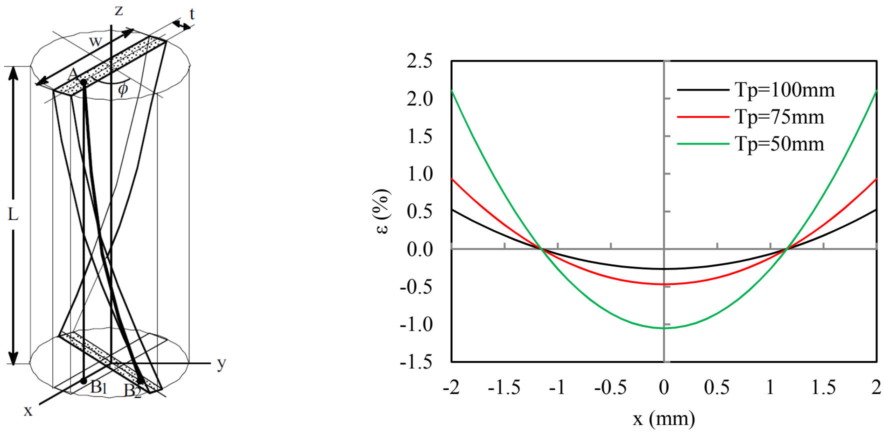

Figure 4.21: Schematic illustration of a single twisted thin rectangular tape (left). The axial strain induced in a 4 mm wide conductor by pure torsion (right).

4.4.3 The I_c dependence of YBCO conductors on bending and twisting

The longitudinal strain induced in a twisted or edge bended tape is not uniform: it is distributed over the conductor width as depicted in figures 4.20-21. The conductor I_c is therefore calculated by integrating the critical current density over the tape cross section. The strain in HTS film is considered to be uniform across film thickness. The conductor thickness in the different expressions is τ.

The I_c dependence under face bending

The strain induced by face bending is homogeneous in the YBCO film and the conductor I_c reduction with bending radius is expressed as:

$$I_c(T, s.f) = \begin{cases} \tau\ w\ J_{c0,\varepsilon_m} \left(1 - \frac{T}{T_e}\right)^k \left(1 - a(T)\left[\frac{y}{R} - \varepsilon_m(T)\right]\right)^2, & \text{for } \ R \geq y/\varepsilon_{irr} \\ 0 & R < y/\varepsilon_{irr} \end{cases} \tag{4.19}$$

Where y is the distance between the HTS layer and the neutral axis for bending, as depicted in figure 4.20. This expressions stands for YBCO in compression or in tension. The I_c reduction with bending radius is progressive down to the point where the I_c drop to zero since the strain is in excess of ε_{irr}. When the YBCO SP tapes is toward the inside radius, the HTS layer is in compression. The irreversible strain in compression is larger than the one in tension. The conductor I_c is less sensitive for YBCO in compression than for YBCO in tension. This is easily explained by the negative values of ε_m for YBCO conductors. In figure 4.22 the normalized I_c of YBCO conductor as a function of the easy bending radius is reported at a temperature of 4 K and 77 K.

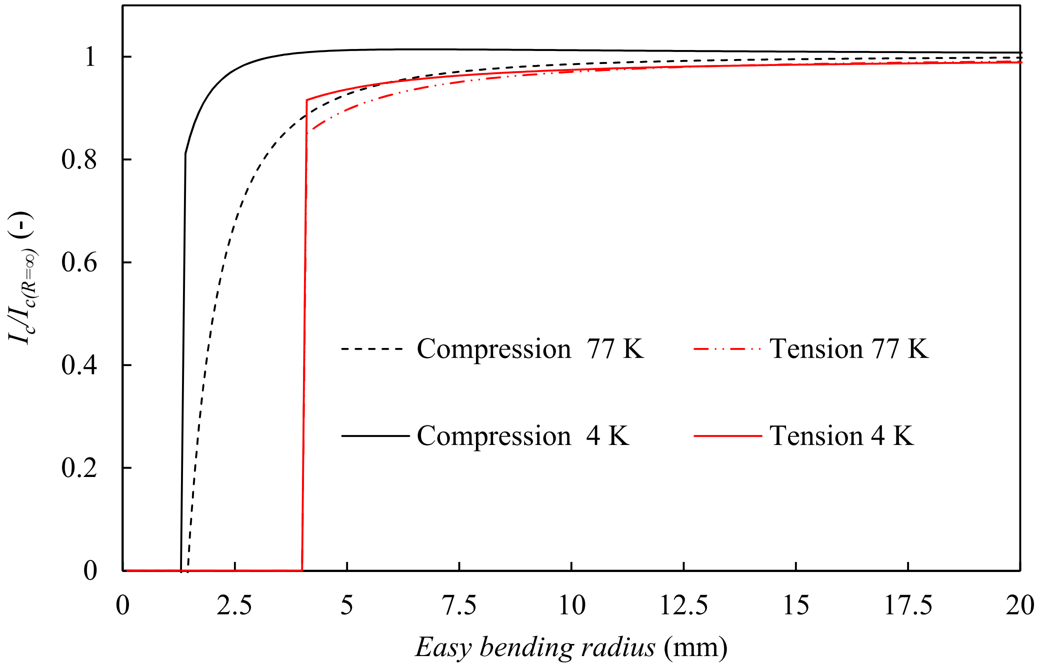

Figure 4.22: The I_c reduction with easy bending radius (expression 4.19) at 77 K and 4 K for compressive and tensile strain in YBCO layer (y=0.28 mm and parameter values of table 4.11).

The I_c dependence under edge bending

For the integration of expressions 4.13 and 4.14 over the film width, three distinctive regimes of bending radius are considered: the large, the medium and the small. The three regimes are delimited by $R_{i,t}$ and $R_{i,c}$, respectively the radius for which strain at conductor edge is equivalent to $\varepsilon_{irr,t}$ and $\varepsilon_{irr,c}$. The $R_{i,t}$ and $R_{i,c}$ are expressed as:

$$R_{i,t} = \frac{w}{2\varepsilon_{irr,t}} \qquad R_{i,c} = -\frac{w}{2\varepsilon_{irr,c}} \tag{4.20}$$

With $0 < R_{i,c} < R_{i,t}$ since $\varepsilon_{irr,t} < -\varepsilon_{irr,c}$ for YBCO SP and YBCO AMSC conductors.

Large bending radius

In the case of large curvature radius ($R_{i,c} < R_{i,t} < R$) all the YBCO film stays in the reversible axial strain regime and the conductor I_c is given by:

$$I_{c,L}(R) = \tau \int_{-w/2}^{w/2} J_{c,0\varepsilon_m} \left(1 - \frac{T}{T_e}\right)^k \left(1 - a\left|\frac{x}{R} - \varepsilon_m\right|^2\right) dx \tag{4.21}$$

$$= \tau \; w \; J_{c,0\varepsilon_m} \left(1 - \frac{T}{T_e}\right)^k \left(1 - a{\varepsilon_m}^2 - \frac{aw^2}{12R^2}\right)$$

Medium bending radius

In the case of medium curvature radius ($R_i, c \leq R \leq R_i, t$) the tape edge under tension is in the irreversible strain regime whereas the rest of YBCO film is in the reversible strain regime. The tape I_c is given by:

$$I_{c,M}(R) = \tau \int_{-w/2}^{\varepsilon_{irr,t}R} J_{c,0\varepsilon_m} \left(1 - \frac{T}{T_e}\right)^k \left(1 - a\left|\frac{x}{R} - \varepsilon_m\right|^2\right) dx \tag{4.22}$$

$$= \tau \; J_{c,0\varepsilon_m} \left(1 - \frac{T}{T_e}\right)^k \left(\frac{w}{2}\left[1 - a{\varepsilon_m}^2 - \frac{aw^2}{12R^2} - \frac{a\varepsilon_m w}{2R}\right] + R\varepsilon_{irr,t}\left[1 - \frac{a\varepsilon_{irr,t}^2}{3} + a\varepsilon_{irr,t}\varepsilon_m - a\varepsilon_m^2\right]\right)$$

Small bending radius

In the case of small curvature radius ($R < R_{i,c}$) both tape edges are in the irreversible strain regime whereas the center of the YBCO film is in the reversible strain regime. The tape I_c is given by:

$$I_{c,S}(R) = \tau \int_{\varepsilon_{irr,c}R}^{\varepsilon_{irr,t}R} J_{c,0\varepsilon_m} \left(1 - \frac{T}{T_e}\right)^k \left(1 - a\left|\frac{x}{R} - \varepsilon_m\right|^2\right) dx \tag{4.23}$$

$$= \tau \; J_{c,0\varepsilon_m} \left(1 - \frac{T}{T_e}\right)^k \left(-\varepsilon_{irr,c}\left[1 - \frac{a\varepsilon_{irr,c}^2}{3} + a\varepsilon_{irr,c}\varepsilon_m - a\varepsilon_m^2\right] + \varepsilon_{irr,t}\left[1 - \frac{a\varepsilon_{irr,t}^2}{3} + a\varepsilon_{irr,t}\varepsilon_m - a\varepsilon_m^2\right]\right)$$

The I_c of 4, 8 and 12 mm wide YBCO conductors as a function of the bending radius is depicted in figure 4.23 at temperatures of 4 K and 77 K. The critical radius $R_{i,t}$ and $R_{i,c}$ are depicted with markers. At any given bending radius, the widest is the tape, the smallest is the normalized I_c ($I_c/I_{c,R=\infty}$). The I_c reduction with bending radius is more pronounced at 77 K since material is more sensitive to strain. The I_c reduction for bending radius beyond $R_{i,t}$ is limited, it is more pronounced for a smaller bending radius. Most of the I_c reduction is caused by strain exceeding the irreversible strains, which are temperature constant: the I_c dependence on bending radius at 4 K and 77 K is almost identical (within 15%).

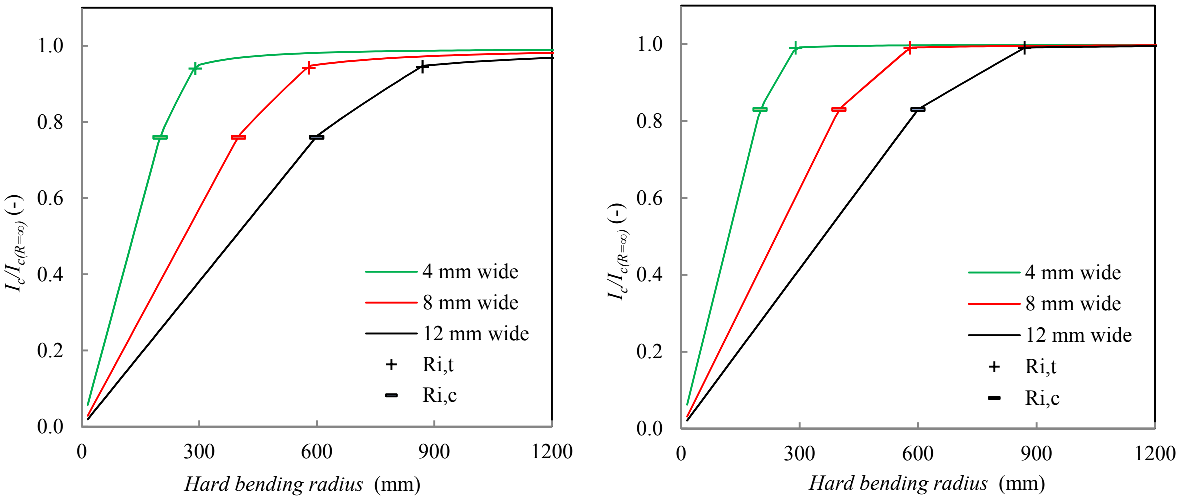

Figure 4.23: The I_c reduction with hard bending at 77 K (left) and 4 K (right) for 4, 8 and 12 mm wide YBCO SP conductors in self flux density.

The I_c dependence on twist pitch (torsion)

The irreversible pitches $T_{p,i,t}$ and $T_{p,i,c}$ are defined as the twist pitch for which the tensile strain at tape edges reaches respectively $\varepsilon_{irr,t}$ and $\varepsilon_{irr,c}$. They are expressed as:

$$T_{p,i,t} = \pi\ w\sqrt{\frac{1}{3\varepsilon_{irr,t}}} \qquad T_{p,i,c} = \pi\ w\sqrt{\frac{1}{6\,|\varepsilon_{irr,c}|}} \tag{4.24}$$

With $T_{p.i.c} < T_{p.i.t}$ since $\varepsilon_{irr,t} < -\varepsilon_{irr,c}$ for YBCO SP and YBCO AMSC conductors.

Long twist pitch

In the case of long twist pitch $T_{p,i,c} < T_{p,i,t} < T_p$ the conductor I_c is given by the integral of J_c over the conductor width:

$$I_c(T_p) = \tau \int_{-w/2}^{w/2} J_{c,0\varepsilon_m}\left(1-\frac{T}{T_e}\right)^k \left(1 - a\left|\frac{2\pi^2}{T_p^2}\left(x^2-\frac{w^2}{12}\right)-\varepsilon_m\right|\right)^2 dx \tag{4.25}$$

$$= \tau\ w\ J_{c,0\varepsilon_m}\left(1-\frac{T}{T_e}\right)^k \left(1-\frac{a}{180}\left(\frac{2\pi^2 w^2}{T_p^2}\right)^2+\frac{\varepsilon_m^2}{2}\right)$$

Medium twist pitch

For medium twist pitch ($T_{p.i.c} < T_p < T_{p.i.t}$) the edges of the tape enter the irreversible strain regime. The tensile irreversible distance ($x_{irr,t}$) is the location in the tape where the axial strain equals the tensile irreversible strain ($\varepsilon(x) = \varepsilon_{irr,t}$). The irreversible distance ($x_{irr,t}$) is expressed as:

$$x_{irr,t} = \sqrt{\varepsilon_{irr,t}\frac{T_p^2}{2\pi^2}+\frac{w^2}{12}} \tag{4.26}$$

The conductor I_c is therefore obtained by the integration of J_c between $-x_{irr,t}$ and $x_{irr,t}$:

$$I_c(T_p) = \tau \int_{-x_{irr,t}}^{x_{irr,t}} J_{c,0\varepsilon_m}\left(1-\frac{T}{T_e}\right)^k \left(1 - a\left|\frac{2\pi^2}{T_p^2}\left(x^2-\frac{w^2}{12}\right)-\varepsilon_m\right|\right)^2 dx \tag{4.27}$$

$$= \tau \, \frac{J_{c,0\varepsilon_m}}{w} \left(1 - \frac{T}{T_e}\right)^k \sqrt{\frac{4\varepsilon_{irr,t}}{c_0} + \frac{w^2}{3}} \left(1 - \frac{a}{270} \left[54\varepsilon_{irr,t}^2 + 270\varepsilon_m^2 + 30c_0\varepsilon_m w^2 + c_0^2 w^4 - 6\varepsilon_{irr,t}(30\varepsilon_m + c_0 w^2)\right]\right)$$

with $c_0 = 2\pi^2/T_p^2$

Small twist pitch

For small twist pitch ($T_p < T_{p.i.c}$) the edges and the central part of the tape are in the irreversible strain regime. The conductor I_c is therefore obtained by the integration of J_c over the range $[-x_{irr,t}, -x_{irr,c}] \cup [x_{irr,c}, x_{irr,t}]$, where $x_{irr,c}$ is the compressive irreversible distance. The $I_c(T_p)$ expression is quite complex and only applicable to small twist pitch where the I_c has already reduced to small values. In addition at small twist pitch large plastic deformations are present in the conductor that are not considered by the model. The analytical description of I_c for small twist pitch ($T_p < T_{p.i.c}$) is therefore not appropriate.

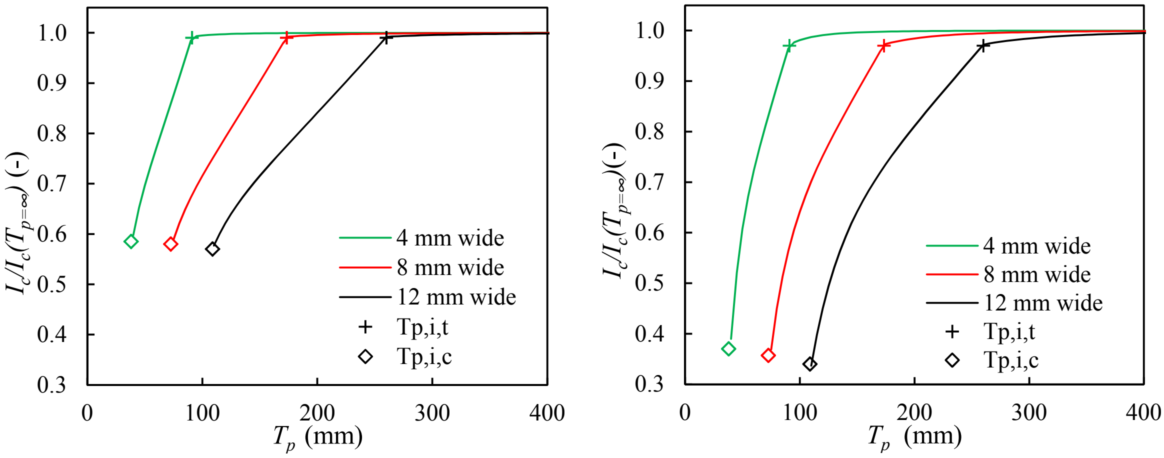

Figure 4.24: The I_c reduction with twist pitch (expressions 4.25 and 4.26) at 4 K (left) and 77 K (right) for 4, 8 and 12 mm wide YBCO SP conductors in self flux density.

4.4.4 Comparison between analytical models and measurements

The electromechanical analytic models of the I_c reduction of YBCO conductor with bending and twisting are compared in figure 4.25 with measurements performed at 76-77 K in self flux density. The models agree well with measurements for both in plane bending and twisting.

4.4.5 Minimum bending radius and twisting pitch of YBCO conductors

The I_c of YBCO conductors dependence on torsion and bending is width, flux density and temperature dependent. For YBCO conductors, we can define the minimum in plane bending radius as R_i, t. The minimum in-plane bending radius is conductor width dependent: 300/870 mm for respectively of 4/12 mm wide YBCO SP tapes. The minimum out of plane bending radius of YBCO conductors depends on the distance between HTS film and neutral axis and on whether the YBCO film is toward the outside radius or the inside radius. For YBCO SP conductors the distance between HTS film and neutral axis is about 27 μm corresponding to a minimum easy bending radius of 4.1 mm (HTS film in tension).

When a YBCO tape is submitted to torsion, edges experience tensile strain. The minimum twist pitch is defined as the pitch for which axial strain at tape edges is equivalent to tensile irreversible strain. For 4/12 mm wide YBCO SP conductor minimum twist pitch is 91/260 mm.

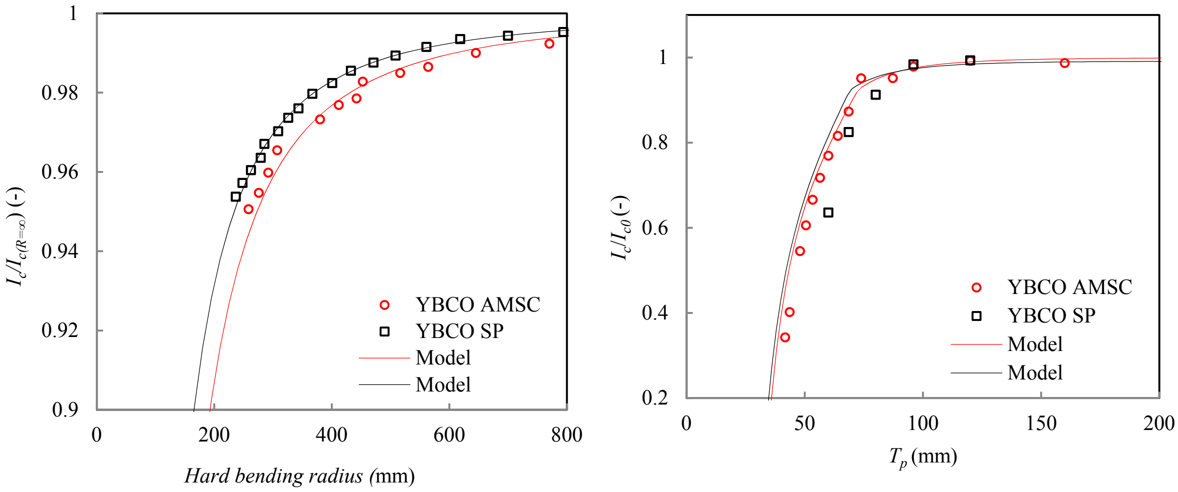

Figure 4.25: The model of I_c reduction with hard bending is compared with reported measurements [203] (left). The model of I_c reduction with twisting is compared with measurements (right).

4.5 Conclusion

Accurate $J_c(B,T)$ parameterizations are derived for the proper use of HTS materials in high flux density magnets. For the promising YBCO SP conductor an empirical formulation of the J_c anisotropy is introduced and a self consistent $J_c(B,T,\theta)$ fit proposed. The fit, accurate over a large temperature and flux density range is then used to compute the operational margins of the YBCO dipole of the EuCARD program. At the bore flux density of 19 T, the critical current margin of the HTS coil is found to be over 14%. The margin along the load line is 9% and the temperature margin is 3.5 K. The use of a small ferromagnetic pole on one hand increases the operational margins, but on the other hand deteriorates the flux density quality. The most critical point of the HTS coil is identified to be at the outermost turns of the top pancake where the flux orientation with respect to the YBCO tapes is maximum.

The design of a YBCO coil has to consider the electromechanical limitations of the conductor. Analytic models of the I_c(T) dependence of YBCO tape on bending and twisting are introduced and used to derive the minimum bending radius and twist pitch that the conductor can withstand. The minimum in-plane bending radius of 4/12 mm wide YBCO SP tapes is respectively 300/870 mm. For out-of-plane bending, the critical radius depends on the architecture of the tape. For a standard tape from SuperPower (50 μm of Hastelloy) the minimum out-of-plane bending was found to be 4.1 mm. The different electromechanical models provide consistent results with respect to performed and reported measurements.

Chapter 5

Characterization of high current HTS cables 4.2 K

High flux density accelerator magnets require multi strand cables with large current capacity. The performance of HTS conductors has been characterized and parametrized in previous chapters. In this chapter two HTS cable topologies made of YBCO conductors have been characterized at 4.2 K in flux densities of up to 9.6 T. The first topology tested is the transposed Roebel cable that exhibited I_c *of up to 11 kA at 7 T. The twisted pair cable was proposed as a new type of electrical transmission cable operating in low flux densities. Its topology it somehow similar to the stacked cable, a promising candidate for application to high flux density magnets. The performance of twisted pair YBCO cables have been measured in flux densities op up to 9.6 T at 4.2 K. The experimental details and the measurements are reported in this chapter.*

High current YBCO cables were characterized at 4.2 K in the test station FRESCA [204]. The test station consists in a 90 mm aperture Nb-Ti dipole magnet, providing an homogeneous flux density of up to 9.6 T over 600 mm [205]. The transport current of the cable was perpendicular to the magnet flux density. The cables tested were about 2 m long and the terminations were placed outside the magnet central flux density. LTS cables were used to carry current to/from station terminals from/to YBCO cables. The cables tested were from the two following topologies:

- **Roebel cables**

  The Roebel cables characterized were made from 10 and 15 YBCO SP conductors. The 12 mm wide and 0.6-0.8 mm thick cables were transposed with pitch of 126 mm and 300 mm. In total, four Roebel cables were measured in FRESCA: two from the manufacturer GCS [81](named respectively GCS1 and GCS2) and two others from the KIT laboratory [77](named respectively KIT1 and KIT2).

- **Twisted pair cables**

  The twisted pair cable was proposed as a new type of electrical transmission cable operating in low flux densities. Nevertheless it topology is similar to the stacked cable that is a promising candidate for high flux density application. Three twisted pair cables, manufactured at CERN, made from respectively 3 YBCO SP, 6 YBCO SP and 6 YBCO AMSC conductors were measured in FRESCA [183]. Cables have a twist pitch of 400 mm and are named respectively TP-SP3, TP-SP6 and TP-AMSC6.

The cable preparation and the measurements are reported in this chapter. The details and the main performances of the different YBCO cables tested in FRESCA are reported in table 5.1. The Roebel cables exhibit I_c in excess of 15 kA in self-field and 12 kA under 7 T of parallel flux density. The twisted pair cables exhibit I_c of up to 7 kA in self-field and 2 kA in 9.6 T.

Table 5.1: Details of HTS cables tested at 4.2 K in FRESCA test station.

Denomination	Topology	Conductor	Number of strands(-)	Width of strands (mm)	I_c in self-field (kA)
GCS1	Roebel	YBCO SP	15	5	11*
GCS2	Roebel	YBCO SP	15	5	15
KIT1	Roebel	YBCO SP	10	5.5	13
KIT2	Roebel	YBCO SP	10	5.5	14
TP-SP3	Twisted Pair	YBCO SP	3	4	4.4
TP-SP6	Twisted Pair	YBCO SP	6	4	6.8
TP-AMSC6	Twisted Pair	YBCO AMSC	6	4.4	6

* *after irreversible I_c degradation*

5.1 Roebel cable characterization

Coated conductors became of specific interests for high flux density accelerator magnets since [72][73] demonstrated their application into transposed Roebel cables in respectively 2006 and 2008. Since these dates, performances of Roebel cables at 77 K and in self-field have been widely reported in the literature [77][206][78], see table 2.6. Measurements of Roebel Assembled Coated Conductor (RACC) cable performances at 4.2 K are necessary to ensure the current transport capacity of these cables for possible application into high flux density magnets. No measurements at 4.2 K of RACC cables have been previously reported: the first characterization at this temperature was carried out in this work [207]. A specific sample holder was developed and used to characterized two different types of RACC cables. Measurements were performed in flux density of up to 9.6 T, oriented perpendicular or parallel with respect to the plane of the cable.

5.1.1 Experimental details

Sample preparation

Two types of RACC cables with different geometries were measured. The two cables consisted of 15 or 10 tapes and they were manufactured respectively by General Cable Superconductors (GCS) and Karlsruhe Institute of Technology (KIT) [81][77]. Coated conductors 12 mm wide, electroplated on both sides with a 20 μm thick copper layer, were punched by the cable manufacturers into the desired meander shape tape and then assembled into Roebel cables. The transposition length of the KIT meander shape tape was 126 mm, while it was 300 mm for the GCS tape. The performances of coated conductors are known to be affected by BaZrO (BZO) doping [208]. At 4.2 K the BZO doped conductors have higher I_c values at low flux densities but with a stronger dependency [137]. The KIT cable used conductors with BZO doping while this was not the case for the GCS cable [209][210]. Over a transposition pitch, a meander shape tape is made of two straight sections and two crossing sections, as depicted in figure 5.1. The angle between the straight and the crossing section is named Roebel angle. Both types of cable have a Roebel angle of 30°. The conductor width differs: in the straight section it was 5 mm for the GCS tape and 5.5 mm for the KIT tape. A remaining gap between two adjacent straight sections of meander shape tape is present at mid-width (see figure 5.1). The main features of the GCS and KIT cables are reported in table 5.2 .

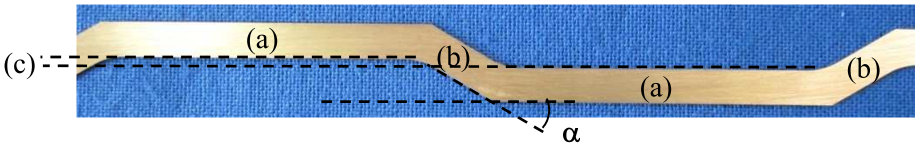

Figure 5.1: The meander shape tape of KIT cable. The longitudinal segments (a), the cross over segments (b), the remaining gap (c) and the Roebel angle between longitudinal and cross over segments α.

Table 5.2: Main features of the two types of Roebel cable tested in FRESCA.

Manufacturer	GCS	KIT
Number of Strands	15	10
Remaining gap (mm)	2	1
Strand width (longitudinal segment) (mm)	5	5.5
Strand width (crossover segment) (mm)	6	5.5
Roebel angle (°)	30	30
Transposition length (mm)	300	126
Cable width (mm)	12	12
Cable thickness (mm)	0.85	0.59

Meander tape I_c inhomogeneity at 77 K

The I_c of each meander shape conductor from the GCS cables was measured by the manufacturer at 77 K and in self-field. The average I_c of the 15 tapes was found to be 165 A with a standard deviation of 13.9% [211]. A large variation between tape I_c was observed: the highest one was 194 A, the lowest one 104 A. After the test at 4.2 K, GCS and KIT cables were disassembled, and the I_c of each meander tape was measured at 77 K and in self-field. The measurements are summarized in table 5.3 and reported in figure 5.2. For GCS cables, a correlation with beforehand measurement (performed by the cable manufacturer) is found. This indicates that no degradation was induced in the cable during the handling, assembly and measurements. For the KIT1 cable, a mean I_c of 126 A with a standard deviation of 16.7% was measured after the test. For both cables, a large variation of the I_c of the meander tapes is observed. For GCS cables the ratio of the highest I_c to the lowest is about 1.9, for KIT cables it is 1.8.

Table 5.3: The meander shape tape I_c of GCS and KIT cables at 77 K and in self-field after and before the electrical test at 4.2 K.

	After electrical measurements at 4.2 K			Beforehand
Roebel cable	GCS1	GCS2	KIT1	GCS [211]
Mean I_c (A)	167	167	126	165
Maximum of I_c(A)	200	205	151	194
Minimum of I_c(A)	106	107	85	104
Standard deviation of I_c (%)	13.9	16.2	16.7	13.9

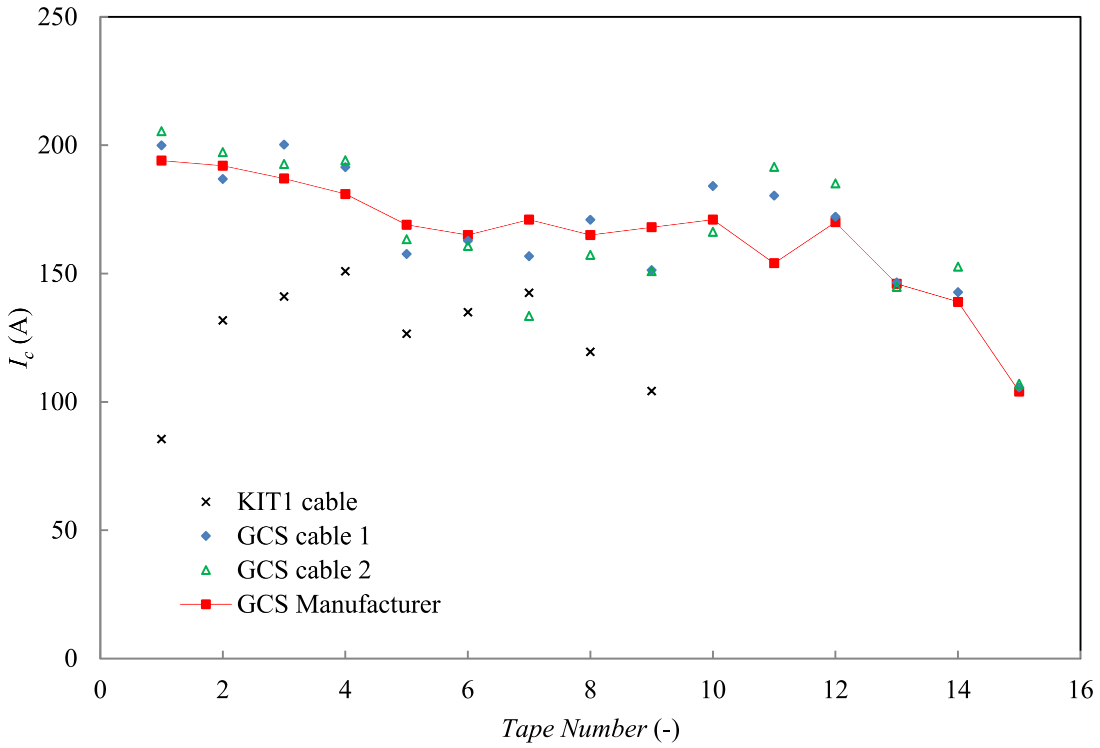

Figure 5.2: The meander shape tape I_c for GCS and KIT cables (at 77 K and in self-field) after the electrical test at 4.2 K. The strand I_c of GCS cable was measured beforehand by the manufacturer [211] at 77 K and in self-field. A large variation of I_c is observed in both cables.

FRESCA test station and sample holder

FRESCA test station

The dipole magnet of the test station FRESCA is put in a separate cryostat (called Outer Cryostat), which is cooled down independently from the samples. The normalized bore flux density of magnet is depicted in figure 5.3 as a function of relative position with respects to the magnetic center. The flux density is homogeneous to within 3% over a length of 600 mm. It drops to 90/50% of central value at a distance of respectively 475/550 mm from magnetic center (see figure 5.3). The sample to be tested is housed in a second cryostat. Both the inner and outer cryostats are vertical double-bath cryostats operating at atmospheric pressure. The sample insert consists of the sample holder, one pair of 32 kA self-cooled current leads and a 300 mm diameter λ plate, fitting tightly into the plate of the inner cryostat. The pair of current leads is connected via water cooled leads to a current supply, made with a modular concept with 8 current sources of 4 kA, 6 V in parallel [204]. The 4 kA sources contain a diode rectifier on the AC mains with a damped L-C filter, a zero voltage switching inverter working at 20 kHz and an output stage (high frequency transformers, Schottky rectifiers and output filters). The current is regulated and measured using two 16 kA DCCTs with a precision better than 10^{-4} [204]. The magnet and sample circuits (including the current leads) are protected against overheating by a 10-channel quench detection system. A total of 25 Platinum and 13 Cernox 1050 sensors are used to monitor the cool-down and warm-up of both cryostats. A Cernox 1050 sensor in combination with a Germanium sensor is used as the reference temperature for the I_c measurement. Both sensors are placed in zero flux density and calibrated with 5 mK accuracy. A possible temperature variation along the 2 m long sample holder is measured by 4 Cernox 1050 sensors. A potential tap package is attached to each sample enabling the measurement of several electrical potential differences over different lengths of the samples. The 16 voltage signals are measured by two Keithley nanovoltmeters via two eight channel nanovolt scanner cards. For a specific test performed on the KIT2 Roebel cable, an array of 26 Hall probes was installed at one edge of the RACC cable in order to measure its self-field. The distribution of the self-field along one cable pitch makes possible to estimate the distribution of the transport current among the strands. A non-uniform distribution can be related to a significant lower I_c-value in one or more strands, or to a non-uniform resistance in the connections on either side of the cable. The Hall probe signals are measured using a Keithley 2000 microvoltmeter coupled with a scanner card.

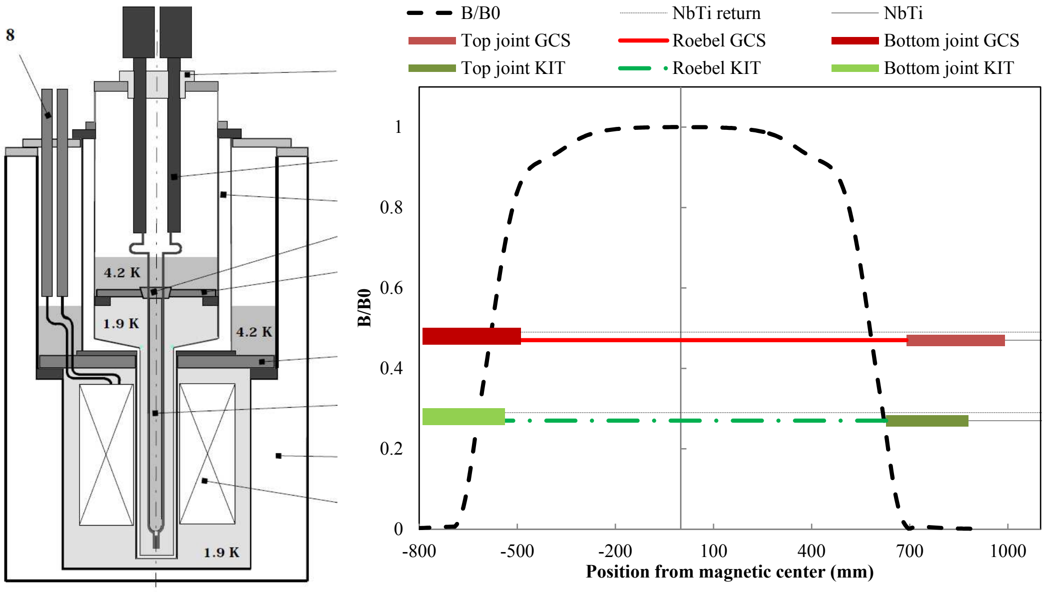

Figure 5.3: Schematic view of the FRESCA test station (left). The flux density profile of FRESCA magnet and the position of RACC cables in regards with the magnetic center (right).

Sample holder

A specific sample holder was developed for the test of the RACC cables in FRESCA. The total length of the GCS/KIT Roebel cable is 1.8/1.65 m. While the magnet operates at 1.9 K, the RACC cables are cooled in a bath of saturated helium at 4.2 K. At 4.2 K three Rutherford Nb-Ti cables carry the current in and out of the RACC cable. Two of these Nb-Ti cables provide the return path of the current (figure 5.5). The electrical joints between the Nb-Ti and the HTS cable have a length corresponding to one transposition pitch for GCS cables and two for KIT cables. This was done in order to ensure both low joint resistance and good current distribution among the HTS tapes. In the electrical connections, RACC and Rutherford cables are soldered together with Sn-Pb eutectic through a thin copper piece. The sample holder consists of a stainless steel plate with a groove which houses the HTS cable (figure 5.5). A pre-stress is applied transversally onto the full cable length to avoid movements during the measurements. The two KIT cables were connected in parallel with a copper shunt (12 mm^2 cross sectional area). The GCS cables were tested without the copper shunt. Epoxy impregnation was not used to avoid potential delamination of the coated conductors [212].

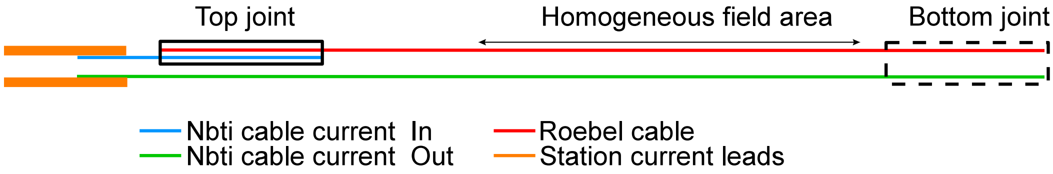

Figure 5.4: A longitudinal schematical view of the Roebel cable sample holder: the top joint is at left side, bottom joint at right side.

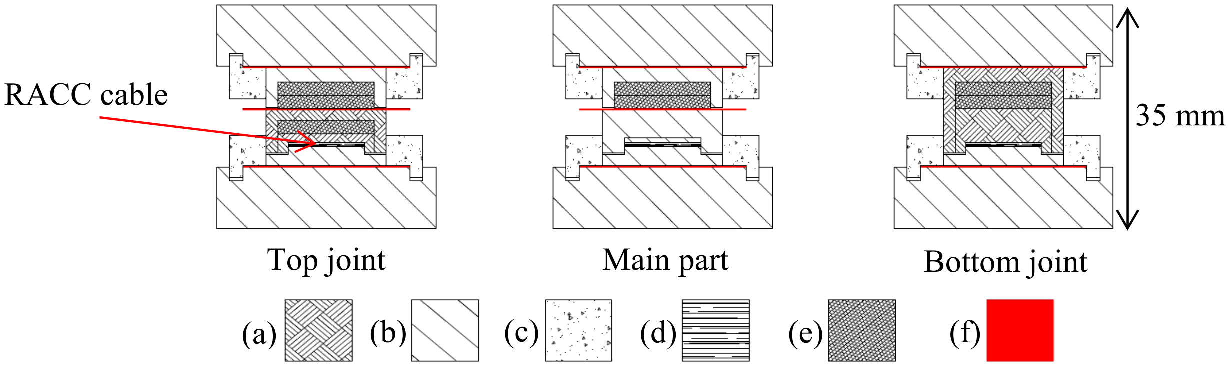

Figure 5.5: Cross section view of the sample holder housing the Roebel cable. The different materials used for the sample holder are also depicted: copper (a), stainless steel (b), G 10 (c), Roebel (d) Rutherford Nb-Ti cable (e) and Polyimide insulation (f)

5.1.2 Cable I_c sensitivity to transverse stress

For the electrical tests at 4.2 K, the RACC cable is housed between two rigid stainless steel plates as depicted in figure 5.5. A pre-stress of about 40 MPa was applied to avoid any cable movement during measurements in flux density. The sensitivity of REBCO coated conductors to uniform transverse compressive stress has been reported [180]. A marginal irreversible I_c degradation was reported for transverse stress of 150 MPa. RACC cables do not have an homogeneous thickness, neither along their length nor across their width. Therefore the applied transverse force is not distributed homogeneously. To measure a possible I_c degradation of the RACC cable when submitted to transverse compression, a RACC GCS cable (150 mm long) was progressively loaded in a mould up to a final average stress of 45 MPa. The cable was loaded at room temperature in the mould by applying a measured torque to the compression screws. The cable was then disassembled and the I_c of four extracted tapes selected among the 15 in the cable was measured at 77 K and in self-field. The RACC cable was then reassembled and submitted to higher stress level. The process was repeated a number of times up to a maximum average stress value of 45 MPa. No I_c irreversible degradation was measured during the tests. The use of Prescale measurement film HS from FujiFilm [213] allowed to print the specific stress distribution in the Roebel cable when submitted to transverse compressive stress. When pressure is applied, red patches appear on the Prescale film. The red color density of Prescale changes depending on the amount of pressure applied. The area with deep red color indicates that the pressure applied was high and conversely the area with light red color indicates that the pressure applied was low. The area with white color indicates no pressure.

For the cables tested at 4.2 K, the stress distribution along the 1.8/1.65 m of cable length was measured by prints on HS films at the nominal pre-stress of 40 MPa required for the test. The cable prints, at the location of potential taps for I_c measurements, are reported in figure 5.6. The 12 mm wide HS films are placed on the top of the Roebel cable. The print pattern of GCS and KIT cables differs because the transposition pitch and the number of strands differs. In figure 5.6 it is possible to identify on both cable types three distinctive areas free of stress all along the cable length: one at the mid-width of the cable and two at the cable edges. The central band free of stress has a width equivalent to 85% of the remaining gap value. The edge bands are 2.1 mm wide for the GCS cable and 2.4 mm wide for the KIT cable. From the prints, the effective area that experiences transverse stress is estimated to be only about 36% for GCS cable and 24% for KIT cable. This implies that a nominal loading up to an average transverse stress of 40 MPa corresponds to a local stress of at least 111 MPa, for the GCS cable, and 167 MPa, for the KIT cable.

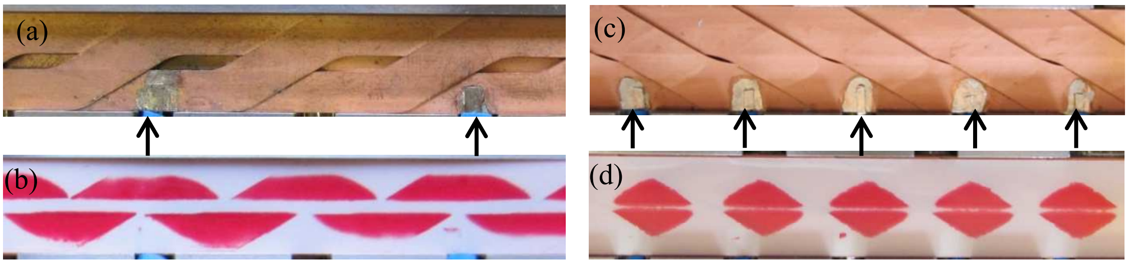

Figure 5.6: Top view of GCS RACC cable in the sample holder after the test at 4.2 K (a). Top view of Fujifilm paper placed on top of GCS RACC cable (b). Top view of KIT RACC cable in the sample holder after test at 4.2 K (c). Top view of Fujifilm paper placed on top of KIT RACC cable (d). The position of potential taps is indicated by arrows. The area with deep red color indicates that the pressure applied was high and conversely the area with light red color indicates that the pressure applied was low. The area with white color indicates no pressure.

5.1.3 Instrumentation of RACC cable

Electric potential taps

The critical current of the RACC cables was determined by measuring the electrical potential difference along individual YBCO tapes. In view of the stress distribution presented in figure 5.6, the largest areas free of transverse stress were chosen for the location of the potential taps. The potential taps consisted in 40 μm thick stainless steel strips electroplated with 5 μm of copper. The presence of soldered potential taps did not affect the stress distribution in the RACC cable. In the homogeneous flux density region 8 strands of the RACC cables were instrumented with pairs of potential taps located at one (GCS cable) or two (KIT cable) transposition pitches distant. Two equipotential taps attached on the LTS cables near each end of the RACC cable were used to measure the electrical potential drop along the RACC cable, splices to Nb-Ti cables included.

Hall probes

A primary motivation for transposed Roebel cable is to promote equal current sharing between strands. However, at low currents the impedance of individual strands within a superconducting cable is dominated by the soldered current contacts, and small differences in solder wetting can lead to different contact resistances and therefore to non-uniform current distribution (see chapter 6 for more details). To determinate the current distribution among strands, the cable self-field along a pitch is measured. The cable self-field is measured using a Hall probe array that consists of 26 Lakeshore HGT-2100 Hall probes, mounted on a circuit board with a spacing of 4.6 mm, see figure 5.7. The active area of the probes is a square with sides of about 1 mm. The first and the last Hall probes are 115 mm apart, which is about one transposition pitch of the KIT cable. The sensitivity of the Hall probes is the ratio between the measured voltage and the flux density present at the Hall probes. A flux density sweep of the magnet between 0 and 3 T in the perpendicular orientation was performed in order to calibrate the sensitivity of each probe. The Hall probes were supplied with a current of 400 μA and sensitivity ranging between 21 mV/T and 24 mV/T was measured. Each Hall probe has an offset that should be determined in no self-field conditions. This criterion is only fulfilled after a cool-down from a temperature higher than T_c, but before the applied flux density or the cable transport current is changed. This means the Hall probe offset can only be measured once every cool-down.

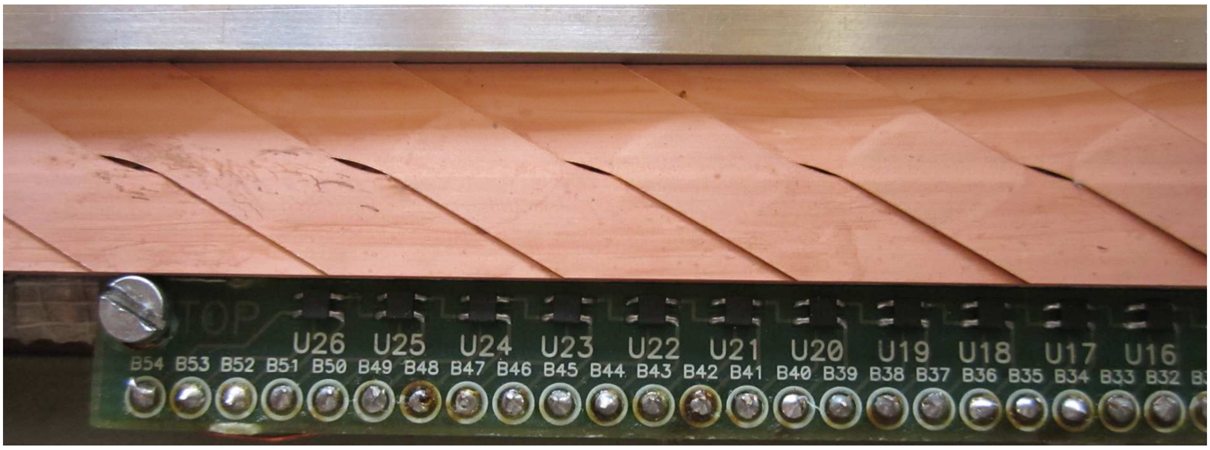

Figure 5.7: The 26 Hall Probe array implemented at the KIT2 cable edge.

5.1.4 Measurements at 4.2 K

In total, four Roebel cables were measured in FRESCA: two from the manufacturer GCS (named respectively GCS1 and GCS2) and two others from the KIT laboratory (named respectively KIT1 and KIT2). Measurements of I_c were performed at 4.2 K and in DC flux densities. The current was ramped up in the sample until a voltage drop corresponding to an electric field of 1 μV/cm was reached across any strands of the cable, then, after a current plateau of few seconds, the current was ramped down with a ramp rate of 50-400 A/s. The ramp-up current rates were varied in a range between 10 A/s and 500 A/s. The sample holder was rotated by 90° to perform measurements both in parallel and perpendicular flux densities. The electric field along individual strands reached during the characterization was too low to compute the cable I_c with the standard criterion of 1 μV/cm. The cable I_c was determined using a 0.2 μV/cm electric field criterion.

Measured cable I_c

The I_c measured on GCS2, KIT1 and KIT2 cables as a function of magnetic flux density, parallel or perpendicular, is reported in figure 5.8. These values were determined from the electric field along respectively tape 5/9 of KIT/GCS cables. In perpendicular flux densities, the I_c vary from 9.9 kA to 10.8 kA at 1 T and 2.4 kA to 3.4 kA at 9.6 T. For flux densities between 6 T and 9.6 T, the decrease in I_c is quasi linear with a slope of about -0.3 kA/T for cables from both manufacturers. The I_c of KIT1 cable was not reached due to a premature resistive transition in the bottom joint. The current limitation of the Nb-Ti Rutherford cables at high flux densities limited measurements to parallel flux densities above 8 T. The cable engineering critical current density (J_{ce}) is defined as the ratio of cable I_c and cable cross section. The J_{ce} of GCS2 and KIT2 cable are depicted in figure 5.8 for perpendicular and parallel flux densities. At low flux density, the KIT2 cable presents higher values of J_{ce} compare to GCS2 cable. On the other hand, the J_{ce} of KIT2 cable is more sensitive to flux density intensity. The deviation in J_{ce} at low flux density is progressively reduced and under perpendicular flux density of 9.6 T the J_{ce} of both cable is similar: 364 A/mm^2 for the GCS2 cable and 332 A/mm^2 for the KIT2 cable.

At 4.2 K the BZO doped coated conductors have higher I_c values at low flux densities but with a stronger dependency [137]. The electrical performance of the Roebel cables clearly depends on the characteristics of the tapes from which it is made.

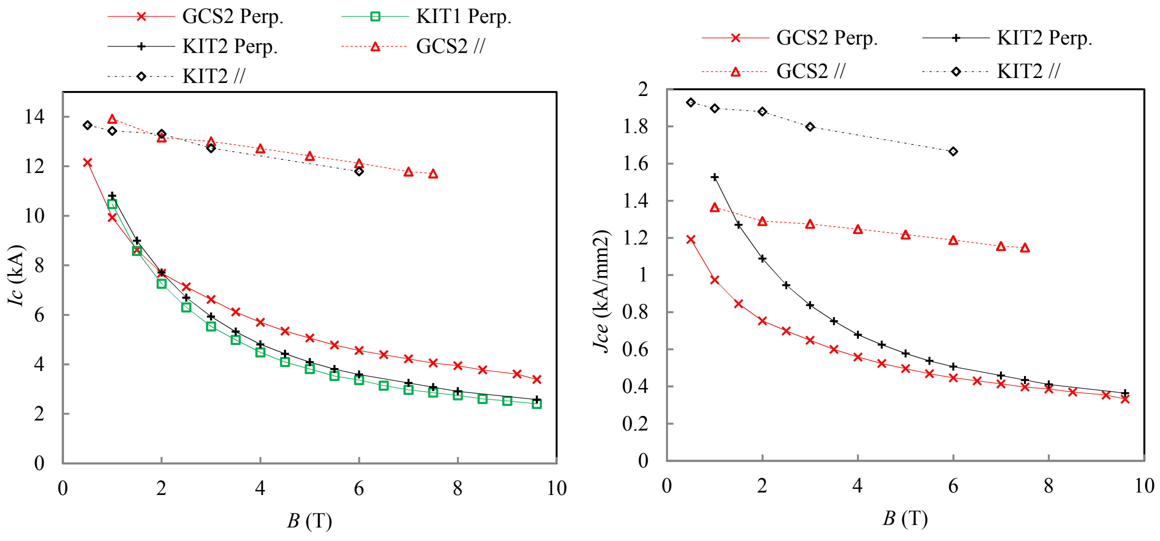

Figure 5.8: The I_c (left) and J_{ce} (right) of Roebel cables at 4.2 K in perpendicular and parallel flux density.

Measurements of joints resistance

The electrical potential drop along the full length of Roebel cable, splices included, (V_{fc}) was measured via equipotential taps soldered on Nb-Ti Rutherford cables. The V_{fc} of KIT2 and GCS2 cables is depicted in figure 5.9 at different perpendicular flux densities. At low cable current ($I < 0.5-0.6I_c$) the V_{fc} present a linear behaviour with current: the V_{fc} signal is generated in the two HTS/LTS splices connected in serial. At higher current, a stiffer slope or even a non-linear rise of V_{fc} is observed: a part of an YBCO tape enters the non-linear resistive transition. The cable current at which the transition occurs between these two behaviours of V_{fc} is named the kink current (I_{kink}). The kink current, is observed to be reduced with flux density. It is 8.8 kA in self-field for GCS2 cable and 3.9 kA at 6 T. The Roebel cable resistance (R_{fc}) is defined as the slope of V_{fc} versus the cable current for cable current lower than I_{kink}. The HTS/LTS splice resistance (R_s) is therefore defined as half of the cable resistance: $R_s = R_{fc}/2$. In figure 5.10, the R_s of the GCS2 and KIT2 cables is reported for perpendicular flux density ranging between 0 and 9.6 T. In self-field, the R_s of KIT2 cable is 2.85 $n\Omega$, it is 1 $n\Omega$ for GCS2 cable.

The lower R_s value of the GCS2 cable is due both to a longer joint and a special procedure adopted during the preparation of the cable: the oxidation layer present on the copper surface of each meander tape was carefully removed before making the joints. The R_s values are weakly increased with external flux density. The bottom joint sees a flux density of up to 80% of that as the magnet center (see figure 5.3): the increase of R_s is easily explained by the magneto resistance of copper and Sn-Pb.

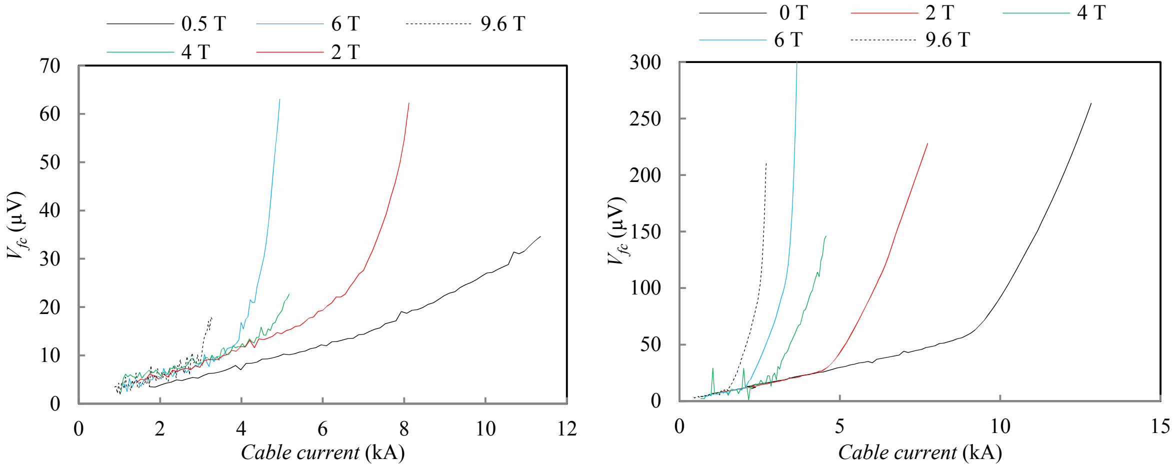

Figure 5.9: The Roebel cable voltage (V_{fc}) of CGS2 cable (left) and KIT2 cable (right) as a function of the cable current at perpendicular flux density ranging between 0 T and 9.6 T.

The splice contact resistivity ($R_s * Surface$) of GCS2 cable is 36 $n\Omega$.cm^2 in self-field. Similar to the 32 $n\Omega$.cm^2 value reported for YBCO SP lap joint at 4.2 K [143]. It should be noted that the HTS/LTS splice of Roebel cables includes a copper piece that contributes as 5 $n\Omega$.cm^2 to the splice resistivity. The normalized deviation of V_{fc} from linear behaviour is defined as:

$$v_{fc} = \frac{V_{fc} - R_{fc} * I_{cab}}{I_{c,cab}} \tag{5.1}$$

Where I_{cab} is the cable current and $I_{c,cab}$ is the cable critical current. The normalized deviation of V_{fc} from linear behaviour is reported as a function of the KIT2 reduced cable current ($i_{cab} = I_{cab}/I_{c,cab}$) in figure 5.10 at different perpendicular flux densities. The reduced kink current ($i_{kink} = I_{kink}/I_{c,cab}$) is observed to be independent of flux density with a value of 0.6. The I_{kink} is therefore correlated to the I_c of the YBCO tapes. For reduced current above i_{kink} the v_{fc} is almost similar for flux densities ranging between 0 and 9.6 T.

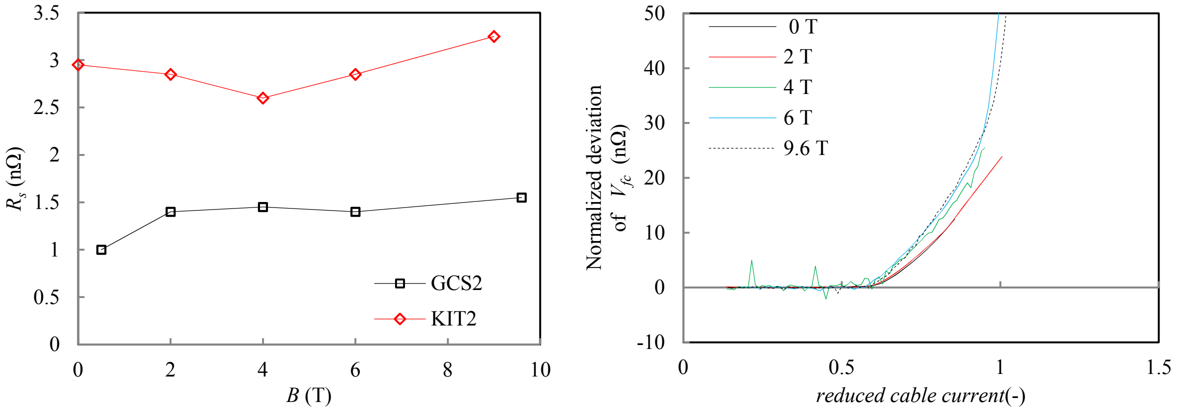

Figure 5.10: The splice resistance (R_s) of GCS2 and KIT2 cables as function of applied perpendicular magnetic flux density (left). The splices are mainly outside the flux density generated by the magnet. On the right is shown the v_{fc} versus the reduced KIT2 cable current at perpendicular flux density ranging between 0 and 9.6 T.

Measurements of the cable self-field

The local self-field of the GCS2 cable was measured by the means of a Hall probe array implemented at one cable edge. The cable self-field was measured by the probes as function of the increasing cable current. The measured cable self-field in a external parallel flux density of 0.5 T is depicted in figure 5.11. Over the different probes, the measured self-field does not increase linearly with the cable current. It could be fitted as a power law with an index inferior to unity. In figure 5.11, the cable self-field measured by the probes 2 and 19 is reported for increasing and decreasing cable current. An hysteresis is observed: the self flux density being higher for ramping up currents. This could be explained by the Bean model [45]. As the current is increased in the Roebel cable, it starts to flow at the edges, screening the interior of the cable from flux density. Then the current penetrates deeper in the width of the YBCO tapes and it contribution to self-field at cable edge is reduced. The cable self-field is therefore not proportional to the cable current. For decreasing cable current, a current density with opposite direction starts to fill the Roebel cable from the edge. Since this current density is in close vicinity to the Hall probes, it contribution to the measured flux density is important. Then the current density penetrates the width of the cable and its contribution is reduced.

In the ideal case of uniform current distribution among strands and across the strand width, the self-field of the cable will be proportional to its current. For the Roebel cable geometry this corresponds to a slope of 110 mT/kA. As already introduced the self-field of Roebel cable is not proportional to the cable current. In figure 5.12, the cable self-field deviation (δ_B) from the linear slope of 110 mT/kA is depicted.

In this plot the specific distribution of self-field along the cable transposition pitch is more evident. The current distribution among the different strands of Roebel cable is not homogeneous and redistribute as the cable current is ramped. The derivative of δ_B with respect to the cable current is depicted in figure 5.12.

At a current of 8 kA, a bump in the derivative of δ_B is observed. This bump corresponds to the cable kink current at this flux density. At this current of 8 kA, the current seems to redistribute among the different strands.

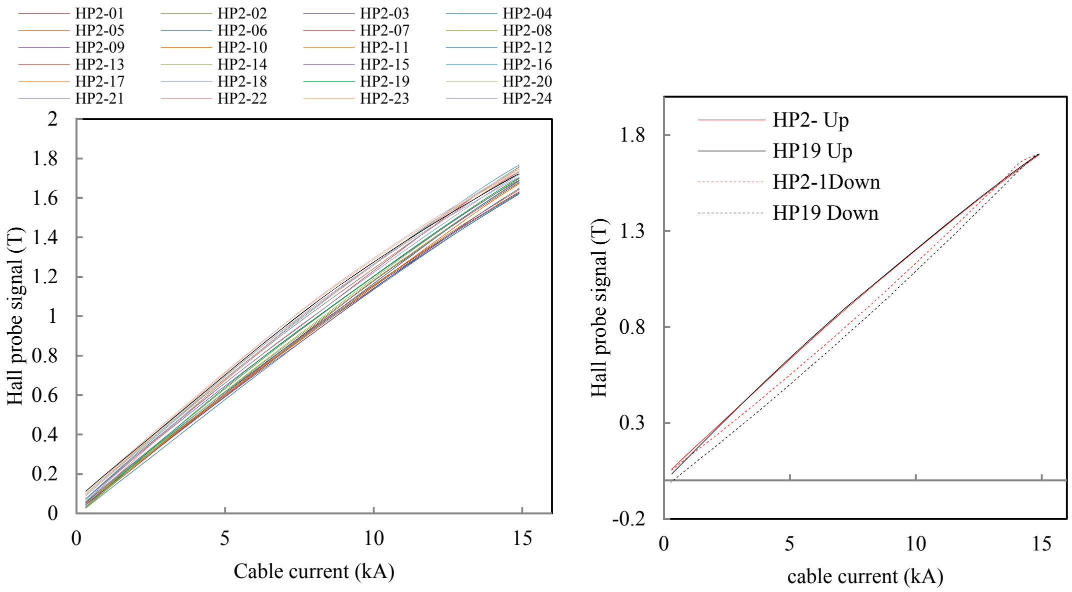

Figure 5.11: The KIT2 cable self-field at a parallel flux density of 0.5 T: as function of the increasing cable current (left) and as function of increasing and decreasing cable current (right).

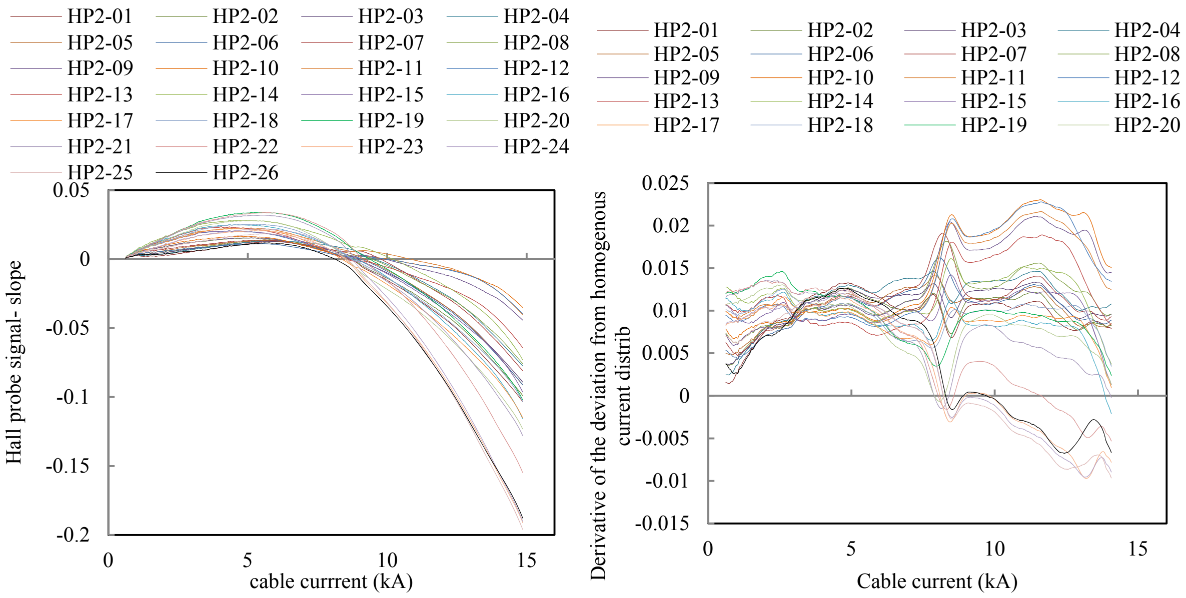

Figure 5.12: The cable self-field deviation from the 110 mT/kA slope (left) and the partial derivative of the cable self-field deviation from the 110 mT/kA slope with respect to the cable current (right).

The electric field along individual tapes

The electric field in perpendicular flux density

In figure 5.13 the electric field along individual tapes is reported as a function of the GCS2 cable current in perpendicular flux density of 7.5 T. At low cable current values, the electric field along the different instrumented tapes is null. At a cable current of 2 kA the electric field in tape 3 starts to increase. The electric field of other tapes increases at higher cable currents of 3.2-4 kA . The increase in electric field for the different tapes is more pronounced as the current approaches the critical one (4.5 kA at this flux density). For currents above the critical current of the cable, the electric fields along individual tapes are identical and increase nonlinearly with current. A similar behaviour is observed in the electric field along the different tapes of KIT2 cable, as depicted in figure 5.13 at a perpendicular flux density of 6 T. The electric field is almost null in all the different tapes up to a current of 2 kA. At this cable current it is increased in 5 of the 8 instrumented tapes. The electric field along the tapes 6 and 2 stays zero and even becomes negative in tape 9. This negative trend indicates a re-circulating current in that specific tape. The measurements have been performed in DC conditions: the negative electric field is not due to an inductive effect. This is highlighted in figure 5.14 where the electric field along tape 9 and tape 8 is depicted as function of increasing and decreasing cable current. The negative electric field along tape 9 is observed at different perpendicular flux densities. The appearance of negative electric field along the tape 9 of KIT1 cable in perpendicular flux density was also observed, as depicted in figure 5.15.

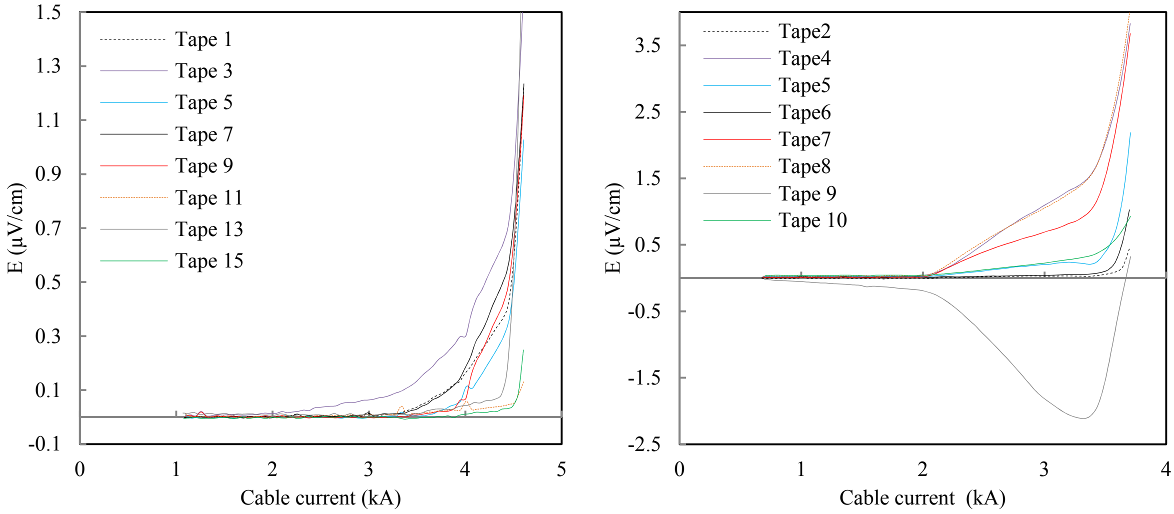

Figure 5.13: The electric field along individual tapes of GCS2 (left) and KIT2 cables (right) as function of cable current at respectively perpendicular flux densities of 7.5 T and 6 T.

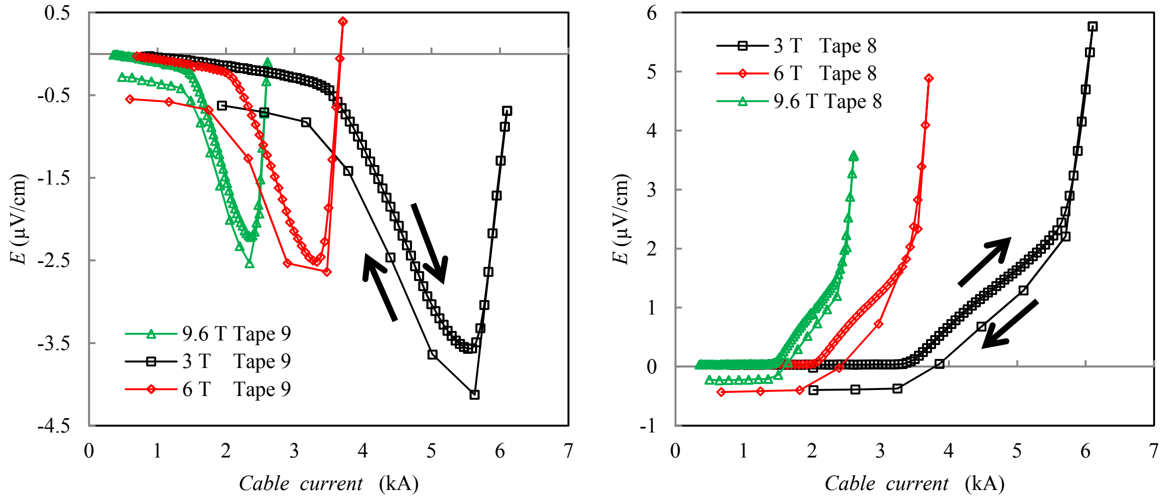

Figure 5.14: The electric field along tape 4 (left) and tape 8 (right) of KIT2 cable at different perpendicular flux densities for increasing and decreasing cable currents.

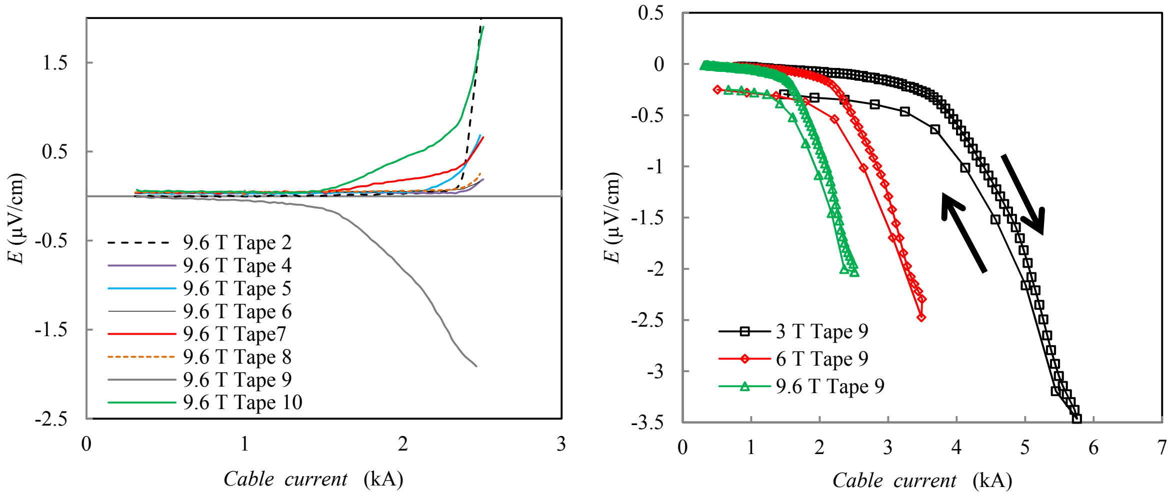

Figure 5.15: The electric field along individual tapes of KIT1 cable at perpendicular flux density of 9.6 T (left). The electric field along tape 9 of KIT1 cable at different perpendicular flux densities for increasing and decreasing cable currents (right).

The electric field in parallel flux density

The electric field along individual tapes of KIT2 and GCS2 cable in parallel flux density of 3 T is depicted in figure 5.16. For KIT2 cable, a behaviour similar to that observed in the perpendicular flux density orientation is observed. The electric field along all the 8 instrumented tapes is null up to 8 kA. Then the electric field increases along 4 tapes whereas it decreases along the tape 9. At 13 kA, almost the cable I_c, all the instrumented tapes undergoes the non-linear resistive transition.

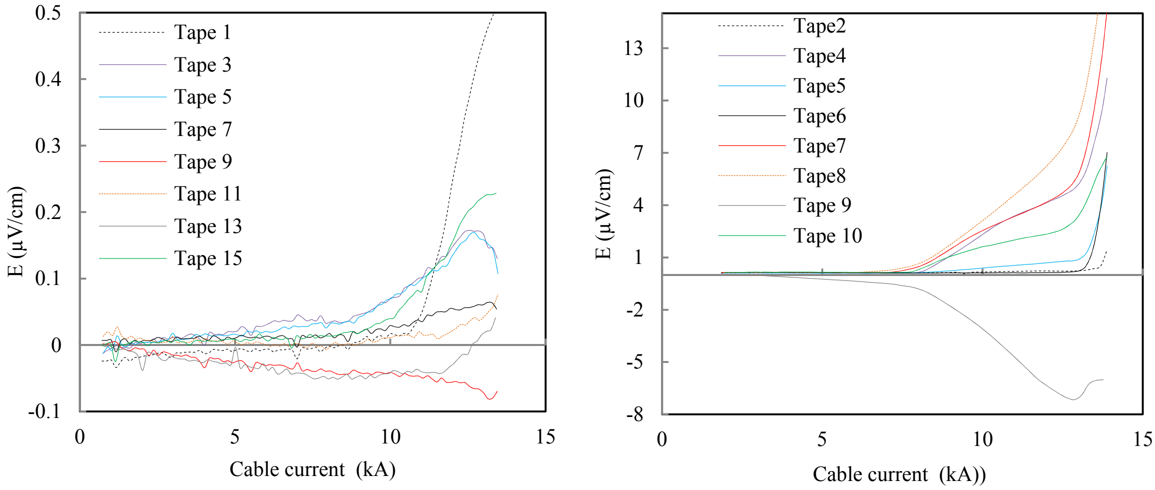

Figure 5.16: The electric field along individual tapes of GCS2 (left) and KIT2 cable (right) as function of cable current at 3 T of parallel flux density.

Ramp rate influence

Characterization of KIT2 cable has been performed at different current ramp rates ranging between 20 A/s and 500 A/s. For current ramp rates in the range 20 A/s and 160 A/s, the electric field along three strands as function of the cable current is depicted in figure 5.17. The EI traces performed at different current ramp rates superimpose up to the cable critical current. Only a small deviation is observed near the cable kink current. This deviation has a small amplitude. The current ramp rate, in the range 20-500 A/s, has no influence on the current distribution among strands of Roebel cables.

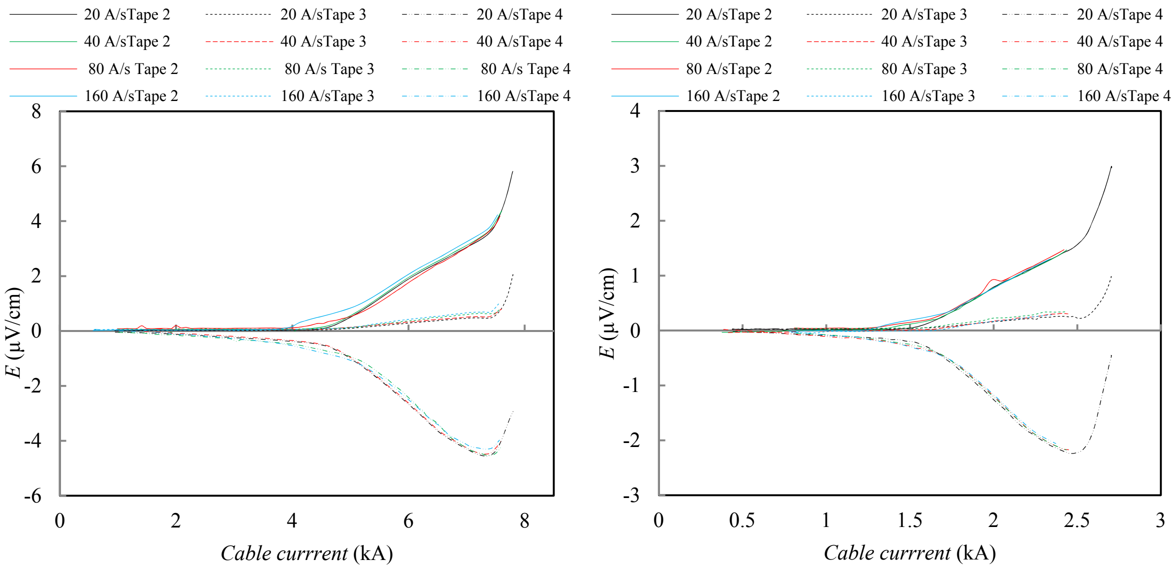

Figure 5.17: The electric fields along conductors of KIT 2 cable as function of cable current at ramp rates of 20, 40, 80 and 160 A/s in perpendicular flux densities of 2 T (left) and 9 T (right).

5.1.5 Interstrand contact resistance measurement

In the Roebel cable topology, adjacent strands are in electrical contact. When the Roebel cable is subjected to a transverse time-varying flux density, the network of interstrand resistances is the seat of current loops that induces losses. If used in accelerator magnet, the current loops also induce dynamic flux density distortions. The flux density distortions are very harmful for accelerator operation, even for a slow-ramping machine, such as the Large Hadron Collider (LHC). The effects of interstrand coupling currents can be limited by developing large interstrand resistances. However, it is also desirable to keep the strands from being electrically insulated from each other, to preserve the possibility of interstrand current redistribution. The interstrand resistance of GCS Roebel cable has been measured at 77 K and in self-field.

Principle of the measurement

The contact resistances between strands of Roebel cable were measured by a four wire measurement at 77 K. The principle of the method is the measurement of the electrical potential difference among opposite strands (strands 1 and 8) of a GCS Roebel cable sample in the superconducting state. The equivalent electrical scheme of the sample is shown on figure 5.18. The circuit consists of two parallel sets of serially connected adjacent contacts (r_a). The adjacent contact resistances are assumed to have uniform value so that the equivalent resistance is given by:

$$R_{eq} = \frac{56}{15}\, r_a \tag{5.2}$$

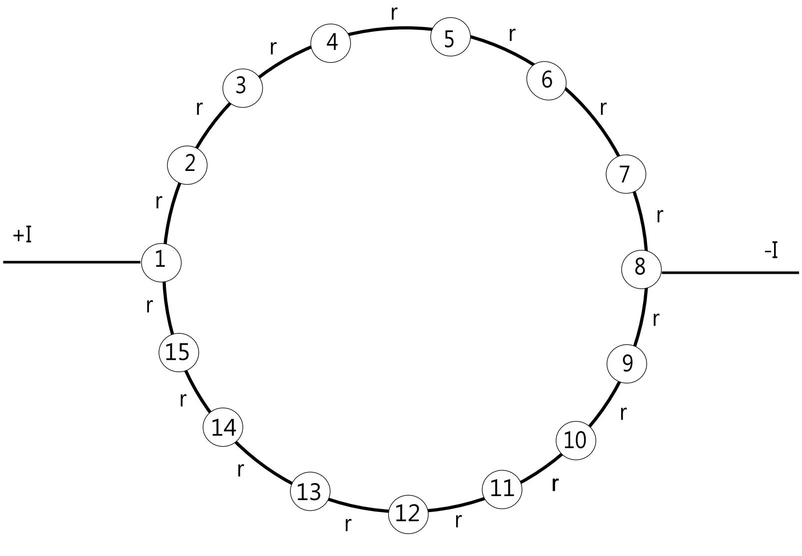

Figure 5.18: The equivalent electrical scheme of the Roebel sample for interstrand contact measurement. The 15 strands of the GCS cable are marked with circles. In Roebel cables only adjacent contact are present.

Experimental set up and measurements

The sample holder consists of a cradle and a piston made of stainless steel. The holder is 300 mm long equivalent to one transposition pitch of GCS cable. The Roebel cable is insulated from the cradle and piston with 25 μm thick polyimide foil. The cable is compressed into the cradle via the piston and screws tightened to predetermined torque values. A pair of potential taps is attached to the strands used as current leads. A current was supplied to the leads, which was varied linearly from 0 to I_{max} to 0, and the electrical potential difference between the instrumented strands were measured. The voltage appears to vary linearly as a function of current, without hysteresis between the up- and down-ramps. The measured equivalent resistance (R_{eq}) between opposite strands was 94 $\mu\Omega$. Over a transposition pitch the adjacent resistance between strands (r_a) is therefore 25 $\mu\Omega$. Roebel cables are not homogeneous in thickness, either along their length or across their width. Therefore the applied transverse force is not distributed homogeneously. The interface contact resistance depends on the contact pressure. It is assumed here that at the location free of transverse stress the contact resistance is infinite. The effective section of Roebel cable that experiences transverse stress was estimated to be only about 36%. The interstrand contact resistivity of GCS cable is therefore computed to be 135 $\mu\Omega.cm^2$. The lap joint resistivity of soldered YBCO SP conductors in the back to face configuration was measured to be about 1 $\mu\Omega.cm^2$ at 77 K and in self-field (see chapter 3). This is two orders of magnitude lower than the interstrand resistivity of Roebel cables. A further measurement performed on a clamped lap joint made from carefully cleaned YBCO SP conductors in the back to face configuration show a splice resistivity of 2 $\mu\Omega.cm^2$ at a transverse pressure of 10 MPa. The large inter strand resistivity of Roebel cable is caused by both the oxides present at strand interface and by the punching process that remove the low resistivity current path at tape edge. In addition the punching process induces delamination between the HTS layer and the stabilizer that could also increase the internal contact resistance of this conductor. A future improvement of the manufacturing process of Roebel strands will be to perform the punching of meander shape tape before the copper electroplating.

5.2 Twisted pair cable characterization

The requirement at CERN for long length power transmission lines operating at temperature of about 20-30 K has led to the design and assembly of a novel type of cable that can be made from pre-reacted, Bi-2223, YBCO or MgB2 tapes [182]. The cable unit consists of an assembly of twisted pair conductors transferring the same current in opposite directions. Each conductor consists of a few HTS tapes (depending on the current capacity requirements) bundled together. Several prototypes were manufactured and characterized at different temperatures [184] and in flux densities of up to 9.6 T [183]. In this work, the experimental details and the main results of the characterization at 4.2 K of three YBCO twisted pair cables are reported.

5.2.1 Experimental details

Cable characteristics

Three twisted pair cables made of YBCO tapes were characterized in the FRESCA test station. One of these cables was made from three YBCO tapes whereas the other two cables were made from six YBCO tapes. For protection requirements, the 3/6 YBCO tapes conductor incorporates 3.2/5.6 mm^2 of copper stabilizer [182]. The protection is assured by the consideration of the copper present in the YBCO conductor and the inclusion of 4 or 7 copper strips interleaved between the YBCO tapes, as depicted in figure 5.19. The copper strips with a residual ratio of resistivity of 100 are 4 mm wide and 0.2 mm thick. The electric insulation of each conductor is provided by Kapton tape [214], 6 mm wide and 50 μm thick, wrapped with 50% overlapping twice around the conductor stacks. The same insulation process is applied to the complete cable unit after twisting. The applied twist pitch of cable assemblies is 400 mm, but some spring back was observed. Since irreversible degradation can occur during twisting, the applied twist pitch was maintained. The total length of the cable unit is 1.8 m. The main cable properties are depicted in table 5.4. The homogeneous flux density of the station, spanning over 600 mm, was applied perpendicular to the longitudinal axis of twisted pair cable. The two cables of the twisted-pair unit were soldered together at one end (HTS/HTS splice), while at the other end they were connected individually to a Nb-Ti Rutherford cable (LTS/HTS splice) transferring the current from/to the bottom end of the station current leads (see figures 5.20-21). The HTS/HTS and LTS/HTS splices are located outside the flux density generated by the magnet. A schematic longitudinal view of the twisted pair unit is depicted in figure 5.20.

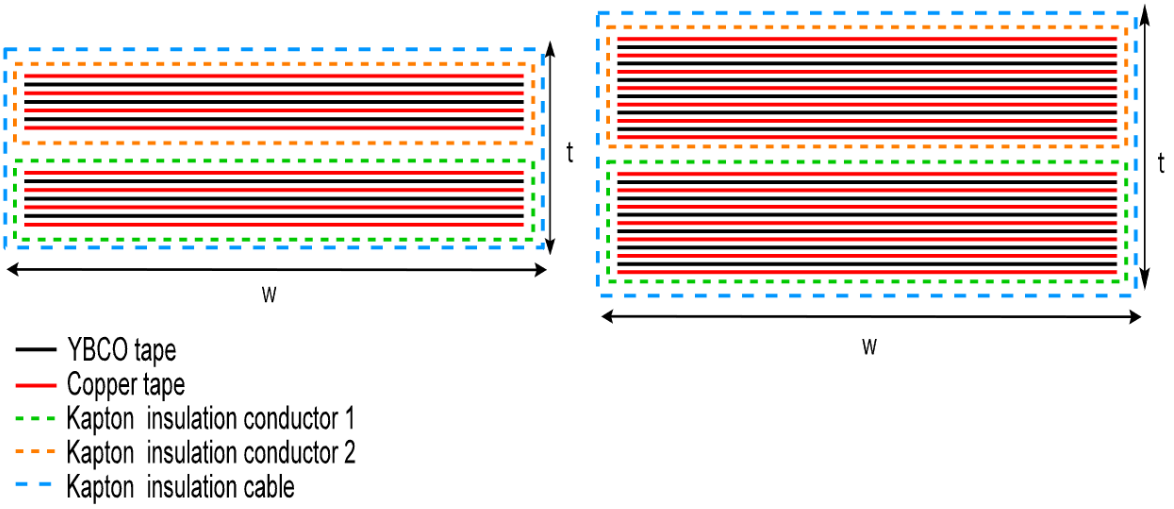

Figure 5.19: Schematical view of the cross section of twisted pair cable made from 3 YBCO tapes (left) and made from 6 YBCO tapes (right).

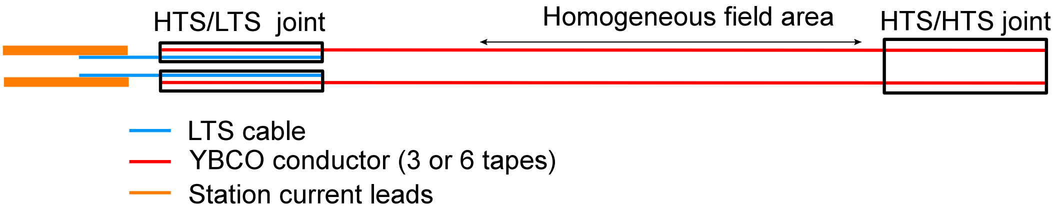

Figure 5.20: Schematical longitudinal view of the twisted pair cable unit for the test in FRESCA.

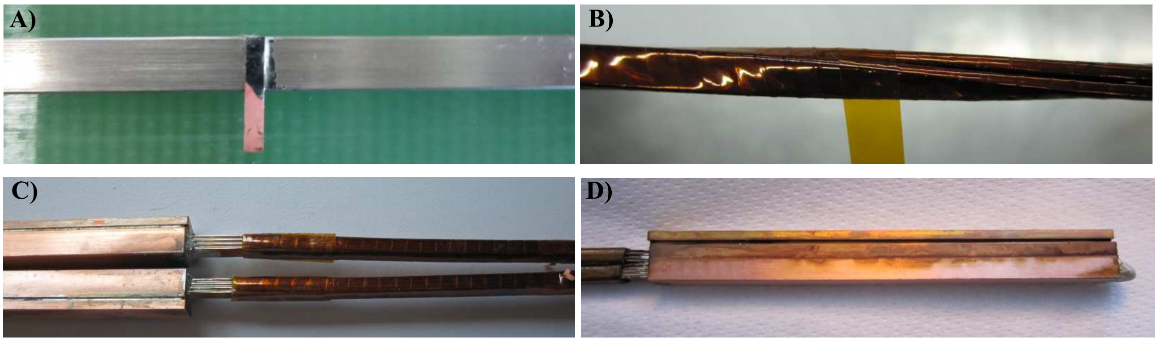

Figure 5.21: The potential taps soldered on the YBCO tape (a), the insulation of the twisted pair unit with Kapton (b), the two HTS/LTS joints (c), the HTS/HTS joint (d).

Table 5.4: Details of the YBCO twisted pair cable assembly tested in FRESCA

Cable ID	TP-SP3	TP-SP6	TP-AMSC6
Number of HTS tape	3	6	6
YBCO tape manufacturer	SP	SP	AMSC
YBCO tape width (mm)	4	4	4.4
Number of copper tapes	4	7	7
Twist pitch applied (mm)	400	400	400
Joint length (mm)	100	240	150
Joint topology	Stack	Stair	Stack

Joint topology

Two different topologies were used for the HTS/HTS and HTS/LTS splices:

- **Stack joint**

  In the stack joint configuration, all the HTS tapes have the same length in the joint, as depicted in figure 5.22. In this configuration, only one HTS tape is directly facing the other cable (HTS or LTS). The manufacturing process of the stack joint topology is easy, but to enter the outermost HTS tape, current has to transit through the innermost ones. This lead to non homogeneous tape splice resistance and a current saturation of the innermost tape. These two phenomenons induce non-uniform current distribution among the different HTS tapes. These issues were addressed by the use of the stair joint topology.

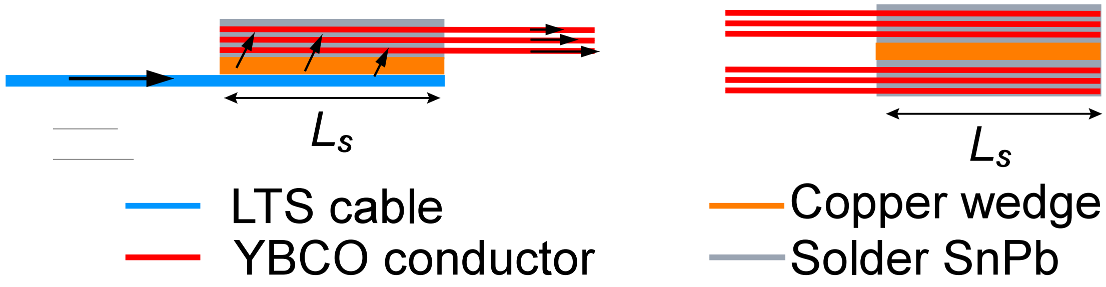

Figure 5.22: Schematical view of a HTS/LTS stack joint (left) and a HTS/HTS stack joint (right).

- **Stair joint**

  The second joint topology is named stair joint. In this configuration all the HTS tapes are directly facing the other cable (HTS or LTS), as depicted in figure 5.23. The length of HTS tapes is not homogeneous in the joints. The innermost YBCO tapes are shorter than the outermost ones. The direct facing of each individual HTS tape over a uniform distance L_s/N_b where L_s is the splice length and N_b the number of tapes in the cable ensure a homogeneous splice resistance and a uniform current distribution among the different HTS tapes. The manufacturing process of stair joint is delicate and the splice length (L_s) increases with respect to the number of tapes in the cable since a minimum direct contact distance (L_s/N_b) should be maintained.

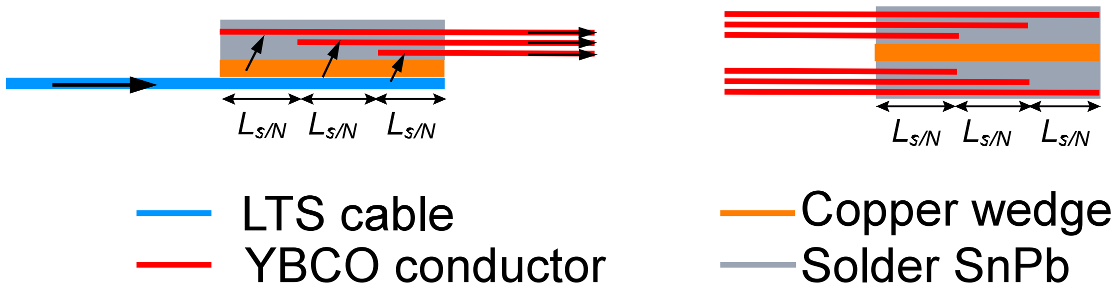

Figure 5.23: Schematical view of a HTS/LTS stair joint (left) and a HTS/HTS stair joint (right).

Instrumentation

Each strand of the twisted pair cables was equipped with pairs of potential taps spanning over 600 mm in the homogeneous flux density area. This length covers more than a cable twist pitch. The implantation of the voltage taps in the cable is depicted in figure 5.24. The taps are placed before the conductor insulation (see figure 5.21). The electrical potential drop along each individual tapes of the cable was simultaneously recorded during cable current increase. These signals are used to compute the cable I_c. To measure the splice resistance, pairs of equipotential taps were soldered on both HTS and LTS cables at a distance of 100 mm from the joint to allow a complete current transfer, as depicted in figure 5.24.

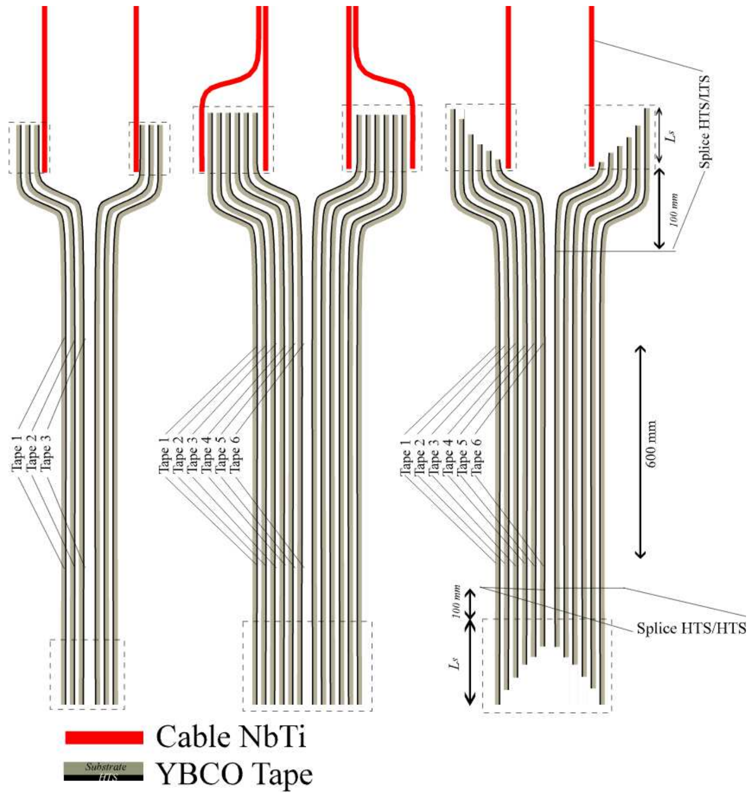

Figure 5.24: Schematical view of the 3 YBCO twisted pair cables tested in FRESCA. The TP-SP3 cable (left), the TP-AMSC cable (middle) and the TP-SP6 cable (right). The position of the potential tapes is also depicted.

5.2.2 Measurements at 4.2 K

Measurements of I_c were performed at 4.2 K and in DC magnetic flux densities. The current was ramped up in the sample at current rates in a range between 10 A/s and 200 A/s. The I_c was measured using the 1 μV/cm electric field criterion.

Measurements of the cable I_c

The electric field along individual tape of TP-SP3 and TP-SP6 cables as a function of the cable current is depicted in figures 5.26-27. Even though the YBCO tapes were in electrical contact, the electric field along each tape was (slightly) different. The cable I_c evaluated from the electric field along the different strands is depicted in figure 5.25. Despite the fact that the electric field strongly differs at low cable current, the cable I_c computed through the electric field along the individual strands is almost uniform. The TP-SP3 cable has an I_c of 4.4 kA in self-field and 0.72 kA at 9.6 T. The TP-SP6 cable has an I_c of 6.8 kA at 0.5 T and 1.4 kA at 9.6 T.

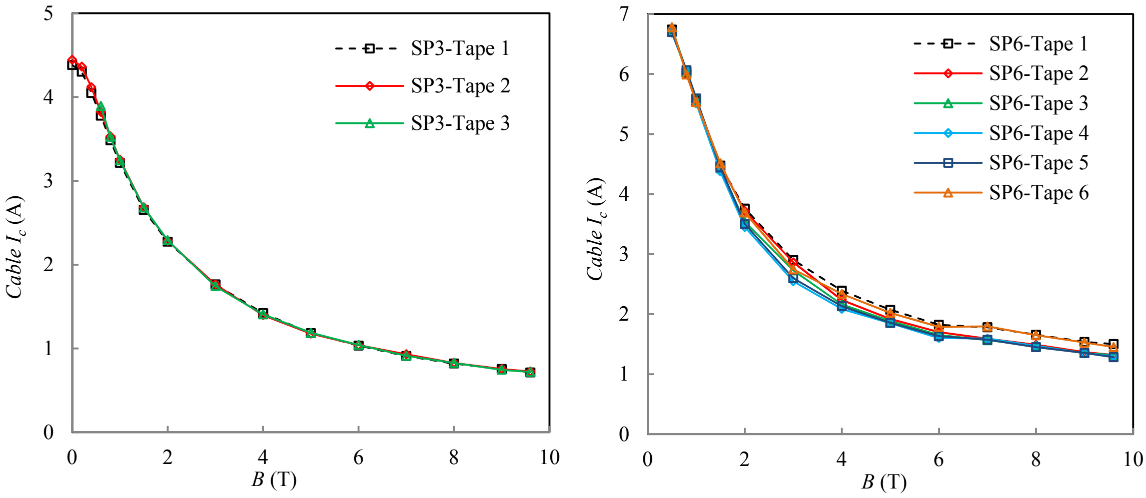

Figure 5.25: The cable I_c computed from the electric field along individual tapes for the TP-SP3 cable (left) and TP-SP6 cable (right).

The electric field along individual tapes

In figures 5.26-27, the electric field along individual tapes of twisted pair cables as a function of the reduced cable current (I/I_c) is depicted. At low reduced currents, the electric field along the different tapes is null. For the TP-SP3 cable the electric field along tape 1 starts to rise at a reduced current of 0.6 whereas it stay zero up to reduced cable current of 0.75 and 0.9 along respectively tapes 2 and 3. As the reduced cable currents approaches unity, the electric field along the different tapes converge to identical values. A similar behaviour is observed for TP-SP6 and TP-AMSC6 cables. The electric field along tapes 6-5 of the TP-AMSC6 cable starts to rise at respectively i_{cab}=0.4 and i_{cab}=0.62. In the TP-SP6 cable, the first electric field to rise is observed at i_{cab}=0.7.

For cable made of stack joints, the appearance of electric field along the strands depends on the number of strands in the cable. The more strands there is, the smaller reduced current the electric field starts to rise. The stair joint promotes homogeneous current distribution among the strands, leading to more homogeneous electrical field along strands.

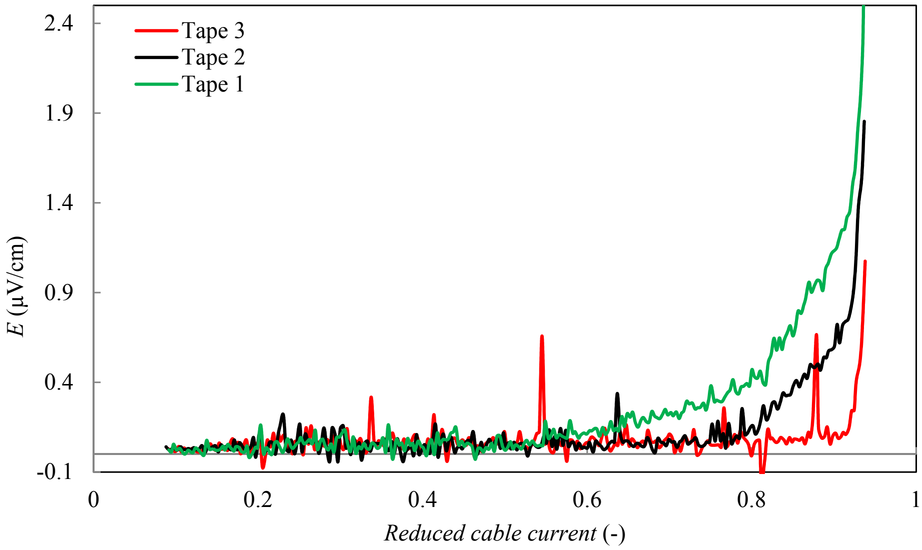

Figure 5.26: The electric field along individual tapes of TP-SP3 cable as a function of the total cable current at flux density of 1 T.

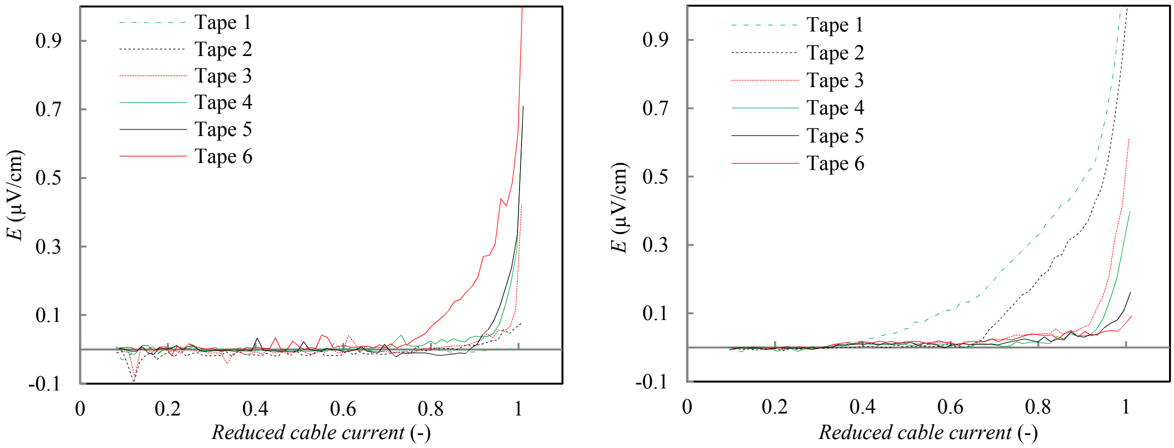

Figure 5.27: The electric field along individual tapes of TP-SP6 (left) and TP-AMSC6 (right) cables as a function of the reduced cable current at flux density of 0.8 T.

Influence of ramp rate

The current ramp rate of TP-SP3 cable was varied between 10 A/s and 200 A/s in self-field. The electric field along strands of TP-SP3 cable as a function of current is depicted in figure 5.28 for different current ramp rates. The electric field along strands depends on current ramp rate. For any ramp rate, electric field along strand 2 is nil up to 2.5-2.8 kA, then it increases linearly up to the critical current where a non-linear rise is observed. The slope of the linear increase is observed to be steeper for larger current ramp rates. The electric field is identical for currents in excess of the cable I_c. The current ramp rates as an influence on the current distribution among strands of twisted pair cables. The strands of twisted pair cables present different self and mutual inductances. This may explain the ramp rate dependence of current distribution.

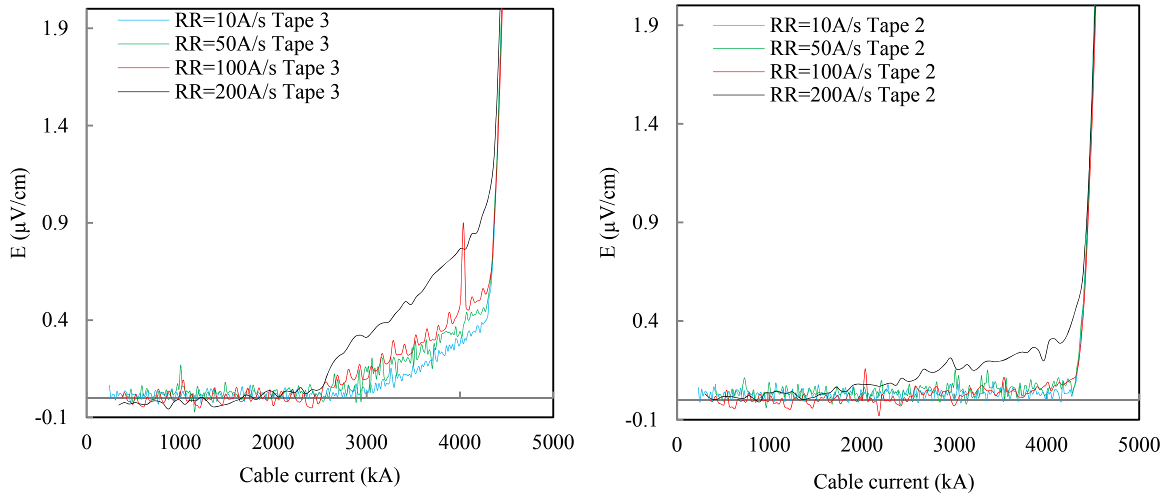

Figure 5.28: The electric fields along individual tape 3 (left) and tape 2 (right) of TP-SP3 cable at different ramp rates and zero external flux density.

Resistance of the HTS/HTS and HTS/LTS joints

The electric potential differences in self-field along the different HTS/HTS and HTS/LTS splices of twisted pair cables as function of the cable current are shown in figure 5.29. At low currents, the voltage across the splices is proportional to the current. At the splice kink current ($I_{s,kink}$), the voltage starts to deviates from the initial slope. The resistances of the HTS/HTS and LTS/HTS joints (R_s) have been obtained by a linear fit of the voltage versus cable currents being lower than $I_{s,kink}$. The splice resistances in self-field are reported in table 5.5. They are ranging between 5 $n\Omega$ and 15 $n\Omega$. The splice resistivity S_c is defined as the product of the splice resistance (R_s) and the splice interfacing area. The reduced cable splice current ($i_{s,kink}$) is defined as the ratio of $I_{s,kink}$ and the cable critical current. The measured $i_{s,kink}$, R_s and S_c are presented in table 5.5. For stack joint, the $i_{s,kink}$ is observed to be reduced with the number of tapes in the cable. At the joint location, all the cable current has to flow through the innermost strand. As the number of strands increases, the current saturation occurs at a reduced i_{cab} value. Large $i_{s,kink}$ and low S_c values are observed for the stair joint topology. The stair joint topology is seen to be far more effective to promote a uniform current distribution among strands.

Table 5.5: Splice resistance of twisted pair cable assembly.

Cable ID	TP-SP3		TP-SP6		TP-AMSC6	
Topology	Stack joint		Stair joint		Stack joint	
	HTS/HTS	LTS/HTS	HTS/HTS	LTS/HTS	HTS/HTS	LTS/HTS
R_s ($n\Omega$)	5.3	5.5	5.1	3	15	7
S_c ($n\Omega.cm^2$)	21.2	22.4	49	34.6	99	46.2
$i_{s,kink}$ (-)	0.59	0.78	0.98	0.95	0.32	0.30

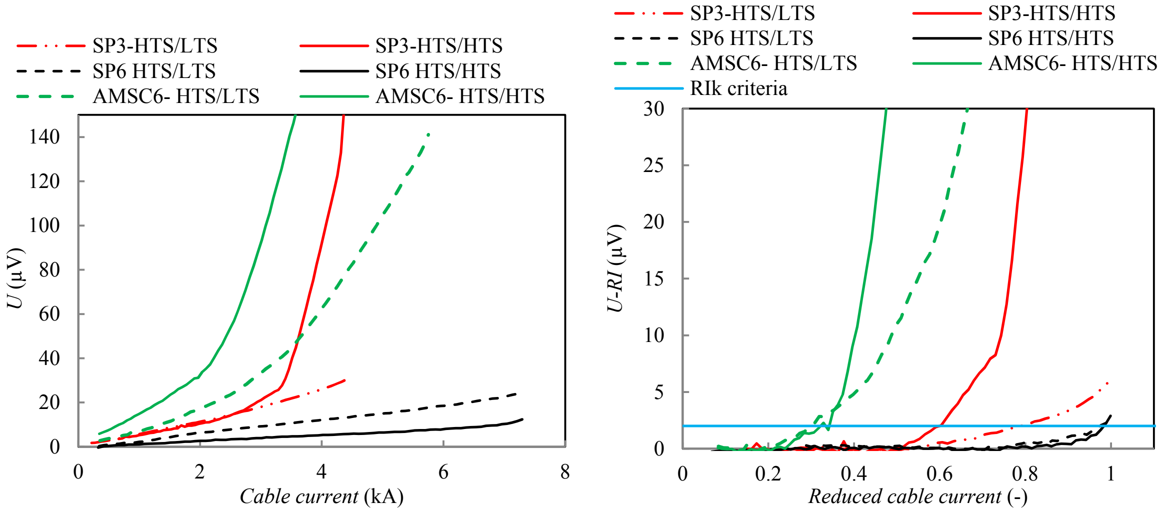

Figure 5.29: The electric potential differences across HTS/HTS and HTS/LTS splices of the twisted pair cables as function of the cable current (left). The voltage across HTS/HTS and HTS/LTS splices reduced from the initial resistive slope (R_s) as function of the reduced cable current (right).

5.3 Roebel cable I_c degradation

Unfortunately at a certain point of the electrical characterization at 4.2 K, the performance of the GCS1 and GCS2 cables were strongly and irreversibly reduced despite the over voltage protection. The threshold of protection was set to 15 mV with an integration time of 10 ms. To avoid a similar I_c degradation, the KIT1 and KIT2 cables were measured in parallel with a copper shunt (12 mm^2 cross sectional area). The chronology of the I_c degradations and the cable damages are discussed in this section.

5.3.1 Chronology of I_c degradation

For the GCS1 cable, a I_c reduction of 27 % occurred under parallel flux density of 6 T and at a current of about 11 kA. This reduction corresponds to the loss of about 4 YBCO tapes among the 15 of the cable. After the incident, the cable was fully characterized in parallel and perpendicular flux density, as depicted in figure 5.30. The occurrence of more than 35 quenches during measurements, didn't irreversibly reduce further the cable I_c. The damaged portion of the GCS1 cable was located in the bottom joint area. The electrical potential differences across the bottom joint before and after the incident are depicted in figure 5.30. Before the incident, the splice kink current was 8 kA, after incident it was 4 kA. The I_c of the GCS2 cable was reduced to zero after a quench occurring at 13.6 kA and 7 T. Before the incident cable was fully characterized in parallel and perpendicular flux density (see figure 5.8). The damaged portion of the GCS2 cable was located also in the region of the lower joint.

5.3.2 Visual observation after incident

After characterization at 4.2 K, the damaged cables were visually inspected. In figure 5.31, the longitudinal position of cable damages is depicted. It is the same (within 26 mm) for the two cables. The damaged cable sections that are 8/36 mm distant from bottom joint, present Sn-Pb flow not present before the characterization, as depicted in figure 5.32. This indicates a temperature in excess of 500 K during the incident. In both cables, two YBCO tapes were locally burnt across their full width. These two tapes are not adjacent in the cable, an YBCO tape is present in between. The YBCO tapes have burnt symmetrically around the cross over segment of the interleaved strand (see figure 5.32). This last tape seems to be damaged along a path that joins the damaged sections of the two other tapes. The

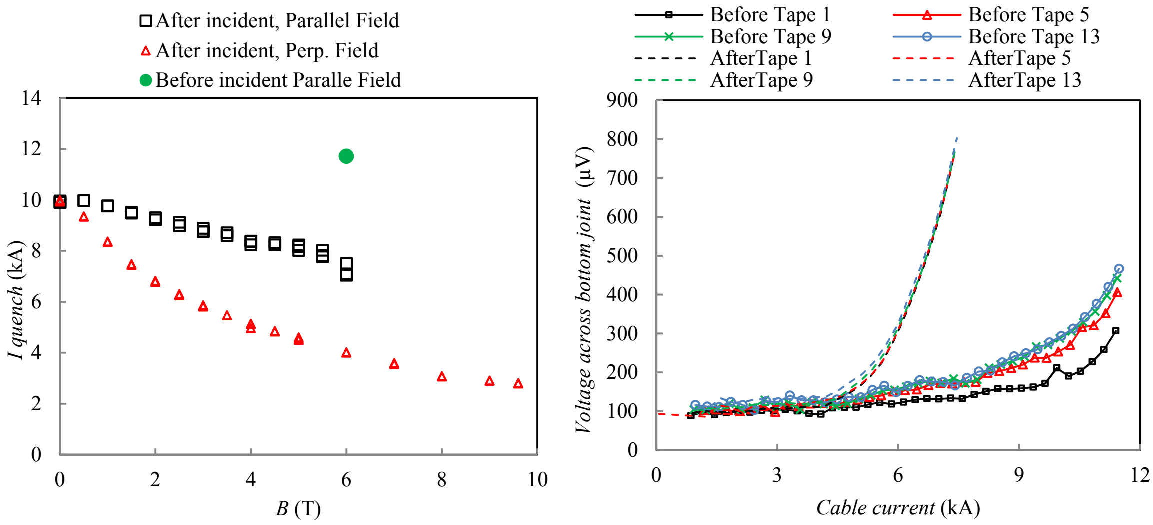

Figure 5.30: The quench current of the GCS1 cable as function of flux density before and after the incident (left). The electrical potential difference across the bottom joint of the GCS1 cable before and after the incident (right).

failure pattern is identical in both cables as depicted in figure 5.32. During the electrical test of the GCS2 cable, a Fujifilm paper was placed on top of the cable. The paper, in contact with the cable was locally burnt during the incident, as depicted in figure 5.32. A red colour of the Fujifilm paper indicate a transverse compressive stress in excess of 10 MPa, the white colour indicate a transverse stress below the paper sensibility of the paper (10 MPa). The Fujifilm paper is burn in area free of stress.

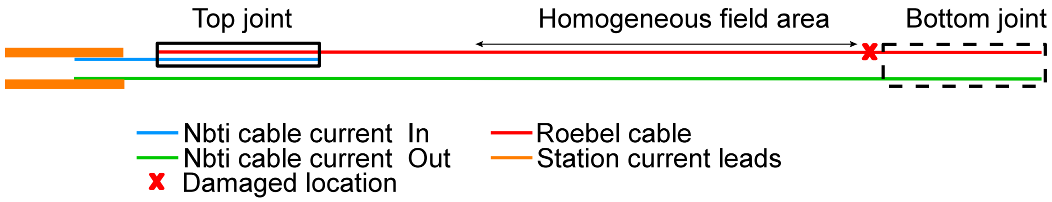

Figure 5.31: Schematic view of the longitudinal position of the damaged section of GCS1 and GCS2 cables.

5.3.3 Microscopic observation after incident

The damaged portions of the cables were prepared for microscopic inspection. The samples were put in a cold mounting resin (ClaroCit from Struers) and then polished successively with grinding papers (P-80, P-180, P-240, P-320, P-600 and P-1200) followed by polishing cloths associated with synthetic diamond liquid. Observations with a Keyence VHX 1000 digital microscope on the longitudinal section down to the defect area were performed [215][216]. The longitudinal microscopic views of the damaged area of GCS1 and GCS2 cable are depicted in figure 5.34. In both cables, an undulation of the cable section is observed at the damaged cable location. During the incident, the temperature of the cable was locally in excess of 500 K whereas the rest of cable was at the helium bath temperature of 4.2 K. This high temperature gradient induced large thermo-differential stresses. As the temperature increased from 4.2 K, the Roebel cable expanded but was constrained longitudinally by boundary conditions: this

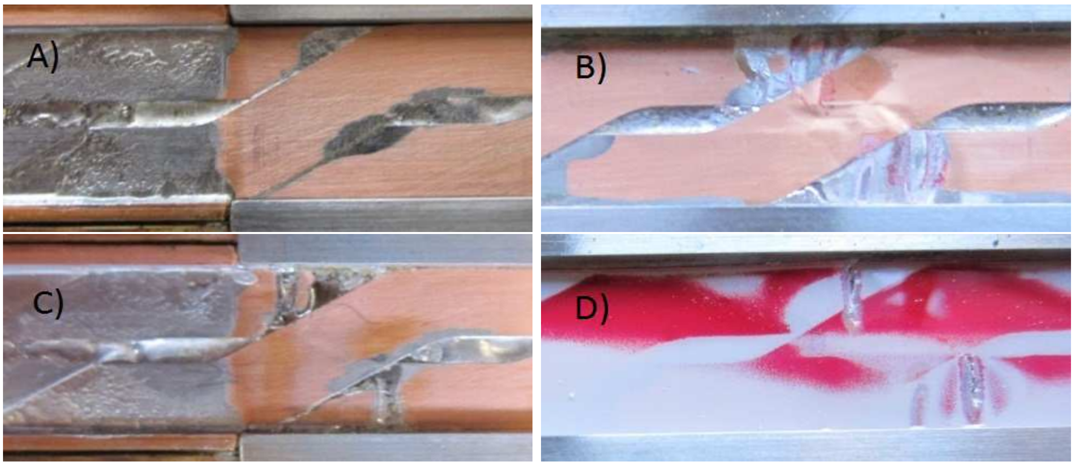

Figure 5.32: Top view of damaged portion of the Roebel cables: Cable GCS1 before the test (A) and after the test (C). Cable GCS2 after the test (C). Fujifilm paper after the test (D).

resulted in the buckling of the cable. When Roebel cables are submitted to transverse compressive stress, only a fraction of the cable section is effective for transverse stress (36% for GCS cable and 24% for KIT cable). Some portions of the cable that are free of transverse stress favours buckling. The radius of curvature of the buckled cable was smaller than the minimum bending radius of YBCO SP conductor, inducing irreversible reduction of I_c. The irreversible reduction of I_c was therefore both due to the burn of the top two YBCO tapes and to the small bending radius induced by cable buckling. The buckling could be prevented with an appropriate impregnation that would prevent the cable from delamination.

5.3.4 Chronology of events

The most probable chronology of events in Roebel cable is the following: a location of the cable presented a low I_c value. Since current was in excess of critical current, a normal zone started to develop but stagnated because normal zone propagation velocity is small in YBCO conductors and copper stabilization of YBCO film was possibly detached (delamination). The temperature rose very locally but at the same time voltage built up was limited due to a reduced spatial extension of normal zone. The protection of sample was activated too late, and the temperature reached locally at least 500 K. Some tapes of the cable were locally burnt, and the cable buckled due to thermo-differential strain. The buckling of Roebel cable induced too small bending radius to all of the YBCO tapes. The cable I_c was irreversibly reduced.

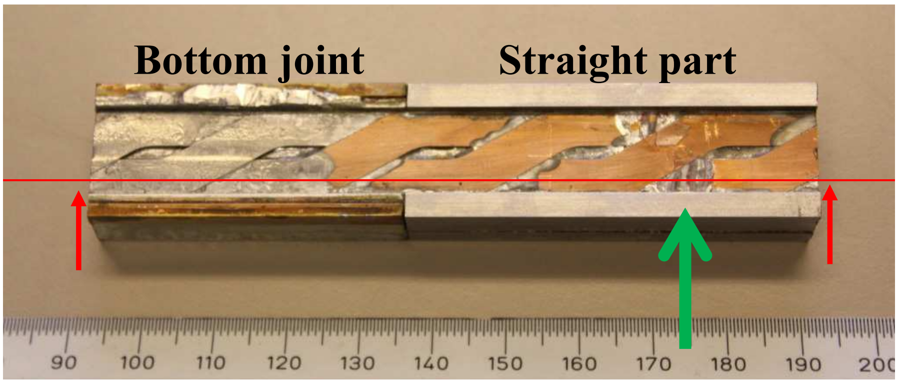

Figure 5.33: The damaged portion of the GCS2 cable: the polished section and the longitudinal position of microscopic observation (figure 5.34) are indicate by respectively a line and an pointer.

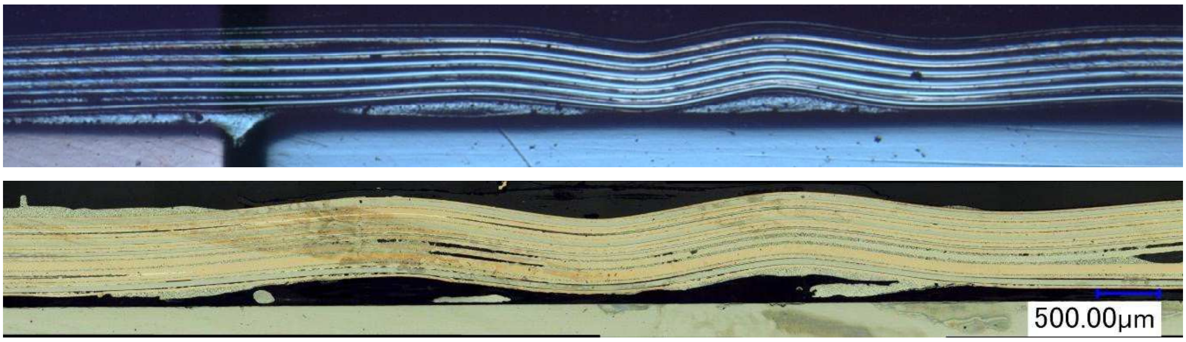

Figure 5.34: Longitudinal microscopic view of the damaged areas of GCS1 (top) and GCS2 (bottom) cable.

5.4 Delamination of YBCO Roebel cable

Delamination of YBCO tapes has been observed in the Roebel cables tested in FRESCA. Delamination can occur between the HTS film and the buffer layer or between the HTS film and the silver cap layer. The delamination of HTS layer in coated conductors has two main consequences:

- a reduction of tape I_c since the HTS film is damaged by the delamination.
- an electrical decoupling of the HTS film and the stabilizing copper layer. In the case of a resistive transition, the copper shunt is no more attached to the YBCO layer. Since the resistance in normal state of YBCO is high and the buffer layers are insulators the power dissipation in HTS is large and the conductor is damaged in case of quench.

The YBCO delamination observed in Roebel cable is firstly introduced and then the reported delamination in YBCO coils is discussed.

5.4.1 YBCO delamination in Roebel cable

Meander shaped tape of Roebel cables have been mechanically punched from fully processed coated conductor, i.e. after the silver and the copper electroplating process. A cross section view of a punched coated conductor is depicted in figure 5.35. At the punched edge of the conductor, plastic deformations and large shear stresses are induced. Coated conductor is a composite conductor (substrate, copper, silver, buffer layers and YBCO layer) and the shear stress induced by the mechanical punching is in excess of the interface shear strength: delamination is initiated at the conductor edge. The silver cap encapsulates the YBCO film and prevents contact with moisture. The punched meander tapes present no sealing of the YBCO film, as depicted in figure 5.35.

The preparation of Roebel cable for characterization in FRESCA includes splicing with Sn-Pb solder at a temperature of about 220°C. During the splicing process, temperature distribution in the RACC cable induces thermo-differential stresses. These stresses may cause a propagation of the delaminated edges of punched tape across their width. Some dummy splices were manufactured between Roebel GCS cable and a copper U-shape piece to study the migration of solder and the propagation of delamination. The splice was 100 mm long and was manufactured using the same procedure as for FRESCA Roebel samples. Since the sample was short and the groove made in the U-shape was slightly loose, the YBCO tapes were not well aligned. A transverse cross section of a dummy splice is depicted in figure 5.36. The delaminations are mainly located at punched edged of meander shape tapes and at the top of the YBCO stack. Cross sections performed on the splices of FRESCA Roebel samples after characterization show delamination at the same locations. At the un-punched edge of meander shape tape, no delamination was observed. Some lap joints of YBCO SP conductors performed with Sn-Pb and Sn-Ag solder were

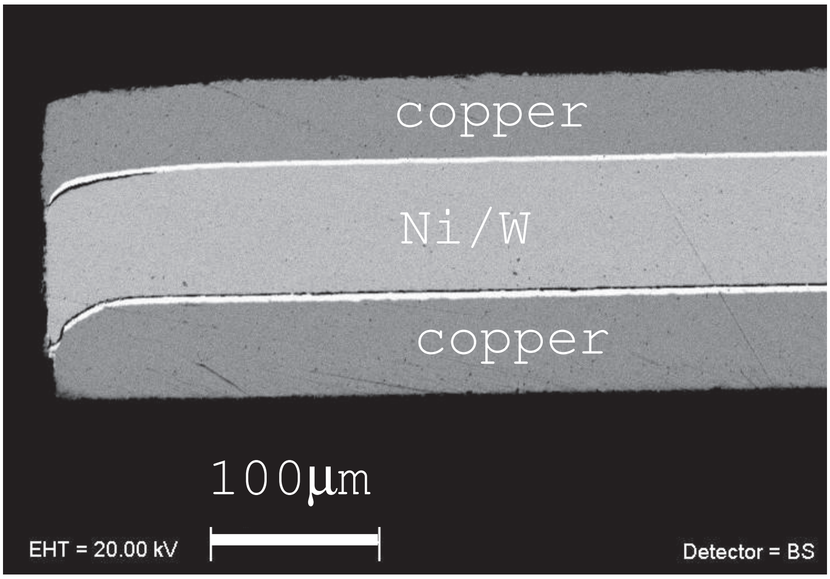

Figure 5.35: The punched edge of meander shape tape.

prepared for microscopic observation with the same protocol (see figure 3.31). No delamination was observed in these samples. The introduction of delamination by the grinding process during sample preparation could therefore be excluded. A longitudinal cable cross section is presented in figure 5.37. Delamination is observed at various locations.

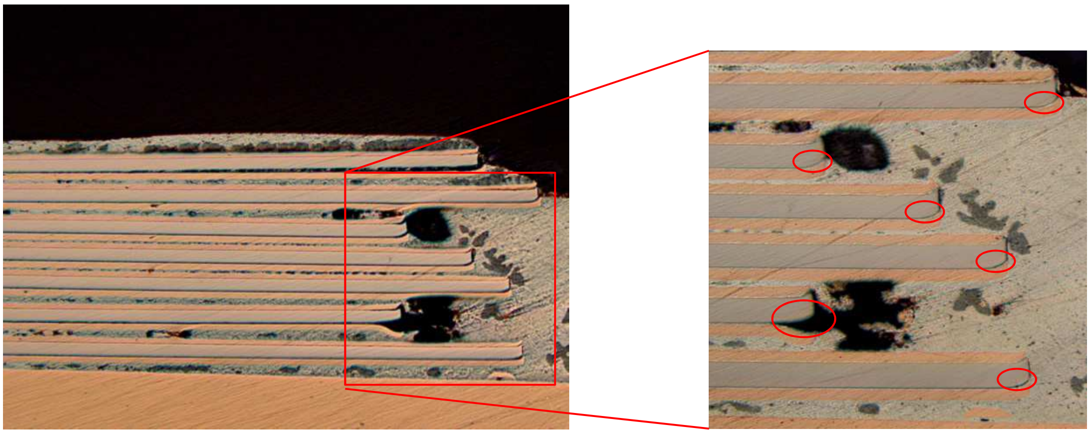

Figure 5.36: Cross view of a dummy Roebel GCS cable splice. The delamination are mainly present at the cut edge of the coated conductor.

\

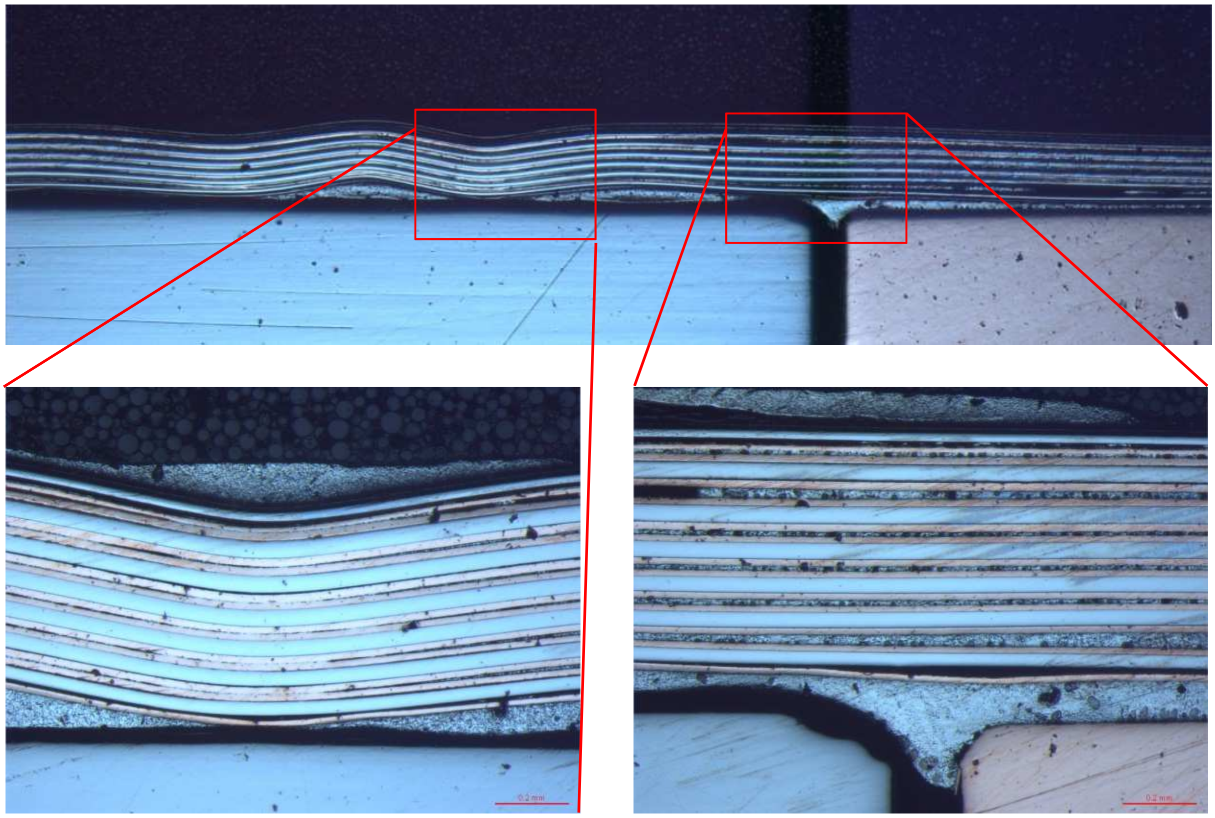

Figure 5.37: Longitudinal view of cable GCS1 in the bottom joint area. Many strands are delaminated. We can also see the undulation of the cable in the damaged portion.

5.4.2 Reported delamination of YBCO tapes in impregnated coils

For high flux density applications, YBCO coils are often epoxy wet-wound or impregnated to homogenize load distribution exerted by the Lorentz forces. The conductors are insulated from turn to turn by Kapton or porous media (such as silk paper). The low viscosity epoxy provided full bonding between the different layers. Failure in fully epoxy-impregnated YBCO coils has been observed by some groups and is attributed to transverse and peel stress concentration causing internal conductor delamination within the buffer and the superconductor stack of layers. Peel stress in particular appears to be an issue in YBCO coated conductors. A technical solution to alleviate this delamination issue was introduced and demonstrated by NHMFL [16]. It consists in the creation of a weak mechanical interface between the epoxy and the coated conductor. If a large stress occurs, the interface, which is the weakest point of the impregnated coil, breaks without affecting the coated conductor internal structure. Technically, this is ensured by inserting the conductor into a thin-walled, cryogenically compatible polyester heat-shrink tube which seals the conductor against seepage of the epoxy resin. A coil produced with this impermeable boundary between the epoxy and the YBCO tapes reached the record DC flux density of 35.4 T without conductor delamination [16].

5.5 Conclusion

Pioneer experimental work has led to the first successful characterization of Roebel cables at 4.2 K and in flux densities of up to 9.6 T. Two types of RACC cables made from 15 and 10 tapes with different geometries were measured. Low joint resistance (1 $n\Omega$) between Roebel cable and Nb-Ti cables were manufactured. The interstrand resistance of Roebel GCS cable is measured to be 25 $\mu\Omega$ at 77 K. This large value is mainly due to the internal strand resistance. The cable critical currents of 12 kA and current densities in excess of 1.1 kA/mm^2 at 7.5 T demonstrate the potential of such cables for application to high flux density accelerator magnets.

The sensitivity of Roebel cables to transverse compression is investigated: an average stress of 45 MPa does not degrade cable performance. Roebel YBCO cables do not have a homogeneous thickness, neither along their length nor across their width. The effective relative sections of GCS/KIT Roebel cables for transverse stresses are respectively only 24/36%.

During characterization at 4.2 K, the I_c of some Roebel cables were irreversibly damaged at current densities in excess of 1.1 kA/mm^2. The degradation was identified to be due to burnt strands and to a cable buckling. Technical solutions to avoid degradation of future Roebel cable are proposed.

Chapter 6

Current distribution in HTS cable

Multi-strand HTS superconducting cables may quench at premature current values. One of the most likely reasons for this behaviour is non-uniform current distribution among strands. In this chapter, the different reasons for unbalanced current distributions are identified and models of current distribution are introduced. In a transposed cable, conductors occupy different positions in the cable cross sections along the transposition pitch. They experience different self-fields along the pitch length and their critical current is therefore not uniform. The performance of HTS strands in transposed cable is calculated by the means of finite element models. The derived cable performances are then compared to the measured ones. Finally a model of current distribution is elaborated and used for interpreting the results of the measurements.

6.1 Uneven current distribution in HTS cables

Superconducting cables with large current carrying capacity (10-20 kA) for accelerator magnets consist of many superconducting strands connected in parallel since the current carrying capacity of a single superconducting wire/tape is not more than 1-3 kA at 4.2 K and in self field. Ideally, the quench current of a multi-strand superconducting cable is expected to equal the product of the critical current of a single strand under the flux density including self field of the cable and the number of strands. However, coils wound with multi-strand superconducting cable may quench at much lower currents than the expected I_c value. One of the reasons for this quench current degradation is non-uniform current distribution among strands before quench.

Generally, the strand current consists of a transient circulating current determined by inductances and a steady state transport current determined by resistances (splices and superconductor in dissipative state). The transient circulating currents superimpose on the steady transport current. Unbalanced current distribution among the strands can push the current of some strands beyond their I_c, such generating a normal conducting region. The resistive heat generated by the normal conducting material is removed both by conduction to the neighbouring parts of the conductor and by convection to the coolant. If the heat generation is lower than the heat removal, the conductor recovers the initial superconducting state. If not, the normal zone propagates. The magnetic energy stored in the winding is then discharged in the resistive normal zone and the magnet needs to be rapidly switched off for protection reasons. The phenomenon of unbalanced current distribution generating a normal conducting region is particularly important during fast flux density ramps and limits the maximum current achievable with a multistrand cable in dynamic powering conditions [217]. For this reason it is generally indicated as ramp rate limitation. In DC mode, uneven current distribution could also limit the cable performances and modify the shape of the transition to normal state.

Unbalanced currents distribution have been observed to induce periodically flux density distortions in accelerator magnets of HERA and LHC colliders, with a period equivalent to the cable transposition pitch and with a complex time and space dependences of the amplitude. These undesirable flux density distortions can be explained by the existence of long range coupling currents, with large decay time constant, between the strands of superconducting cables.

A modelling of the current distribution in HTS cable will help in the choice of optimal cable parameters to avoid these limitations.

6.1.1 Reasons of uneven current distribution in HTS cables

Several possible reasons for non-uniform current distribution among the strands of HTS cable can be identified, among them some are only effective in AC conditions, while others are effective in both AC and DC conditions. In general, unless each strand provides an identical current path in terms of its resistive and inductive properties, imbalances will exist.

- **Differences in the strand self and mutual inductances**

  Unless electrically insulated, the strands are in electrical contact with their neighbours and there are paths for currents to flow from strand to strand. If the strands are not twisted, induced loop voltages will be proportional to the flux density sweep rate and to the geometry of the cable (Faraday's Law). Induced voltages will drive eddy currents which travel along the length of one superconducting strand and return down the length of a neighbouring strand. The resistance encountered is at the contact points where the current crosses strands. If this resistance is low, notable eddy currents can exist and the resulting joule heating will contribute to the AC losses in the cable. This loss may need to be compensated by additional cooling to maintain the conductor below the critical temperature [46]. A way to reduce the coupling between strands is to decrease the electrical conductivity between them. The optimum choice of electrical conductivity between the strands balances the requirement of low AC loss (low conductivity) and an adequate degree of current sharing to help stabilization of superconductors against the effect of localized defects (high conductivity) [46]. In order to reduce the induced currents and the corresponding losses when exposed to external flux density changes, the strands of superconducting cables are twisted and transposed. A "fully transposed" cable, is one which reduces the self-field effect by ensuring that no net self-field flux exists between the strands along a transposition pitch [46]. In this case the self-inductance of every strand is the same and the mutual-inductances between strands exactly balance. This can be achieved by a cabling pattern in which the strands travel in the cable cross-section in such a way that each spends an equal amount of time at each position in the cable space. Transposed strands in a changing external flux density experience an electric field which changes direction every half transposition pitch length. The maximum induced voltages will thus be proportional to the transposition pitch length rather than the length of the cable [46]. Even with perfectly transposed strands, a large gradient of the flux density sweep rate along the cable length can give rise to long range induced coupling currents flowing along the whole cable length.

- **Uneven joint Resistances**

  To minimize the heat generation, high current HTS cables have to be connected with low joint resistances to the current leads. At low excitation, each strand current is lower than the strand critical current. No resistive voltage is built up in the HTS strands and the steady-state current distribution is governed by the joint resistances for times larger than the induced current time constant. It has been shown experimentally by Faivre et al. [218] that the cable steady state transport current can be homogeneously distributed by balancing the resistances at the joints to the current leads. It is not technically possible to realize a perfectly identical contact between the different strands of HTS cable: firstly because the soldering processes cannot be so strictly controlled and secondly because the internal resistance of YBCO conductors may vary from one conductor to another. This leads to variations in the joint resistances between the strands and therefore to unbalanced steady state current distribution. This is a valid concern, as a poorly manufactured joint would affect both the DC performance of a magnet and the ramping performance.

- **Uneven strands I_c**

  The critical current of coated conductors, are known to vary along their length. A I_c standard deviation of 4% is reported in 100 m unit length of 4 mm wide conductors. The performance of Bi-2212 conductors is highly sensitive to the temperature and oxygen migration during the coil heat treatment. In addition the HTS conductors are sensitive to strain. Uneven strands I_c in HTS cables may result from any of these different reasons. Moreover, at high current excitation, at least one strand current reaches or oversteps the strand I_c and this will lead to unbalanced steady state current distribution among the strands.

6.1.2 Decay time constant of induced coupling current

In order to better clarify the origin and the properties of induced circulating currents, it can be useful to distinguish between cables with electrically insulated strands and cables with non-insulated strands.

Cable made of insulated strands

The situation in cables made of insulated strands can be schematized with a lumped parameter circuit model with l the self inductance, M the mutual inductance and R the sum of the joint resistance. The inductive terms (M and l) determine the transient circulating current, while the resistive term (R) determines the steady transport current. The dynamic response of coupling currents is characterized by a decay time constant τ_c. The decay time constant of the induced transient circulating current, is given by [219][220]:

$$\tau_c = \frac{2(l-M)}{R} \tag{6.1}$$

The self inductance of a straight rectangular shape conductor with large aspect ratio of cross section is given by the formula:

$$l = \frac{\mu_0}{2\pi}\frac{L}{}\left(\ln\frac{2L}{w+t_h}+\frac{1}{2}\right) \tag{6.2}$$

where w, t_h and L are respectively the width, the thickness and the length of the conductor. The FRESCA samples are about 1.5 m long between the joints. In this experiment, the tapes were 4 mm, 5 mm and 5.5 mm wide for respectively the twisted pair, the GCS and the KIT Roebel cables. The corresponding strand self inductances are respectively 2.14μH, 2.07μH and 2.04μH.

The mutual inductance between two straight rectangular shape conductors with large aspect ratio of cross section is given by the formula:

$$M_{i,j} = \frac{\mu_0}{2\pi}\frac{L}{}\left(\ln\frac{2L}{R_m}-\ln k-1+\frac{R_m}{L}-\frac{R_m^2}{4L^2}\right) \tag{6.3}$$

Where R_m is the geometric mean distance between the i and j rectangular conductors and $\ln k = 1.0787$, taken from Groover tables [221], depends on geometric parameters. In twisted pair cable, the YBCO tapes are 0.3 mm distant corresponding to mutual inductance between adjacent conductors of 1.75 μH. The mutual inductance between the innermost and the outermost strands of TP SP3 and TP SP6 cable is respectively 1.69 μH and 1.56 μH.

For large scale applications, HTS cables are always terminated in a low resistance joint (about nΩ) in order to reduce the heat generation. The inductance difference over the loops considered can be large and the decay time constant of the induced circulating current can therefore be important, and much larger than the time scale of charging up the coil.

Cable made of non-insulated strands

In HTS cables, the conductors are in electrical contact (continuous or discrete) along their full length but the transverse resistance between the strands in the joint is much less than the transverse resistance in the cable itself. Two distinctive current loops may therefore be present, namely the short and the long range coupling currents. The short range coupling currents that extend over a transposition pitch are often indicated as interstrand coupling current. The long range coupling currents who closed up in the low joint resistances are often indicated as boundary induced coupling currents or supercurrents. The two current loops have a specific decay time constant and are schematically depicted in figure 6.1.

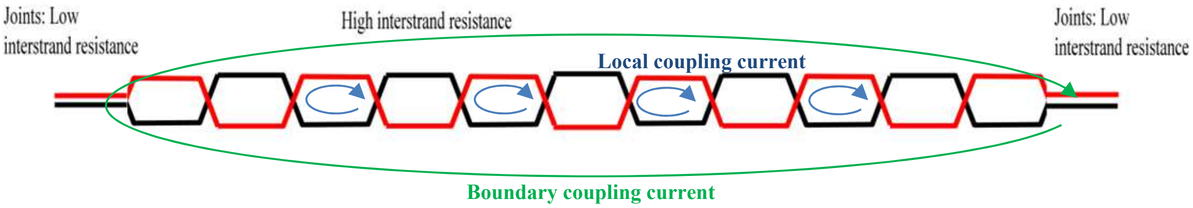

Figure 6.1: The short and the long range coupling currents in HTS cable made of non-insulated strands.

Decay time constant of interstrand coupling currents

The interstrand coupling current time constant is defined as the ratio of the conductor inductance and the inter-strand resistance over half the cable transposition pitch. In Roebel cable, the adjacent inter strand contact resistance over a transposition pitch has been measured to be 25 $\mu\Omega$ at 77 K and in self field (see chapter 5). This large resistance value is mainly due to both the conductor internal resistance and to the resistance of the oxide layer present at the conductor surface. These two resistances are almost independent of temperature. In Roebel cables, the decay time constant of interstrand coupling current is about 10 ms, which is much smaller than the time required for ramping up the samples to I_c.

Decay time constant of boundary induced coupling currents

Even with perfectly transposed strands, large gradient of the flux density sweep rate along the cable length may give rise to long range coupling currents flowing along the whole cable length. Since the boundary induced coupling currents are governed by the cable inductance (that is much higher than the local inductance) and by the joint resistance (much lower than the interstrand resistance), their time development is much slower than that of the local eddy currents. The typical decay time constant of the boundary coupling current in the Roebel cable tested in FRESCA is estimated to be about 1300 s. The measurements in FRESCA were carried out by increasing cable current at fixed external flux density. Boundary coupling current were not observed in the HTS cables characterized.

6.2 Model of current distribution in HTS cable

The twisted pair and the Roebel cables tested in FRESCA were made from non-insulated strands and were terminated by low resistance joints to LTS cables. Nevertheless, the transverse resistance between the strands in the joint was much less than the transverse resistance in the cable itself. Two models of current distribution are elaborated from this observation. In the first model, the strands are assumed to be insulated from each other along the cable length: the current distribute only at joints. In a second model, a certain level of current sharing between the different strands is allowed. The current could redistribute all along the cable length.

6.2.1 Cable made of insulated strands

In the case of cable made of insulated strands (or with very high interstrand resistance) the cable is modelled as an electric circuit with different branches, one for each superconducting strand. For a cable made of N_b strands, the basic model scheme consist of N_b parallel paths of current of length L, which go from one termination to the other termination. Figure 6.2 gives a graphical representation of this model.

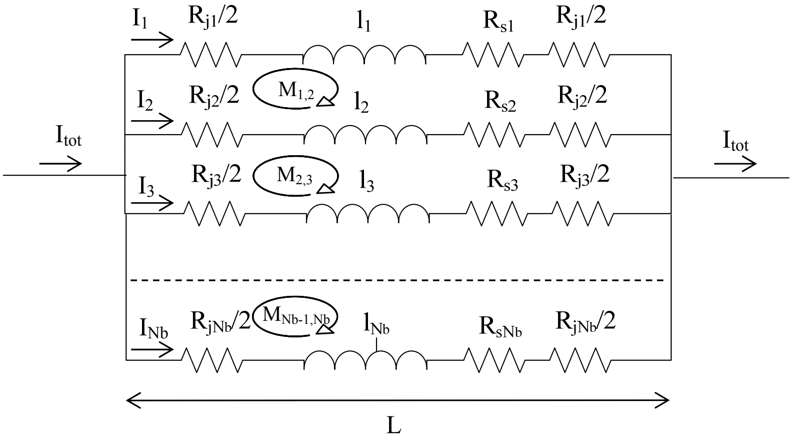

Figure 6.2: The equivalent electrical circuit of an HTS cable made of N_b insulated strands.

Each strand (i) has a superconductor resistance (R_{si}), a joint resistance to the current source (R_{ji}), a self inductance (l_i) and a mutual inductance ($M_{i,j}$), depending on the geometrical configuration. The joint resistance R_{ji} that is the sum of the joint resistances at each cable termination is considered as being independent of cable current. The non linear superconductor resistance (R_{si}) of the i_{th} branch is given by:

$$R_{s,i} = \frac{L\ E_c}{I_{c,i}} \left(\frac{I_i}{I_{c,i}}\right)^{n_i - 1} \tag{6.4}$$

where I_i, $I_{c,i}$ and n_i are respectively the current, the critical current and the n-value of the i_{th} branch. The electrical field criterion E_c is assumed to be equal to 1μV/cm and the equivalent splice resistance of the cable ($R_{j,eq}$) is defined as :

$$\frac{1}{R_{j,eq}} = \sum_{i=1}^{N_b} \frac{1}{R_{j,i}} \tag{6.5}$$

The voltage in each branch (V_i) is given by:

$$\begin{pmatrix} V_1 \\ V_2 \\ V_3 \\ ... \\ V_i \end{pmatrix} = \begin{pmatrix} l_1 & M_{12} & M_{13} & .. & M_{1i} \\ M_{21} & l_2 & M_{23} & ... & M_{2i} \\ M_{31} & M_{32} & l_3 & ... & M_{3i} \\ ... & ... & ... & ... & ... \\ M_{i1} & M_{i2} & M_{i3} & ... & l_i \end{pmatrix} \begin{pmatrix} \dot{I}_1 \\ \dot{I}_2 \\ \dot{I}_3 \\ ... \\ \dot{I}_i \end{pmatrix} + \begin{pmatrix} R_{s,1} + R_{j,1} \\ R_{s,2} + R_{j,2} \\ R_{s,3} + R_{j,3} \\ ... \\ R_{s,i} + R_{j,i} \end{pmatrix} \begin{pmatrix} I_1 \\ I_2 \\ I_3 \\ ... \\ I_i \end{pmatrix} \tag{6.6}$$

The Kirchhoff's current and voltage laws are applied respectively to each node and each mesh of the electrical circuit. These two laws are stated mathematically as follows:

$$\sum_h I_h = 0 \qquad \sum_k V_k = -\frac{d\phi}{dt} \tag{6.7}$$

Where $d\phi/dt$ is the time rate of change of the external flux density through the mesh. The index h indicates all of the currents connected to a given node and index k indicates every resistive or inductive element along a given mesh. The currents flowing in each branch of the circuit are not independent, but are linked to the value imposed by the current source (I_{tot}):

$$\sum_{i=1}^{N_b} I_i = I_{tot} \tag{6.8}$$

A full set of non-linear equations is derived from equations (6.4-6.8) and resolved by the Newton's method. Solutions to a system of equations can be found when the number of unknowns matches the number of equations. Thus, we wish to find solutions to systems that have the form:

$$\begin{aligned} f_1(x_1, x_2, x_3, ..., x_n) &= 0 \\ f_2(x_1, x_2, x_3, ..., x_n) &= 0 \\ &. \\ &. \\ &. \\ f_n(x_1, x_2, x_3, ..., x_n) &= 0 \end{aligned}$$

For convenience we can think of (x_1, x_2, x_3, . . . , x_n) as a vector $\boldsymbol{x}$ and (f_1, f_2, . . . , f_n) as a vector valued function $\boldsymbol{f}$. With this notation, we can write the system of equations simply as:

$$\boldsymbol{f}(\boldsymbol{x}) = \boldsymbol{0} \tag{6.9}$$

i.e. we wish to find a vector that makes the vector function equal to the zero vector. Newton method was derived by considering the linear approximation of the function $\boldsymbol{f}$ at the initial guess $\boldsymbol{x_0}$. The following is the linear approximation of $\boldsymbol{f}$ at $\boldsymbol{x_0}$, for vectors and vector-valued functions:

$$\boldsymbol{f}(\boldsymbol{x}) = \boldsymbol{f}(\boldsymbol{x_0}) + D\boldsymbol{f}(\boldsymbol{x_0})(\boldsymbol{x} - \boldsymbol{x_0}) \tag{6.10}$$

Here $D\boldsymbol{f}(\boldsymbol{x_0})$ is an n $*$ n matrix whose entries are the various partial derivative of the components of $\boldsymbol{f}$:

$$D\boldsymbol{f}(\boldsymbol{x_0}) = \begin{pmatrix} \frac{\partial f_1}{\partial x_1}(\boldsymbol{x_0}) & \frac{\partial f_1}{\partial x_2}(\boldsymbol{x_0}) & \cdots & \frac{\partial f_1}{\partial x_n}(\boldsymbol{x_0}) \\ \frac{\partial f_2}{\partial x_1}(\boldsymbol{x_0}) & \frac{\partial f_2}{\partial x_2}(\boldsymbol{x_0}) & \cdots & \frac{\partial f_2}{\partial x_n}(\boldsymbol{x_0}) \\ . & . & . & . \\ \frac{\partial f_n}{\partial x_1}(\boldsymbol{x_0}) & \frac{\partial f_n}{\partial x_2}(\boldsymbol{x_0}) & \cdots & \frac{\partial f_n}{\partial x_n}(\boldsymbol{x_0}) \end{pmatrix} \tag{6.11}$$

We need to start with an initial guess $\boldsymbol{x_0}$. In theory, the more variables one has, the harder it is to find a good initial guess. In practice, this must be overcome by using physically reasonable assumptions about the possible values of a solution. We wish to find $\boldsymbol{x}$ that makes $\boldsymbol{f}$ equal to the zero vector, so choose $\boldsymbol{x_1}$ such that

$$\boldsymbol{f}(\boldsymbol{x_0}) + D\boldsymbol{f}(\boldsymbol{x_0})(\boldsymbol{x_1} - \boldsymbol{x_0}) = \boldsymbol{0}. \tag{6.12}$$

First we solve the equation

$$D\boldsymbol{f}(\boldsymbol{x_0})\Delta\boldsymbol{x} = -\boldsymbol{f}(\boldsymbol{x_0}) \tag{6.13}$$

Since $D\boldsymbol{f}(\boldsymbol{x_0})$ is a known matrix and $\boldsymbol{f}(\boldsymbol{x_0})$ is a known vector, this equation is just a system of linear equations, which can be solved efficiently and accurately. Once we have the solution vector $\Delta\boldsymbol{x}$, we can obtain our improved estimate $\boldsymbol{x_1}$ by:

$$\boldsymbol{x_1} = \boldsymbol{x_0} + \Delta\boldsymbol{x} \tag{6.14}$$

For subsequent steps, we have the following process:

$$Solve \quad D\boldsymbol{f}(\boldsymbol{x_i})\Delta\boldsymbol{x} = -\boldsymbol{f}(\boldsymbol{x_i}) \quad for\ \Delta\boldsymbol{x} \tag{6.15}$$

$$Let \quad \boldsymbol{x_{i+1}} = \boldsymbol{x_i} + \Delta\boldsymbol{x} \tag{6.16}$$

The process is repeated until the vector $\boldsymbol{f}(\boldsymbol{x_0})$ converge to the zero vector.

6.2.2 Cable made from non-insulated strands

In HTS cable made of non-insulated strands some current sharing between adjacent strands is present. The current sharing allows the current to redistribute between the different strands along the cable length. A model that gives local information about the currents flowing in every strand and the level of current sharing is applied to Roebel and twisted pair cables cables in this section.

The network model

In 1973 Morgan [222] suggested calculating the coupling currents in unsaturated Rutherford cable by modelling it as a network of nodes interconnected by strands and cross-contact resistances R_c. In the Morgan's model, the Faraday's and Kirchhoff's equations are applied to all the loops formed by two adjacent strands of one layer crossing any two adjacent strands of the other layer. Since the Morgan Network model, other models [223][224][225] have been developed that can also handle saturated strands, the time dependent behaviour of coupling currents and non-uniformities which are likely to be present in the cable of accelerator coils. The network model describes in great detail every contact between strands and permits to obtain local informations about the currents flowing in every strand and the power dissipated in the cable. It also permits to take into account variations of the cable parameters across the cable width and along cable length. The network models show good agreement with experimental data measured on Rutherford cable [223]. The main drawback of the network model is that the number of unknowns is very high (about 5 000 for a transposition pitch in Roebel cable), increasing quickly with the cable length and the number of strands. This makes very difficult to study the problem of current distribution in real long cables made of some tens of strands.

In Roebel and twisted pair cables the adjacent strands are in distributed continuous electrical contact. The discretization of the contact resistance by the network model introduces a bias. The problem of current distribution in Roebel and twisted pair cables could also be tackled with a continuum model directly based on the flux density theory [226][227]. In the framework of this model, the cable is viewed as a continuum with anisotropic conductivity, obeying the Maxwell's equations. This model requires the assumption that a relatively high density of electrical contacts between the strands exists, as is the case for Roebel and twisted pair cable.

Only the network model is applied to Roebel and twisted pair cables in this work.

Geometry and equations

The HTS cables are modelled as a three-dimensional network of nodes interconnected by strand sections and adjacent contact resistances (R_a) (see figure 6.3). The strands are represented by lines (with an infinitely small diameter located at tape mid width and mid thickness. The coupling currents (I_a) between the strands of the cable flow through the contact resistances R_a. The currents I_{str} denotes the total current in a strand, i.e. the sum of the strand transport currents, the interstrand coupling currents, and additionally the boundary-induced coupling currents. In the Roebel cable, each band consists of (N_b) calculation cells and has ($2N_b$) unknown currents: N_b strand currents (I_{str}) and N_b contact current between adjacent strands (I_a). In the twisted pair cable cable, each band consists of (N_b-1) calculation cells and has ($2N_b$-1) unknown currents: N_b strand currents (I_{str}) and (N_b-1) contact currents between adjacent strands (I_a).

The Kirchhoff's current and voltage laws are applied to each calculation mesh of the network model. The voltage (U_{str}) over a strand element consists of a resistive part U_R and an inductive part U_{ind}. The resistive voltage is given by the power law:

$$U_{r,i} = L_b \; E_c \left(\frac{I_i}{I_{c,i}} \right)^{n_i} \tag{6.17}$$

Where L_b is the length of the mesh considered. The inductive voltage U_{ind} of strand element i is given by:

$$U_{ind,i} = \sum_{j=1}^{N_{tot}} M_{i,j} \frac{dI_j}{dt} \tag{6.18}$$

where $M_{i,j}$ is the mutual inductance between the two strand elements i and j. The mutual inductance between two tapes of finite length placed in arbitrary positions has been given by Groover [221]. The summation of the mutual inductances has to be made over all the N_{tot} strand elements of the cable. However, in this network model the summation is confined to strands within a length of about 10 calculation bands. The computing time is then significantly reduced while the introduced error in the inductive voltage remains small. Boundary currents have to be defined for the first and the last band of the cable. The model that consists in a system of non linear equations is resolved by the Newton's method as described in previous section.

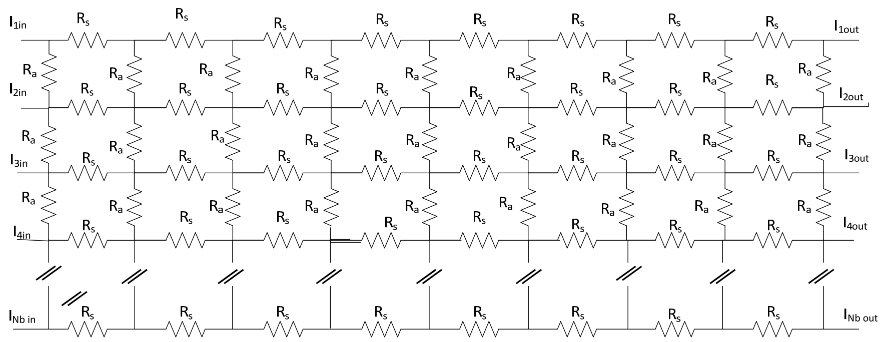

Figure 6.3: The network model of twisted pair cable. Only the strand resistances (R_s) and the contact resistances (R_a) are depicted.

6.3 Parametric study of steady state current distribution in HTS cable made of insulated strands

As already introduced, there are several reasons for unbalanced current distribution in superconducting cables. In steady state, the current distribution among strands is fully determined by their impedances. Each strand impedance has two components: the splice impedance and the superconductor impedance. The superconductor impedance is highly non linear with typical n values of about 50-80 for YBCO conductors at 4 K. The sharp non linear transition between the superconducting and the normal state may be approximated by a step function. The impedance of strand is zero for current lower than the critical current and considered as infinite for current beyond. In reality, the impedance is finite for currents above I_c but many orders of magnitude larger than in the superconducting state. The step function is approximated with an infinite n value. The cable length has an impact on the steady state current distribution only if finite strand n values are considered.

Based on a simplified cable layout, a parametric study of the steady state current distribution in HTS cable made of insulated strands is carried out here. The parameter impacts are firstly regarded individually and then compared.

6.3.1 Uneven strand joint resistance

One of the most likely reason for unbalanced steady state current distribution in HTS cable is non-homogeneous joint resistance.

Cable with infinite strand n-values

Let us consider a cable made of three strands with uneven strand joint resistances to the current leads, with $R_1 < R_2 < R_3$. The equivalent cable joint resistance (R_{eq}) is defined as :

$$R_{eq} = \frac{R_1 R_2 R_3}{R_2 R_3 + R_1 R_3 + R_1 R_2} \tag{6.19}$$

The different strands are considered to have the same $I_{c,str}$ and to undergo a sharp superconducting transition (n-value= ∞). The cable critical current ($I_{c,cab}$) is defined as the sum of the strand critical current. It is convenient to define the strand reduced current ($i_{str,i}$) as the ratio of the strand current ($I_{str,i}$) and the strand critical current ($I_{c,str}$). The cable reduced current (i_{cab}) is therefore defined as the ratio of the cable current (I_{cab}) and the cable critical current ($I_{c,cab}$):

$$i_{str,i} = \frac{I_{str,i}}{I_{c,str}} \qquad i_{cab} = \frac{I_{cab}}{I_{c,cab}} \tag{6.20}$$

For reduced cable current below i_1 (see figure 6.4), the current is not balanced among strands: most of the cable current is carried by strand 1 since it has the lowest joint resistance. Strand 3 carries the least since it has the largest joint resistance. The current per strand (for $i_{cab} < i_1$) is given by:

$$I_{str,i} = I_{cable}\frac{R_{eq}}{R_i} \tag{6.21}$$

At $i_{cab} = i_1$ the strand 1 reaches it I_c and the current is then only increased in the other two strands. The i_1 value is defined as:

$$i_1 = \frac{I_{c,str}}{I_{c,cab}}\frac{R_1}{R_{eq}} \tag{6.22}$$

At the reduced cable current i_2, the critical current of the second strand is reached and the current then only increases in the third and last strand. The i_2 value is defined as:

$$i_2 = \frac{I_{c,str}}{I_{c,cab}}\frac{R_2 + R_3}{R_3}\left(1 - \frac{R_1}{R_2} + \frac{R_1 R_3}{R_{eq}}\right) \tag{6.23}$$

At i_{cab}=1, the three strands have reached their I_c and the current distribution among the different strands is balanced. In figure 6.4, the strand currents as a function of the reduced cable current are depicted for different distribution of strand joint resistances. The equivalent cable joint resistances (R_{eq}) of the two cables considered in figure 6.4 are the same. For cable with large distribution of strand joint resistances, the i_1 and i_2 values are observed to be reduced, as described by (6.22) (6.23).

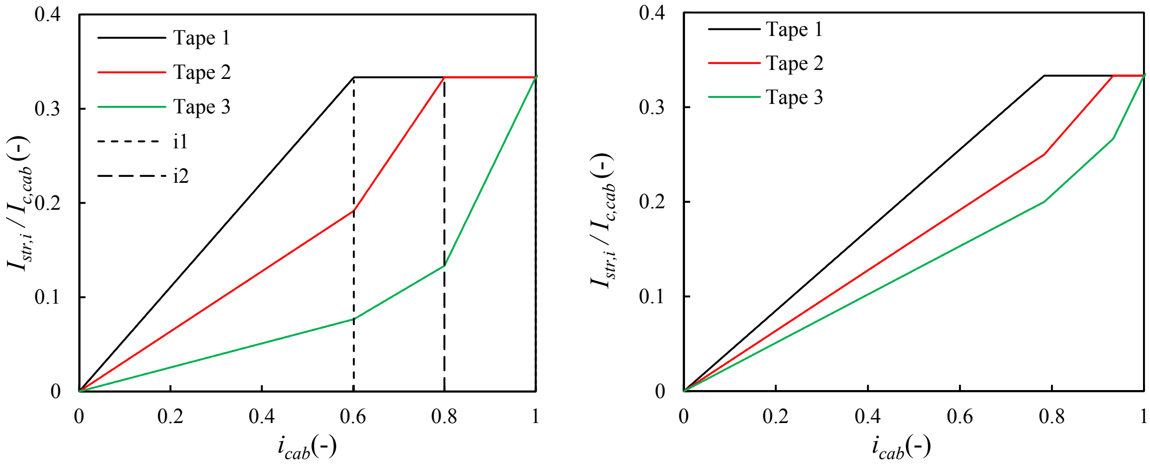

Figure 6.4: The current distribution in cables made of three insulated strands with uneven strand joints resistance and infinite n-value.The R_{eq} of the two cable is 12.8 nΩ with R_1, R_2 and R_3 of respectively 23, 40 and 100 nΩ (left) and R_1, R_2 and R_3 of respectively 30, 40 and 50 nΩ (right).

Cable with finite strand n-values

In the case of strands with finite n values, the cable length has an impact on the steady state current distribution. The HTS cables tested in FRESCA were about 2 m long whereas in magnet coils they will be at least two orders of magnitude longer. The current distribution in a cable made of three strands is investigated here as a function of the cable length. The three strands are considered to have homogeneous I_c and n values of respectively 1300 A and 60. The strand joint resistances are respectively 10, 50 and 100 nΩ. Three cable lengths are considered (1 m, 10 m and 100 m), in figure 6.5 the strand currents as a function of the reduced cable current are depicted. The current distribution is almost identical up to almost i_{cab}=0.4 for the different cable lengths. Then the current distribution slightly differs up to the cable critical current. Despite the two order of magnitude difference in cable length, only a relative small deviation in terms of current distribution is observed. This is explained by the highly non linear impedance of superconductors around the critical current: a tiny variation of current may give rise to a large variation of voltage. The n value of strands has also an impact on the steady state current distribution of cable with unbalanced strand resistances. In the right plot of figure 6.5, the current distribution in a 1.5 m long cable with strand joint resistances of respectively 10, 50 and 100 nΩ is depicted. Lowering the n value tends to homogenise the current distribution, but with a limited amplitude.

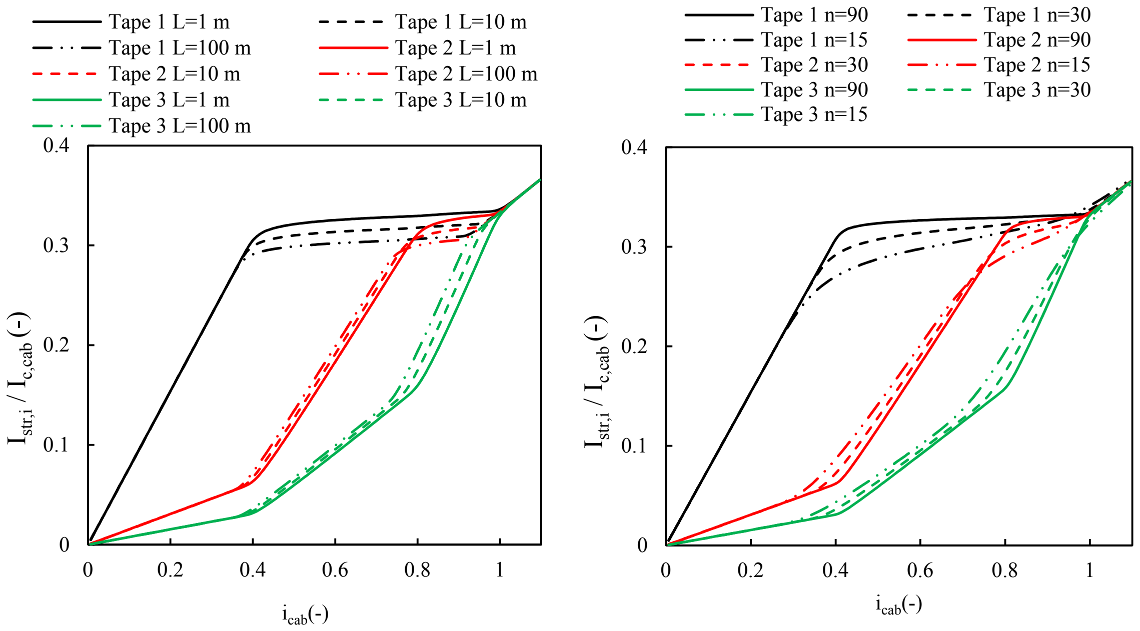

Figure 6.5: Influence of cable length (left) and n values (right) on the steady state current distribution of three insulated strands cable with unbalanced strand joint resistances.

6.3.2 Uneven strands I_c

In coated conductors, a large I_c fluctuation along and between unit length is usually observed. In large current HTS cable made of few strands, this could results in uneven strand I_c. The strand I_c of Roebel cables tested in FRESCA were measured at 77 K and in self field. For the KIT1 cable, the highest I_c was 151 A, the lowest one 84 A with a standard standard deviation of 17%. Based on a simple HTS cable layout made of three insulated strands, the influence of uneven strand I_c on steady state current distribution is illustrated here. It is convenient to distinguish between cable made of strands with infinite n values from cable made from strands with finite n values.

Cable with infinite strand n-values

Let us consider a cable made of three strands with uneven critical current ($I_{c1} < I_{c2} < I_{c3}$) and homogeneous strand joint resistance. If the strand n values are infinite, the current distribution is independent of cable length and is homogeneous in the different strands up to the reduced cable current i_4 at which the tape 1 reaches it critical current (see figure 6.6). The i_4 is simply defined a: $i_4 = 3I_{c1}/I_{c,cab}$. For reduced cable currents above i_4 the current increases only in strands 2 and 3. At current i_5 the tape 2 reaches it I_c and the current then only increases in strand 3 up to the cable I_c ($i_{cab} = 1$).

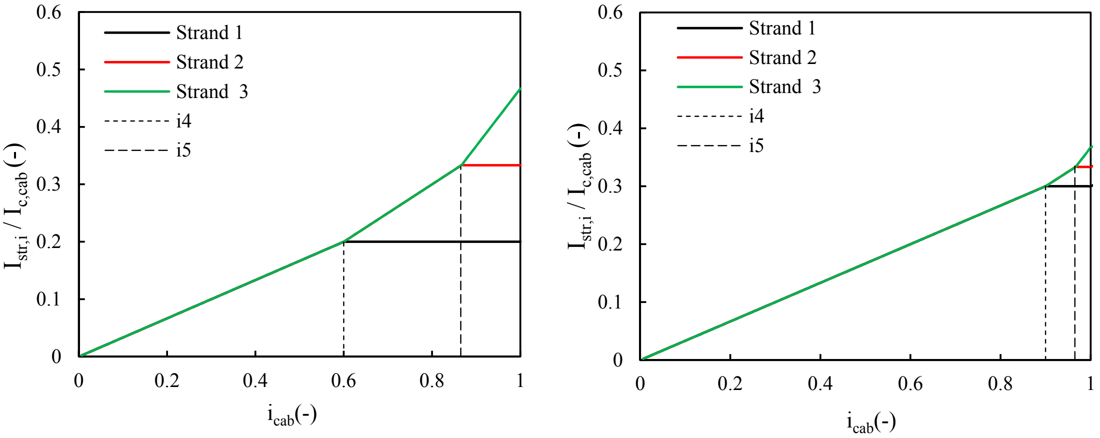

Figure 6.6: The current distribution in a cable made of three insulated stands with homogeneous strand joint resistance but with un balanced I_c. I_{c1}, I_{c2} and I_{c3} of respectively 300, 500 and 700 A (left) and 450, 500 and 550 A (right).

Cable made from strands with finite n-values

In the case of strands with finite n-values the current distribution depends on cable length and on n values. The impact of these two parameters on the current distribution of cable made from strands with uneven I_c is reported in figure 6.7. The cable length and n value have only a small impact on the steady state current distribution of HTS cable.

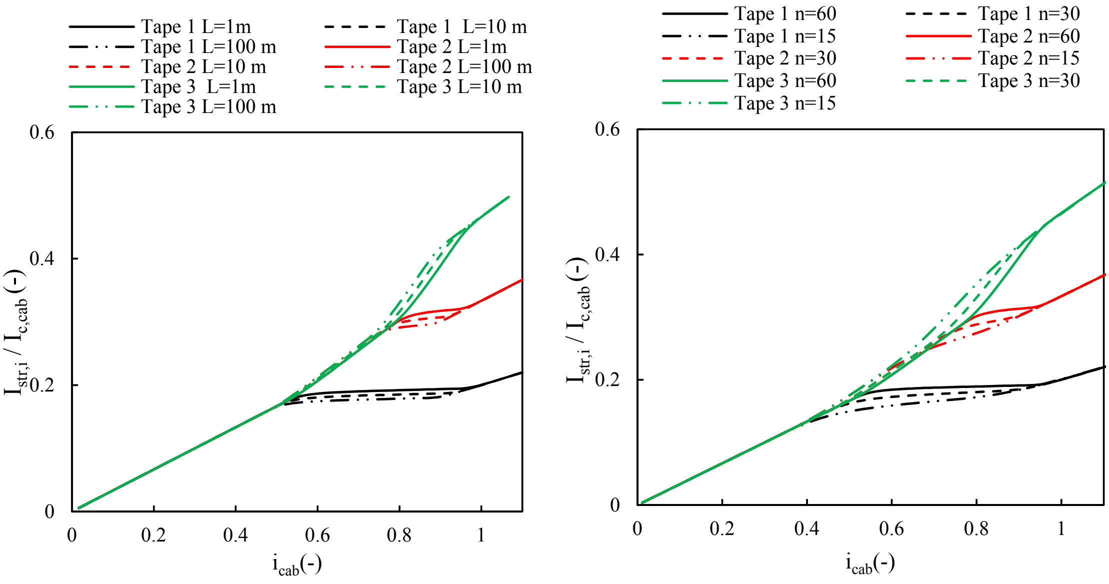

Figure 6.7: The current distribution in a 1.5 m long cable made of three stands with homogeneous strand joint resistance but with unbalanced I_c.I_c. I_{c1}, I_{c2} and I_{c3} of respectively 300, 500 and 700 A at different n-values (left). The resulting electrical potential difference along individual strands (right).

6.3.3 Impact of uneven strand joint resistance and uneven I_c on steady state current distribution

The two main reasons of uneven steady state current distribution in HTS cables are non-uniform joint resistance and strand I_c. These two reasons impact on the current distribution at different level of reduced cable currents. To compare the sensitivity of steady state current distribution on these two parameters, a cable made of three insulated strands is considered. The current distribution is regarded as the ratio between the maximum strand current and the minimum strand current ($I_{str,max}/I_{str,min}$). A 10% and 30% deviation between the maximum and minimum values of strand I_c and strand joint resistance are considered. For these two deviations, the ratio $I_{str,max}/I_{str,min}$ is depicted in figure 6.8 as a function of the reduced cable current for cable of different lengths. Non-uniform strand joint resistances induce uneven current distribution among strands at low reduced cable current. The uneven strands I_c induce non-uniform current distribution only at high reduced cable current. The amplitude of the ratio $I_{str,max}/I_{str,min}$ is in both case proportional to the deviation in I_c and R_j.

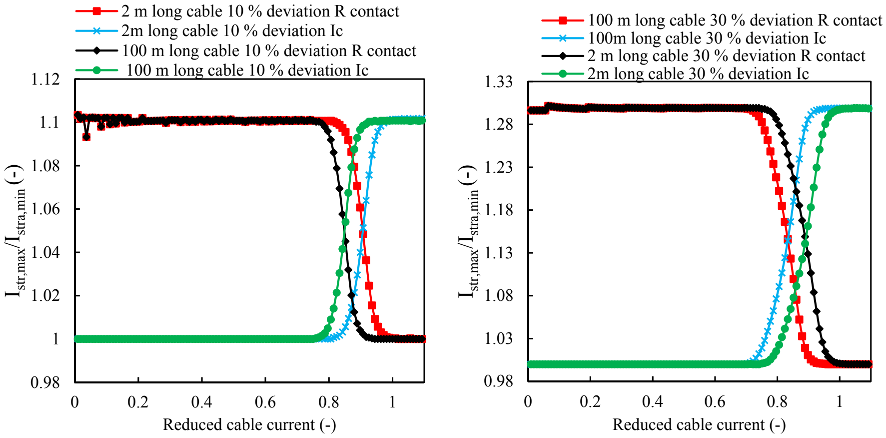

Figure 6.8: The ratio of the maximum and the minimum strand current in a cable made of three strands width 10% (left) and 30 % imbalance (right) in the strand I_c or strand joint resistances.

6.4 Strand and cable I_c

The self field significantly influences the performances of high current cables and the calculation of the cable self-field is necessary for estimating the cable critical current. In a transposed cable, the conductors take all the different positions in the cable cross section along a pitch. They experience different flux density strengths and orientations and their I_c is therefore modulated. Since in a given cable cross section, the strands are in different positions, they present different critical currents. This may give rise to current redistribution if the interstrand contact resistance is low. In this section the strand I_c as a function of its position in the cable cross section is calculated by the means of a finite element method (FEM). In order to validate the model, the cable I_c derived from the computed strand I_c is compared to the measurements performed on Roebel and twisted pair cables.

6.4.1 The 2D FEM model

In twisted pair cable, the cable transverse dimension (4 mm), is much smaller than the transposition pitch (400 mm). The flux density distribution could therefore be considered as two dimensional. In the Roebel cable topology, the crossing segments (about 20 mm) are relatively short compared to the cable transposition pitch (126-300 mm). The errors in neglecting the 3D complexity in self field of Roebel cable are assumed here to to be small. For the twisted pair and the Roebel cable topologies, only a two dimensional study is carried out. The YBCO tapes are assumed to be infinitely long, straight, with current flowing only perpendicular to their cross sections. The high aspect ratio of YBCO tapes has always been a problem in modelling it in any finite element scheme. The thickness of the HTS layer is only about 1 μm for width of 4-5.5 mm. For the purposes of this model, the YBCO SP tape is represented by its superconducting layer with a thickness of 30 μm. The J_c of YBCO have been proportionally reduced to account for this thickness modification. All other components such as substrate (Hastelloy), buffer and stabilization are meshed as vacuum since their influence on the flux density is negligible. The model is implemented in the FEM commercial software package Comsol [199]. The FRESCA Nb-Ti dipole magnet cross section is also implemented in the code and an external flux density is applied on the HTS cable by the flow of appropriate current density in the coils. The HTS section is filled to its critical current density value $J_c(B,T,\theta)$ with vector potential as a state variable. The local J_c dependence on the local flux density B and its direction θ with respect to the wide face of the superconducting tape is implemented in the model through expression 3.6. Note that completely uniform properties of YBCO $J_c(B,T,\theta)$ are assumed in the calculations; differences of critical current density in the cable cross-section are caused only by the cable self-field. In real YBCO tapes, random defects from the manufacturing process decrease locally the critical current density. The coated conductors I_c have a typical standard deviation of about 4%. This value has been observed to be even larger (17 %) in the strands of Roebel cables. The calculation performed here does not take into account the local properties of the conductors used for the experiment.

The 2D model applied to YBCO cables tested in FRESCA

The geometry of the twisted pairs and Roebel cables tested in FRESCA is implemented in the 2D FEM model, as depicted in figure 6.9. The twisted pair cables carry the same current but in opposite direction. Therefore, for symmetry reasons, only one cable is modelled with the following Dirichlet boundary condition: magnetic potential (A) equal to zero at y=0. The Roebel cables were tested together with two Nb-Ti Rutherford cables providing the return current path to the station leads. In addition, GCS Roebel cables were made from odd number of strands. No specific symmetry could therefore be found in the 2D cross section and the full cable geometry is implemented in the model. The Roebel cable carry the same amount of current but in opposite direction than the Nb-Ti Rutherford cables. This constraint is implemented in the model as follows:

$$\iint\limits_{D_+} J_c(B,T,\theta)dxdy = -\iint\limits_{D_-} J_{c,0,NbTi}(B,T)dxdy \tag{6.24}$$

Where the domains D_+ and D_- are depicted in figure 6.9 and $J_{c,0,NbTi}$ is a scaled critical current density of Nb-Ti expressed as:

$$J_{c,0,NbTi}(B,T) = v\ J_{c,NbTi}(B,T) \tag{6.25}$$

where $J_{c,NbTi}$ is the description of critical surface in Nb-Ti [28] and the scaling factor v is set to balance equation (6.24).

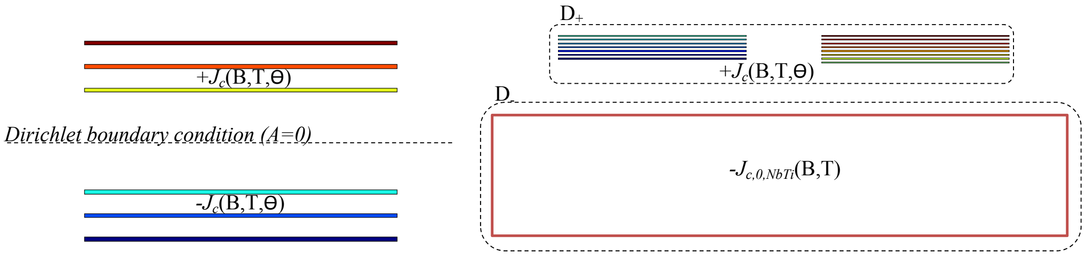

Figure 6.9: The 2D FEM model of the twisted pair cable (left) and the Roebel cable (right).

The external flux density orientation

In this chapter, the orientation of external flux density with respect to the cable refers to the deviation from aligned self and external flux density, as depicted in figure 6.10. The parallel orientation (θ=0°) stands therefore for parallel self and external flux densities. The anti-parallel orientation (θ=180°) is for self and external flux densities with opposite direction. The Roebel cable have been measured in two specific orientations: the perpendicular one and the anti-parallel one.

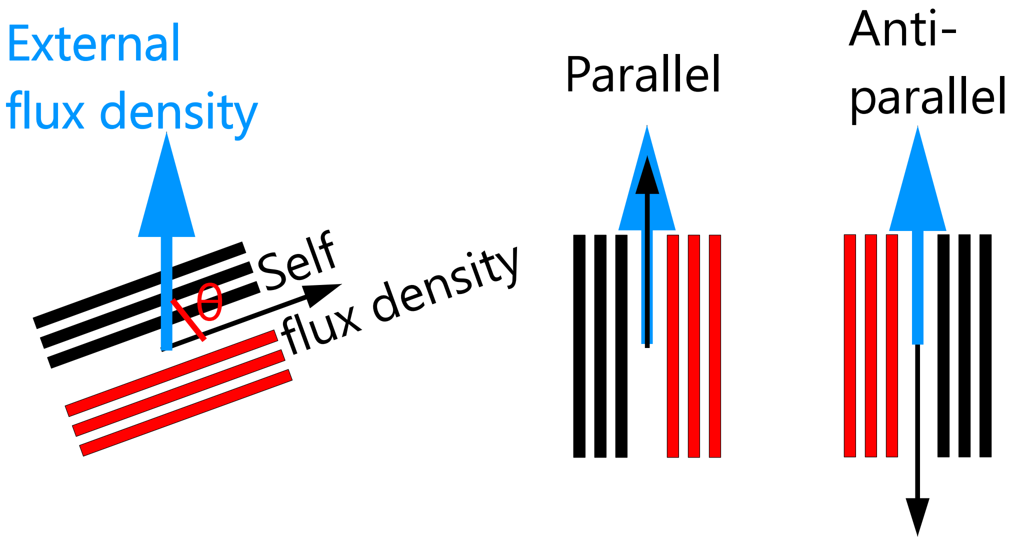

Figure 6.10: Schematic view of the external flux density orientation with respect to the twisted pair cable.

6.4.2 Twisted pair cable

The J_c distribution in self field

The J_c distribution in the cable cross section is dictated by the flux density map. The self field and the related J_c distribution of a twisted pair cable made of 3 YBCO tapes are depicted in figure 6.11. The self field is parallel to conductor tape planes between the different cables of the twisted pair assembly. The self field closes at cable edges. In YBCO conductors the perpendicular flux density has a more reducing effect on the J_c than the parallel one. The lowest J_c is therefore observed at cable edges where the strength of perpendicular flux density is maximum. The highest J_c are observed both in the innermost strands, where flux density is parallel to tape plane and at mid width of outermost tapes where flux density is almost zero.

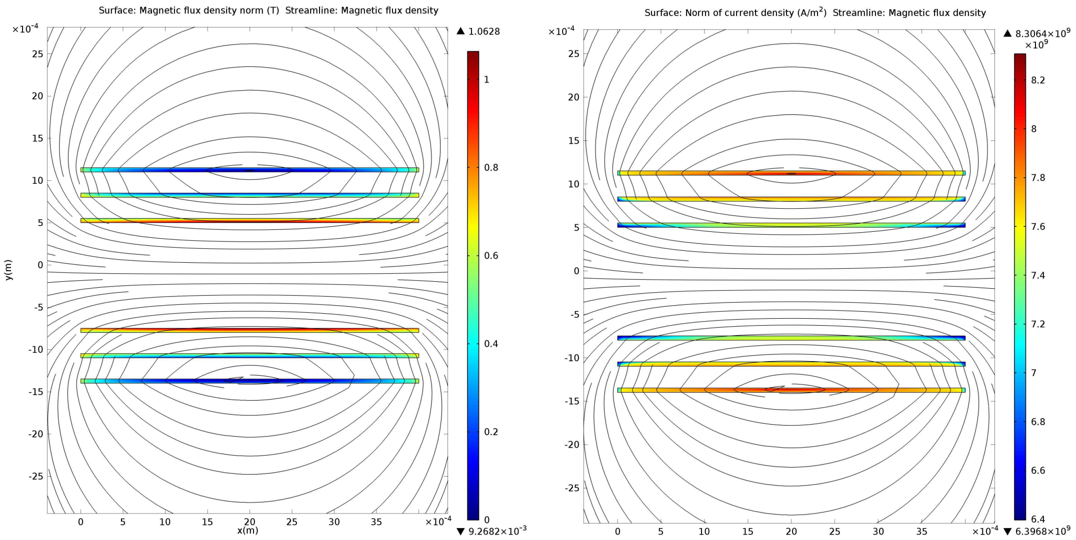

Figure 6.11: The distribution of the flux density (surface) and the magnetic vector potential (isolevels) (left) and the distribution of critical current density (right) in the TP-SP3 cables without external flux density.

The J_c distribution in external flux density

When an external flux density is applied to the twisted pair cable, it adds to the cable self field. The J_c distributions in perpendicular (θ=90°), parallel (θ=0°) and anti-parallel (θ=180°) external flux densities of respectively 0.5 T and 9 T are depicted in figure 6.12. In the perpendicular orientation (θ=90°) the external flux density is either increased or decreased at the different cable edges by the cable self field. Asymmetric distributions of J_c with respect to the strand mid widths are induced. As the external flux density increases, the J_c asymmetry progressively reduces since the J_c sensitivity to perpendicular flux density decreases. In the parallel orientation (θ=0°), the highest J_c is observed in the outermost strands at 0.5 T, thanks to the reduction of external flux density by the self one. In the anti-parallel orientation (θ=180°), the highest J_c is observed at the innermost strands for similar reasons.

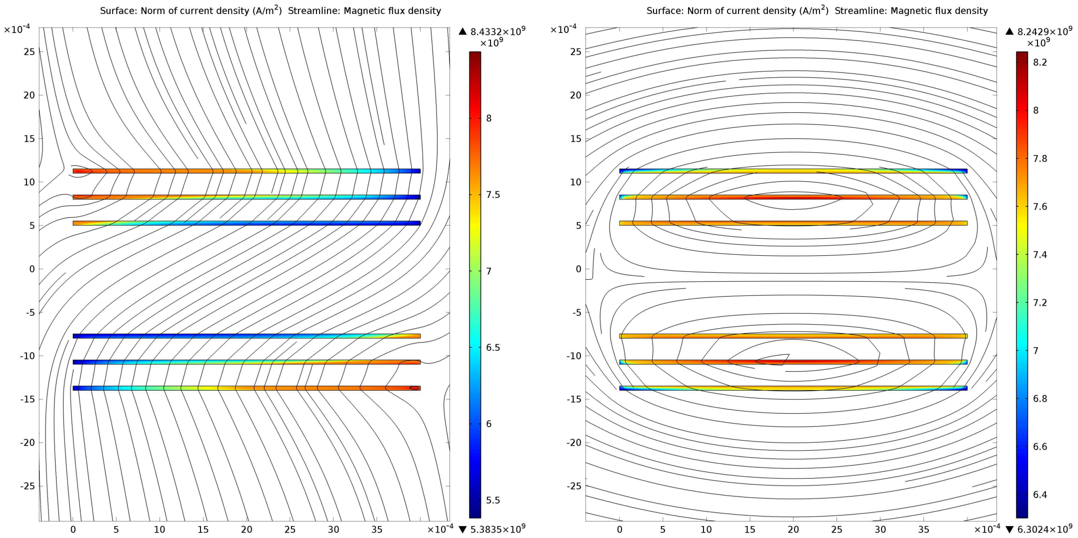

Figure 6.12: The distribution of critical current density (surface) and the magnetic vector potential (isolevels) in the TP-SP3 cable in perpendicular orientation (left), and parallel orientation (right) at external flux density of 0.5 T.

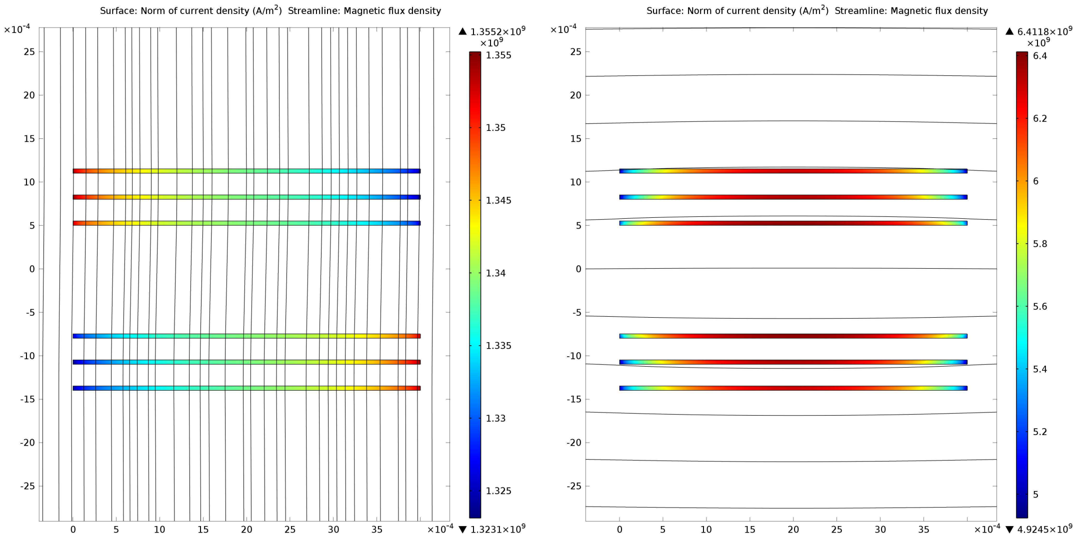

Figure 6.13: The distribution of critical current density (surface) and the magnetic vector potential (isolevels) in the TP-SP3 cable in perpendicular orientation (left), and parallel orientation (right) at external flux density of 9 T.

Strand I_c in cable cross section

The strand I_c are computed by integration of J_c over the YBCO films. For the perpendicular and the anti-parallel orientations, the strand I_c of TP-SP3 and TP-SP6 cables is depicted in figure 6.14 as a function of the external flux density. Without external flux density, the outermost strand of TP SP3 cable has the highest I_c (1550 A), the innermost strand the lowest one (1450 A). By increasing the external flux density in the perpendicular orientation, the I_c of the different tapes progressively reduces but deviates one from the other up to flux densities of about 1.5 T. For higher flux densities, the different tapes present almost the same I_c. This is easily explained by the relatively small value of the perpendicular self field compared to the external one. For parallel flux densities above 2 T, the strand I_c have the same dependence with flux density but deviate from each other. This is mainly explained by the distribution of the cable perpendicular self field.

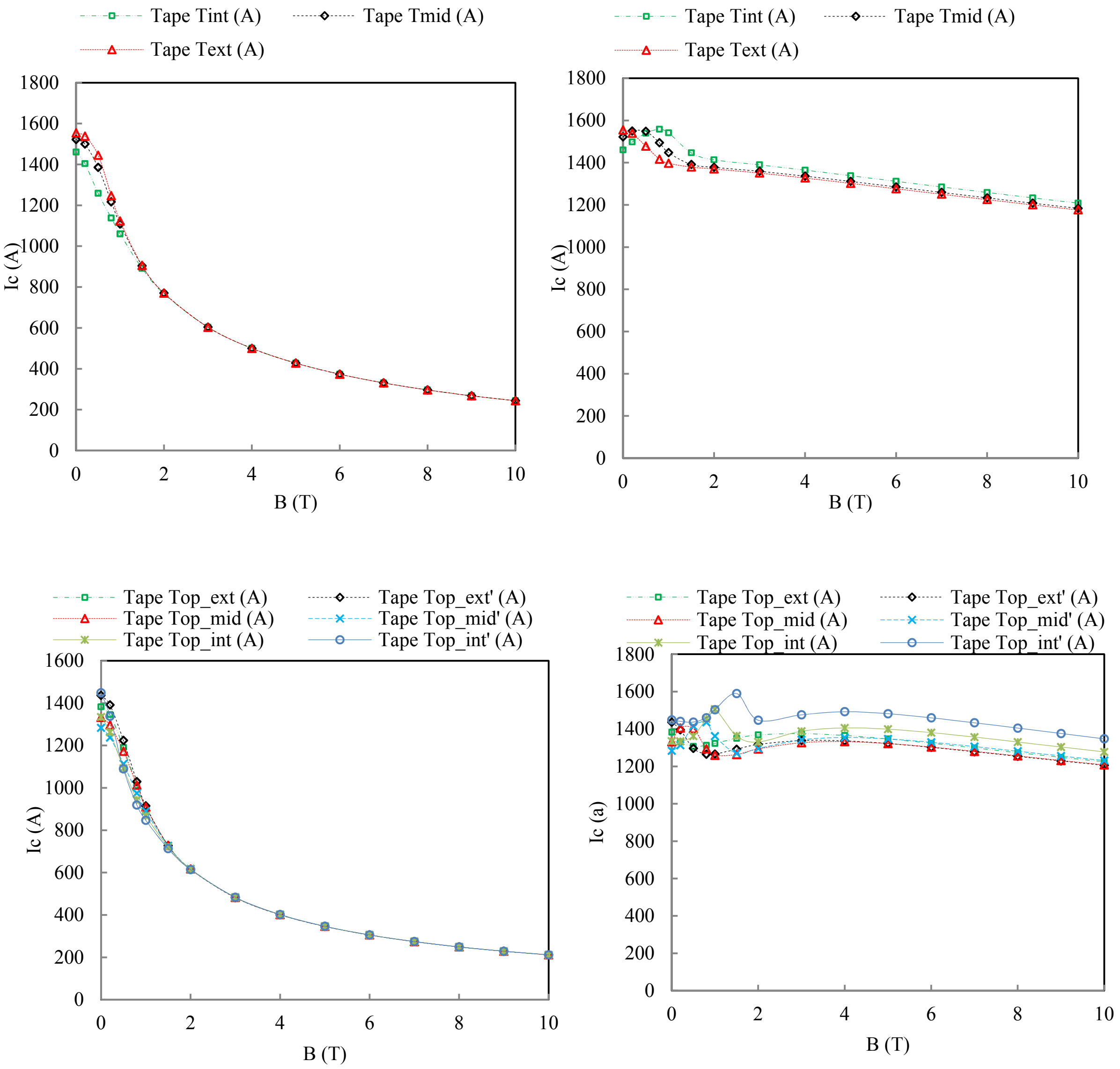

Figure 6.14: The strand I_c of TP-SP3 (top) and TP-SP6 (bottom) cables as a function of external flux densities in the perpendicular orientation (left) and the anti-parallel orientation (right)

Strand I_c along cable pitch

The twisted pair cables tested in FRESCA were exposed to homogeneous external flux density over a length longer than the cable twist pitch. The YBCO cables encountered therefore all the different external flux density orientations. Since the twist of the cable is assumed to be uniform along a pitch, the dependence of the external flux density orientation with longitudinal position along cable is linear, as depicted in figure 6.15. The strand I_c computed at discrete location along the pitch (t_p) of cable TP-SP3 is depicted in figure 6.16 at external flux densities of 0.8 T, 3 T and 9 T. For the different flux densities, a modulation of strand I_c is observed along the cable twist pitch. At low flux density, the strands I_c differs. They are almost the same, with maximums in the parallel (t_p= 0.25) and anti-parallel (t_p= 0.75) orientations, for flux densities above 3 T. As the flux density increases, the width of the peaks around these two specific orientations progressively reduces to become cusp-like at 9 T.

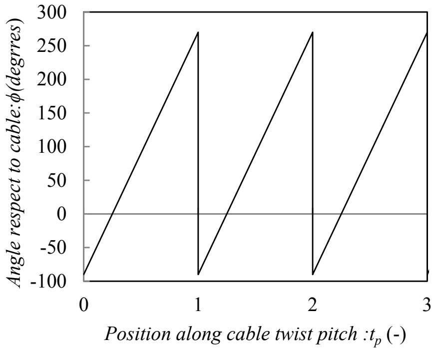

Figure 6.15: The angle of external flux density with respect to the twisted pair cable assembly as a function of the position along twist pitch (t_p).

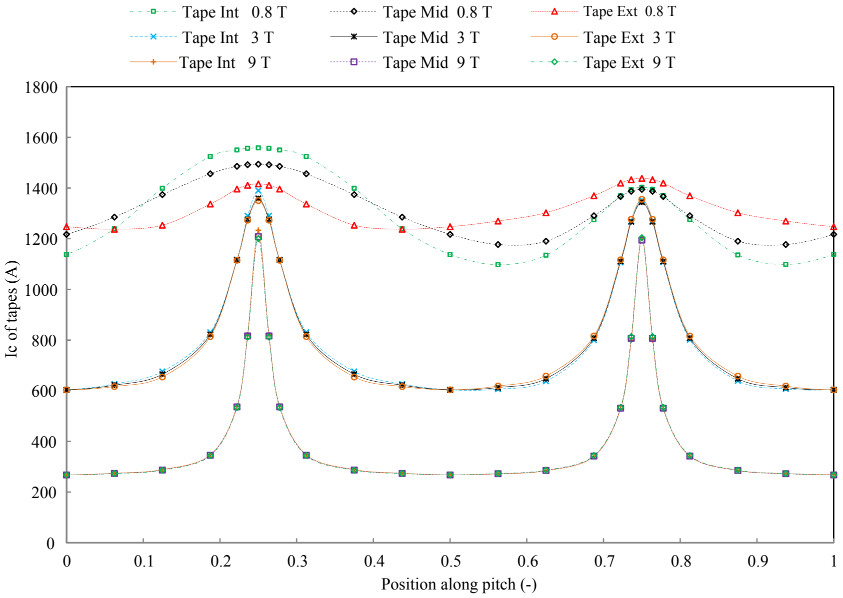

Figure 6.16: Variation of the strand I_c of TP3 cable over one twist pitch at 0.8 T, 3 T and 9 T. The parallel orientation is at t_p= 0.25 and the anti-parallel orientation at t_p= 0.75.

Twisted pair cable I_c

Twisted pair cables are made of 3 or 6 strands connected in parallel. Strands are not transposed over a pitch as they do not take identical positions in the cable cross section. If the strands are insulated from each other, which means no current sharing, the strand I_c is imposed by the weakest spot along a pitch ($I_{ci,min}$) which is almost in the perpendicular orientation. The cable strands present different values of $I_{ci,min}$ since the magnetic and electric boundary conditions differs for each tape on a length scale larger than twist pitch. The cable critical current in the no current sharing assumption is therefore defined as:

$$I_{c,cab} = \sum_{i=0}^{N_b} I_{ci,min} \tag{6.26}$$

On the other hand, if the strands are connected without any electrical resistance along their length, balancing current can share the current between the strands. This is named the complete current sharing. The redistribution of the current does not require additional energy and the local cable critical current $I_{c,cab,loc}$ at a given position along the transposition pitch is therefore estimated by the integration of the J_c over the cable HTS section. Assuming a sharp transition from superconducting to normal state, the twisted pair cable I_c over a transposition pitch is defined as the minimum of $I_{c,cab,loc}$. In figure 6.17, the $I_{c,cab,loc}$ of TP SP6 cable is depicted at different flux densities along the cable twist pitch.

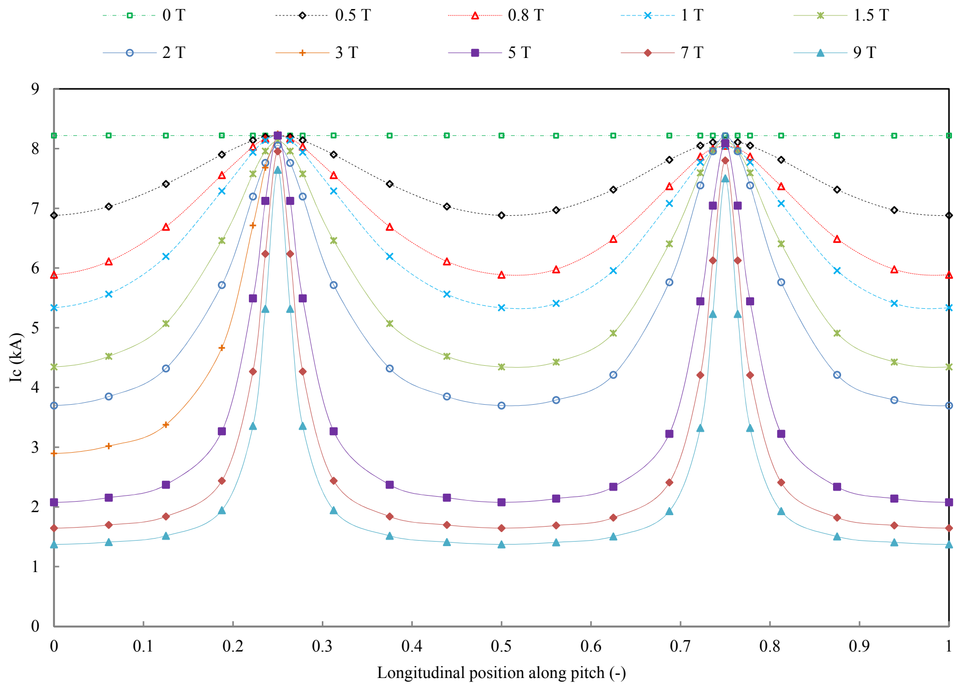

Figure 6.17: The local cable critical current ($I_{c,cab,loc}$) of TP SP6 cable at 4 K along the cable twist pitch.

Cable I_c: simulations and measurements

In figure 6.18, the measured and computed cable I_c of TP SP3 and TP SP6 cables are compared. The computed cable I_c in the complete and the no current sharing approximations are almost identical for both cables.The computed cable I_c are accurate with respect to the measurements over the full flux density range.

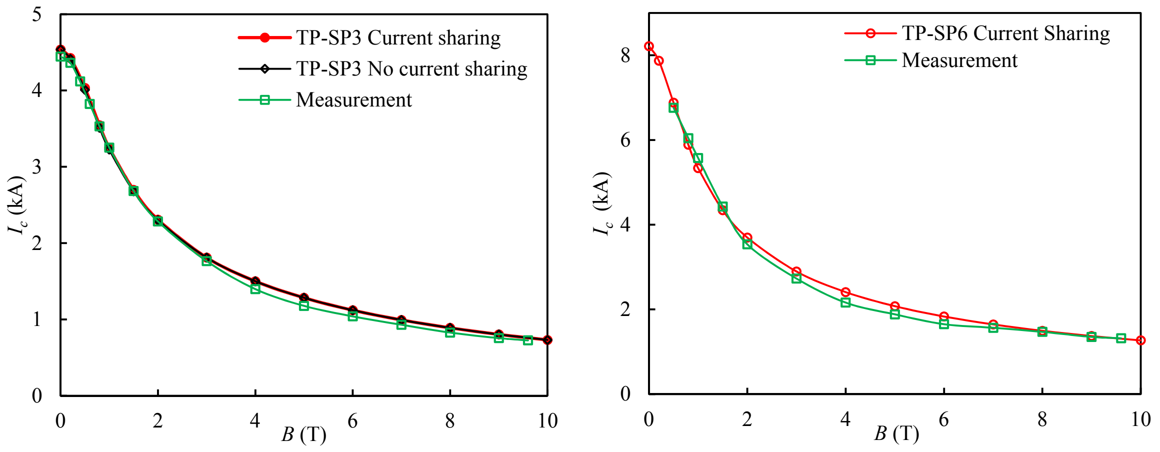

Figure 6.18: The measured and the simulated I_c of TP SP3 (left) and TP SP6 cables (right) as a function of external flux density.

6.4.3 Roebel cable

J_c distribution

The self-field of KIT Roebel cable at 4.2 K is depicted in figure 6.19. It is almost parallel to the central part of innermost strands and closed up at cable edges. Two areas with almost zero flux density are present in each stack of strands. The highest J_c are observed in these two areas. The lowest is observed at cable edges where perpendicular self field is maximum.

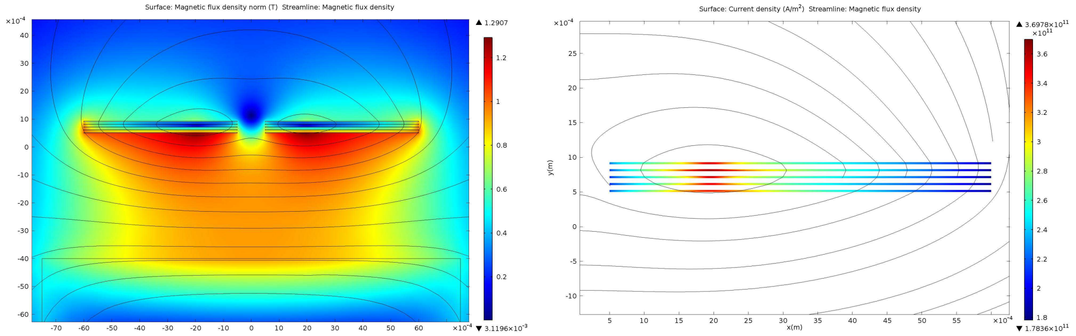

Figure 6.19: The flux density (surface) and the magnetic vector potential (isolevels) (left) and the critical current density (right) in the KIT Roebel cable without external flux density.

Strand I_c in cable cross section

The strand I_c is computed by the integration of J_c over the HTS film cross section. The strand I_c of KIT and GCS cables are depicted in figures 6.20-21 in the perpendicular and parallel orientations. In perpendicular orientation ($\theta = 90°$), the strand I_c is homogeneous for flux densities above 4 T. At lower flux densities, non-uniform values are observed. This is easily explained by the different direction of the perpendicular cable self-field at both cable edges. For parallel external flux densities ($\theta = 0°$) above 4 T, the outermost HTS tapes carry more current than the innermost ones. This is explained by the different direction of cable self field they experience.

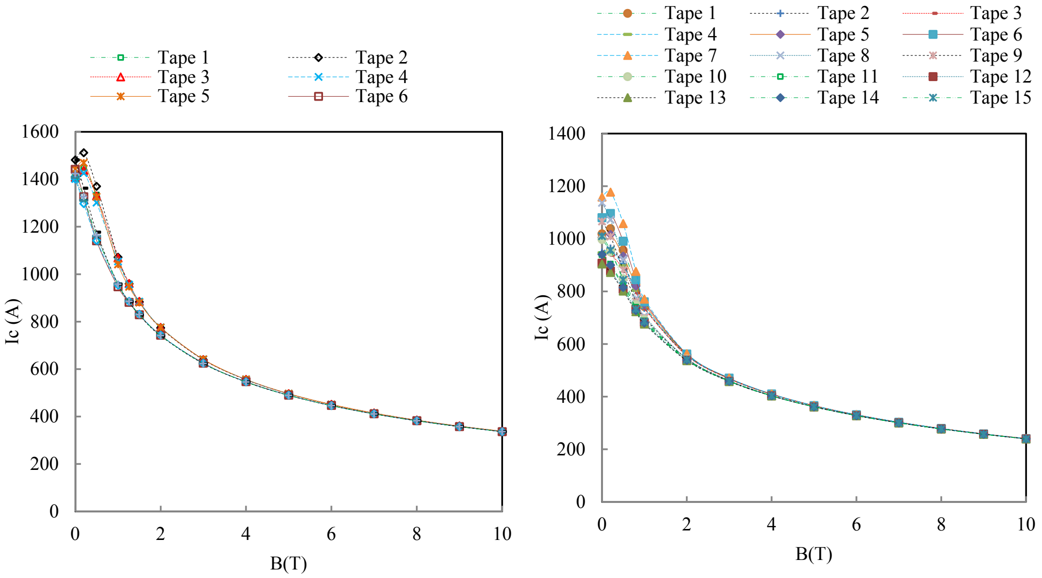

Figure 6.20: The strand I_c of KIT (left) and GCS (right) cables in perpendicular flux densities.

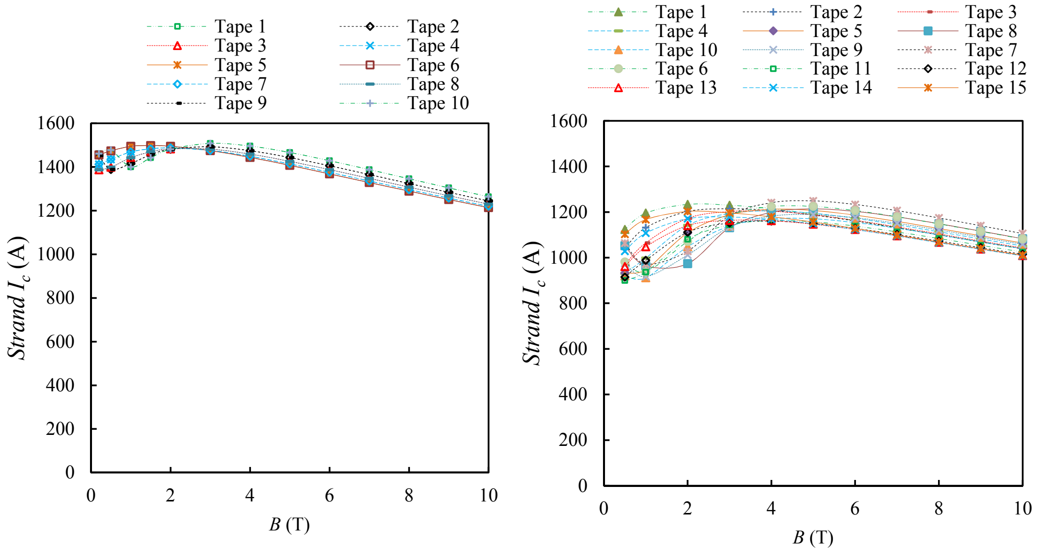

Figure 6.21: The strand I_c of KIT (left) and GCS (right) cables in parallel flux densities.

Strand I_c along cable transposition pitch

Along a transposition pitch, each tape occupies each position in the Roebel cable cross section. This means that the cross section view of the cable can be represented by different positions of a single tape along its length. As shown in figure 6.22 for the 10-strand RACC cable from KIT, there are 10 positions along the meander structure of a tape which are the equivalent to the strands in the cross section view. This transforms the two-dimensional critical current distribution to one dimension. The simulated critical current densities of a meander structured tape along its length are shown in figure 6.23 for the investigated RACC cable in perpendicular ($\theta = 90°$), anti-parallel ($\theta = 180°$) and parallel ($\theta = 0°$) orientations. The dots are the data points gained from the 2D to 1D transformation while the connecting lines are a linear interpolation in each segment.

At perpendicular flux densities above 3 T, the strand I_c are almost homogeneous along the transposition pitch. For lower flux densities, a modulation of strand I_c is observed. The largest variation of I_c is observed at the cable mid pitch (t_p=0.5)

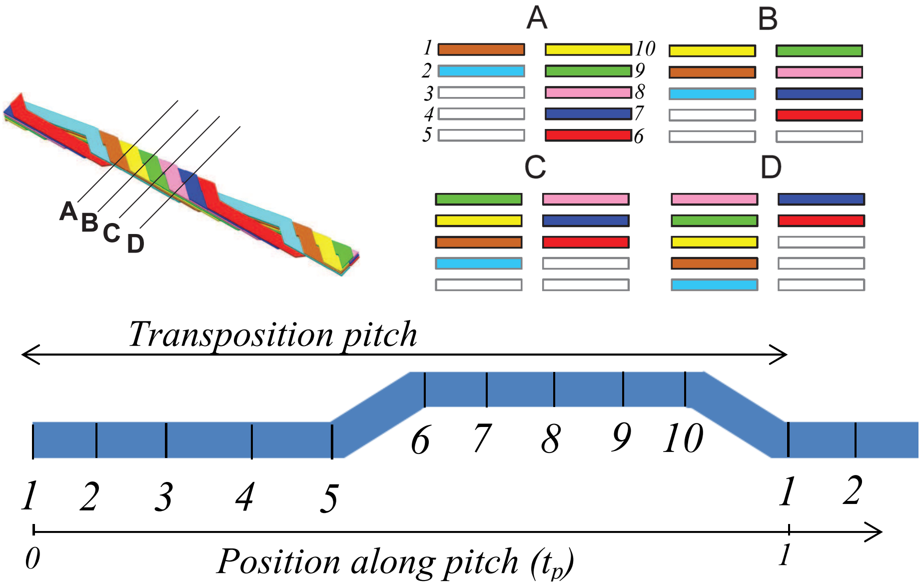

Figure 6.22: Arrangement of the strands in the Roebel cable. The 3D view, with the four marked transverse planes (top left) and the cross-sectional views in these planes (top right). Corresponding positions in the meander structure of a single tape to the strands in the cross section view of a Roebel cable with 10 strands (bottom).

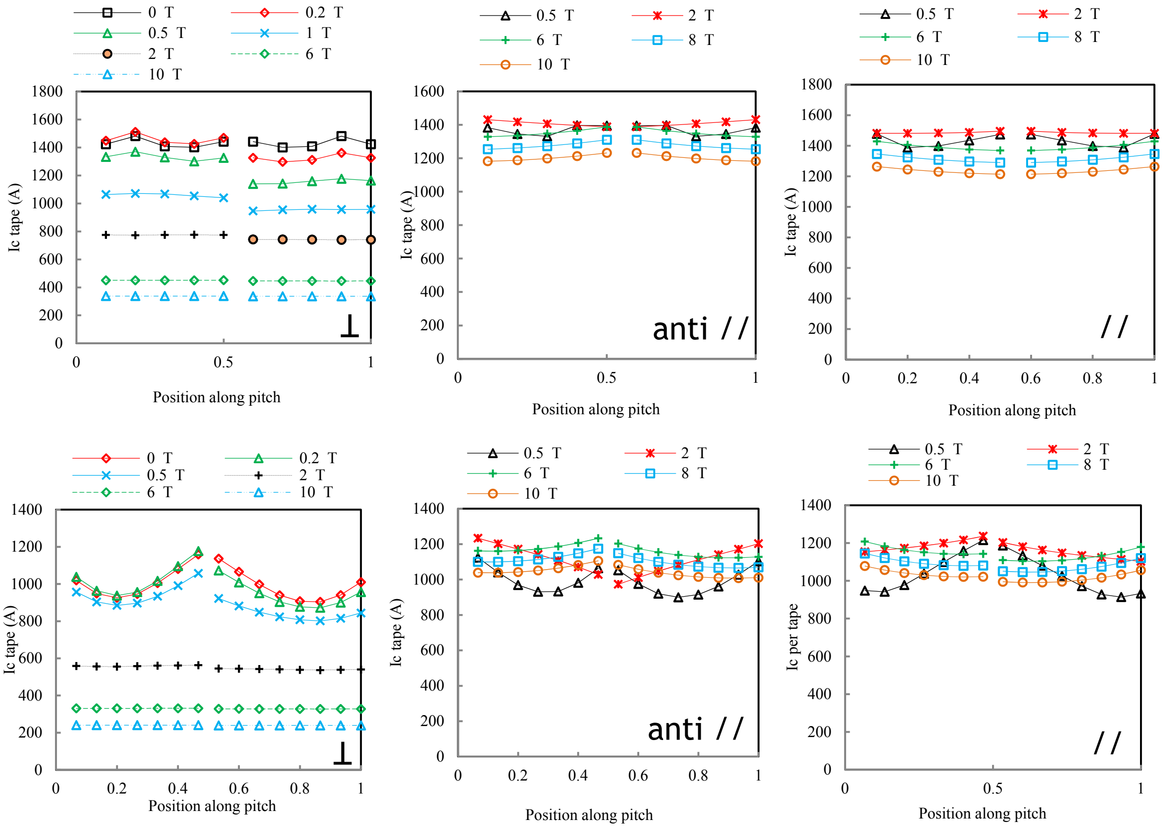

Figure 6.23: Variation of the strand I_c over one transposition length of the KIT (top) and the GCS Roebel cables (bottom) at different flux density orientations: perpendicular (left), anti-parallel (middle) and parallel (right).

Roebel Cable I_c

The Roebel cables are made of 10 or 15 transposed strands connected in parallel. Due to the complete transposition of the strands, their boundary conditions on a length scale larger than a transposition pitch are the same. If the strands are isolated from each other, which means zero current sharing, the weakest point ($I_{c,min}$) along a transposition pitch dictates the I_c of the strand. As the cable is transposed each strand exhibits the same weak spots that causes all the strands to have the same $I_{c,min}$. In the no current sharing assumption, the critical current of a Roebel cable made from N_b strands is therefore $I_{c,cab} = N_b I_{c,min}$. On the other hand, if the strands are connected without any transverse electrical resistance along their length, balancing current can share the current between the strands (complete current sharing assumption).

The computed KIT and GCS Roebel cables I_c in perpendicular and parallel orientations are depicted in figure 6.24 in the complete- and the no -current sharing approximations. The largest deviations between the two approximations are observed at low flux densities. The I_c variation between no current and current sharing is negligible at high perpendicular flux density. It should be noted that the complete current sharing approximation gives by definition larger I_c values than the no sharing one.

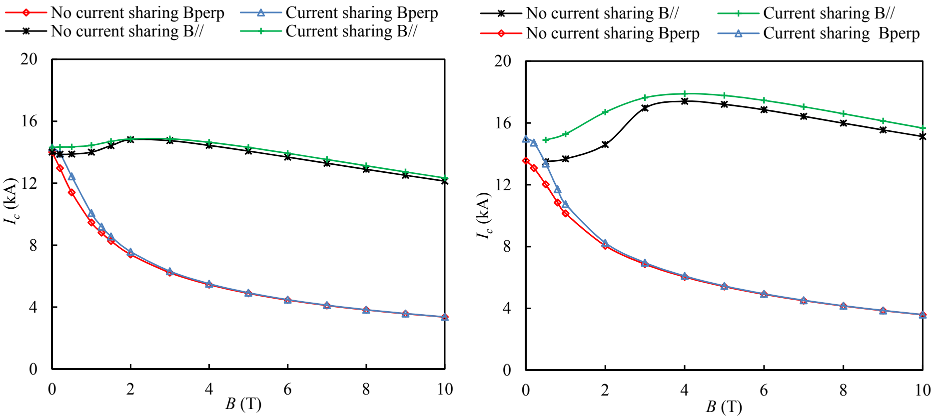

Figure 6.24: The cable I_c of KIT(left) and GCS(left) Roebel cable at 4 K in the no and the complete current sharing approximations.

Cable I_c: experiments and simulations

The inter strand resistance of Roebel cables was measured to be high (25 $\mu\Omega$ at 77 K over a transposition pitch). The level of current sharing is therefore far from complete. The level of current sharing could also be determined by calculating the transport current of a Roebel cable for both cases and comparing these with the measured one. The expected I_c of KIT and GCS cables with and without current sharing are compared with measurement in perpendicular and parallel flux density in figure 6.25. For the perpendicular orientation, a strong agreement is found between measured and simulated values for both cable types. For the parallel orientation, the computed I_c is in accordance with measurements at low flux density but for flux density above 1 T the measurements gives lower values than the model. The linear decrease of the cable I_c with flux densities above 3 T observed in the measurements is also given by the model. Both the 2D approximation of the cable topology and an inappropriate J_c anisotropy implemented in the model may be responsible for this deviation.

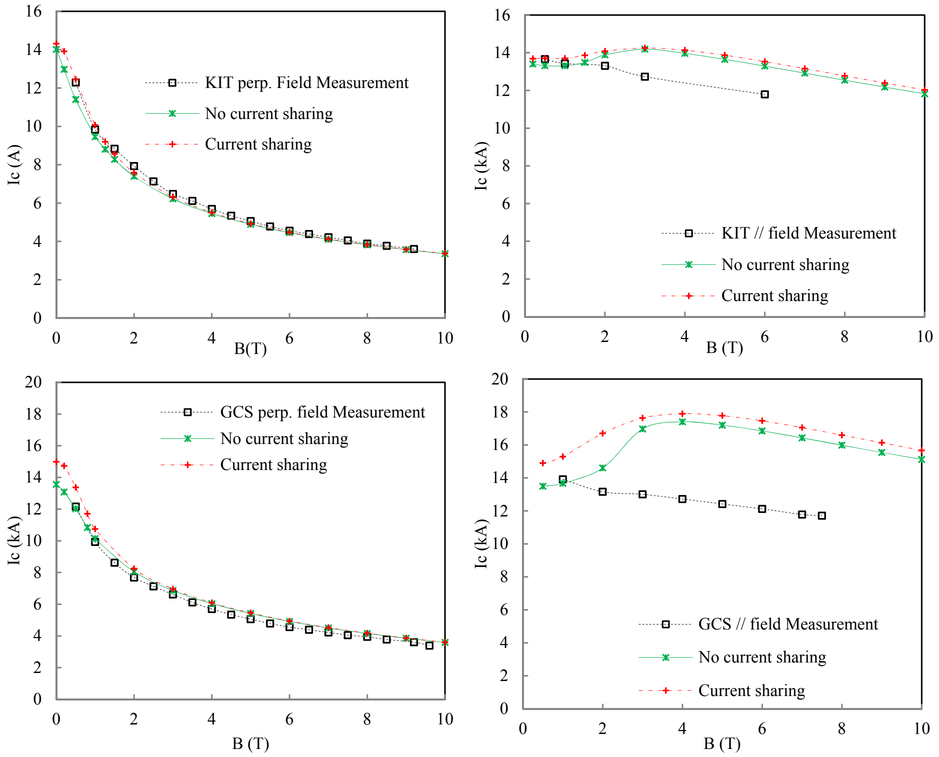

Figure 6.25: The I_c measurements of Roebel cables are compared with the no- and the complete -current sharing simulations. The KIT (top left) and the GCS cables (bottom left) in perpendicular flux density. The KIT (top right) and the GCS cables (bottom right) in perpendicular flux density.

6.5 Current distribution in HTS cable : experiments and simulations

During the characterization of Roebel and twisted pair cables, the current distribution among strands was not measured. Only the electric potential difference along individual strands was recorded. The comparison of the experiments and the simulations is performed therefore through this last parameter. The strands of Roebel and twisted pair cables present n index of about 40-80 at low temperatures, the relation between the current flowing in a strand and the electric field is therefore highly non linear. A small deviation between the simulations and the measurements can therefore be assumed to correspond to a negligible difference in term of current distribution. The simulation results reported here are based on the insulated strand model of current distribution .

In the case of cable made of insulated strands (or with very high interstrand resistance) the cable is modelled as an electric circuit with different branches, one for each superconducting strand. As it was introduced in a previous section, the strand I_c is modulated along the cable pitch. To account for this, the non linear strand resistance of the i_{th} branch defined in eq. (6.4) is replaced with:

$$R_{s,i} = \int_0^L \frac{E_c I_i^{n_i-1}}{I_{c,i}^{n_i}(z)} dz \tag{6.27}$$

Where $I_{c,i}(z)$ is the critical current of the i_{th} strand along the cable pitch which has been computed by the 2D FEM model presented in previous section. Note that to be rigorous, the n_i index should be expressed as a function of the longitudinal location. For the sake of simplification, this dependence will not be considered here and therefore the n index should be seen as being only dependent on external flux density strength. The substrate of AMSC conductor is magnetic and the $I_{c,i}(z)$ of this YBCO tape has not been computed by the mean of the FEM model. Nevertheless, the strand electrical resistances of TP AMSC6 cable have been scaled from the one computed for SuperPower strands.

6.5.1 Twisted pair cable

The only fitting parameters of the simulations of current distribution in twisted pair cables made from insulated strands are the strand joint resistances. These parameters are nevertheless constrained by the fact that the equivalent strand joint resistance should be equivalent to the one measured. For the different twisted pair cables, the measured and computed electrical field along individual strands are reported in figure 6.26 as a function of the reduced cable current. Over the different cables, good agreement between measurements and simulations is found. The corresponding strand joint resistances are reported in table 6.1. Homogeneous R_j values are found for the TP SP6 cable which use the stair joint topology. A large distribution is observed in both the TP SP3 and TP AMSC6 cables which use the stack joint topology. In cable TP SP3, the innermost strand presents the lowest strand contact resistance, the outermost one the highest. The current is injected in the TP AMSC6 cable by the means of two Nb-Ti cables. The HTS strands are stacked together and interleaved between the two Nb-Ti cables. The simulations shows that the outermost strand present the lowest joint resistance and the innermost the highest.

The current distribution among the strands of twisted pair cables is depicted in figure 6.26. The current distribution is much more balanced for the TP SP6 cable (stair joints) than for TP AMSC6 cable (stack joints). In this last, strand 6 carry about three times more current than strand 1 at reduced cable currents lower than 0.4. As already introduced, the stair joint topology promotes balanced current distribution among strands. In twisted pair cables strands are not transposed. On a length scale longer than cable twist pitch their integrated I_c differ (see section 6.4). This explain the uneven current distribution among strands at cable currents equal or above the critical one. Even better fits of electrical field are obtained using the model of current distribution based on non-insulated strands. The interstrand resistance plays a significant role in the current distribution among strands of FRESCA sample if it is more than 1% of the strand splice resistance.

Table 6.1: The best fitting trand joint resistances of twisted pair cables in insulated strand simulations.

	Strand joint resistance (nΩ)		
	TP SP3	TP SP6	TP AMSC6
Strand 1	44	49	32
Strand 2	26	44	45
Strand 3	15	44	83
Strand 4	-	44	95
Strand 5	-	40	112
Strand 6	-	36	123
R_{eq} (nΩ)	7.8	7	11
Standard deviation (nΩ)	15	3	26

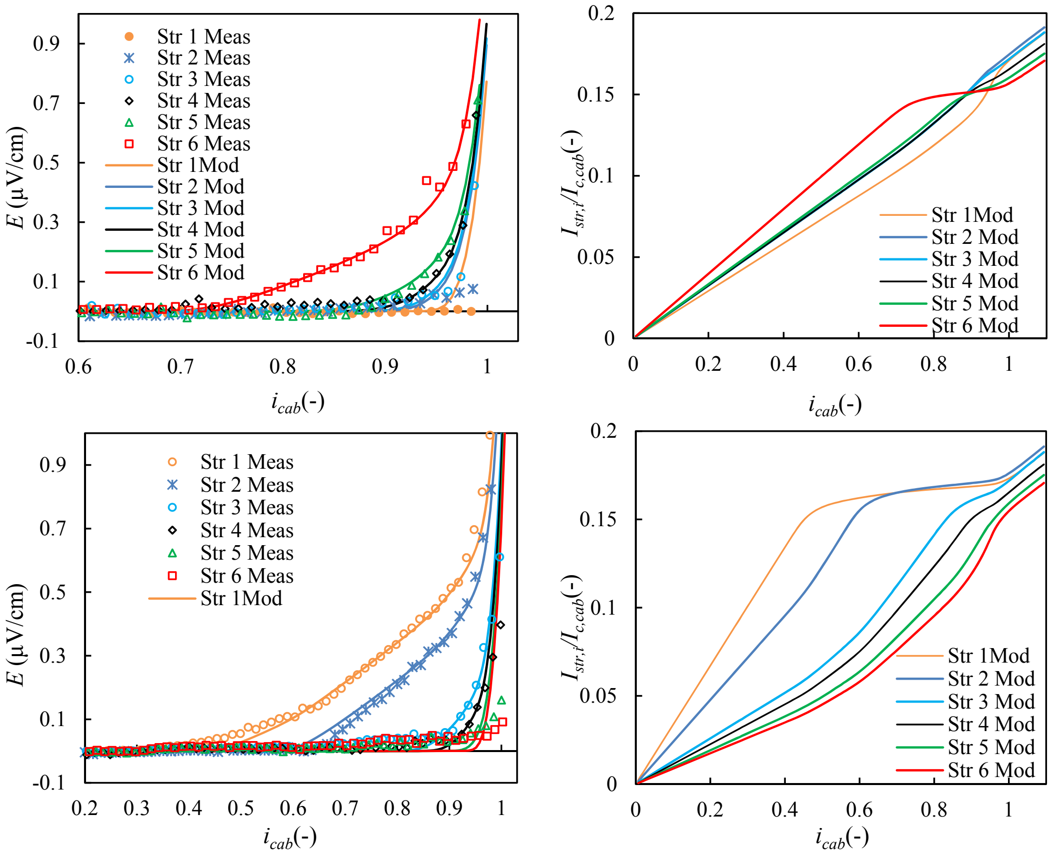

Figure 6.26: Insulated strand simulations (fitting parameters R_j): measured and simulated electrical field along individual strands of TP SP6 (top left) and TP AMSC6 cable (bottom left) as a function of the reduced cable current at 0.8 T. The equivalent current distributions among strands for TP SP6 (top right) and TP AMSC6 cable (bottom right).

6.5.2 Roebel cable

In Roebel cable, strands are transposed; which means that they experience the same magnetic conditions over a twist pitch; they should therefore present the same I_c. In reality, this is far from being true. The ratio between the highest and the lowest I_c in Roebel GCS and KIT cables at 77 K and in self field was measured to be about 1.8. To account for this, in addition to the strand joint resistances, the I_c of the strand are considered as fitting parameters. During Roebel cable characterization, the potential difference was only measured along 8 strands among the 10 and 15 of respectively KIT and GCS cables. For simplicity, in this section the results of the simulation are only depicted for the instrumented strands.

Fitting parameters: strand joint resistances

In a first simulation, only the strand joint resistances of GCS2 cable are considered as fitting parameters. The measured and computed electrical field along individual strands are reported in figure 6.27 as a function of the reduced cable current. Good agreements between measurements and simulation are found. The corresponding strand joint resistances are reported in table 6.2. A large variation of R_j is observed. Micrograph inspections of Roebel cable splices reveal the presence of numerous areas of local delamination of YBCO tapes (see chapter 5). The delaminations increase the contact resistance and thereby induce non uniformity in the strand contact resistance. Even with a limited number of variables (1 per strand), the model describe well the electrical behaviour of the GCS Roebel cable.

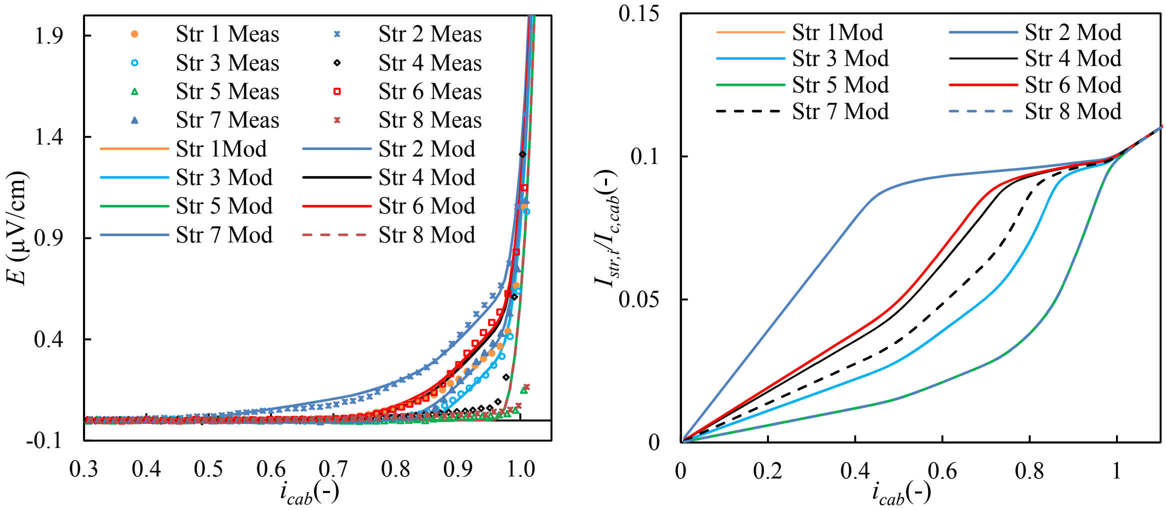

Figure 6.27: Insulated strands simulations (fitting parameters R_j): measured and simulated electrical field along individual strands of GCS2 cable as a function of the reduced cable current at perpendicular flux density of 8.5 T (left). The equivalent current distributions among strands (right) .

Fitting parameters: strand joint resistances and strands I_c

As the strand I_c of Roebel cable have been measured to be non-uniform, they are considered here as fitting parameters. The sum of the critical currents of the strand must nevertheless equal the measured cable I_c. The measured and computed electrical field along individual strands of respectively GCS2 and KIT2 cables are reported in figure 6.28 as a function of the reduced cable current. The corresponding fitting parameters values are reported in table 6.2. A large variation of R_j is observed in both cables. The simulations are in good agreement with the measurements for the GCS2 cable. For the KIT2 cable, however, some discrepancy is observed. In this cable the measured electrical field increases simultaneously in 5 of the 8 instrumented strand at a reduced cable current of 0.6 and it decreases to negative values along strand 4. The insulated strand model could not reproduce perfectly the electrical behaviour of KIT Roebel cables. With the model of non-insulated strand, a specific current redistribution due to a contribution of both a local defect and a specific interstrand resistance distribution may induces negative electric field in a specific strand of a Roebel cable.

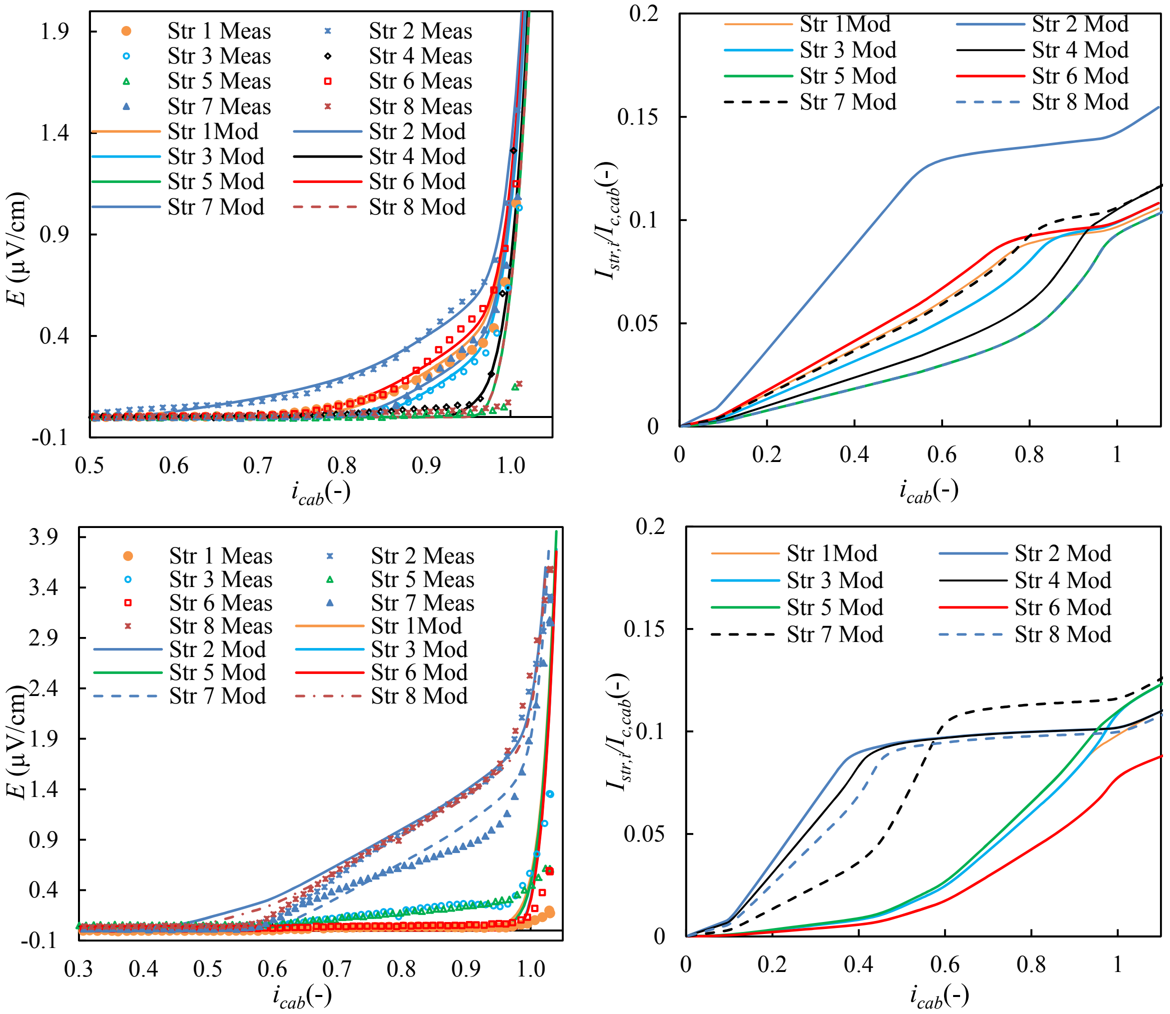

Figure 6.28: Insulated strand simulations (fitting parameters R_j and I_c): simulated and measured electric field along each individual tapes of the GCS2 (top left) and KIT2 Roebel cable (bottom left) under perpendicular flux density of respectively 8.5 T and 8 T. The corresponding current distribution among strands in the GCS (top right) and KIT Roebel cable (bottom right).

Table 6.2: The best fitting strand joint resistances and I_c of the 8 instrumented strands of the Roebel cable.

	Fitting parameters R_j	Fitting parameters R_j and I_c			
Cable ID	GCS2	GCS2		KIT2	
	R_j (nΩ)	R_j (nΩ)	I_c (A)	R_j (nΩ)	I_c (A)
Strand 1	60	74	410	461	250
Strand 2	37	31	600	38	250
Strand 3	77	88	420	462	280
Strand 4	110	117	450	45	250
Strand 5	150	152	400	423	280
Strand 6	60	67	420	654	200
Strand 7	66	76	450	104	286
Strand 8	116	152	400	55	245
Over the 10 and 15 strands of respectively KIT and GCS cables					
R_{eq} (nΩ)	3.5	3.26		3.08	
Standard deviation of R_j (nΩ)	43	47		246	

Comparison of simulated and measured by hall probes current distribution

During the test of the KIT2 Roebel cable, the flux density next to the cable edge was measured along cable pitch by a hall probe array. In the test configuration, the return Nb-Ti cables were placed in vicinity of the Roebel cable. The hall probe array was therefore measuring the contribution to self field of the current flowing in the different strands of both cables. The current distribution among the HTS strands is difficult to derive from the flux density measurements, but a qualitative comparison between measurements and model could nevertheless be performed. The simulated current distribution among the strands of the cable is depicted in figure 6.28. The partial derivative of the simulated ratio of current per strand with respect to the reduced cable current is shown in figure 6.29. In the different strands, bumps in the derivative are observed at the reduced cable current where individual strand reach their I_c.

The measured cable self field is proportional to the cable current (see section 5.1). The partial derivative of the cable self field with respect to the reduced cable current is depicted in figure 6.29. All the different hall probes present a bump in the derivative at reduced cable current of about 0.6. This reduced cable current value corresponds to the point where the electric field along the different strands starts to increase or decrease (see figure 5.13). Although the derivatives of strand current and cable self field are not in complete agreement, similar behaviour is observed.

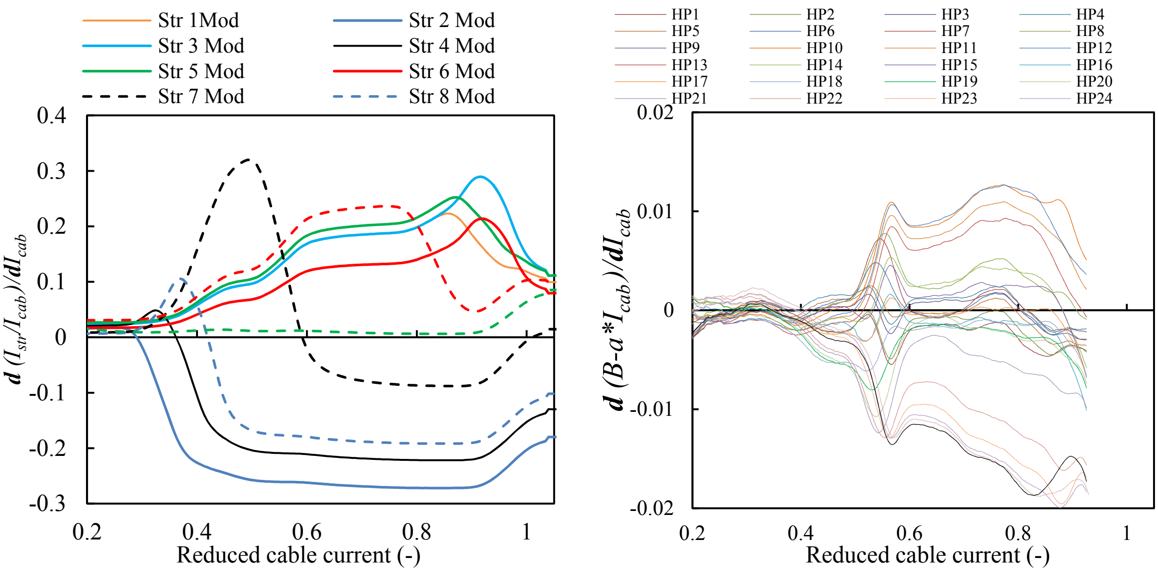

Figure 6.29: The derivative of the flux density measured by the hall probe as a function of the reduced cable current (left). The derivative of the ratio of the computed tape current and cable current as a function of the reduced cable current (right)

6.6 Perspectives for the reduction of I_c anisotropy in YBCO conductors for magnet applications

Coated conductors made of YBCO are very promising for high flux density magnet applications because of their high current carrying capability, high irreversibility flux density and high mechanical strength especially in the versions made on high strength Hastelloy substrates. At low temperatures and high flux densities, the anisotropy of YBCO conductors is in the form of a cusp-like peak around the parallel flux density orientation. A reduction of the conductor I_c anisotropy in the next years may increase the potential performance of HTS magnets built using these conductors. To reduce the YBCO conductor anisotropy there are mainly two scenarios considered here: in the first scenario the J_c peak around the parallel orientation is widened. Such reduction of anisotropy has already been demonstrated by the inclusion of $BaZrO_3$ (BZO) nanodots and nanorods in coated conductors. Since YBCO was until recently mainly developed for application at 77 K, where different pinning mechanism govern the performance, room is foreseen for large improvements in the next years at 4 K. In the second scenario of anisotropy reduction, the width of the J_c peak around the parallel orientation is not modified but the ratio of critical current in parallel and perpendicular flux density ($J_{c,par}/J_{c,per}$) is decreased. The effect of applying these strategies is illustrated in figure 6.30.

The benefits of conductor anisotropy reduction depend on the application. We will consider here only high flux density accelerator magnets operating at low temperatures. In such devices, the coated conductors may be used in insert coils nested in LTS coils. In insert block coil dipoles, the flux density is almost parallel to conductor plane everywhere. The largest deviation (about 13° for the HTS insert of EuCARD program, see chapter 4) is observed at the outermost conductors of the pancakes, farthest away from magnet mid plane. With the anisotropy of present-day coated conductor at high flux densities, a 10-15° deviation from the parallel orientation has a strong reducing effect on conductor I_c. By widening the J_c peak a substantial benefit on HTS coils performance is expected. For the different J_c anisotropies depicted in figure 6.30, the cable margins of the HTS insert of EuCARD program are reported in figure 6.31 (see section 4.3). At the nominal cable current of 2.8 kA the central bore flux density of the

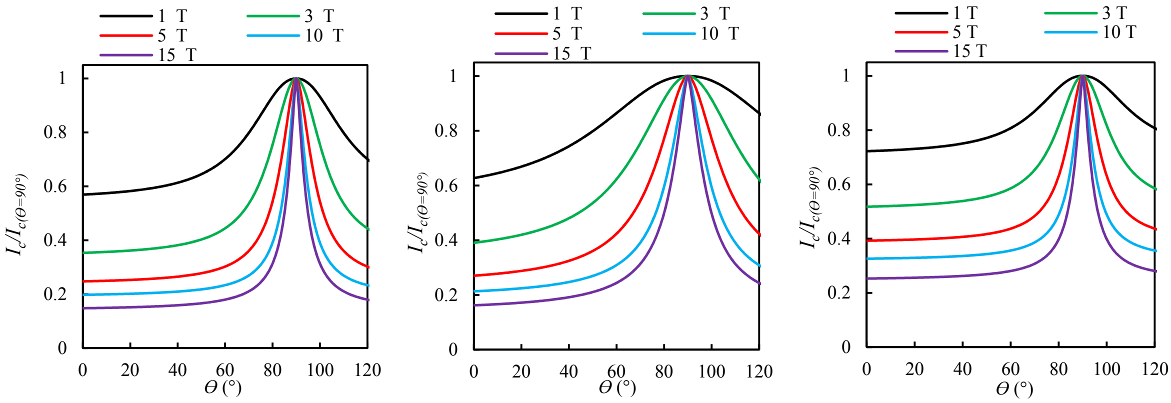

Figure 6.30: The observed J_c anisotropy of present-day YBCO SP tapes at 4.2 K (left). The centre picture shows the effect of reducing the J_c anisotropy by widening the J_c peak around the parallel flux density orientation. Reducing the J_c anisotropy by reducing the ratio of $J_{c,par}/J_{c,per}$ is shown on the right.

magnet is 19.3 T (LTS+HTS) . At this operating point, widening the J_c peak almost tripled the current margins whereas it is doubled by decreasing the ratio $J_{c,par}/J_{c,per}$. As the cable current increases above the nominal, the current margins reduce. The quench current of the magnet increases strongly with a reduction of conductor anisotropy. From 3.34 kA with the anisotropy of present coated conductors, the quench current reaches 4.1 kA by decreasing the I_c ratio and 4.4 kA by widening the J_c peak.

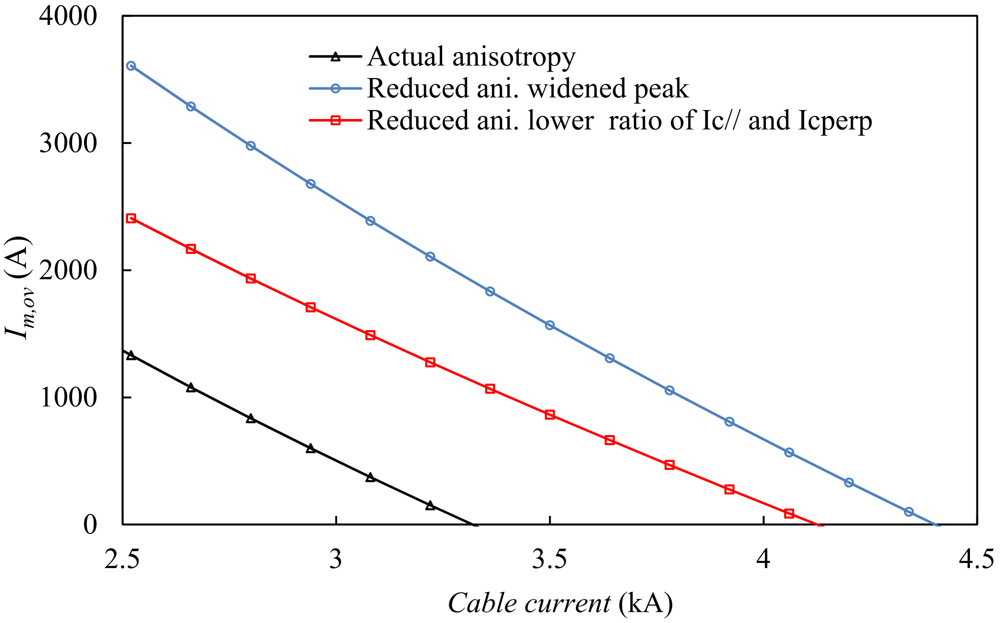

Figure 6.31: The current margin of the cable from the HTS insert of EuCARD program with different conductor J_c anisotropies as a function of the cable current.

At some point of the development of such insert dipole, the HTS cable will have to be characterized. Usually the measurements are carried out in test station similar to FRESCA where the cable is arranged as a single go and return current line in the bore of a dipole. In such a magnetic configuration, the cable self field creates a troublesome perpendicular component of flux density at the edge of the cable.

In figure 6.32, the I_c of a GCS like Roebel cable in perpendicular and parallel flux density are reported for the different J_c anisotropies depicted in figure 6.30. In the parallel orientation, only the widening of the J_c peak is efficient to increase cable performance. On the other hand, in the perpendicular flux density orientation, the cable performance is significantly increased only by reducing the ratio of $J_{c,par}/J_{c,per}$.

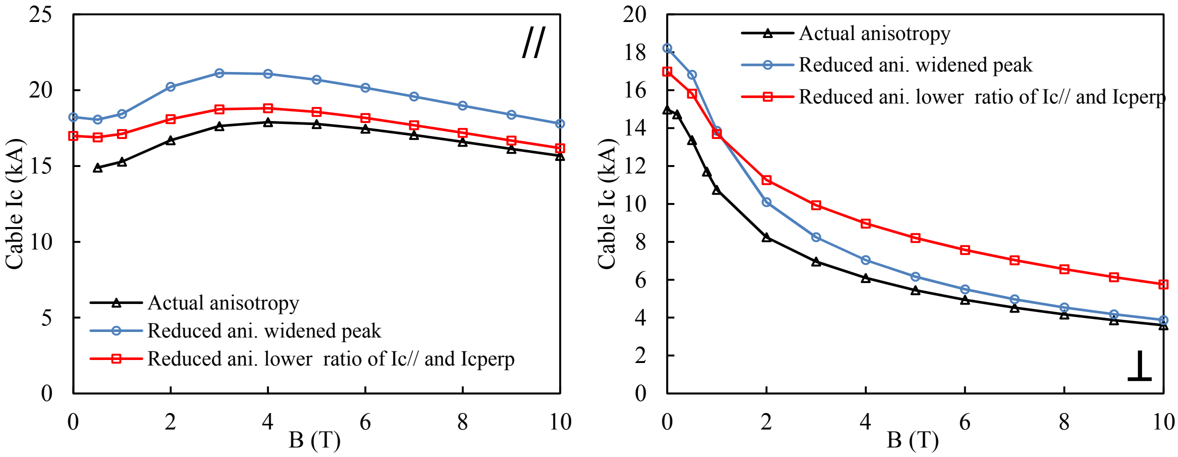

Figure 6.32: The I_c of GCS Roebel cable in perpendicular (left) and parallel flux density (tight) with different conductor J_c anisotropies.

In insert bloc coils, the flux density is almost parallel to the coated conductors and the widening of the J_c peak around the parallel orientation is very efficient to increase the magnet performance. On the other hand, if the flux density is almost perpendicular to the YBCO conductors, as in sector coils, the magnet performance is only increased by a reduction of the ratio $J_{c,par}/J_{c,per}$.

6.7 Conclusion

Multi-strand HTS superconducting cables may quench at current values lower than the expected ones. One of the most likely reasons for this behaviour is non-uniform current distribution among strands. In this chapter, the different reasons for unbalanced current distributions are identified and models of current distribution are introduced. In a transposed cable, conductors occupy different positions in the cable cross sections along the transposition pitch. They experience different self-fields along the pitch length and their critical current is therefore not constant. The performance of HTS strands in transposed cable is calculated by the means of finite element models. The derived cable performances are then compared to the measured ones and globally good agreement has been observed. For the case of Roebel cable in the parallel orientation, the model gives somewhat over-optimistic predictions when compared to the measured results. This discrepancy may be due to both the 2 D simplification of the Roebel cable geometry an a different J_c anisotropy of meander shape strands as compared to that reported. Finally a model of current distribution is elaborated and used for interpreting the results of the measurements. The unbalanced steady state current distribution among the HTS strands of Roebel and twisted pair cable was identified to be driven by non-uniform strand joint resistance.

Conclusion

This work is concentrated on the study of high temperature superconductors and of high temperature superconducting cables optimized for integration in high flux density accelerator magnets. For this application, cables with large current/current density are required. The YBCO and the Bi-2212 materials have critical temperatures of respectively 93 K and 95 K and present very high irreversible flux density and current density when operated at 4.2 K. These materials will enable an increase of the maximum flux density generated by superconducting magnets above the 9 T and 14 T limits obtained with devices made from classical Nb-Ti and Nb_3Sn materials.

Starting from the 2-D electromagnetic design of accelerator dipoles and taking into account the performance of HTS conductors available today, a semi-analytical formula providing an estimate of the ultimate flux density in HTS accelerator dipoles has been derived. The possibility of generating operational flux densities above 20 T with HTS coils was demonstrated. The performance of HTS conductors was studied and characterized under the various operating conditions that they may encounter in magnet winding. Their performance was described with mathematical expressions that enable the computing of their margins when operated in high flux density magnets.

The concept of a transposed Roebel high-current cable made from YBCO conductor was introduced in 2006. Since then, its performances were measured by several groups, but only at 77 K and in self-fields. A pioneer experimental work led to the first successful characterization of Roebel cables at 4.2 K and in flux densities of up to 9.6 T. The measurement of critical currents of 12 kA and current densities in excess of 1.1 kA/mm^2 at 7.5 T demonstrated the potential of such cables for application to high flux density accelerator magnets.

Numerical tools have been implemented to support the comprehension of the performance and of the current distribution in Roebel cables. Measured cables reached their expected performance with an uneven current distribution among the strands. The main reason for such unbalanced distribution has been identified as being due to an uneven strand contact resistance at the splices. Even with the splice designed to promote balanced current distribution, the conductor internal resistance was found to be responsible for the non-uniform splice contact resistance. Another issue in YBCO high current cables is the quench protection. The present configuration of Roebel cables was identified to be critical as regards to protection against quench. Technical solutions were proposed to the cable manufacturer to improve this aspect.

Electrical and mechanical characteristics of YBCO conductors improve continuously, and cable performance improve correspondingly. Experimental and numerical tools introduced and implemented in this work can be used to further quantify and evaluate performance of new cables for accelerator magnets.

Appendix A

Standard J_C(B,T) parameterization of HTS conductors

Accurate $J_c(B,T)$ parametrization are required for a proper use of HTS materials in high flux density magnets. In this appendix, an extensive review of the most significant J_c parameterizations for HTS conductors is performed. Some of the $J_c(B,T)$ parameterization reviewed are similar to the well known functions describing the critical surface of LTS conductors. These functions are briefly introduced in the first part of this appendix. Finally, a self consistent $J_c(B,T)$ parameterization is set for the different HTS conductors.

A.1 $J_c(B,T)$ parameterization of LTS materials

In Low Temperature Superconductors the concept of the critical state was introduced by Bean [45]. This critical state model, developed later on by [97][95], provides the magnetic hysteresis in type II superconductors in flux density between the onset of flux penetration and the upper bulk critical flux density B_{c2}. The pinning of the flux line lattice with various crystal imperfections in type II superconductor is responsible for the existence of a critical current density (J_c). A pinning force density (F_p) can be defined as the critical value of the Lorentz force per unit volume $F_p = J_c\ B$. A function of the reduced flux density ($b = B/B_{c2}$) was introduced by Fietz and Webb [228] to scale the pinning force density for Nb based materials:

$$F_p = J_c\ B \propto b^p\,(1-b)^q \tag{A.1}$$

The reduced flux density at which occurs the maximum of pinning force ($F_{p,max}$) is named b_{max}. For reduced flux density below b_{max} the flux motion occurs by de-pinning of individual fluxoid, whereas for reduced flux density above b_{max}, the flux motion occurs by synchronous shear of the flux line lattice around line pins too strong to be broken [229]. It has been observed than $F_{p,max}$ is dependent on temperature but occurs at constant value of reduced flux density $b_{max} = p/(p+q)$ [228]. The value of b_{max} and $F_{p,max}$ are sensitive to metallurgical treatment [228]. The normalized Fietz and Webb function is depicted versus the reduced pinning force of Nb-Ti and Nb_3Sn conductors in figure A.1.

A.1.1 The temperature dependence of B_{c2}

The pinning force density explicitly depends on temperature through the critical flux density dependence which enters the definition of the reduced flux density. For Nb-Ti and Nb_3Sn materials, an empirical relation for the temperature dependence of B_{c2} was introduced by respectively Lubell [132] and Summers [30]:

$$B_{c2,NbTi}(T) = B_{c2,0}\left(1 - t^{1.7}\right) \tag{A.2}$$

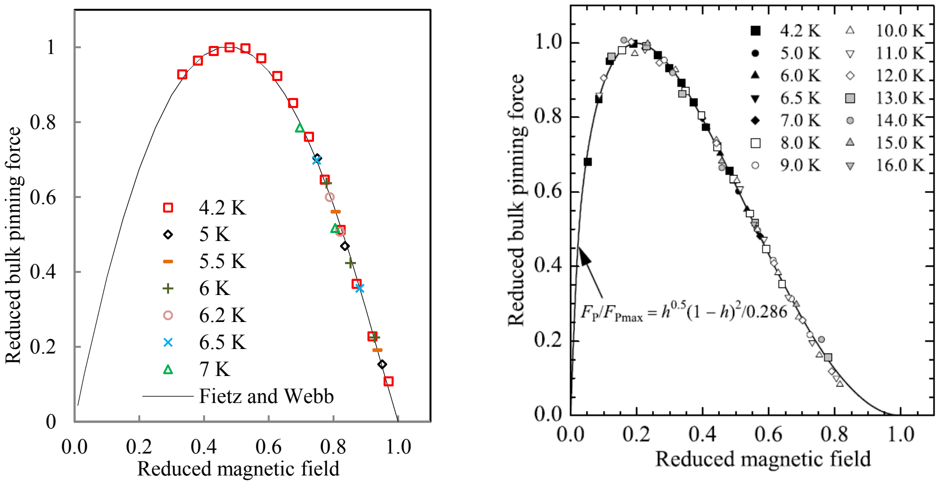

Figure A.1: Sketch of the flux density dependence of the bulk pinning force ($f_p = F_p/F_{p,max}$) as function of the reduced flux density for Nb-Ti conductors [189](left) and Nb$_3$Sn conductors [98] (right).

$$B_{c2,Nb3Sn}(T) = B_{c2,0}\left(1-t^2\right)\left(1-0.31\ t^2\left(1-1.77\ \ln t\right)\right) \tag{A.3}$$

where the reduced temperature t is defined as the ratio of the temperature and the critical temperature in zero external flux density ($t = T/T_{c,0}$). The parameter $B_{c2,0}$ expresses the upper critical flux density at 0 K. For Nb-Ti conductors, $T_{c,0} = 9.2$ K and $B_{c2,0} = 14.5$ T [132]. For Nb$_3$Sn conductors, $T_{c,0} = 18.3$ K and $B_{c2,0} = 27$ T [30].

By using the Maki and De Gennes approximation [230][231], a microscopic based temperature dependence of B_{c2} of Nb$_3$Sn was provided by Godeke [98].

$$B_{c2,Nb3Sn}(T) = B_{c2,0}(1-t^{1.52}) \tag{A.4}$$

This function provide a good fit to data over the full temperature range. The temperature dependence of the Ginzburg-Landau parameter given by the empirical Summers fit is not accurate. The Godeke's description of B_{c2} provides an accurate temperature dependence of the Ginzburg-Landau parameter, rendering the empirical description of Summers redundant.

A.1.2 The temperature and flux density dependence of J_c

A self-consistent parameterization, that provides a temperature and flux density dependence of J_c, was introduced by Bottura [28] for Nb-Ti materials:

$$J_{c,NbTi}(B,T) = \frac{C_0(1-t^{1.7})^m}{B}\left(\frac{B}{B_{c2}}\right)^p\left(1-\frac{B}{B_{c2}}\right)^q \tag{A.5}$$

With the following typical parameters values [28] : $p = 0.57 - 0.8$, $q = 0.75 - 1.10$, $m = 1.76 - 2.3$, $B_{c2,0} = 14.2 - 14.4$ T, $T_{c,0} = 8.5 - 9.35$ K and $C_0 = 23.8 - 37.7$ AT/mm^2. The critical current density of Nb-Ti conductors at 4.2 K is 3000 A/m^2. A similar expression has been introduced by Godeke [98] for Nb$_3$Sn conductors:

$$J_{c,Nb3Sn}(B,T) = \frac{C_0(1-t^{1.52})(1-t^2)}{B}\left(\frac{B}{B_{c2}}\right)^{0.5}\left(1-\frac{B}{B_{c2}}\right)^2 \tag{A.6}$$

where $T_{c,0} = 16.8$ K, $B_{c2,0} = 30.7$ T and $C_1 = 46.6$ kAT/mm^2. These two J_c parameterizations are compared with reported measurements in figure A.2. The standard deviation of the fits is of the order of 5% or better over an extended validity range of flux density from 0 T to 9 T and temperature from 1.9 K to 9 K [28]. This accuracy is generally sufficient for design purpose, extrapolation and scaling of measured results.

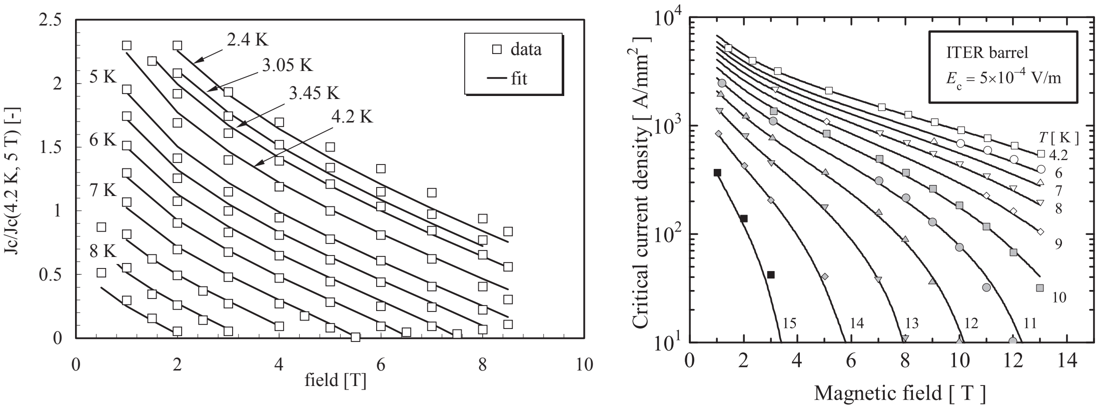

Figure A.2: Flux density dependence of the normalized J_c ($J_c(T,B)/J_c(4.2\ K, 5\ T,)$ in Nb-Ti wires [28] (left). Flux density dependence of J_c in Nb$_3$Sn wire (ITER barrel) at temperature ranging between 4.2 K and 15 K [98] (right).

A.2 $J_c(B,T)$ parameterization of HTS materials

Accurate $J_c(B,T)$ parameterization are required for a proper use of HTS materials in high flux density magnets. An extensive review of the most significant J_c parametrizations for HTS conductors is performed in this section. The most appropriate fit for recent HTS materials is then selected with the help of representative J_c data sets. Appropriate descriptions of the irreversibility flux density and pinning force are then provided and finally a self-consistent formulae of J_c dependence on temperature and flux density is elaborated for HTS materials.

A.2.1 $J_{c,sf}(T)$ parameterization

In some applications such as current leads and transmission line cables [182], HTS materials are operated without background flux density. In self field, the J_c dependence on temperature of HTS materials could be described with the simple consistent formulation [232][233]:

$$J_{c,s.f}(T) = J_{c0.s.f}\left(1 - \frac{T}{T_e}\right)^k \tag{A.7}$$

where k is a fitting parameter, T_e is the fitting critical temperature and $J_{c0,s.f}$ is the critical current density at 0 K. The stoichiometric T_c of YBCO, Bi-2212 and Bi-2223 is respectively 93 K, 85 K and 108 K. The fitting parameter T_e is within 10 K of the stoichiometric T_c. The temperature dependence of J_c in self field for YBCO SP, YBCO AMSC, Bi-2223 SEI, Bi-2223 BHTS and Bi-2212 OST conductors has been reported [234][36][114][127][34]. The best fitting parameters values of expression (A.7) with respect to the data sets are reported in table A.1. The exponent k=1.2-1.5 provides a satisfactory fit for YBCO and Bi-2223 conductors. The Bi-2212 conductors have shown a higher value of 3.2. In figure A.3, the reported measurements (markers) are compared with the fits (lines). Over the full temperature range, the parameterization is in good agreement with measurements.

Table A.1: The parameter values of $J_{c,s.f}(T)$ parameterization for YBCO SP, YBCO AMSC, BSCCO SEI, BSCCO BHTS and BSCCO OST conductors.

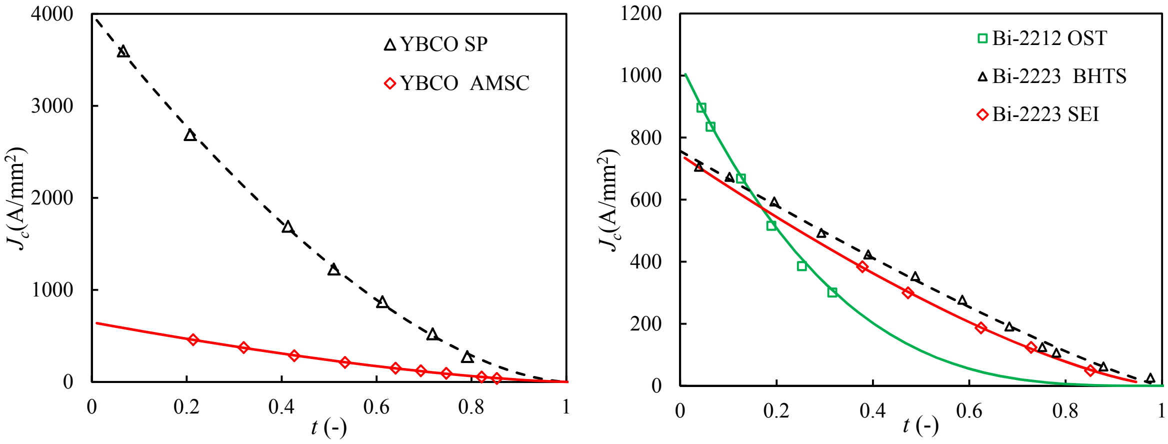

Figure A.3: The $J_{c,s.f}(T)$ of YBCO SP and YBCO AMSC conductors (left). The $J_{c,s.f}(T)$ of BSCCO SEI, BSCCO BHTS and BSCCO OST conductors (right).

Conductor	k	T_e (K)	J_{c0} (A/mm^2)	Ref.
YBCO SP	1.64	98	3997	[234]
YBCO AMSC	1.45	94	648	[36]
Bi-2223 SEI	1.40	105	745	[114]
Bi-2223 BHTS	1.2	103	760	[127]
Bi-2212 OST	3.21	92	1040	[34]

A.2.2 $J_c(B,T)$ parameterization

Accurate $J_c(B,T)$ parameterization are required for efficient use of HTS materials in high flux density magnets. Several practical fits were proposed in the literature; the most relevant, empirical or physical based, are reviewed in this section. The performance of HTS conductors has improved greatly over the last decade and starts to approach the intrinsic limitations of the cuprates. An evaluation of the fit accuracy with respect to recent conductor performance is therefore necessary. Over the different parameterizations reviewed, the most appropriate to describe the J_c dependence on flux density strength and temperature of YBCO, Bi-2223 and Bi-2212 conductors is determined.

Review of J_c parameterization

The most relevant J_c parameterizations for HTS materials are reviewed in this section. To make the comparison easier between the different parameterizations, the parameters are standardized. The different expressions are reported in table A.2.

- Hsiang and Finnemore
  By considering the decay of the superconducting wave function trough Superconducting-Normal-Superconducting state junctions (SNS), De Gennes [235] showed than the critical current could be expressed in an exponential form. This work has been extended by Hsiang and Finnemore [236] to include the flux density dependence of the characteristic decay length, using a phenomenological model (see expression 1 in table A.2). Similar parameterization was used by [237][238][239].

- Flux creep theory
  The flux creep theory was developed for LTS materials. It explains the origin of J_c by the pinning of magnetic vortex to pinning centers [229]. In LTS superconductors, impurities, defects, precipitates,

and grain boundaries work as strong pinning centers [240]. The London penetration depth of the HTS superconductors is very long [241][242]. The internal flux density in the vortex lattice is almost uniform, and thus the pinning force due to the magnetic interaction is very weak [46]. In addition, the coherence length is very short [243] and thus the vortex core size is very small. The interaction of the vortex core with impurities, defects, precipitates, and grain boundaries will not yield a strong pinning in HTS [191]. On the other hand, experiments imply that some strong pinning force acts on the vortices in the HTS superconductors. The CuO_2 layers of HTS crystals and their vicinities are strongly superconducting and the layers with CuO chains and their vicinities are weakly superconducting. The superconducting order parameter is modulated along the c-axis of the crystals with the period of the lattice constant (a_c). Since the coherence length along the c−axis is shorter than a_c except in the vicinity of T_c, the radius of the vortex core along the c axis is smaller than a_c. The superconducting order parameter inside the core almost vanishes. Therefore the loss of the superconducting cohesive energy due to inclusion of the vortex is the least when the vortex is placed around the layers with CuO chains where the superconducting order parameter is the smallest [191]. Since the vortex is stabilized the most in these layers, the modulation of the order parameter works as natural pinning centers. The J_c parameterization based on flux creep theory has been widely used for HTS materials [244][245][246] (see expression 2 in table A.2).

- Muller
  The J_c dependence on flux density in the Muller et al. [247] parameterization, is determined by the Josephson vortices critical current densities across grain boundaries (see expression 3 in table A.2). These in turn depend on the shape of the cross-sectional areas of the grain boundary junctions as well as on the angle at which the flux density threads the junctions relative to their edges.

- Kobayashi
  A simple empirical logarithmic function to express the J_c of Bi-2223 samples over a large range of temperature and flux density was proposed by Kobayashi et al. [248] (see expression 4 in table A.2).

- Verebelyi and Uglietti
  A good prediction of the J_c of YBCO samples with different grain alignment was obtained by Verebelyi et al. [249] using an empirical formulation (see expression 5 in table A.2). Using the same expression, Uglietti et al [138] found good agreements when measuring J_c of a YBCO sample under perpendicular flux density between 12 T and 26 T at 4.2 K.

- Yamafuji
  In studying current voltage characteristics near the glass liquid transition Yamafuji et al. [250] found that the J_c obeys to a power law expression (see expression 6 in table A.2).

- Matsushita
  Different temperature dependences of the B_{irr} in low and high temperature regions of Bi-2212 single grains was observed by Matsushita [251]. This was ascribed to different pinning centers. Pointlike defects were believed to be effective at low temperature. For this temperature region, based on the activated flux motion, the J_c was expected to vary with temperature and flux density respect to expression J_1 (see expression 7 in table A.1). For high temperature region, non-superconducting particles of the Bi-free phases were expected to be effective. This contribution J_2 uses the same expression but with different parameters values. The J_c density is expressed in table A.2 (see expression 7 in table A.2).

- Van der Laan
  Based on the rail switch model [252] and classical flux-creep theory, Van der Laan [253] assumes that a superconducting current is running in two distinct parallel paths. The first current path with a cross sectional area (A_1), and a current density (J_1) is formed by grains that are connected at angles below 4° that form a strongly linked network. The second one, with a cross sectional

area (A_2), and a current density (J_2) is formed by superconducting grains that are connected at intermediate angles (4°-8°) where dissipation occurs at the grain boundaries. Dissipation in both linked networks is well described by classical flux-creep theory. The total cross sectional area (A) of the current path is, obviously, the sum of A_1 and A_2. The overall transport J_c is described as the summation of contributions of both networks (see expression 8 in table A.2).

- Weijers
  Based on measurements performed at 4.2 K, Weijers [254] proposed an J_c description based on contribution from both a strongly (J_{cs}) and a weakly linked network current paths (J_{cw}) (see expression 9 in table A.2). The parameters J_{cs0} and J_{cw0} are respectively the critical current density of the strongly and weakly linked network at zero external applied flux density. B_{sc} and B_0 are the characteristic flux density of the two networks. The J_{cw} and J_{cw} expressions are derived from collective pinning theory. The total current is expressed as the arithmetic sum of both contributions.

- Staiger
  The parameterization proposed by Staiger [255] for Bi-2223 tapes, assumed a network of platelike grains coupled by weak links to explain the superconducting current through the tape (see expression 10 in table A.2). At high temperatures the critical current is governed by flux creep of pancake vortices within the grains. At temperatures below 40 K this intragrain critical current exceeds the intergrain Josephson current leading to a weak link limitation in the tape. The intragranular current density is described by J_p in table A.2 where J_w is the critical Josephson current density across weakly coupled grains in c direction. The parameter a describes the volume fraction of well coupled grains near the silver sheath.

Table A.2: The reviewed J_c parameterization of HTS materials.

	Expression ID	Expression	Nb. of fitting parameters
Hsiang and Finnemore	(1)	$J_c = J_{c0}\exp(-B/B_0)$	2
Flux creep theory	(2)	$J_c = \frac{J_{c0}}{B}\left(\frac{B}{B_0}\right)^p\left(1-\frac{B}{B_0}\right)^q$	4
Muller	(3)	$J_c = J_{c0}\frac{1}{(1+\lvert B\rvert/B_0)^p}$	3
Kobayashi	(4)	$J_c = \frac{J_{c0}}{\log(B_0/B_1)}\log(B/B_1)$	3
Verebelyi	(5)	$J_c = \frac{J_{c0}}{\sqrt{B}}$	1
Yamafuji	(6)	$J_c = J_{c0}\left(\frac{\lvert B_0-B\rvert}{B_0}\right)^p$	3
Matsushita	(7)	$\begin{cases} J_c = \sqrt{J_1^2+J_2^2} \\ J_{i,i=1,2} = \frac{J_{c0,i}}{B}(\frac{B}{B_{0,i}})^{p_i}(1-\frac{B}{B_{c,i}})^{q_i} \end{cases}$	8
Van der Laan	(8)	$\begin{cases} J_c = \frac{A_w}{A}J_{c,w} + \frac{A_s}{A}J_{c,s} \\ J_{i,i=w,s} = J_{c0,i}\exp\left[-\left(\frac{J_{c0,i}}{B}\right)^{n_i}\ln\frac{E_{0,i}}{E_c}\right] \end{cases}$	9
Weijers	(9)	$J_c = \frac{J_{c0,1}}{1+B/B_{0,1}} + J_{c0,2}\exp\left(-B/B_{0,2}\right)$	4
Staiger	(10)	$\begin{cases} J_c = \begin{cases} J_p & forJ_p < J_w \\ (1-a)J_w + aJ_p & forJ_p > J_w \end{cases} \\ J_p = J_{p,0}exp(-\frac{B}{B_1}) \\ J_w = J_{w,0}\left(\frac{B_0}{B}\right)^c \end{cases}$	6

Selection of J_c(B,T) parameterization for HTS materials

In order to determinate which J_c parameterization is the most accurate for present HTS materials, representatives J_c data sets of YBCO, Bi-2223 and Bi-2212 are used. By scaling the flux density and normalizing the J_c to the self field value one can superpose easily the J_c performances of HTS materials at different temperatures, as depicted in figure A.4. The determination of the most accurate J_c parameterization could therefore be carried out at a specific temperature. Figure A.4 shows the typical J_c of HTS materials as a function of applied flux density and identifies what we call in this work the exponential, the low and the high flux density regime, delimited by B_1 and B_2. At medium flux density ($B_1 < B < B_2$), an exponential behaviour occurs as depicted in figure A.4. The exponential fit underestimates measurements at low flux density ($B < B_1$) whereas it overestimates measurements for high flux density ($B > B_2$). The J_c measurements performed at low temperature doesn't extend over the three flux density regimes since the B_{irr} of HTS materials is high (above 100 T [32][33]) and the highest DC flux density available for characterization is 45 T [101]. At high temperatures, the B_{irr} is lower (10-20 T at 70 K) and the three regimes are observed. Representatives data sets of YBCO Bi-2223 and Bi-2212 that shows the three regimes are used to determinate which J_c parameterization is the most appropriate for today's HTS materials. The different data sets used are presented in table A.3.

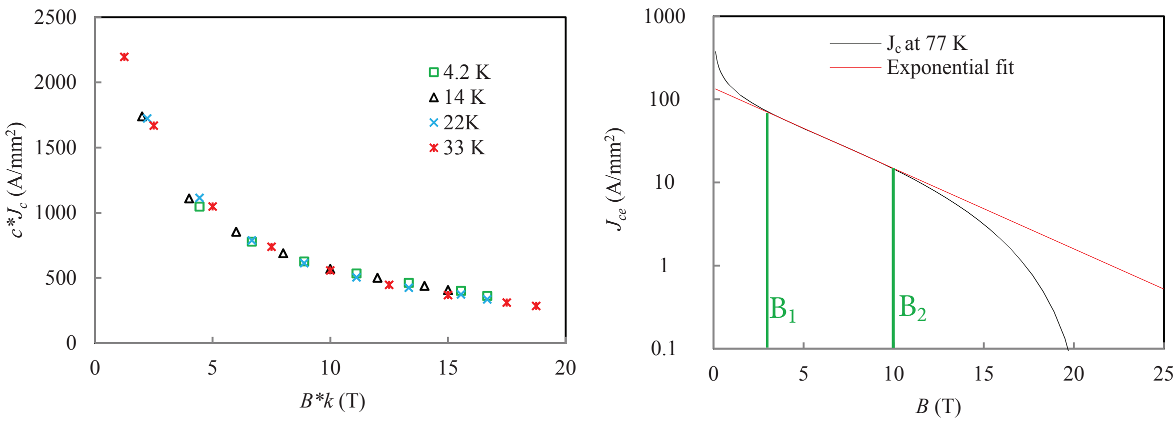

Figure A.4: The superposition of J_c data at different temperature (data from [112]) (left). The three flux density regime: the low for $B < B_1$, the exponential for $B_1 < B < B_2$ and the high for $B > B_2$ (right).

Table A.3: J_c datasets used to discuss parameterization accuracy

Material	Flux density orientation	Dataset ID	Ref	Temperature (K)	Flux density Range (T)
YBCO	Parall	1	[256]	80	2-17
YBCO	Perp	2	[256]	65	2-17
YBCO	Parall	3	[244]	60	0.5-24
Bi-2212	-	4	[34]	12	0-15
Bi-2223	Parall	5	[114]	40	0-10
Bi-2223	Perp	6	[114]	20	0-10

The parameter values of table A.2 have been optimized (RMS J_c minimization) in respect with the different J_c data sets listed in table A.3. The optimization, in a first step, is carried out on the full flux density range. Unfortunately some fit are only able to be in accordance with data over a limited range. In a second step, the optimization is performed on this specific limited flux density range. The different fits are therefore accurate with respect to measurements over the most extended flux density range. The normalized RMS J_c error for each data set is reported in table A.4. For each parameterization, the normalized RMS J_c error over the different data sets is averaged. It comes out from this quantitative study than the J_c parameterization based on flux creep theory is the most appropriate for HTS materials. The fits based on two currents networks are also quite accurate but require more fitting parameters. The J_c parameterization based on flux creep theory for HTS materials is in the form:

$$J_c(B,T) = \frac{C\ F_{p,max}}{B}\left(\frac{B}{B_{irr}}\right)^p\left(1-\frac{B}{B_{irr}}\right)^q \tag{A.8}$$

where C is a normalization constant. The temperature dependence is given implicitly through $F_{p,max}$ and B_{irr} which are temperature dependent. The temperature dependence of these two parameters is introduced in next sections.

Table A.4: Normalized RMS error of the J_c parameterization of table A.2 versus the data sets of table A.3.

	Normalized RMS Error						
Data set ID	1	2	3	4	5	6	Overall
Hsiang and Finnemore	13.5	29.8	3.7	5.5	1.6	2.7	9.5
Flux creep theory	1.5	1.5	1.0	1.1	1.1	1.0	1.2
Muller	3.1	5.0	3.1	1.0	2.8	4.0	3.2
Kobayashi	4.8	10.3	1.0	7.9	1.4	2.5	4.6
Verebelyi	13.8	10.4	7.0	9.0	4.0	20.7	10.8
Yamafuji	12.1	32.7	5.6	2.1	15.2	44.2	18.7
Matsushita	1.4	4.9	4.7	6.9	1.0	2.6	3.6
Van der Laan	2.1	1.0	1.1	1.1	1.3	2.2	1.5
Weijers	1.3	1.6	1.4	4.2	1.0	17.5	4.5
Staiger	1.0	1.4	1.1	1.2	2.3	1.0	1.3

Temperature dependence of B_{irr}

The irreversibility flux density (B_{irr}) is defined as the flux density beyond which the J_c of superconductors is null. Unfortunately, as it was the case for the Nb_3Sn in the $70^{'}s$, the direct measurements of HTS irreversibility flux density at low temperature is not possible due to the limited (45 T) flux density available for characterization in DC mode [101]. The measurement of B_{irr} in AC flux density have been carried out on YBCO and BSCCO materials, and values of B_{irr} exceeding 100 T at 4.2 K was reported [32][33]. The B_{irr} of HTS materials measured in DC mode have been reported at different temperatures, for different flux density orientations, down to temperature of about $0.4 - 0.6\ T_c$. Few relevant B_{irr} parameterizations reported in literature are presented in table A.5. In figure A.5, the different fits are optimized in respect with a measurement data set. The different fits are accurate over the full range of measurements but deviate from one another at lower temperatures. An absolute estimation of the most appropriate B_{irr} parameterization is therefore not possible directly. The most appropriate expression is found to be that one which leads to the best fit to J_c data when used in expression (A.8). The most appropriate B_{irr} description is in the form:

$$B_{irr}(T) = B_{irr,0}(1-t^{m_1})^{m_2} \tag{A.9}$$

where m_1 and m_2 are fitting parameters and $B_{irr,0}$ is the irreversibility flux density at 0 K.

Table A.5: parameterization of B_{irr} dependence on temperature.

Expression	Ref.	Expression
(1)	[251][257][258]	$B_{irr} = B_{irr,0}\,(1-t)^{m_3}$
(2)	[259][255]	$B_{irr} = B_{irr,0}\,(1/t-1)^{m_3}$
(3)	[233]	$B_{irr} = B_{irr,0}\exp -t$
(4)	[260][246][245]	$B_{irr} = B_{irr,0}\left(1-t^2\right)^{m_3}$
(5)	[261][244]	$B_{irr} = \frac{B_{irr,0}}{1-m_4}(1-t)\left[1-\frac{m_3}{1-t}\sqrt{\left(1+\frac{m_3}{1-t}\right)^2-\frac{4m_4m_3}{1-t}}\right]$

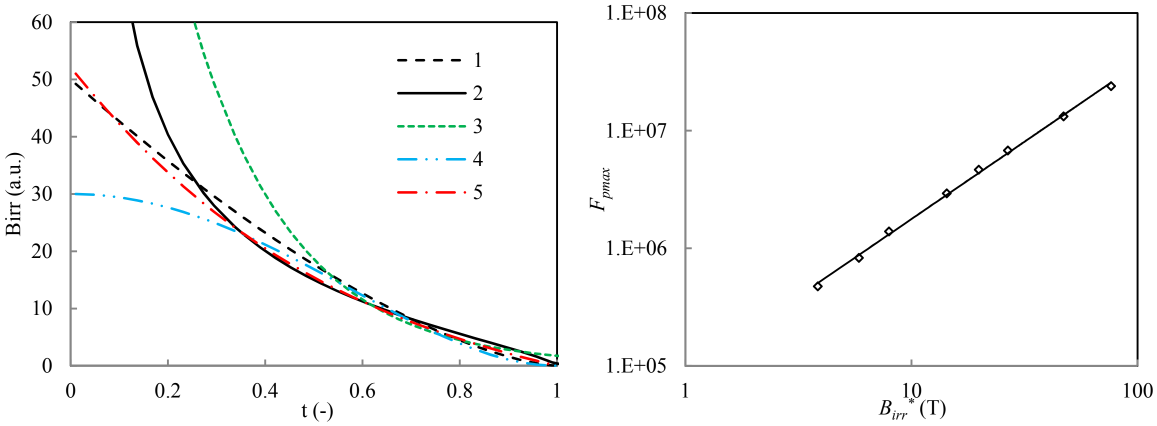

Figure A.5: B_{irr} as function of the reduced temperature for the different expressions listed in table A.5 (left). The maximum of the pinning force as function of the scaled irreversibility field (right)

Temperature dependence of $F_{p,max}$

The J_c of HTS materials, and therefore the pinning force density, depend on temperature. The maximum of the pinning force density ($F_{p,max}$), occurring at the reduced flux density $b_{max} = (p+q)/p$ has been observed in LTS materials to vary as a power law of B_{irr} [229]. The transposition of this expression to HTS materials has already been reported [244][262][232]. This power law description provides a satisfactory fit to J_c data when inserted in expression (A.8). The $F_{p,max}$ is therefore expressed as :

$$F_{p,max} \propto B_{irr}^{n_1} \tag{A.10}$$

where n_1 is a constant.

Standard self consistent parameterization of the $J_c(B,T)$ of HTS conductors

A self consistent formulation of the J_c dependence on flux density and temperature for HTS materials could be set by inserting expression (A.9-10) in expression (A.8):

$$J_c(B,T) = \frac{C_0\left((1-t^{m_1})^{m_2}\right)^{n_1}}{B}\left(\frac{B}{B_{irr}}\right)^p\left(1-\frac{B}{B_{irr}}\right)^q \tag{A.11}$$

with $B_{irr}(T)$ defined in equation (A.9). In figure A.6, this self consistent formulation is compared with the J_c measured on a to 50 μm wide YBCO sample in perpendicular and parallel flux density [102]. The small width of the sample limits the effect of the self field on the conductor J_c. The fit provides a really good agreement with data over the full range of measurements and this in both flux density orientations.

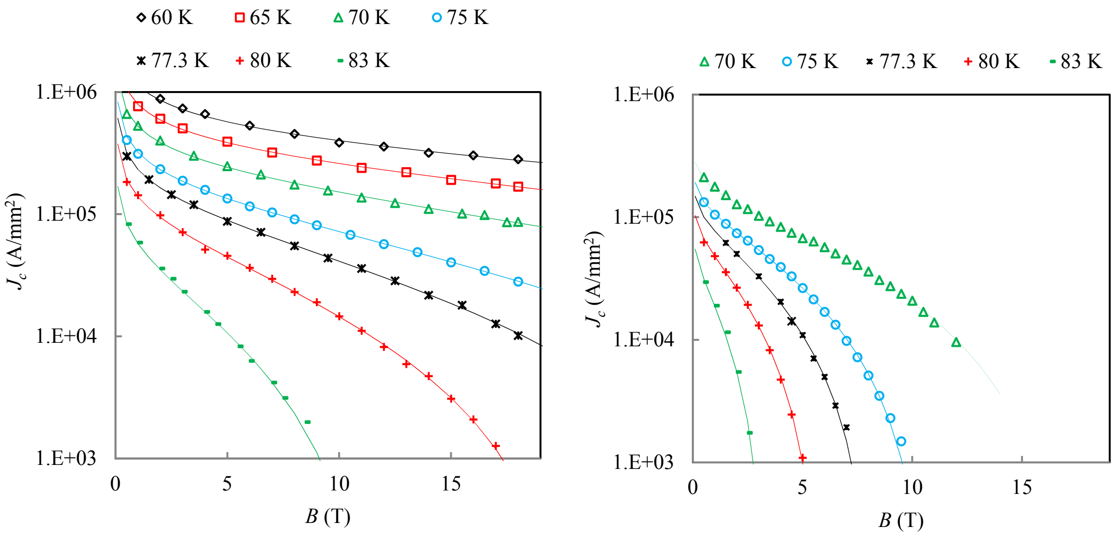

Figure A.6: Comparison of the J_c parameterizations and measurements [102] performed on YBCO coated conductors in parallel (left) and perpendicular (right) flux density orientations.

Appendix B

Symbols

Symbol	Description	Unit
a	Sensitivity to axial strain	-
A_{core}	Rutherford cable core cross section	m^2
A_c	Superconducting cross section of HTS cable	m^2
a_0, a_1, a_2	Fitting parameters of the material strain sensitivity	-
B_{c1}	Lower critical flux density	T
B_{c2}	Upper critical flux density	T
B_{irr}	Irreversible flux density	T
$B_{iir,0}$	Irreversible flux density at 0 T	T
B_n	Flux density harmonics	T
B_p	Peak flux density	T
B_x	Perpendicular flux density with respect to YBCO tape	T
B_y	Parallel flux density with respect to YBCO tape	T
B_0	Magnet bore flux density	T
$B_{0,ss}$	Bore flux density at short sample limit	T
B_3	First allowed flux density harmonic in dipole made of symmetric four folds	T
C_0	Constant	
D	Strand diameter	m
D_m	Length of measurement	m
d	Fitting parameter	$A/(T.mm^2)$
D_0	The lap joint interfacing distance	m
D_1	Length required for electrical junction	m
D_2	Length required for current transfer	m
E	Young modulus	$N.m^{-2}$
e,f	Fitting parameters	
e_0,e_1	Fitting parameters	
F_p	Bulk pinning force density	$N.m^{-3}$
$F_{p,max}$	Maximum Bulk pinning force	$N.m^{-3}$
F_x,F_y	Lorentz force components	$N.m^{-1}$
g_0,g_1,g_2		
H_c	Critical field	$A.m^{-1}$

H_{c2}	Upper critical field	A.m^{-1}
H_{irr}	Irreversibility field	A.m^{-1}
I	Current	A
I_c	Critical current	A
I_{cab}	Cable current	A
i_{cab}	Reduced cable current	-
$I_{c,cab}$	Critical cable current	A
I_{c0}	Critical current density at infinite bending radius or infinite twist pitch	A
I_{cc}	Corrected critical current to 4.22 K	A.m^{-2}
I_{cme}	Critical current measured at the temperature T_{me}	A.m^{-2}
I_{kink}	Kink current	A
i_{kink}	Reduced kink current	-
$I_{m,loc}$	Local current margin	A
$I_{m,ov}$	Global current margin	A
I_{nom}	Nominal current	A
I_{op}	Cable operating current	A
$I_{q,loc}$	Quench current (local margin)	A
$I_{q,ov}$	Quench current (global margin)	A
I_q	Cable quench current	A
$i_{str,i}$	Strand reduced current	-
$I_{s,kink}$	Splice kink current	A
$i_{s,kink}$	Reduced cable splice current	-
I_{tot}	Current deliver by power supply	A
i_1, i_2, i_4, i_5	Inflection of reduced strand current	-
J_c	Critical current density	A.m^{-2}
J_w	Current density in the magnet winding	A.m^{-2}
J_{ce}	Engineering critical current density	A.m^{-2}
J_{wt}	Winding current density threshold	A.m^{-2}
J_e	Engineering current density	A.m^{-2}
$J_{c,perp}$	Critical current density in perpendicular flux density	A.m^{-2}
$J_{c,parall}$	Critical current density in parallel flux density	A.m^{-2}
J_{HTS}	Current density in the HTS layer	A.m^{-2}
$J_{c,min}$	Minimum of critical current density over the HTS winding	A.m^{-2}
J_{c0,ε_m}	Critical current density at uniaxial strain	A.m^{-2}
$J_{c,s.f}$	Critical current density in self flux density	A.m^{-2}
J_{ce}	Engineering critical current density	A.m^{-2}
K	Dilution factor	-
k		
L'	Chord length after tape torsion	m
L_s	Sample length	m
L_s	Splice length	m
l_i	Self inductance	H
$M_{i,j}$	Mutual inductance	H
m_1,m_2	Fitting parameters of the irreversible field	-

n_1	Fitting parameters of the irreversible field versus the $F_{p,max}$	
N_b	Number of strands in superconducting cable	-
p,q	Fitting parameters of the pining force	
P_f	Packing factor	-
R_m	Geometric mean distance	m
R_{si}	Superconductor resistance	Ω
R_{ji}	Joint resistance	Ω
R_a	Adjacent contact resistances	Ω
R_{eq}	Equivalent cable joint resistance	Ω
R_{fc}	The Roebel cable resistance	Ω
R_s	HTS/LTS splice resistance	Ω
R	Resistance	Ω
R_i	Magnet coil inner radius	m
r	Radial position in the coil	m
r_a	Adjacent strand contact resistance	Ω
r_0	Fitting parameter	
$R_{i,t}$	Irreversible in plane bending radius for compression	m
$R_{i,c}$	Irreversible in plane bending radius for compression	m
R	Bending curvature radius	m
S_m	Winding cross sectional area	m^2
s	Fitting parameter	-
S_c	Splice resistivity	Ω.m^2
T_{me}	Temperature of measurement	K
T_{cf}	Fitting critical temperature	K
Tp_i	Irreversible twist pitch	m
T_{op}	Operating temperature	K
T_q	Quench temperature	K
T_c	Critical temperature	K
$T_{rp,min}$	Minimum transposition pitch of Roebel cable made from rectilinear conductors	m
$T_{q,loc}$	Local quench temperature	K
$T_{q,ov}$	Global quench temperature	K
T_e	Fitting critical temperature at 0 K, 0 T	K
T_p	Twist pitch	m
$T_{p,i,c}$	Irreversible twist pitch for compression	m
$T_{p,i,t}$	Irreversible twist pitch for tension	m
t_m	Cable average thickness	m
U_{ind}	Inductive voltage of strand element	V
V_{fc}	Electrical potential drop along the full length of Roebel cable	V
v_{fc}	Normalized deviation of V_{fc} from linear behaviour	
w_c	Magnet coil width	m
w_m	Cable average width	m
W	Cable width	m

w	Strand width	mm
x_{irr}	Irreversible distance for torsion	m
x	Distance to the neutral axis for edge bending	m
y	Distance to the neutral axis for face bending	m
α	Cable pitch angle	rad
α	Roebel crossing angle	rad
α	Deviation of flux density with respect to YBCO tape	rad
$\varepsilon_{irr,c}$	Uni-axial irreversible compressive irreversible strain	
$\varepsilon_{irr,t}$	Uni-axial irreversible tensile irreversible strain	
$\varepsilon_{fb})$	Uni-axial strain induced by face bending	-
$\varepsilon_{eb,edge}$	Uni-axial strain induced by edged bending	-
ε_{t}	Uni-axial strain induced by torsion	-
ε_{0}	Uni-axial global compressive strain induced by torsion	-
ε_{tw}	Uni-axial strain induced by pure torsion	-
ε_{m}	Uni-axial strain at which J_c is maximum	
ε_{m0} ,ε_{m1}	Fitting parameters of HTS material strain sensitivity	-
$\varepsilon_{eb,x=0} = 0$	Strain induced by edged bending at tape mid width	-
ε_{irr}	Irreversible strain threshold	-
γ_0	Characteristic of the coil layout	Tm/A
γ_2	Anisotropy ratio of the material	
ψ	Torsion angle	rad
$\phi_0 = h/2e$		
ϕ	Extend of the sector coil	$^\circ$
θ	Angle between the flux density and the YBCO tape plane	deg
σ_x	Transverse compressive stress on conductor	N.m^{-2}
σ	Axial stress	N.m^{-2}
σ_ϕ	Azimuthal compressive stress on the coil mid plane	N.m^{-2}
τ	Decay time constant of induced coupling currents	s

Acronym	
AMSC	American Superconductor
BHTS	Bruker HTS
BB	back to back lap joint configuration
BF	f ace to back lap joint configuration
CEA	Commissariat à l'énergie atomique
CT-OP	controlled overpressure sintering process
DMM	Digital multi-meter
EuCard	European Coordination for Accelerator Research and Development
FF	face to face lap joint configuration
HERA	Hadron Electron Ring Accelerator
HTS	High Temperature Superconductor
IBAD	Ion beam assisted deposition
IHEP	Institute for High Energy Physics
INFN	Istituto Nazionale di Fisica Nucleare
LBNL	Lawrence Berkeley National Laboratory
LTS	Low Temperature Superconductor
LHC	Large Hardon Collider
MOCVD	Metallo-Organic Chemical Vapor Deposition
MOD	Metal Organic Deposition
MRI	Magnetic resonance imaging
NHMFL	National High Magnetic Field Laboratory
NMR	Nuclear magnetic resonance
NSRRC	National Synchrotron Radiation Research Center
NZPV	normal zone propagation velocity
OST	Oxford instruments Superconducting Technology
PIT	Powder in Tube
RACC	Roebel Assembled Coated Conductor
RABiTS	Rolling Assisted Biaxially Texture route
RHIC	Relativistic Heavy Ion Collider
RRC	Roebel cable from Rectilinear Conductor
R&W	React and wind route
SEI	Sumitomo electric Industry
SP	SuperPower
TS2	Test Station Nb.2 of CERN bd. 163
TS4	Test Station Nb.4 of CERN bd. 163
UniGe	Univeriste de Geneve
W&R	Wind and react route

Bibliography

[1] L. Rossi and L. Bottura. Superconducting Magnets for Particle Accelerators. *Reviews of Accelerator Science and Technology*, 5, 2012.

[2] O. Brüning, P. Collier, P. Lebrun, S. Myers, R. Ostojic, J. Poole, and P. Proudlock. LHC Design Report. *Internal CERN*, 2004.

[3] E. Todesco and J.-P. Koutchouk. Scaling laws for Beta in the LHC Interaction Regions. *LHC-LUMI*, 2006.

[4] U.P. Trociewitz, B. Czabaj, S. Hong, Y. Huang, D.C. Knoll, D.C. Larbalestier, W.D. Markiewicz, H. Miao, M. Meinesz, X. Wang, and J. Schwartz. Quench studies on a layer-wound $Bi_2Sr_2CaCu_2O_x$/AgX coil at 4.2 K. *Supercond. Sci. Technol.*, 21, 2008.

[5] T. Lecrevisse. *Contribution a l' Etude des aimants supraconducteurs utilisant des materiaux supraconducteurs a haute temperature de transition*. PhD thesis, Universite de Grenoble, 2012.

[6] A. Ballarino, S. Mathot, and D. Milan. 13000 a HTS current leads for the LHC accelerator: from conceptual design to prototype validation. *LHC Project Report 69*, 2004.

[7] A.R. Hafalia, S.E. Bartlett, S. Caspi, L. Chiesa, D.R. Dietderich, P. Ferracin, M. Goli, S.A.Gourlay, C.R. Hannaford, H. Higley, A.F. Lietzke, N. Liggins, S. Mattafirri, A.D. McInturff, M. Nyman, G.L. Sabbi, R.M. Scanlan, and J. Swanson. HD1: Design and Fabrication of a 16 Tesla Nb_3Sn Dipole Magnet. *Physical Review*, 91(9), 2005.

[8] P. Ferracin, B. Bingham, S. Caspi, D.W. Cheng, D.R. Dietderich, H. Felice, A. Godeke, A.R. Hafalia, C.R. Hannaford, J.M. Joseph, A.F. Lietzke, J. Lizarazo, G.L. Sabbi, F. Trillaud, and X.R. Wang. Assembly and Test of HD2 and a 36 mm Bore High Field Nb_3Sn dipoe magnet. *IEEE Trans. Appl. Supercond.*, 19(3), 2009.

[9] E. Rochepault, P. Vedrine, and F. Bouillault. 2D Analytical Magnetic Optimizations for Accelerator Dipole Block Designs. *IEEE Trans. Appl. Supercond.*, 22(3), 2012.

[10] M. Bruchon, M. Durante, M. Karppinen, F. Kircher, P. Manil, A. Milanese, L. Oberli, J.C. Perez, J.M. Rifflet, G. de Rijk, F. Rondeaux, and E. Todesco. EuCARD-HFM dipole model design options. *Note EuCARD-HFM Project*, 2010.

[11] A.D. McInturff et al. Test Results for a High Field (13 T) Nb_3Sn Dipole. *Part. Accel. Conf.*, 1997.

[12] P. Fessia, F. Regis, and E. Todesco. Parametric Analysis of Forces and Stresses in Superconducting Dipoles. *IEEE Trans. Appl. Supercond.*, 19(3), 2009.

[13] N. Cheggour, J.W. Ekin, C.C. Clickner, D.T. Verebelyi, C.L.H. Thieme, R. Feenstra, A. Goyal, and M. Paranthaman. Transverse Compressive Stress Effect in Y-Ba-Cu-O Coatings on Biaxially Textured Ni and Ni-W Substrates. *IEEE Trans. Appl. Supercond.*, 13(2), 2003.

[14] C.S. Li, E. Mossang, B. Bellin, A. Antonevici, and P.X. Zhang. Effects of compressive stress on the critical current of Bi-2223 tapes. *Physica C*, 463-465, 2007.

[15] J.G. Bednorz and K.A. Müller. Possible High T$_c$ Superconductivity in the Ba - La- Cu- 0 System. *Z. Phys. B - Condensed Matter*, 64(189), 1986.

[16] U.P. Trociewitz, M. Dalban-Canassy, M. Hannion, D.K. Hilton, J. Jaroszynski, P. Noyes, Y. Viouchkov, H.W. Weijers, and D.C. Larbalestier. 35.4 T field generated using a layer-wound superconducting coil madeof (RE)$Ba_2Cu_3O_7 - x$(RE : rare earth) coated conductor. *Appl. Phys. Lett.*, 99(202506), 2011.

[17] N. Zangenberg, G. Nielsen, N. Hauge, B.R. Nielsen, A. Baurichter, C.G. Pedersen, L. Bräuner, B. Ulsoe, and S.P. Moller. Conduction Cooled High Temperature Superconducting Dipole Magnet for Accelerator Applications. *IEEE Trans. Appl. Supercond.*, 22(3), 2012.

[18] M. Okada, K. Tanaka, T. Wakuda, K. Ohata, J. Sato, T. Kiyoshi, H. Kitaguchi, and H. Wada. Bi-2212/Ag high-field magnets. *Physica C*, 335, 2000.

[19] H.W. Weijers, U.P. Trociewitz, K. Marken, M. Meinesz, H. Miao, and J. Schwartz. The generation of 25.05 T using a 5.11 T $Bi_2Sr_2CaCu2_2$ O_x superconducting insert magnet. *Supercond. Sci. Technol.*, 17, 2004.

[20] H.W. Weijers, W.D. Markiewicz, K.W. Pickard, P.D. Noyes, U.P. Trociewitz, J. Jiang, and D.C. Larbalestier. Tests of HTS insert coils above 30 T. *Presentation*, 2010.

[21] D.W. Hazelton, V. Selvamanickam, J.M. Duval, D.C. Larbalestier, W.D. Markiewicz, H.W. Weijers, and R.L. Holtz. Recent Developments in 2G HTS Coil Technology. *IEEE Trans. Appl. Supercond.*, 19(3), 2009.

[22] H.W. Weijers, U.P. Trociewitz, W.D. Markiewicz, J. Jiang, D. Myers, E.E. Hellstrom, A. Xu, J. Jaroszynski, P. Noyes, Y. Viouchkov, and D.C. Larbalestier. High Field Magnets With HTS Conductors. *IEEE Trans. Appl. Supercond.*, 20(3), 2010.

[23] M. Beckenbach, F. Hornung, M. Kläser, P. Leys, B. Lott, and Th. Schneider. Manufacture and Test of a 5 T Bi-2223 Insert Coil. *IEEE Trans. Appl. Supercond.*, 15(2), 2005.

[24] C.K. Yang, C.S. Hwang, J.C. Jan, F.Y. Lin, C.H. Chang, M. Fee, and M. Christian. Design, Fabrication and Performance Tests of a HTS Superconducting Dipole Magnet. *IEEE Trans. Appl. Supercond.*, 22(3), 2012.

[25] A. Godeke, P. Acosta, D. Cheng, D.R. Dietderich, M.G.T. Mentink, S.O. Prestemon, G.L. Sabbi, M. Meinesz, S. Hong, Y. Huang, H. Miao, and J. Parrell. Wind-and-react Bi-2212 coil development for accelerator magnets. *Supercond. Sci. Technol.*, 23, 2010.

[26] A. Godeke, D. Cheng, D.R. Dietderich, C.D. English, H. Felice, C.R. Hannaford, S.O. Prestemon, G. Sabbi, R.M. Scanlan, Y. Hikichi, J. Nishioka, and T. Hasegawa. Development of Wind-and-React Bi-2212 Accelerator Magnet Technology. *IEEE Trans. Appl. Supercond.*, 18(2), 2008.

[27] A.I. Ageev, I.I. Akimov, A.M. Andriishchin, I.V. Bogdanov, S.S. Kozub, K.P. Myznikov, D.N. Rakov, A.V. Rekudanov, P.A. Shcherbakov, P.I. Slabodchikov, A.A. Seletsky, A.K. Shikov, V.V. Sytnik, A.V. Tikhov, L.M. Tkachenko, and V.V. Zubko. Test Results of HTS Dipole. *IEEE Trans. Appl. Supercond.*, 12(1), 2002.

[28] L. Bottura. A practical Fit for the Critical Surface of NbTi. *IEEE Trans. Appl. Supercond.*, 22(1), 2000.

[29] E. Todesco and P. Ferracin. Limits to High Field Magnets for Particle Accelerators. *IEEE Trans. Appl. Supercond.*, 22(3), 2012.

[30] L.T. Summers, M.W. Guinan, J.R. Miller, and P.A. Hahn. A model for the prediction of Nb_3Sn critical current as a function of field and temperature and strain and radiation damage. *IEEE Trans. Magn.*, 27(2), 1991.

[31] A.D. Ouden, S. Wessel, E. Krooshoop, and H. ten Kate. Application of Nb_3Sn Superconductors in High-Field Accelerator Magnets. *IEEE Trans. Appl. Supercond.*, 7(2), 1997.

[32] T. Sekitania, N. Miuraa, S. Ikedaa, Y.H. Matsudaa, and Y. Shiohara. Upper critical field for optimally-doped YBa_2Cu_3O. *Physica B*, 346-347, 2004.

[33] A.I. Golovashkin, O.M. Ivanenko, Y.B. Kudasov, K.V. Mitsen, A.I. Pavlovsky, V.V. Platonov, and O.M. Tatsenko. Low temperature direct measurements of H_{c2} in HTSc using megagauss magnetic fields. *Physica C*, 185-189, 1991.

[34] V. Lombardo, E. Barzi, D. Turrioni, and A.V. Zlobin. Critical Currents of $YBa_2Cu_3O_{7-\delta}$ Tapes and $Bi_2Sr_2CaCu_2Ox$ Wires at Different Temperatures and Magnetic Fields. *FermiLab Note*, (296-TD), 2010.

[35] N. Ayai, T. Kato, J. Fujikami, S. Kobayashi, M. Kikuchi, K. Yamazaki, S. Yamade, T. Ishida, K. Tatamidani, K. Hayashi, K. Sato, R. Hata, H. Kitaguchi, H. Kumakura, K. Osamura, and J. Shimoyama. DI-BSCCO wire with I_c over 200 A at 77 K. *Journal of Physics: Conference Series*, 97, 2008.

[36] S. Fleshler, D. Buczek, B. Carter, P. Cedrone, K. De Moranville, J. Gannon, J. Inch, X. Li, J. Lynch, A. Otto, E. Podtburg, D. Roy, M. Rupich, S. Sathyamurthy, J. Schreiber, C. Thieme, E. Thompson, D. Tucker, K. Nagashima, and M. Ogata. Scale-up of 2G wire manufacturing at American Superconductor Corporation. *Physica C*, 469, 2009.

[37] A. Xu, J. Jaroszynski, D. Larbalestier, Y. Chen, Y.Y. Xie, and V. Selvamanickam. Angular Dependence of J_c of YBCO Coated Conductors at Low Temperature and Very High Magnetic Fields. *National High Magnetic Field Laboratory and research report*, 2009.

[38] L. Rossi and E. Todesco. Electromagnetic design of superconducting dipoles based on sector coils. *Phys. Rev. ST Accel. Beams*, 91(9), 2007.

[39] L. Rossi and E. Todesco. Conceptual design of 20 T dipoles for high-energy LHC. *CERN Yellow Report*, 2011.

[40] M. Anerella et al. The RHIC magnet system. *Nuclear Instruments and Methods in Physics Research*, 499, 2003.

[41] K.H. Mess, P. Schmüser, and R. Wolff. *Superconducting Accelerator Magnets.* World Scientific, 1996.

[42] H.T. Edwards. The Tevatron energy doubler: A Superconducting Accelerator. *Ann. Rev. Nucl. Part. Sci.*, 35, 1985.

[43] L. Roebel. . *German Patent (BBC company)*, 1912.

[44] J.W. Ekin. Relationships between critical current and stress in NbTi. *IEEE Trans. Magn*, MAG-23, 1987.

[45] C.P. Bean. Magnetization of hard superconductors. *Phys. Rev. Lett.*, 8(250), 1962.

[46] M.N. Wilson. *Superconducting Magnets.* Oxford: Clarendon, 1983.

[47] L. Bottura and A. Godeke. Superconducting Materials and Conductors: Fabrication and Limiting Parameters. *Reviews of Accelerator Science and Technology*, 5, 2012.

[48] W.T. Nachtrab, T. Wong, X.T. Liu, and J. Schwartz. The Effect of Filament Diameter on Filament Count Bi2212/Ag Round Wire. *IEEE Trans. Appl. Supercond.*, 19(3), 2009.

[49] S.C. Kim, D.W. Ha, S.S. Oh, I.Y. Han, J.G. Oh, and H.S. Sohn. Effect of Filament Configuration on Critical Current Density of Bi2212/Ag Wires With Low Ag Ratio. *IEEE Trans. Appl. Supercond.*, 18(2), 2008.

[50] F. Sumiyoshi, S. Kawabata, A. Kawagoe, N. Hirano, and S. Nagaya. Inter-Strand Coupling Losses in Bi-2212 Rutherford Cables. *IEEE Trans. Appl. Supercond.*, 16(2), 2006.

[51] M.D. Sumption, E.W. Collings, and P.N. Barnes. AC loss in striped (filamentary) YBCO coated conductors leading to designs for high frequencies and field-sweep amplitudes. *Supercond. Sci. Technol*, 18, 2005.

[52] D.B. Thomas and M.N. Wilson. Filamentary Superconductor for pulsed application. *Proc. of 4th International conference on magnet technology*, 1972.

[53] M.N. Wilson. NbTi superconductors with low ac loss: A review. *Cryogenics*, 48, 2008.

[54] E. Barzi, D. Turrioni, A. Kikuchi, M. Lamm, A. Rusy, R. Yamada, and A.V. Zlobin. BSCCO-2212 wire and cable studies. *AIP Conf. Proc.*, 986(431), 2008.

[55] S. Caspi. Test Results of 15 T Nb_3Sn Quadrupole Magnet HQ01 with a 120 mm Bore for the LHC Luminosity Upgrade. *IEEE Trans. Appl. Supercond.*, 21(3), 2011.

[56] S. Caspi. Test Results of LARP Nb_3Sn Quadrupole Magnets Using a Shell-Based Support Structure (TQS). *IEEE Trans. Appl. Supercond.*, 21(3), 2009.

[57] G. Ambrosioi. Test Results of the First 3.7 m Long Nb_3Sn Quadrupole by LARP and Future Plans. *IEEE Trans. Appl. Supercond.*, 21(3), 2011.

[58] Y. Aoki, T. Koizumi, N. Ohtani, T. Hasegawa, L. Motowidlo, R.S. Sokolowski, R.M. Scanlan, and S. Nagaya. Development of a large current capacity conductor using Bi-system superconductors. *Physica C*, 355, 2000.

[59] E. Barzi, V. Lombardo, D. Turrioni, F.J. Baca, and T.G. Holesinger. BSCCO-2212 Wire and Cable Studies. *IEEE Trans. Appl. Supercond.*, 21(3), 2011.

[60] T. Hasegawa, J. Nishioka, N. Ohtani, Y. Hikichi, R. Scanlan, R. Gupta, N. Hirano, and S. Nagaya. 12 kA HTS Rutherford Cable. *IEEE Trans. Appl. Supercond.*, 14(2), 2004.

[61] A. Malagoli, F. Kametani, J. Jiang, U.P. Trociewitz, and E.E. Hellstrom. Evidence for long range movement of Bi-2212 within the filament bundle on melting and its significant effect on J_c. *Supercond. Sci. Technol*, 24, 2011.

[62] J. Jiang, W.L. Starch, M. Hannion, F. Kametani, U.P. Trociewitz, E.E. Hellstrom, and D.C. Larbalestier. Doubled critical current density in Bi-2212 round wires by reduction of the residual bubble density. *Supercond. Sci. Technol.*, 24, 2011.

[63] D. Leroy. Review of the RD and Supply of the LHC Superconducting Cables. *IEEE Trans. Appl. Supercond.*, 16(2), 2006.

[64] E. Barzi, N. Andreev, C. Boffo, E. Borissov, L. Elementi, L. Del Frate, R. Yamada, and A.V. Zlobin. Development and study of Rutherford-type cables for high-field accelerator magnets atFermilab. *Supercond. Sci. Technol.*, 17(9), 2004.

[65] R.K. Maix, D. Salathé, S.L. Wipf, and M. Garber. Manufacture and testing of 465 km superconducting cable for the HERA dipole magnets. *IEEE Trans. Magn.*, 25(2), 1989.

[66] A.F Greene, M.G. Garber, A.K. Ghosh, D. McChesney, A. Morgillo, R. Shah, S. DelRe, G. Epstein, S. Hong, J. Lichtenwalner, P. OLarey, D. Smathers, M. Boivin, and R. Meserve. Manufacture and Testing of the Superconducting Wire and Cable for the RHIC Dipoles and Quadrupoles. *IEEE Trans. Appl. Supercond.*, 5(2), 1995.

[67] V. Hussennether, M. Oomen, M. Leghissa, and H.-W. Neum öller. DC and AC properties of Bi-2223 cabled conductors designed for high-current applications. *Physica C*, 401, 2004.

[68] D.S. Beard, W. Klose, S. Shimamoto, and G. Vecsey. The IEA Large Coil Task; development of superconducting toroidal field magnets for fusion reactors. *Fusion Engineering and design*, 7, 1988.

[69] C. Suzuki, K. Goto, T. Saitoh, and T. Nakatsuka. Strain properties of transposed segment conductors for a transmission cable. *Physica C*, 392-396, 2003.

[70] K. Miyoshi, M. Mimura, S. Meguro, T. Hasegawa, T. Saitoh, N. Kashima, and S. Nagaya. Development of HTS Coil With Bi-2223 Transposed Segment Conductor. *IEEE Trans. Appl. Supercond.*, 14(2), 2004.

[71] M.P. Oomen, M. Leghissa, N. Proelss, and H.W. Neumüller. Transposed-Cable Coil Saddle Coils of HTS for Rotating Machines: Test Results at 30 K. *IEEE Trans. Appl. Supercond.*, 19(3), 2009.

[72] W. Goldacker, R. Nast, G. Kotzyba, S.I. Schlachter, A. Frank, B. Ringsdorf, C. Schmidt, and P.Komarek. High current DyBCO-ROEBEL Assembled Coated Conductor. *Journal of Physics: Conference Series*, 43, 2006.

[73] N.J. Long, R. Badcock, P. Beck, M. Mulholland, N. Ross, M. Staines, H. Sun, J Hamilton, and R G Buckley. Narrow strand YBCO Roebel cable for lowered AC loss. *Journal of Physics: Conference Series*, 97, 2008.

[74] R.A. Badcock, N.J. Long, M. Mulholland, S. Hellmann, A. Wright, and K.A. Hamilton. Progress in the Manufacture of Long Length YBCO Roebel Cables. *IEEE Trans. Appl. Supercond.*, 19(3), 2009.

[75] N.J. Long, R.A. Badcock, K. Hamilton, A. Wright, Z. Jiang, and L.S. Lakshmi. Development of YBCO Roebel cables for high current transport and low AC loss applications. *J. of Physics: Conf. Series*, 234, 2010.

[76] W. Goldacker, A. Frank, A. Kudymow, R. Heller, A. Kling, S. Terzieva, and C. Schmidt. Improvement of Superconducting Properties in ROEBEL Assembled Coated Conductors (RACC). *IEEE Trans. Appl. Supercond.*, 19(3), 2009.

[77] W. Goldacker, A. Frank, R. Heller, S.I. Schlachter, B. Ringsdorf, K.-P. Weiss, C. Schmidt, and S. Schuller. ROEBEL Assembled Coated Conductors (RACC):Preparation and Properties and Progress. *IEEE Trans. Appl. Supercond.*, 17(7), 2007.

[78] V. Lombardo, E. Barzi, D. Turrioni, A.V. Zlobin, N.J. Long, and R.A. Badcock. Fabrication and Qualification and Test of High J_c Roebel $YBa_2Cu_3O_{7-\delta}$Coated Conductor Cable for HEP magnets. *IEEE Trans. Appl. Supercond*, 21(3), 2011.

[79] S. Terzieva, M. Vojenčiak, E. Pardo, F. Grilli, A. Drechsler, A. Kling, A. Kudymow, F. GÂ¨omÂ¨ory, and W. Goldacker. Transport and magnetization ac losses of ROEBEL assembled coated conductor cables: measurements and calculations. *Supercond. Sci. Technol.*, 23, 2010.

[80] M. Vojenčiak, F. Grilli, S. Terzieva, W. Goldacker, M. Kovacov, and A. Kling. Effect of self-field on the current distribution in Roebel-assembled coated conductor cables. *Supercond. Sci. Technol.*, 24, 2011.

[81] `http://www.gcsuperconductors.com/`.

[82] C.W. Bumby, R.A. Badcock, and N.J. Long. Critical Current Behavior of HTS Roebel Cable under Tensile Stress. *IEEE Trans. Appl. Supercond.*, 23(3), 2013.

[83] C. Barth, K.P. Weiss, M. Vojenčiak, and S. Schlachter. Electro-mechanical analysis of Roebel cables with different geometries. *Supercond. Sci. Technol.*, 25, 2012.

[84] E.H. Brandt and M. Indenbom. Type-II-superconductor strip with current in a perpendicular magnetic field. *Phys. Rev. B*, 48(17), 1993.

[85] F. Grilli, S.P. Ashworth a, and S. Stavrev. Magnetization AC losses of stacks of YBCO coated conductors. *2006*, 434, Physica C 434.

[86] L.S. Lakshmi, K.P. Thakur, M.P. Staines, R. Alan B., and N.J. Long. Magnetic AC Loss Characteristics of 2G Roebel Cable. *IEEE Trans. Appl. Supercond.*, 19(3), 2009.

[87] D.W. Hazelton, J.A. Rice, Y.S. Hascicek, H.W. Weijers, and S.W. Van Sciver. Development and Test of a BSCCO-2223 HTS High Field Insert Magnet for NMR. *IEEE Trans. Appl. Supercond.*, 5(2), 1995.

[88] M. Devaux, F. Debray, J. Fleiter, P. Fazilleau, T. LÃ©crevisse, C. Pes, J.M. Rey, J.M. Rifflet, M. Sorbi, A. Stenvall, P. Tixador, and G. Volpini. HTS Insert Magnet Design Study. *IEEE Trans. Appl. Supercond.*, 22(3), 2012.

[89] H. Lee, E.S. Bobrov, J. Bascunan, S.Y. Hahn, and Y. Iwasa. An HTS Insert for Phase 2 of a 3-Phase 1-GHzLTS/HTS NMR Magnet. *IEEE Trans. Appl. Supercond.*, 15(2), 2005.

[90] S. Hanai, M. Kyoto, M. Takahashi, K. Tasaki, T. Kurusu, H. Takigami, M. Urata, G. Nishijima, S. Awaji, and K. Watanabe. Design and Test Results of 18.1 T Cryocooled Superconducting Magnet With Bi2223 Insert. *IEEE Trans. Appl. Supercond.*, 17(2), 2007.

[91] D.C. van der Laan. $YBa_2Cu_3O_{7-\delta}$ coated conductor cabling for low ac-loss and high-field magnet applications. *Supercond. Sci. Technol.*, 22, 2009.

[92] D.C. van der Laan, L.F. Goodrich, and T.J. Haugan. High-current dc power transmission in flexible RE-$Ba_2Cu_3O_{7-\delta}$ coated conductor cables. *Supercond. Sci. Technol.*, 25, 2012.

[93] D.C. van der Laan, X.F. Lu, and L.F. Goodrich. Compact $GdBa_2Cu_3O_7$-Î´ coated conductor cables for electric power transmission and magnet applications. *Supercond. Sci. Technol.*, 24, 2011.

[94] J. Bardeen, L.N. Cooper, and J.R. Schrieffer. Theory of superconductivity. *Phys. Rev.*, 108(1175), 1957.

[95] W. Anderson. Theory of flux creep in hard superconductors. *Phys. Rev. Lett*, 9(7), 1962.

[96] A.A. Abrikosov. On the Magnetic Properties of Superconductors of the Second Group. *Sov. Phys. JETP*, 5(6), 1957.

[97] Y.B. Kim, C.F. Hempstead, and A.R. Strnad. Critical persistent currents in hard superconductors. *Phys. Rev. Lett*, 9(7), 1962.

[98] A. Godeke. Performance boundaries in Nb_3Sn superconductors. *PhD Thesis*, 2005.

[99] A. Xu, J.J. Jaroszynski, F. Kametani, Z. Chen, D.C. Larbalestier, Y.L. Viouchkov, Y. Chen, Y. Xie, and V. Selvamanickam. Angular dependence of J_c for YBCO coated conductors at low temperature and very high magnetic fields. *Supercond. Sci. Technol.*, 23(9), 2010.

[100] K. Tachikaw, K. Itoh, H. Wadax, D. Gould, H. Jones, C.R. Walters, L.F. Goodrich, J.W. Ekin, and S.L. Bray. Intercomparison of critical current measurement in Nb_3Sn wires. *IEEE Trans. Magn.*, 25(2), 1989.

[101] M.D. Bird, S. Bole, I. Dixon, Y.M. Eyssa, B.J. Gao, and H.J. Schneider-Muntau. The 45 T hybrid insert: recent achievements. *Physica B*, 294-295, 2001.

[102] M. Inoue, T. Kiss, Y. Tsuda, H. Sawa, M. Takeo, S. Awaji, K. Watanabe, Y. Iijima, K. Kakimoto, T. Saitoh, J. Matsuda, Y. Tokunaga, T. Izumi, and Y. Shiohara. High Magnetic Field Properties of Critical Current Density in $Y_1Ba_2Cu_3O_{7-\delta}$ Coated Conductor Fabricated by Improved TFA-MOD Process. *IEEE Trans. Appl. Supercond.*

[103] C.R. Walters, I.M. Davidson, and G.E. Tuck. Long sample high sensitivity critical current measurements under strain. *Cryogenics*, 26(7), 1986.

[104] M. Sugano, K. Itoh, and T. Kiyoshi. Strain Dependence of Critical Current in Bi2212 W and R Wires Under Magnetic Field Up to 30 T. *IEEE Trans. Appl. Supercond.*, 16(2), 2006.

[105] M. Sugano, S. Choi, A. Miyazoe, K. Miyamatsu, T. Ando, K. Itoh, T. Kiyoshi, H. Wada, and V. Selvamanickam. Strain Analysis of Ic(e) characteristic of YBCO Coated Conductor Measured by a Walters Spring. *IEEE Trans. Appl. Supercond.*, 18(2), 2008.

[106] D. Uglietti, B. Seeber, V. Abacherli, A. Pollini, D. Eckert, and R Flukiger. A device for critical current versus strain measurements up to 1000 A and 17 T on 80 cm long HTS and LTS technical superconductors. *Supercond. Sci. Technol.*, 16, 2003.

[107] B. ten Haken, A. Godeke, and H.H.J. ten Kate. New devices for measuring the critical current in a tape as a the axial and transverse strain and the magnetic field and temperature. *IEEE Trans. Appl. Supercond.*, 3(1), 1993.

[108] D.C. van der Laan, J.W. Ekin, J.F. Douglas, C.C. Clickner, T.C. Stauffer, and L.F. Goodrich. Effect of strain and magnetic field and field angle on the critical current density of $YBa_2Cu_3O_{7-\delta}$ coated conductors. *Supercond. Sci. Technol.*, 23(3), 2010.

[109] P. Sunwong, J.S. Higgins, and D.P. Hampshire. Angular, Temperature, and Strain Dependencies of the Critical Current of DI-BSCCO Tapes in High Magnetic Fields. *IEEE Trans. Appl. Supercond.*, 21(3), 2011.

[110] J.D. Jorgensen, B.W. Veal, A.P. Paulikas, L.J. Nowicki, G.W. Crabtree, H. Claus, and W.K. Kwok. Structural properties of oxygen-deficient $YBa_2Cu_3O_7$. *Phys. Rev. B*, 41(4), 1990.

[111] J. Auge, U. Riidiger, H. Frank, H.G. Roskos, G. Giointherodt, and H. Kurz. Oxygen control of dc sputtered $Bi_2Sr_2CaCu_2O_{8+\delta}$ films. *Appl. Phys. Lett.*, 64(378), 1994.

[112] `http://www.superpower-inc.com/`.

[113] `http://www.amsc.com/`.

[114] `http://global-sei.com/`.

[115] `http://www.bruker-est.com/`.

[116] `http://www.oxford-instruments.com/`.

[117] X. Xiong, S. Kim, K. Zdun, S. Sambandam, A. Rar, K.P. Lenseth, and V. Selvamanickam. Progress in High Throughput Processing of Long-Length and High Quality, and Low Cost IBAD MgO Buffer Tapes at SuperPower. *IEEE Trans. Appl. Supercond.*, 19(3), 2009.

[118] M.W. Rupich. Advances in second generation high temperature superconducting wire manufacturing and RD at American Superconductor Corporation. *Supercond. Sci. Technol.*, 23, 2010.

[119] R. Hühne, J. Eickemeyer, V.S. Sarma, A. Güth, T. Thersleff, J. Freudenberger, O. de Haas, M. Weigand, J.H. Durrell, L. Schultz, and B. Holzapfel. Application of textured highly alloyed Ni-W tapes for preparing coated conductor architectures. *Supercond. Sci. Technol.*, 23, 2010.

[120] W. Zhang, M.W. Rupich, U. Schoop, D.T. Verebelyi, C.L.H. Thieme, X. Li, T. Kodenkandath, Y. Huang, E. Siegal, D. Buczek, W. Carter, N. Nguyen, M. Prasova J. Schreiber, J. Lynch, D. Tucker, and S. Fleshler. Progress in AMSC scale-up of second generation HTS wire. *Physica C*, 63-465, 2007.

[121] N. Ayai, M. Kikuchi, K. Yamazaki, S. Kobayashi, S. Yamade, E. Ueno, J. Fujikami, T. Kato, K. Hayashi, K. Sato, R. Hata, J. Iihara, K. Yamaguchi, and J. Shimoyama. The Bi-2223 Superconducting Wires With 200A-Class Critical Current. *IEEE Trans. Appl. Supercond.*, 17(2), 2007.

[122] H. Miao, K.R. Marken, M. Meinesz, B. Czabaj, and S. Hong. Development of Round Multifilament Bi-2212/Ag Wires for High Field Magnet Applications. *IEEE Trans. Appl. Supercond.*, 15(2), 2005.

[123] A. Malagoli, C Bernini, V. Braccini, G. Romano, M. Putti, X. Chaud, and F. Debray. Large critical current density improvement in Bi-2212 wires through groove-rolling process. *Submitted to publication*, 2013.

[124] C.C. Clickner, J.W. Ekin, N. Cheggour, C.L.H. Thieme, Y. Qiao, Y.Y. Xie, and A. Goyal. Mechanical properties of pure Ni and Ni-alloy substrate materials for Y-Ba-Cu-O coated superconductors. *Cryogenics*, 46, 2006.

[125] M. Sugano, K. Osamura, W. Prusseit, R. Semerad, K. Itoh, and T. Kiyoshi. Tensile fracture behaviour of RE-123 coated conductors induced by discontinuous yielding in Hastelloy C-276 substrate. *Supercond. Sci. Technol.*, 18, 2005.

[126] K. Osamura, S. Machiya, H. Suzuki, S. Ochiai, H Adachi, N. Ayai, K. Hayashi, and K. Sato. Mechanical behavior and strain dependence of the critical current of DI-BSCCO tapes. *Supercond. Sci. Technol.*, 21, 2008.

[127] R. Dietrich. Bi-2223 HTS data sheet. *http://www.bruker-est.com*.

[128] A.L. Mbarukua and J. Schwartz. Statistical analysis of the electromechanical behavior of AgMg sheathed $Bi_2Sr_2CaCu_2O_{8+x}$ superconducting tapes using Weibull distributions. *J. of Appl. Phys.*, 101, 2007.

[129] T. Boutboul et al. and. Critical current test facilities for LHC superconducting NbTi cable strands, journal = CERN and European Organization for Nuclear Research. 91(9), 2001.

[130] `http://www.keithley.com/`.

[131] `http://www.ni.com/labview/`.

[132] M.S. Lubell. Empirical scaling formulas for critical current and critical field for commercial NbTi. *IEEE Trans. Magn.*, 19(3), 1983.

[133] J. Fleiter, A. Ballarino, P. Chambouvet, L. Oberli, and P.F.Jacquot. I_c chracaterization of YBCO tapes. *CERN Internal note*, 2010.

[134] Y. Miyoshi. Private communication. 2012.

[135] S. Choi, T. Kiyoshi, S. Matsumoto, D. Uglietti, K. Zaitsu, T. Hase, and M.Hamada. The Electrical and Mechanical Characterization of Metal-Reinforced Bi-2223/Ag Conductors for High Field Insert Coil. *IEEE Trans. Appl. Supercond.*, 19(3), 2009.

[136] J.E. Evetts and B.A. Glowacki. Relation of critical current irreversibility to trapped flux and microstructure in polycrystalline YBaCuO. *Cryogenics*, 28, 1988.

[137] V. Braccini, A. Xu, J. Jaroszynski, Y. Xinand D.C. Larbalestier, Y. Chen, G. Carota, J. Dackow, I. Kesgin, Y. Yao, A. Guevara, T. Shi, and V. Selvamanickam. Properties of recent IBAD-MOCVD coated conductors relevant to their high field and low temperature magnet use. *Supercond. Sci. Technol.*, 24, 2011.

[138] D. Uglietti, H. Kitaguchi, S. Choi, and T. Kiyoshi. Angular Dependence of Critical Current in Coated Conductors at 4.2 K and Magnet Design. *IEEE Trans. Appl. Supercond.*, 19(3), 2009.

[139] D. Turrioni, E. Barzi, M. Lamm, V. Lombardo, C. Thieme, and A.V. Zlobin. Angular measurements of HTS critical current for high field solenoids. *AIP Conf. Proc.*, 986, 2008.

[140] P.M. Leys, M. Klaeser, F. Schleissinger, and Th. Schneider. Angle-Dependent U(I) Measurements of HTS Coated Conductors. *ieee*, to be published.

[141] P. Sunwong, J.S. Higgins, and D.P. Hampshire. Critical current measurements of DI-BSCCO tapes as a function of angle in high magnetic fields. *Journal of Physics: Conference Series*, 234, 2010.

[142] N. Ayai et al. Electrical and Mechanical Properties of DI-BSCCO Type HT Reinforced With Metallic Sheathes. *IEEE Trans. Appl. Supercond.*, 19(3), 2009.

[143] Y. Zhang, R.C. Duckworth, T.T. Ha, and M.J. Gouge. Solderability study of RABiTS-based YBCO coated conductors. *Physica C*, 471, 2011.

[144] J.H. Kim and J. Joo. A superconducting joint between Bi-Pb-Sr-Ca-Cu-O multifilamentary tapes. *Supercond. Sci. Technol.*, 15, 2002.

[145] T. Hase, K. Shibutani, S. Hayashi, M. Shimada, Y. Kawate R. Ogawa, T. Kiyoshit, and K. lnouet. Operation of superconductively jointed Bi-2212 solenoidal coil in persistent current mode. *Cryogenics*, 37, 1997.

[146] T. Maebatake, N. Mori, R. Teranishi, M. Mukaida, K. Yamada, M. Miura, M. Yoshizumi, and T. Izumi. Effects of joining conditions on the structures and properties of joints of REBCO coated conductors. *Physica C*, 470, 2010.

[147] H.S. Kim, N.Y. Kwon, K.S. Chang, T.K. Ko, H.M. Kim, W.S. Kim, C. Park, and H. Lee. Joint Characteristics of the YBCO Coated Conductor (CC) by Chemical Etching. *IEEE Trans. Appl. Supercond.*, 19(3), 2009.

[148] SuperPower corporation. SuperPower 2G HTS Wire: Soldering Instructions.

[149] American Superconductor Corporation. Guidelines for Hand-Assembled Splicing of Amperium Wire.

[150] SEI Splice. Guideline for Handling of DI-BSCCO.

[151] R.C. Duckworth, Y. Zhang, M.J. Gouge, C.M. Rey, D.C. van der Laan, and C. Clickner. Voltage distribution and mechanical strength in splice joints made from as manufactured YBCO coated conductors. *AIP Conf. Proc.*, 1219, 2010.

[152] `http://www.indium.com`.

[153] `http://www.lucasmilhaupt.com`.

[154] `http://www.fransor-industrie.fr`.

[155] `http://vitta.com`.

[156] D.K. Park, M.C. Ahn, H.M. Kim, H.G. Lee, K.S. Chang, S.J. Lee, S.E. Yang, and T.K. Ko. Analysis of a Joint Method Between Superconducting YBCO Coated Conductors. *IEEE Trans. Appl. Supercond.*, 17(2), 2007.

[157] J. Lu, K. Han, W.R. Sheppard, Y.L. Viouchkov, K.W. Pickard, and W.D. Markiewicz. Lap Joint Resistance of YBCO Coated Conductors. *IEEE Trans. Appl. Supercond.*, 21(3), 2011.

[158] J. Lu, E.S. Choi, and H.D. Zhou. Physical properties of Hastelloy ® C-276 ^{TM} at cryogenic temperatures. *J. of Appl. Phys.*, 103, 2008.

[159] `http://www.eckelsengineering.com/`.

[160] `http://tdk.com/`.

[161] `http://www.ni.com/pxi/`.

[162] T. Golod, A. Rydh, V.M. Krasnov, I. Marozau, M.A. Uribe-Laverde, D.K. Satapathy, Th. Wagner, and C. Bernhard. High bias anomaly in $YBa_2Cu_3O_7$/$LaMnO_3$/$YBa_2Cu_3O_7$ Superconductor/Ferromagnetic Insulator/Superconductor junctions: Evidence for a long-range superconducting proximity effect through the conduction band of a ferromagnetic insulator.

[163] M.A.A.M. van Wijck, M.A.J. Verhoeven, E.M.C.M. Reuvekamp, G.J. Gerritsma, D.H.A. Blank, and H. Rogalla. CeO2 as insulation layer in high Tc superconducting multilayer and crossover structures. *Appl. Phys. Lett.*, 68(4), 1996.

[164] F. Heringhaus and T.A. Painter. Magnetoresistance of selected Sn- and Pb-based solders at 4.2 K. *Materials Letters*, 57, 2002.

[165] A.B. Pippard. Magnetoresistance in metals in: Cambridge Studies in Low Temperature Physics. *Cambridge Univ. Press and New York*, 1989.

[166] N. Cheggour, J.W. Ekin, C.C. Clickner, D.T. Verebelyi, C.L.H. Thieme, R. Feenstra, and A. Goyal. Reversible axial-strain effect and extended strain limits in Y-Ba-Cu-O coatings on deformation-textured substrates. *Appl. Phys. Lett.*, 83(20), 2003.

[167] D.C. van der Laana and J.W. Ekin. Large intrinsic effect of axial strain on the critical current of hightemperature superconductors for electric power applications. *Applied physics letters*, 90, 2007.

[168] H.S. Shin, J.R.C. Dizon, R.K. Ko, T.H. Kim, D.W. Ha, and S.S. Oh. Reversible tensile strain dependence of the critical current in YBCO coated conductor tapes. *Physica C*, 2007.

[169] D.C. van der Laan, J.F. Douglas, C.C. Clickner, T.C. Stauffer, L.F. Goodrich, and H.J.N. van Eck. Evidence that the reversible strain effect on critical current density and flux pinning in $Bi_2Sr_2Ca_2Cu_3Ox$ tapes is caused entirely by the pressure dependence of the critical temperature. *Supercond. Sci. Technol.*, 24, 2011.

[170] N. Cheggour, X.F. Lu, T.G. Holesinger, T.C. Stauffer, J. Jiang, and L.F. Goodrich. Reversible effect of strain on transport critical current in $Bi_2Sr_2CaCu_2O_8+x$ superconducting wires: a modified descriptive strain model. *Supercond. Sci. Technol.*, 25, 2012.

[171] D.C. van der Laan, T.J. Haugan, P.N. Barnes, D. Abraimov, F. Kametani, D.C. Larbalestier, and M.W. Rupich.

[172] W.E. Pickett. Uniaxial Strain Dependence of T_c in $YBa_2Cu_3O_7$: Internal Strain Induced Intralayer Charge Transfer. *Phys. Rev. Lett.*, 78(10), 1997.

[173] U. Welp, M. Grimsditch, S. Fleshier, W. Nessler, J. Downey, G.W. Crabtree, and J. Guimpel. Effect of Uniaxial Stress on the Superconducting Transition in $YBa_2Cu_3O_7$. *Phys. Rev. Lett.*, 69(14), 1992.

[174] G.L. Belenky, S.M. Green, A. Roytburd, C.J. Lobb, S.J. Hagen, R.L. Greene, M.G. Forrester, and J. Talvacchio. Effect of stress along the ab plane on the Jc and Tc of $YBa_2Cu_3O_7$ thin films. *Phys. rev. B*, 44(18), 1991.

[175] M. Sugano, K. Shikimachi, N. Hirano, and S. Nagaya. The reversible strain effect on critical current over a wide range of temperatures and magnetic fields for YBCO coated conductors. *Supercond. Sci. Technol.*, 23, 2010.

[176] J.S. Higgins and D.P. Hampshire. Critical Current Density of YBCO Coated Conductors Under High Compression in High Fields. *IEEE Trans. Appl. Supercond.*, 21(3), 2011.

[177] D.C. van der Laan, F. Douglas, L. Goodrich, C. Clickner, and T. Stauffer. Electromechanical Studies for Coated Conductor Development. *Presented at the 2010 U.S. Department of Energy, Advanced Cables and Conductors Program Peer Review.*

[178] D.C. van der Laan, D. Abraimo, A.A. Polyanskii, D.C. Larbalestier, J.F. Douglas, R. Semerad, and M. Bauer. Anisotropic in-plane reversible strain effect in $Y_{0.5}Gd_{0.5}Ba_2Cu_3O_7$ coated conductors. *Supercond. Sci. Technol.*, 24, 2011.

[179] H. Kierspel, H. Winkelmann, T. Auweiler, W. Schlabitz, B. Btichner, V.H.M. Duijn, N.T. Hien, A.A. Menovsky, and J.J.M. Franse. Thermal expansion and specific heat and uniaxial pressure dependences of T_c in $Bi_2Sr_2CaCu_2O_8$. *Physica C*, 262, 1996.

[180] N. Cheggour, J.W. Ekin, C.L.H. Thieme, and Y.Y. Xie. Effect of Fatigue Under Transverse Compressive Stress on Slit Y-Ba-Cu-O Coated Conductors. *IEEE Trans. Appl. Supercond.*, 17(2), 2007.

[181] V. Lombardo, E. Barzi, G. Norcia, M. Lamm, D. Turrioni, T. Van Raes, and A.V. Zlobin. Study of HTS insert coils for high field solenoids. *AIP Conf. Proc.*, 1218, 2010.

[182] A. Ballarino. Alternative Design Concepts for Multi-Circuit HTS Link Systems. *IEEE Trans. Appl. Supercond.*, 21(3), 2011.

[183] A. Ballarino, J. Fleiter, J. Hurte, M. Sitko, and G. Willering. First tests of twisted-pair HTS 1 kA range cables for use in superconducting links. *Physics Procedia*, 36, 2012.

[184] Y. Yang, E.A. Young, W.O.S. Bailey, C. Beduz, and A. Ballarino. First Electrical Characterization of Prototype 600 A HTS Twisted-pair Cables at Different Temperatures. *Physics Procedia*, 36, 2012.

[185] H.S. Shin, J.R.C. Dizon, T.H. Kim, D.W. Ha, and S.S. Oh. Critical Current Degradation Behavior in YBCO Coated Conductors Under Torsional Strain. *IEEE Trans. Appl. Supercond.*, 17(2), 2007.

[186] K.P. Weiss, W. Goldacker, and M. Nannini. Finite Element Analysis of Torsion Experiments on HTSC Tapes. *IEEE Trans. Appl. Supercond.*, 21(3), 2011.

[187] H.S. Shin and K. Katagiri. Critical current degradation behaviour in Bi-2223 superconducting tapes under bending and torsion strains. *Supercond. Sci. Technol.*, 16, 2003.

[188] T. Takao, T. Iwamura, Y. Fukasawa, S. Minowa, H. Sato, T. Asano, A. Ishiyama, J. Kato, T. Machi, K. Nakao, and Y. Shiohara. Influence of Bending and Torsion Strains on Critical Currents in YBCO Coated Conductors. *IEEE Trans. Appl. Supercond.*, 17(2), 2007.

[189] B. Bordini, L. Bottura, and J. Fleiter. Critical Current Scaling Laws for the NbTi wires used in the ITER Poloidal Field Coils. *Internal Note*, EDMS Nr: 1105766, 2010.

[190] I. Pong, A. Vostner, B. Bordini, M. Jewell, F. Long, Y. Wu, L. Bottura, A. Devred, D. Bessette, and N. Mitchell. Current sharing temperature of NbTi SULTAN samples compared to prediction using a single pinning mechanism parametrization for NbTi strand. *Supercond. Sci. Technol.*, 25, 2012.

[191] M. Tachiki and S. Takahashi. Strong vortex pinning intrinsic in high T_c oxide superconductors. *Solid State Communications*, 20(3), 1989.

[192] M. Tinkham. Angular dependence of the superconducting nucleation field. *Phusics Letters*, 9(3), 1964.

[193] W. Lawrence and S. Doniach. Theory of layer structure superconductors. *Proc. 12th Inter. Conf. on Low Temperature Physics*, 1971.

[194] V. Ginzburg and L. Landau. On the theory of superconductivity. *Zh. Eksp. Teor. Fiz.*, 20, 1965.

[195] Review of anisotropy in HTs conductors.

[196] N.J. Long. Model for the angular dependence of critical currents in technical superconductors. *Supercond. Sci. Technol.*, 21, 2008.

[197] Y. Lee, H. Yamasaki, and M. Furuse. Magnetic-field angle dependent critical current densities and flux pinning in commercial YBCO tapes at liquid nitrogen temperatures. *Cryogenics*, 10, 2010.

[198] `http://eucard.web.cern.ch/eucard/activities/research/WP7`.

[199] `http://www.comsol.com/`.

[200] J. Ekin. Strain scaling law for flux pinning in practical superconductors. Part 1: Basic relationship and application to Nb_3Sn conductors. *Cryogenics*, 20(11), 1980.

[201] M. Sugano, T. Nakamura, T. Manabe, K. Shikimachi, N. Hirano, and S. Nagaya. The intrinsic strain effect on critical current under a magnetic field parallel to the c axis for a MOCVD-YBCO-coated conductor. *Supercond. Sci. Technol.*, 21, 2008.

[202] S. Timoshenko. Strength of Materials. *New York: D. Van Nostrand Compagny and 3rd edn*, 2, 1955.

[203] D.C. van der Laan and J.W. Ekin. Dependence of the critical current of $YBa_2Cu_3O_{7-\delta}$ coated conductors on in-plane bending. *Supercond. Sci. Technol.*, 21, 2008.

[204] A.P. Verweij, J. Genest, A. Knezovic, D.F. Leroy, J.P. Marzolf, and L.R.Oberli. 1.9 K test facility for the reception of the superconducting cables forthe LHC. *IEEE Trans. Appl. Supercond*, 91(9), 1999.

[205] D. Leroy, G. Spigo, A.P. Verweij H. Boschman, R. Dubbeldam, and J. Gonzltlez Pelayo. Design and Manufacture of a Large-Bore 10 TSuperconducting Dipole for the CERN Cable Test Facility. *IEEE Trans. Appl. Supercond*, 910(9), 2000.

[206] K.P. Thakur, Z. Jiang, M.P. Staines, N.J. Long, R.A. Badcock, and A. Raj. Current carrying capability of HTS Roebel cable. *Physica C*, 471, 2011.

[207] J. Fleiter, A. Ballarino, L. Bottura, and P. Tixador. Electrical characterization of RE-123 Roebel cables. *Supercond. Sci. Technol.*, 26, 2013.

[208] F. Lu, F. Kametani, and E.E. Hellstrom. Film growth of $BaZrO_3$-doped $YBa_2Cu_3O_{7-\delta}$ by using fluorine-free metal organic deposition. *Supercond. Sci. Technol*, 25, 2012.

[209] N. Long. Private communication. 2012.

[210] W. Goldacker. Private communication. 2012.

[211] N. Long. Private communication. 2010.

[212] T. Takematsu, R. Hua, T. Takao, Y. Yanagisawa, H. Nakagome, D. Uglietti, T. Kiyoshi, M. Takahashi, and H. Maeda. Degradation of the performance of a YBCO-coated conductor double pancake coil due to epoxy impregnation. *Physica C*, 470, 2010.

[213] `http://www.fujifilm.com/`.

[214] `http://www2.dupont.com`.

[215] A. Gerardin. Failure analysis of superconducting Roebel type cable. *CERN internal note EDMS: 1161662*, 2011.

[216] A. Gerardin. Failure analysis of superconducting Roebel type cable -2-. *CERN internal note EDMS: 1209793*, 2012.

[217] N. Koizumi, Y. Takahashi, M. Nishi, T. bono, H. Tsuji, M. Ono, T. Hamajimat, and T. Fujiokat. Ramp-Rate limitation due to current imbalance in a large cable-in-conduit conductor consisting of chrome-plated strands. *Cryogenics*, 37, 1997.

[218] D. Faivre and B. Turck. Current sharing in an insulated multistrand cable in transient and steady state current conditions. *IEEE Trans. Magn.*, 17(1), 1981.

[219] N. Koizumi, K. Okuno, Y. Takahashi, H. Tsuji, and S. Shimamoto. Current imbalance due to induced circulation currents in a large cable-inconduit superconductor. *Cryogenics*, 36, 1996.

[220] D. Ciazynski, B. Turck, J.L. Duchateau, and C. Meuris. AC losses and current distribution in 40 kA NbTi and Nb3Sn conductors for NET/ITER. *IEEE Trans. Appl. Supercond.*, 3(1), 1993.

[221] F.W. Groover. Inductance calculations -working formulas and tables. *Dover Publications*, 1946.

[222] G.H. Morgan. Eddy currents in flat metal-filled superconducting braids. *J. Appl. Phys.*, 44, 1973.

[223] A. Verweij. Electrodynamics of superconducting cables in accelerator magnets. *PhD Thesis, University of Twente*, 1995.

[224] E.M.J. Niessen. Continuum electromagnetics of composite superconductors. *PhD Thesis, University of Tewente*, 1993.

[225] V.E. Sytnikov, G.G. Svalov, S.G. Akopov, and I.B. Peshkov. Coupling losses in superconducting transposed conductors located in changing magnetic fields. *Cryogenics*, 29, 1989.

[226] M. Breschi. Current distribution in multistrand superconducting cables. *PhD thesis, University of Bologna*, 2001.

[227] A. Akhmetov, L. Bottura, M. Breschi, and P.L. Ribani. A Theoretical investigation on Current Imbalance in Flat Two Layer Superconducting Cables. *Cryogenics*, 40, 2000.

[228] W.A. Fietz and W.W. Webb. Hysteresis in Superonducting Alloys Temperature and Field Dependence of Dislocation Pinning in Nobium Alloys. *Phys review*, 178(2), 1968.

[229] E.J. Kramer. Scaling laws for flux pinning in hard superconductors. *J. Appl. Phys.*, 44(3), 1973.

[230] K. Maki. . *Physics*, 1964, 1.

[231] P.G. De Gennes. Behavior of dirty superconductors in high magnetic fields. *Phys. kondens. Materie*, 1964.

[232] Y. Mawatari, H. Yamasaki, S. Kosaka, and M. Umeda. Critical current properties and vortex-glass-liquid-transition in Ag-sheathed Bi-2223 tapes. *Cryogenics*, 35, 1995.

[233] R. Wesche. Temperature dependence of critical currents in superconducting Bi-2212/Ag wires. *Physica C*, 246, 1995.

[234] V. Braccini, J. Jaroszynski, and D.C. Larbalestierand A. Xu. Presentation at Houston. 2012.

[235] P.G. de Gennes. Boundary effect in Superconductors. 27(2), 1966.

[236] T.Y. Hsiang and D.K. Finnemore. Superconducting critical current for thick and clean superconductor-normal-metal -superconductor junctions. *Physical review B*, 22(1), 1992.

[237] L. Le Lay, C.M. Friend, T. Maruyam, K. Osamura, and D.P. Hampshire. Evidence that pair breaking at the grain boundaries of $Bi_2Sr_2Ca_2Cu_3Ox$ tapes determines the critical current density above 10 K in high magnetic fields. *J. Phys.: Condens. Matter*, 6, 1994.

[238] J. Horvat, S.X. Dou, H.K. Liu, and R. Bhasale. Critical currents through strong links in Ag/Bi-Sr-Ca-Cu-O superconducting tapes. *Physica C*, 271, 1996.

[239] C.M. Friend, J. Tenbrink, and D.P. Hampshire. Critical current density of Bi2212 monocore and multifilamentary wires from 4.2 K up to T_c in high magnetic fields. *Physica C*, 258, 1996.

[240] H. Ullamier. Irreversible Properties of Type II Superconductors. *Springer Tracks in Modern Physics*, 73, 1975.

[241] Y.J. Uemura, V.J. Emery, A.R. Moodenbaugh, and M. Suenaga. Systematic variation of magnetic-field penetration depth in high-T and superconductors studied hy muon-spin relaxation. *Physical review B*, 38(1), 1988.

[242] A.T. Fiory, A.F. Hebard, P.M. Mankiewich, and R.E. Howard. Penetration depths of high T_c films measured by two wcoU mutual inductances. *1988*, 52, Appl. Phys. Lett.

[243] H. Jiang, T. Yuan, H. How, A. Widom, and C. Vittoria. Measurements of anisotropic characteristic lengths in YBCO films at microwave frequencies. *J. Appl. Phys.*, 73, 1993.

[244] M. Inoue, T. Kiss, D. Mitsui, T. Nakamura, T. Fujiwara, S. Awaji, K. Watanabe, A. Ibi, Y. Yamada S. Miyata, and Y. Shiohara. Current Transport Properties of 200 A-200 m-Class IBAD YBCO Coated Conductor Over Wide Range of Magnetic Field and Temperature. *IEEE Trans. Appl. Supercond.*, 17(2), 2007.

[245] T. Matsushita, E.S. Otabe, and B. Ni. Irreversibility lines in oxide and metallic superconductors. *Supercond. Sci. Technol*, 5, 1992.

[246] M. Kiuchi, S. Takayama, E.S. Otabe, T. Matsushita, J. Fujikami, K. Hayashi, and K. Sato. Critical current properties in multifilamentary Bi-2223 tape produced by the over pressure processing. *Physica C*, 463, 2007.

[247] K.-H. Müller, D.N. Matthews, and R. Driver. Critical current density of ceramic high-temperature superconductors in a low magnetic field. *Physica C*, 191, 1992.

[248] S. Kobayashi, T. Kaneko, T. Kato, J. Fujikami, and K. Sato. A novel scaling of magnetic field dependencies of critical currents for Ag-sheathed Bi2223 superconducting tape. *Physica C*, 258, 1996.

[249] D.T. Verebelyi, D.K. Christen, R. Feenstra, C. Cantoni, A. Goyal, D.F. Lee, M. Paranthaman, P.N. Arendt, R.F. DePaula, and J.R. Groves andC. Prouteau. Low angle grain boundary transport in $YBa_2Cu_3O_7d$ coated conductors. *Appl. Phys. Lett.*, 76(13), 2000.

[250] K. Yamafuji and T. Kiss. Current-voltage characteristics near the glass-liquid transition in high-T c superconductors. *Physica C*, 290, 1997.

[251] T. Matsushita, A. Matsuda, and K. Yanagi. Irreversibility line and flux pinning properties in high-temperature superconductors. *Physica C*, 213, 1993.

[252] B. Hensel, G. Grasso, and R. Flukiger. Limits to the citical transport current in superconducting (Bi,Pb) $_2Sr_2Ca_2Cu_3O_{10}$ silver sheated tapes : The railway-switch model. *Physical review B*, 51(21), 1995.

[253] D.C. van der Laan, J. Schwartz, B.ten Haken, M. DhallÃ©, and H.J.N. van Eck. Limits to the critical current in $Bi_2Sr_2Ca_2Cu_3Ox$ tape conductors: The parallel path model. *Physical review B*, 77, 2008.

[254] H.W. Weijers, B. ten Haken, H.H.J. ten Kate, and J. Schwartz. Critical Currents in Bi-Sr-Ca-Cu-0 Superconductors up to 33 T at 4.2 K. *IEEE Trans. Appl. Supercond.*, 11(1), 2001.

[255] T. Staiger et al. Critical Current in Silver Sheathed Bi-2223 Tapes. *IEEE Trans. Appl. Supercond.*, 7(2), 1997.

[256] M. Inoue, T. Kiss, K. Motoyama, S. Awaji, K. Watanabe, M. Yoshizumi, Y. Yamada, T. Izumi, and Y. Shiohara. Critical current property in YBCO coated conductor fabricated by improved TFA-MOD process. *Physica C*, 469, 2009.

[257] S.M. Green, C.J. Lobb, and R.L. Greene. The irreversibility line of $(Bi,Pb)_2Sr_2Ca_2Cu_3O_{10}$ determined by DC magnetization. *IEEE Trans. Magn.*, 27(2), 1991.

[258] A. Gladun, G. Fuchs, K. Fischer, D. Busch, R. Eujen, and J. Huedepohl. Critical current densities and activation energy of BiPbSrCaCuO tapes. *IEEE Trans. Appl. Supercond.*, 3(1), 1993.

[259] A. Schilling, R. Jin, J.D. Guo, and h.R. Ott. Irreversibility line of Monocrystalinnine Bi2212: Experimental evidence for a dimensional crossover of the vortex ensemble. *Phys. Rev. Lett.*, 71(12), 1993.

[260] M. Inoue, T. Kiss, M. Kiuchi, M. Takeo, S. Awaji, and K. Watanabe. Angular dependence of E-J characteristics under high magnetic fields in YBCO thin films. *Physica C*, 357-360, 2001.

[261] M. Inoue. High Magnetic Field Properties of Critical Current Density in YBaCuO Coated Conductor Fabricated by Improved TFA-MOD Process. *IEEE Trans. Appl. Supercond.*, 15(2), 2005.

[262] T. Kiss, M. Inoue, S. Nishimura, T. Kuga, T. Matsushita, Y. Iijima, K. Kakimoto, T. Saitoh, S. Awaji, K. Watanabe, and Y. Shiohara. Distribution of pinning strength and scaling behavior in YBCO coated IBAD tape. *Physica C*, 282, 2002.